Materials Science in Additive Manufacturing

eISSN: 2810-9635
Volume 5 Issue 1, March 2026

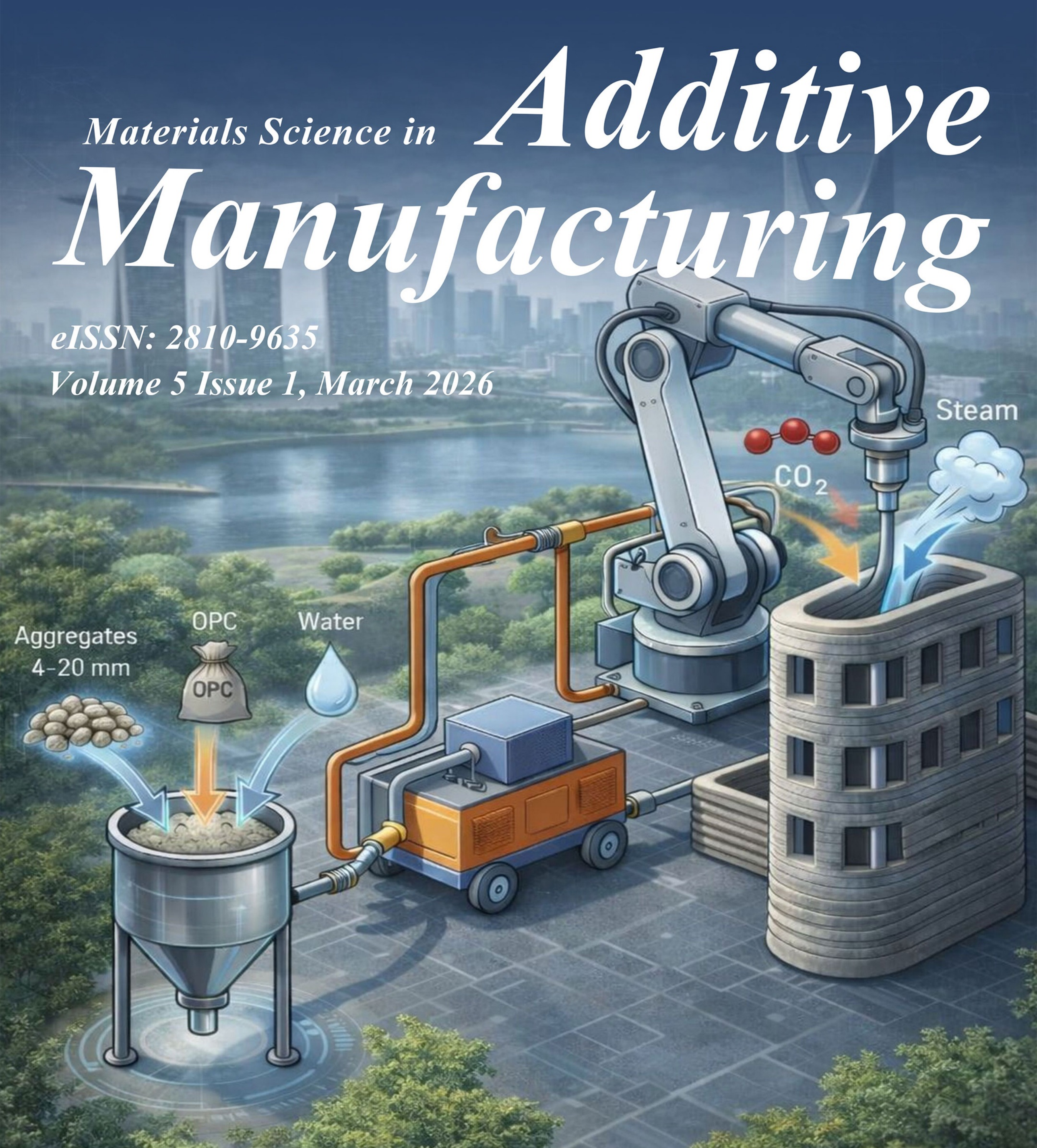

武汉科技大学 WUHAN UNIVERSITY OF SCIENCE AND TECHNOLOGY 1898
ACCSCIENCE PUBLISHING

ACCSCIENCE PUBLISHING

Materials Science in Additive Manufacturing

Online ISSN: 2810-9635

Materials Science in Additive Manufacturing aims to bridge the cutting-edge research between additive manufacturing and the entire spectrum of materials science. The journal covers all applied and fundamentals of processing, synthesis, structure, composition, properties and performance of materials designed or manipulated for additive manufacturing. The journal covers a wide scope of innovative techniques, processes, methods, and applications.

About the Publisher

AccScience Publishing is a publishing company based in Singapore. We publish a range of high-quality, open-access, peer-reviewed journals and books from a broad spectrum of disciplines.

Contact Us

Managing Editor
msam.office@accscience.sg

AccScience Publishing
9 Raffles Place, Republic Plaza 1 #06-00 Singapore 048619.

Volume 5 • Issue 1 • March 2026
ISSN 2810-9635 (online)

MATERIALS SCIENCE IN ADDITIVE MANUFACTURING

Editor-in-Chief

Chee Kai Chua

Singapore University of Technology and Design, Singapore

ACCSCIENCE PUBLISHING

MATERIALS SCIENCE IN ADDITIVE MANUFACTURING

ISSN: 2810-9635 (online)

Editorial and Production Credits

Publisher: AccScience Publishing
Managing Editor: Rhea Chen
Editorial Assistant: Flora Kang
Production Editor: Puva Ramakrishnan
Article Layout and Typeset: Sinjore Technologies (India)

Supplementary file

Supplementary files of articles can be obtained at https://accscience.com/journal/MSAM/5/1.

Disclaimer

AccScience Publishing is not liable to the statements, perspectives, and opinions contained in the publications. The appearance of advertisements in the journal shall not be construed as a warranty, endorsement, or approval of the products or services advertised and/or the safety thereof. AccScience Publishing disclaims responsibility for any injury to persons or property resulting from any ideas or products referred to in the publications or advertisements. AccScience Publishing remains neutral with regard to jurisdictional claims in published maps and institutional affiliations.

Material Science in Additive Manufacturing

Editorial Board

ACCSCIENCE PUBLISHING

Volume 5 | Issue 1 | March 2026 |

Materials Science in Additive Manufacturing

https://accscience.com/journal/msam

CONTENTS

ACCSCIENCE PUBLISHING

Materials Science in Additive Manufacturing

REVIEW ARTICLE

Influence of porous structures on the degradation behavior of additively manufactured magnesium and magnesium alloy orthopedic implants

Haoxuan Zeng[1], Huiwen Huang[1,2]*, Qiao Li[2]*, Chunli Song[3,4,5], Lizhen Wang[1,2], and Yubo Fan[1,2]

[1]Medical Engineering and Engineering Medicine Innovation Center, Hangzhou International Innovation Institute, Beihang University, Hangzhou, Zhejiang, China

[2]Key Laboratory of Biomechanics and Mechanobiology of the Ministry of Education, Beijing Advanced Innovation Center for Biomedical Engineering, School of Biological Science and Medical Engineering, Beihang University, Beijing, China

[3]Department of Orthopedics, Peking University Third Hospital, Beijing, China

[4]Beijing Key Laboratory of Spinal Diseases, Department of Orthopedics, Peking University Third Hospital, Beijing, China

[5]Engineering Research Center of Bone and Joint Precision Medicine, Ministry of Education, Peking University Third Hospital, Beijing, China

***Corresponding authors:**
Huiwen Huang
(huang_huiwen@buaa.edu.cn)
Qiao Li
(qiaoli@buaa.edu.cn)

Citation: Zeng H, Huang H, Li Q, Song C, Wang L, Fan Y. Influence of porous structures on the degradation behavior of additively manufactured magnesium and magnesium alloy orthopedic implants. *Mater Sci Add Manuf*. 2026;5(1):025290063. doi: 10.36922/MSAM025290063

Received: July 15, 2025

Revised: August 11, 2025

Accepted: August 12, 2025

Published online: October 7, 2025

Abstract

The escalating incidence of bone defects has prompted a substantial demand for orthopedic implants, and additively manufactured biodegradable porous magnesium and magnesium alloy orthopedic implants have demonstrated significant potential for clinical applications. However, the mismatch between degradation-induced changes in mechanical properties and tissue regeneration remains a major challenge hindering their applications. As porous structure is a critical factor influencing the degradation behavior of magnesium/magnesium alloy orthopedic implants, this study aims to comprehensively review the current state of research in this area. The degradation behavior of magnesium/magnesium alloy orthopedic implants has been investigated using both experimental and numerical simulation methods. Degradation experiments have enabled direct observations of the influences of structures on degradation behavior and underlying mechanisms. Numerical simulations have been employed to analyze the stress and strain distributions within the structure during degradation and surrounding tissue regeneration, facilitating the investigation of the "structure-stress-tissue regeneration" regulation on degradation. Porous structures play critical roles in regulating mechanical properties, bearing physiological loads, and establishing a localized mechanical microenvironment of magnesium/magnesium alloy orthopedic implants. Design variables, including porosity, specific surface area, pore size, shape, and interconnectivity, influence the macroscopic mechanical properties, structural deformation, stress distribution, and contact with surrounding tissues, thereby regulating degradation behavior and tissue regeneration of implants. However, models that quantitatively describe the "porous structural variables-degradation-tissue regeneration" interaction remain to be developed. This study systematically summarizes the influences of porous structures on the degradation behavior of additively manufactured magnesium/

magnesium alloy orthopedic implants and the "structure-mechanics-degradation-biology" interaction mechanisms. This review provides a systematic understanding of the state-of-the-art research and future directions to guide the development and applications of orthopedic implants.

Keywords: Magnesium alloy; Porous orthopedic implants; Microstructures; Degradation behavior; Tissue regeneration

1. Introduction

The global incidence of bone defects resulting from trauma, bone tumors, infection, and osteoporosis is escalating annually, affecting over 20 million individuals per year.[1,2] In China, the number of newly diagnosed cases of bone defects exceeds 3 million yearly.[3] This rate is projected to further increase with the growing global aging population.[4] Bone repair surgery offers an effective means to restore or replace damaged bone tissues and facilitate their functional recovery. Autologous bone grafting, considered the gold standard in clinical bone defect repair, remains a widely applied surgical approach.[5] However, the application of autologous bone grafting is limited by donor site morbidity, restricted availability of graft material, and prolonged surgical duration,[6,7] potentially leading to extended post-operative pain for patients.[8] Compared with autologous bone grafting, orthopedic implants offer a broader range of sourcing options for bone tissue repair and replacement.[3] Orthopedic implants can overcome the limitations of autologous grafts, such as donor site morbidity and limited availability, leading to increased interest and broader applications.

The escalating incidence of bone defects has generated a substantial demand for orthopedic implants. To effectively repair and replace the damaged bone tissues, the ideal orthopedic implants should possess several properties. First, they must exhibit mechanical compatibility. The mechanical properties of the implant should closely match those of the surrounding bone tissues at the repair site. Excessively high stiffness in the orthopedic implant can lead to stress shielding,[9] hindering bone remodeling and potentially resulting in bone resorption and aseptic loosening.[10,11] Conversely, insufficient stiffness of the orthopedic implant may fail to provide adequate mechanical support for the regenerating bone tissues,[12] increasing the risk of secondary injury to the affected area.[13] Second, they should possess fatigue resistance, which defines the ability of orthopedic implants to withstand cyclic loading over an extended period without experiencing progressive damage or failure. Given that bones are the critical load-bearing structures in the human body,[14,15] they bear the complex physiological loads generated by daily activities.[16] Such a mechanical environment requires adequate fatigue resistance in orthopedic implants to ensure long-term functionality without fatigue failure.[17] Third, the implants must be biocompatible to ensure the safety and efficacy of medical devices. During prolonged interactions with the surrounding tissues, orthopedic implants must be non-toxic and elicit minimal or no adverse immune responses,[18] ensuring their safety and reliability *in vivo*. Finally, successful implants require osseointegration. Osseointegration is defined as the direct and intimate connections between the implant and surrounding bone tissues without an intervening fibrous connective tissue layer,[19,20] which enhances the mechanical strength of newly formed bone and promotes successful bone repair. Traditional solid orthopedic implants often exhibit a significant mismatch in the elastic modulus compared to that of native bone tissues.[21] This pronounced stress-shielding effect impedes the process of bone regeneration. Furthermore, bone tissues have limited capacity to grow into the interior of solid implants,[22] hindering the formation of a strong interface and resulting in poor osseointegration.[23] Compared with solid implants, porous orthopedic implants offer several advantages, such as reduced stress-shielding effect and enhanced osseointegration performance. The elastic modulus of porous structures can be adjusted to more closely match that of bone tissue, effectively mitigating the stress-shielding effect.[24] By adjusting the porous geometry, it is possible to achieve a favorable mechanical compatibility between the implant and the host bone tissues.[25] In addition, the porous structures provide ample space for the adhesion and proliferation of osteogenic cells[26] and facilitate the transport of nutrients and metabolic waste products,[27,28] thereby improving osseointegration efficiency.[29]

Additive manufacturing (AM) is the general term for technologies that successively merge materials to create physical objects as specified by three-dimensional (3D) model data.[30] Over the past few years, AM has been increasingly utilized in the fabrication of porous orthopedic implants.[24] Compared to conventional manufacturing techniques, AM offers several advantages. One such

advantage is that AM minimizes or eliminates material waste.[31] The layer-by-layer construction principle enables efficient raw material utilization and allows residual materials to be reused.[32] Furthermore, AM facilitates the customization of porous orthopedic implants to conform to irregular bone defects.[33] This customization process can incorporate patient-specific anatomical data for precise adjustment.[34] In addition, AM enables the design of microstructural features, such as pore size and porosity, to optimize osseointegration.[35] Commonly used porous orthopedic implants are fabricated from non-degradable metallic materials such as titanium/titanium alloys. However, these materials necessitate a second surgical procedure for removal and are associated with potential drawbacks, including chronic inflammation and abnormal angiogenesis.[36] Biodegradable metal-derived porous orthopedic implants offer a promising alternative, as they are completely resorbed *in vivo*, eliminating the need for secondary surgery and reducing patients' discomfort and economic burden,[37] thereby addressing the limitations of non-degradable porous orthopedic implants. Among various biodegradable metals, magnesium/magnesium alloy porous orthopedic implants have demonstrated significant application potential. Magnesium, as an essential macronutrient for the human body, is involved in numerous fundamental cellular biochemical reactions and promotes tissue regeneration. Furthermore, the density of magnesium is nearly identical to that of bones, significantly mitigating the stress-shielding effect. Magnesium is also one of the most readily machinable metals, enabling the fabrication of complex geometries.[38] However, the application of biodegradable magnesium/magnesium alloy orthopedic implants is currently hindered by several challenges. Primarily, the excessively rapid degradation rates of magnesium/magnesium alloys lead to the premature decline in mechanical properties, failing to provide reliable mechanical support for immature bone tissues.[39] Secondly, the degradation behavior of magnesium/magnesium alloys is difficult to control, resulting in a mismatch between degradation rates and bone repair rates.[40] Numerous factors influence the degradation behavior of magnesium/magnesium alloy porous orthopedic implants, including structural design,[41] material composition,[42,43] loading conditions,[44,45] and physiological environment.[46,47] Among these factors, structural design is a critical determinant. This paper focuses on the impacts of porous structures on the degradation behavior of magnesium/magnesium alloy orthopedic implants to provide a comprehensive overview of the current research status in this field. In subsequent sections of this review, the methodologies used to investigate the degradation behavior of magnesium/magnesium alloy-porous orthopedic implants are summarized, the relationships between porous structures and degradation behavior of implants are systematically analyzed, and the "structure-mechanics-biology" interaction mechanisms and limitations of the existing research are discussed. This study aims to provide a systematic understanding and summary of the current research state and future research directions in this field, ultimately guiding the structural optimization and application of biodegradable magnesium/magnesium alloy orthopedic implants.

2. AM and degradation assessments of porous magnesium/magnesium alloy orthopedic implants

2.1. AM of porous magnesium/magnesium alloy orthopedic implants

AM methods can be categorized based on the initial state of the material, such as liquid, filament/paste, powder, and solid sheet.[32] Alternatively, they can be classified according to their manufacturing principle. Magnesium and magnesium alloys maintain a strong connection with various industries. Their high specific strength makes them highly suitable as structural materials in aerospace, automotive, and electronics industries. Concurrently, magnesium and magnesium alloys have garnered significant attention within the medical field due to their inherent biodegradability and their lower elastic modulus, which closely mimics that of natural bone.[30] At present, the primary AM methods (Figure 1) employed for magnesium/magnesium alloy primarily include[48] powder bed fusion (PBF), directed energy deposition (DED), indirect AM (I-AM), wire arc AM (WAAM), friction stir AM (FSAM), fused filament fabrication (FFF), solvent-cast 3D printing (SC-3DP), binder jetting (BJ), paste extrusion deposition (PED), and sheet lamination (SL).[49,50] FSAM and WAAM have limited applicability for medical uses due to the potentially coarse scaffold structures produced.[51,52] Other novel AM techniques are also suitable for fabricating porous bone implants from magnesium/magnesium alloys, such as DED with an externally applied ultrasonic field[53] and DED with arc oscillation.[54]

PBF and DED are currently among the most frequently utilized AM methods. A representative technique of PBF is selective laser melting (SLM), which has been successfully applied in the fabrication of implant materials such as 316L stainless steel and Ti6Al4V, and is progressively being extended to the manufacturing of magnesium/magnesium alloy implants.[55] SLM offers several advantages, including excellent mechanical properties, high precision, efficient material utilization, and near-net-shape capability,[56] along with well-defined grain morphology and good structural integrity.[57] However, SLM also presents notable drawbacks,

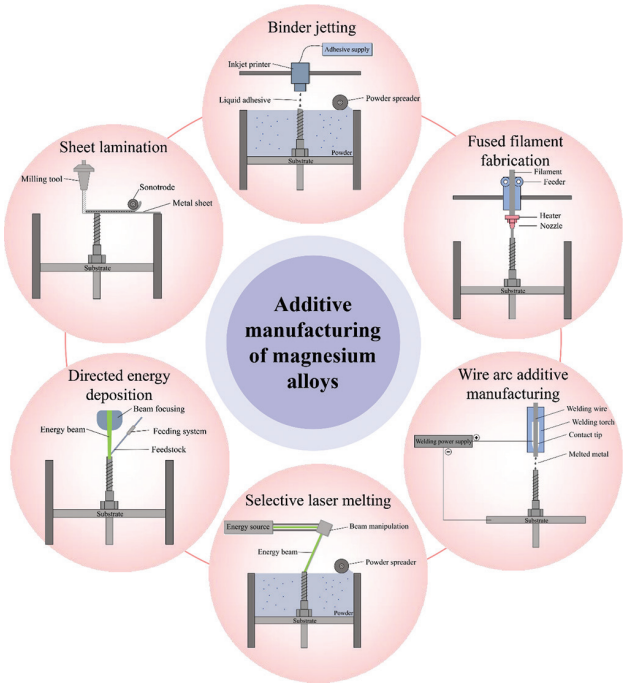

Figure 1. The process of additive manufacturing of porous magnesium/magnesium alloy structures

such as long manufacturing times and high residual stress.[58] Furthermore, due to the large surface area of magnesium powder, its high flammability poses operational safety concerns when using laser melting.[59] Selective electron beam melting (SEBM), another PBF technique, utilizes an electron beam as the energy source instead of a laser. SEBM offers shorter manufacturing times and lower residual stresses compared to SLM, while maintaining comparable precision and structural fidelity. However, SEBM is limited to conductive materials due to its reliance on electrical conductivity.[58] In contrast to PBF, DED does not require powder materials to be spread on a bed, and the materials can be added to a substrate and existing components.[60] Laser-engineered net shaping, a common form of DED, offers superior cooling effects and better remanufacturing capabilities compared to PBF.[61] Due to its high cooling rate, laser engineered net shaping can produce parts with excellent mechanical properties. However, this technique also has drawbacks, such as low manufacturing efficiency and high surface roughness.[62]

Other AM methods are employed less frequently. I-AM requires modeling in software, followed by the generation of a polymer template using AM techniques. This template is then infiltrated with a sodium chloride (NaCl) slurry, and the polymer is removed through a heating process. Subsequent sintering forms a negative NaCl template, into which molten magnesium is cast. The desired magnesium implant is obtained after dissolving the NaCl.[51] I-AM offers high precision, but the resulting negative NaCl template is susceptible to corrosion, and replicating complex geometries can be challenging.[63] Another technique, FFF, involves heating a filament composed of magnesium alloy and a polymer binder to a molten state, followed by extrusion through a nozzle and layer-by-layer deposition along a predetermined path, solidifying on cooling. FFF is popular due to its low cost and ability to provide personalized prototyping of complex shapes without requiring expensive molds.[64] SC-3DP, an emerging AM technique, extrudes an ink containing metal or other powder particles, along with a binder system composed of polymers and volatile solvents, through a nozzle. The 3D-printed structure then undergoes debinding and sintering. SC-3DP offers high precision, enables 3D printing at room temperature, and fabricates complex structures with hierarchical porosity and desired alloy compositions. However, the high reactivity of magnesium powder limits the selection of the binder component.[59] BJ involves spreading a layer of powder on a build plate, followed by the deposition of a binder that hardens and bonds the particles. This process is repeated layer by layer until the desired geometry is achieved.[61] BJ technology exhibits good material adaptability and precision, enabling the creation of complex shapes and internal structures that are difficult to achieve with traditional processes.[51] PED is a process in which a paste is extruded from a syringe onto a substrate, with the substrate moving relative to the syringe to form the desired 3D contour. This method is primarily used for implants containing organic components that cannot withstand high temperatures, but it suffers from lower precision.[65] Ultrasonic AM (UAM) and laminated object manufacturing (LOM) are two common methods of SL. UAM is an ultrasonic welding technique that merges metal sheets, while LOM can heat or pressurize metal sheets using a heated cylindrical roller. UAM and LOM can construct layers with good accuracy and resolution, but achieving geometric accuracy in the Z-direction is difficult, thus limiting overall structural fidelity.[58] Different AM methods offer distinct advantages and disadvantages, and the selection of a specific method should be based on the particular manufacturing requirements.

Different processing methods lead to distinct microstructural evolutions, and these evolutions enhance the mechanical properties of implants through mechanisms such as homogenization, solid solution strengthening, and second-phase strengthening.[66] Compared to conventionally processed counterparts, magnesium/magnesium alloy orthopedic implants fabricated through AM techniques exhibit superior mechanical properties (Table 1).[67] This is attributed to the moderate cooling rates experienced during the AM process, resulting in a finer

Table 1. The mechanical properties of various magnesium alloys

Magnesium alloy	Production method	Mechanical properties			References
		Yield strength (MPa)	Ultimate tensile strength (MPa)	Elongation (%)	
WE43	Laser powder bed fusion	296	308	12	[69]
WE43	Extrusion	284	306	22	
WE43	Casting	145	189	4	
AZ80M	Wire arc additive manufacturing	119	237	12	[70]
AZ80M	Extrusion	207	324	17	
AZ80M	Casting	76	158	7	
GZ151K	Selective laser melting	345	368	3	[71]
GZ151K	As cast	184	277	5	
AZ61	Selective laser melting	219	272	3	[72]
AZ61	As cast	99	149	5	

and more homogeneous microstructure.[68] Such a fine and homogeneous microstructure, in turn, contributes to improved strength and hardness of magnesium/magnesium alloy bone implants.[67]

Process parameters in AM techniques are critical factors influencing the microstructure of orthopedic implants,[67] and the specific parameters of interest vary across different AM technologies. For instance, PBF focuses on powder size, energy density, laser power, scanning speed, and layer thickness. At lower energy densities, less elemental evaporation occurs, leading to a higher density in the final implant. WAAM is concerned with actuator precision, welding parameters, pattern, and arc thermal stability. Grain size decreases with increasing pulse frequency, resulting in a finer microstructure in the final implant. FSAM considers tool speed, travel speed, plunge depth, tool geometry, and feed rate, with different microstructures observed due to temperature gradients and spatial strain distributions. BJ prioritizes printing direction, printing speed, scanning technique, heating power ratio, and powder distribution. Optimized binders can effectively penetrate fine pores to form strong and uniform neck connections, ensuring the mechanical strength of the implant.[51] Therefore, it is crucial to select the specific AM technique and its process parameters based on the particular requirements of the implant.

2.2. Research methodologies for degradation behavior of porous magnesium/magnesium alloy orthopedic implants

The degradation behavior of magnesium/magnesium alloy orthopedic implants has been investigated using both experimental and numerical simulation methods. These methodologies offer distinct advantages and limitations in characterizing and describing the degradation process.

2.2.1. Degradation experiments

Degradation experiments are the most direct and commonly employed method to study the degradation behavior of magnesium/magnesium alloy orthopedic implants. Degradation experiments are typically categorized as *in vitro* or *in vivo* experiments (Figure 2). *In vitro* degradation experiments necessitate the establishment of a simulated physiological environment. To mimic the physiological environment of the human body, the temperature of the *in vitro* degradation experiment is consistently maintained at approximately 37°C.[73] Commonly used solutions for simulating body fluid environments include phosphate-buffered saline,[74] physiological saline solution,[75] Hank's balanced salt solution,[76] and Dulbecco's Modified Eagle Medium.[77] While each of these solutions can be used to simulate the body fluid environment, their fidelity to actual physiological conditions varies. The phosphate-buffered saline and physiological saline solutions lack the essential buffering components of the human body,[78] which may lead to pH fluctuations and deviations from the actual situation. Hank's solution lacks the common proteins of the human body,[79] influencing the degradation rate of magnesium/magnesium alloy orthopedic implants and affecting the accuracy of experimental results.[80,81] The Dulbecco's Modified Eagle Medium provides a better simulation of the actual body fluid environment, but is susceptible to bacterial contamination, which may increase the content of collected carbon dioxide and hydrogen gas, leading to inaccurate measurements of the magnesium/magnesium alloy orthopedic implant degradation rate.[82] After the establishment of a simulated body fluid environment, magnesium/magnesium alloy orthopedic implants are immersed within the solution. The immersion conditions can be classified into three

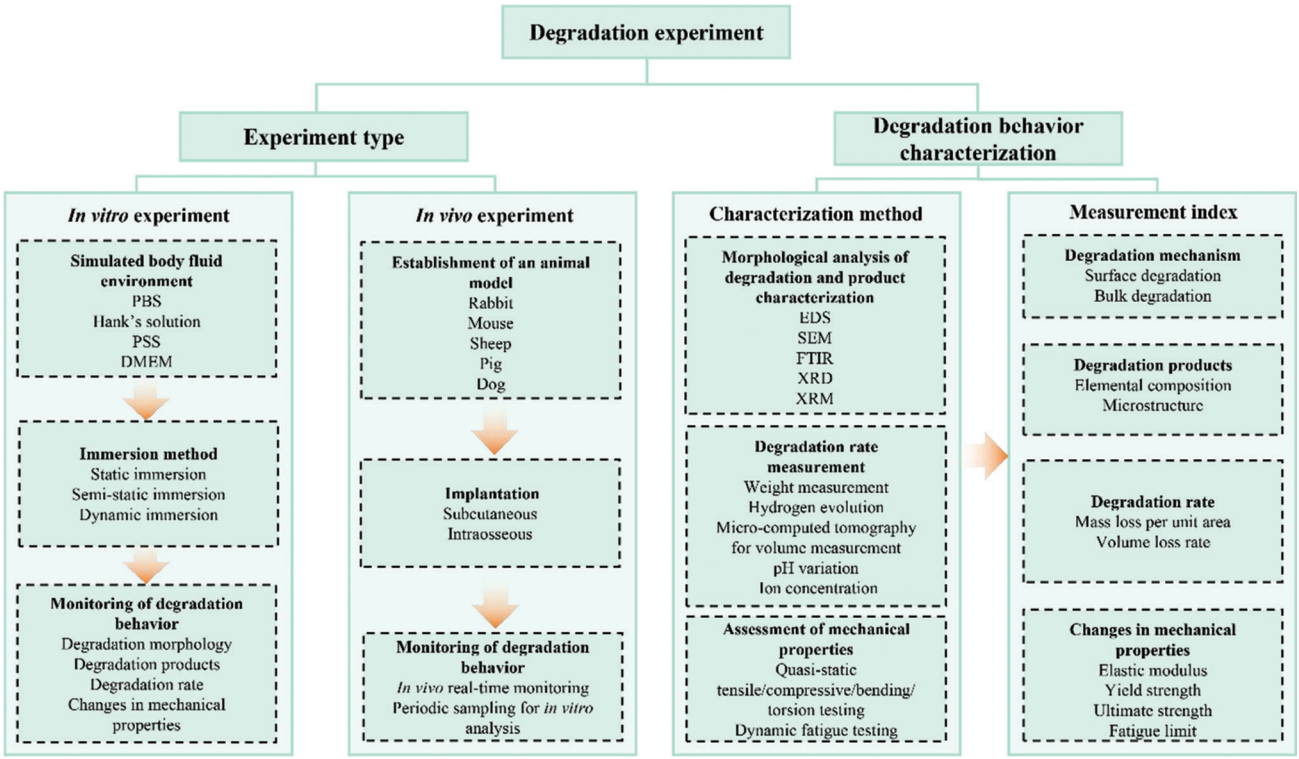

Figure 2. Workflow of the degradation experiments
Abbreviations: DMEM: Dulbecco's Modified Eagle Medium; EDS: Energy dispersive spectroscopy; FTIR: Fourier-transform infrared spectroscopy; PBS: Phosphate-buffered saline; PSS: Physiological saline solution; SEM: Scanning electron microscopy; XRD: X-ray diffraction; XRM: X-ray microscopy

types: static,[74] semi-static,[83] and dynamic.[84] Semi-static conditions are achieved through periodic replacement of the solution,[83] while dynamic conditions are realized by controlling the flow of the solution at a specific flow rate through the peristaltic pump.[84] Most studies employed the static or semi-static immersion conditions. Under the static conditions, corrosion products accumulate on the implant surface, forming a protective layer that reduces the degradation rate compared with the dynamic conditions.[74] Furthermore, the static and semi-static conditions fail to simulate the body fluid flow features of the *in vivo* environment.[85] Dynamic conditions simulate the body fluid flow, thereby offering a more accurate simulation of the *in vivo* environment compared with the static and semi-static conditions. The flow rate of the simulated body fluid adopted in the *in vitro* experiments is generally set to 2 mL/(100 mL·min), which is close to the body fluid flow rate observed in the musculoskeletal system.[86] The *in vitro* degradation experiments enable a direct observation of the structural changes and the measurement of degradation rates in magnesium/magnesium alloy orthopedic implants during degradation.[87] However, the duration of *in vitro* experiments is often limited to 28 days or less,[88,89] making it difficult to observe the long-term degradation behavior of magnesium/magnesium alloy orthopedic implants and to simulate the influences of surrounding bone tissue growth. In contrast, the *in vivo* degradation experiments, which involve implanting magnesium/magnesium alloy orthopedic implants into animals for extended periods, can address this limitation[87] and provide a more accurate assessment of the practical degradation behavior of magnesium/magnesium alloy orthopedic implants in the physiological environment.[90]

Based on the *in vitro* or *in vivo* degradation experiments, the degradation behavior of magnesium/magnesium alloy orthopedic implants can be further characterized and analyzed after various immersion/implantation periods. This process typically includes the characterization of degradation morphologies, the measurement of degradation rates, and the evaluation of mechanical properties. Characterization methods for the degradation morphologies of magnesium/magnesium alloy orthopedic implants include scanning electron microscopy equipped with energy-dispersive X-ray spectroscopy, X-ray diffraction, Fourier-transform infrared spectroscopy, and X-ray microscopy.[84,85] Scanning electron microscopy equipped with energy-dispersive X-ray spectroscopy enables the observation of macroscopic and microscopic surficial features of magnesium/magnesium alloy orthopedic implants,[76] allowing the degradation mode and

uniformity analysis.[89] Furthermore, the X-ray diffraction and Fourier-transform infrared spectroscopy techniques can be used to identify and analyze the chemical structure of degradation products,[89] facilitating the investigation of the micro-mechanisms of degradation product deposition. The X-ray microscopy analysis enables further exploration of the 3D distribution of degradation products,[85] providing more comprehensive experimental data for the degradation behavior analysis of magnesium/magnesium alloy orthopedic implants. The degradation rate of magnesium/magnesium alloy orthopedic implants, as a function of degradation time, can be quantitatively described by directly measuring the mass loss after different degradation periods.[91,92] However, the chromic acid used in this process can produce carcinogenic substances and requires cautious handling.[93] For structures with large surficial area and small pore sizes, the mass loss measurement results may be unreliable.[89] During the degradation of magnesium/magnesium alloys, the release of hydrogen gas and magnesium ions increases the pH value and osmotic pressure of the simulated body fluid.[85] In addition, the pore size of porous magnesium/magnesium alloy orthopedic implants increases with the degree of degradation; thus, the change in pore size distribution can directly reflect the degree of degradation.[83] Therefore, the degradation rate of magnesium/magnesium alloy orthopedic implants can also be indirectly and qualitatively characterized by measuring the variation of pH values,[91] the release of magnesium/calcium/phosphorus ions,[65] the osmotic pressures of the simulated body fluid, and the distribution of the pore size.[83] By measuring the hydrogen evolution rate and converting it to mass loss based on the magnesium corrosion equation,[83] the real-time degradation rate of magnesium/magnesium alloy orthopedic implants can be obtained, without being affected by the deposition of degradation products. Compared to the direct mass loss measurement, this method provides a more accurate measurement of the degradation rate.[94] In addition to mass loss, volume loss is also an important indicator to quantitatively describe the degradation rate of magnesium/magnesium alloy orthopedic implants. In general, the 3D models of the implant before and after degradation can be obtained through micro-computed tomography scanning, where the volume change can be calculated.[95,96] The mechanical properties, including elastic modulus, yield strength, and ultimate tensile strength, of magnesium/magnesium alloy orthopedic implants after different degradation periods can be assessed through mechanical tests.[89] Based on the mechanical testing data, the relationships between the mechanical properties and degradation behavior can be quantitatively analyzed. In the *in vivo* degradation experiments, the degradation rate of magnesium/magnesium alloy orthopedic implants located relatively superficially under the skin can be monitored by contacting the tip of a highly hydrogen-sensitive biosensor to the skin above the air cavity at the implantation site. A miniature positioner (Figure 3) can be used to move the biosensor tip if needed.[97] Moreover, the degradation rate of magnesium/magnesium alloy orthopedic implants can be monitored by placing a visual hydrogen sensor on the skin at the center of the visible air cavity.[98] Compared to the *in vivo* degradation rate monitoring techniques, the visual hydrogen sensor method is simpler, more convenient to operate, and requires less stringent experimental conditions. It can accurately and quantitatively measure the hydrogen concentration in the air cavity in real-time, especially for the rapidly corroding implants. However, the time required for the color of the visual hydrogen sensor to change is relatively long.[98] Moreover, the visual hydrogen sensor method cannot measure the overall corrosion rate over the entire implantation period.[98] The degradation morphology characterization, degradation rate measurement, and mechanical testing results obtained through degradation experiments provide basic experimental data, based on which the factors influencing the degradation behavior of magnesium/magnesium alloy orthopedic implants and the corresponding mechanisms can be analyzed and investigated further.

2.2.2. Numerical simulation of degradation

Based on the degradation morphology characterization, degradation rate, and mechanical properties changes obtained through degradation experiments, numerical simulation methods can be applied to further investigate the mechanical regulation mechanisms governing the degradation behavior of magnesium/magnesium alloy orthopedic implants (Figure 4). Numerical simulation models commonly used to simulate the degradation

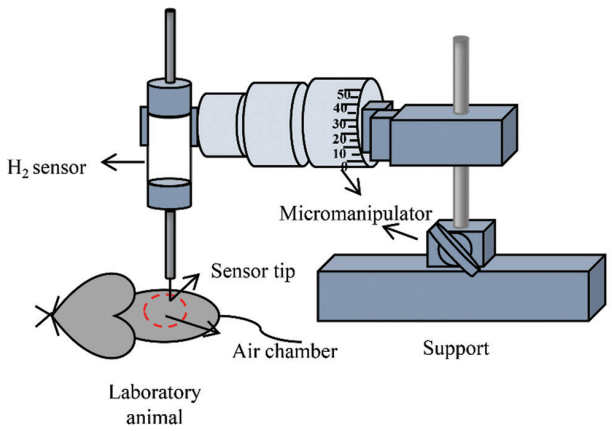

Figure 3. Schematic diagram of the visual hydrogen (H_2) sensor setup. Figure 3 was created with Microsoft PowerPoint 2021 (Microsoft Corporation) by Haoxuan Zeng (2025)

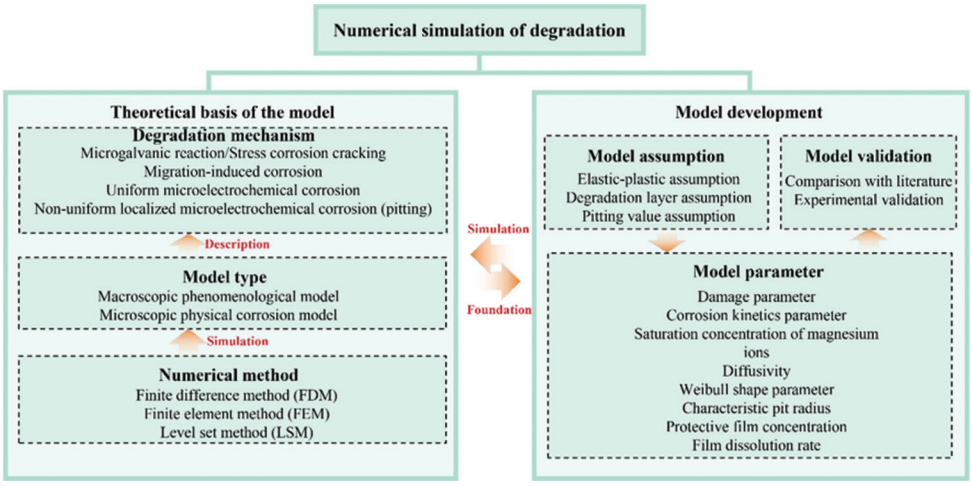

Figure 4. Workflow of the degradation numerical simulations

of magnesium/magnesium alloy orthopedic implants can be categorized into macroscopic phenomenological models and microscopic corrosion physics models.[99] The macroscopic phenomenological models focus on describing the overall material loss during the degradation process,[99] while microscopic corrosion physics models offer a more detailed simulation of the degradation process. The microscopic corrosion physics models are capable of capturing the potential chemical interactions, thereby enabling the simulations of processes such as coating effects, protective layer formation, and pH changes[100] and effectively complementing macroscopic phenomenological models.[101] The degradation mechanisms of magnesium/magnesium alloy orthopedic implants under physiological conditions are complex, including micro-electroplating reactions, uniform micro-electrochemical corrosion, non-uniform pitting micro-electrochemical corrosion, stress corrosion cracking, and migration-driven corrosion.[102] Some studies focused on the development of degradation models to thoroughly and meticulously describe a specific mechanism,[101,103] while others developed degradation models that comprehensively considered multiple mechanisms to simulate actual degradation behavior more accurately.[104,105] The commonly used numerical calculation methods include the finite difference method,[106] the finite element method,[107] and the level set method.[37] The finite difference method is among the earliest methods adopted in numerical simulation and can be used to simulate the one-dimensional degradation behavior of materials. More recent studies employed a combination of the finite difference method and the finite volume method, which were able to simulate the degradation behavior in higher dimensions.[108] Furthermore, the level set method enables the acquisition of locally refined meshes without the need to re-mesh the entire domain, thereby reducing the computational costs.[106]

After determining the degradation mechanism and numerical calculation method for model development, reasonable assumptions must be established for the developed numerical simulation model. The most fundamental assumption involves the simplification of material properties. The most widely accepted simplification is the elastoplasticity hypothesis, wherein the elastic deformation phase is described using linear and isotropic behavior, while the plastic deformation phase is described using the J_2 flow theory with non-linear isotropic hardening.[103] Apart from the simplified assumptions of material properties, other assumptions adopted in the model are determined based on the specific research focus. For example, Gartzke *et al.*[37] focused on the influence of the degradation layer on degradation. In their simulation model, a constant magnesium concentration was assumed in the undegraded core of the structure, while the magnesium concentration in the degradation layer decreased from the interior toward the exterior.[37] Quinn *et al.*[109] primarily considered the influence of the β-phase component on degradation and assumed a continuous distribution of pitting values generated using a set of continuous random numbers. Parameters in the degradation model are critical elements influencing the accuracy of the model in simulating the actual degradation behavior of magnesium/magnesium alloy orthopedic implants and are closely related to the type of developed model.[109] The critical parameters in macroscopic phenomenological models include damage and corrosion kinetics parameters,[103] while in microscopic corrosion physics models, the critical parameters include magnesium ion saturation concentration and diffusivity.[101] Furthermore, some parameters are closely related to the specific degradation mechanisms, such as the Weibull shape parameter and characteristic pit radius in non-

uniform pitting micro-electrochemical corrosion,[110] the concentration of the protective film formed on the surface, and the reaction rates of film formation/dissolution in migration-driven corrosion.[102] Existing studies generally assigned values to the parameters in numerical simulation models of degradation by referencing previous literature. However, the validation and calibration of these parameters are necessary to ensure the effectiveness and usability of the developed numerical simulation models.[111] The model validation and calibration are commonly conducted through comparison with literature data[112] or collected degradation experimental data.[113] Comparison metrics often include the primary indicators of concern in degradation experiments, such as mass loss,[111] hydrogen evolution,[114] pH values,[112] and magnesium ion concentration.[37] Furthermore, some studies applied the well-validated and calibrated models to further demonstrate their advantages in the simulation of degradation. For example, Barzegari *et al.*[100] verified the effectiveness and usability of a degradation numerical simulation model established based on Bayesian optimization, then used hydrogen evolution as an input parameter to simulate the output pH value results.[100] The simulated pH values differed by 5.35% in NaCl solution and 1.03% in simulated body fluid. Subsequently, they simulated a 42-day degradation process of a degradable bone screw within 9 h and characterized the magnesium ion concentration and mass loss during the degradation process.[100] It was validated that the established numerical simulation model effectively predicted the degradation behavior of pure magnesium-based biomaterials and improved the computational efficiency.[100]

Numerical simulations enable the analysis of the influence of various factors on the degradation behavior of magnesium/magnesium alloy orthopedic implants by adjusting model parameters and boundary conditions, offering a more efficient and resource-saving approach compared with degradation experiments. Through numerical simulations, the stress and strain distributions in the structure during degradation can be computed, which are difficult to obtain through *in vitro* degradation experiments and crucial for the prediction of failure of magnesium/magnesium alloy orthopedic implants.[115] Moreover, the influence of the magnesium/magnesium alloy orthopedic implant structure on the growth of surrounding bone tissues can be modeled through numerical simulation. The computational fluid dynamics models can be used to simulate the distributions of the internal flow fields of magnesium/magnesium alloy orthopedic implants, which facilitate the analysis of the interacting mechanisms of "structure-stress-degradation-tissue repair."[116,117] Combined with degradation experiments, numerical simulation enables the in-depth analysis of the mechanical mechanisms by which various factors influence the degradation behavior of magnesium/magnesium alloy orthopedic implants. The results of numerical simulations can be cross-validated with those of degradation experiments, providing a basis for the design optimization of magnesium/magnesium alloy orthopedic implants. However, the numerical simulations of magnesium/magnesium alloy orthopedic implants' degradation behavior also possess limitations. The parameters used in the numerical model may not perfectly match the practical physiological conditions, leading to deviations between the simulation results and the actual situations. In addition, it is difficult to simultaneously balance the accuracy and universality of the model. Different numerical simulation models are necessary to simulate the degradation behavior of orthopedic implants with various material compositions and structural designs.

3. Influences of porous structures on the degradation behavior of magnesium/magnesium alloy orthopedic implants

3.1. Degradation mechanisms of magnesium/magnesium alloy implants

The degradation mechanisms of magnesium/magnesium alloys in physiological environments are complex, including uniform micro-electrochemical corrosion, non-uniform pitting micro-electrochemical corrosion, and stress corrosion cracking, as well as galvanic corrosion, crevice corrosion, fretting corrosion, and erosion corrosion mechanisms.[118] Despite the diverse and complex nature of these corrosion mechanisms, existing research commonly employs the electrochemical reaction of magnesium with water to describe the degradation mechanism of magnesium/magnesium alloy orthopedic implants.[119] The overall reaction is divided into anodic and cathodic reactions. In the anodic reaction, magnesium corrodes, releasing magnesium ions and electrons. In the cathodic reaction, water reacts with the electrons released from the anodic reaction to produce hydrogen gas and hydroxyl ions. Magnesium ions then combine with these hydroxyl ions to form magnesium hydroxide.[12] The final degradation products are magnesium hydroxide and hydrogen gas. The overall chemical equations are as follows (Equations I-III):[119]

$$\text{Overall reaction: } Mg(s) + 2H_2O\,(aq) \rightarrow Mg(OH)_2\,(s) + H_2\,(g) \quad \text{(I)}$$

$$\text{Anodic reaction: } Mg\,(s) \rightarrow Mg^{2+}(aq) + 2e^- \quad \text{(II)}$$

$$\text{Cathodic reaction: } 2H_2O\,(aq) + 2e^- \rightarrow H_2\,(g) + 2OH^-\,(aq) \quad \text{(III)}$$

3.2. Influences of alloy composition and surface treatments on the degradation behavior of magnesium/magnesium alloy orthopedic implants

The degradation rate of magnesium alloy orthopedic implants can be controlled by altering their alloy composition.[42] Furthermore, alloying is also an effective method for improving the mechanical properties and biocompatibility of metals.[120] At present, common magnesium alloy types used in biomedical applications include magnesium-calcium alloys,[121] magnesium-zinc alloys,[122] magnesium-strontium alloys,[123] and magnesium-neodymium alloys.[124] Alloying has led to varying degrees of improvement in the mechanical properties of metals, alongside products with good biocompatibility and non-toxic degradation. Specifically, magnesium-calcium alloys are widely utilized due to their biocompatibility and degradation characteristics, with calcium playing a key role in bone integration. Magnesium-zinc alloys enhance mechanical strength and promote osteogenesis through zinc's biological functions. Magnesium-strontium alloys are employed because strontium positively influences bone metabolism and healing. Magnesium-neodymium alloys aim to improve mechanical strength and control degradation, while aiding bone repair due to neodymium's effects.[120]

Surface treatments can also control the degradation rate by influencing surface roughness.[125] To enhance the corrosion resistance of magnesium/magnesium alloy bone implants, methods such as electroplating, chemical vapor deposition coatings, physical vapor deposition coatings, and organic coatings are employed.[126] When the same surface treatment yields different surface roughness values, the degradation rate increases with increasing surface roughness.[125]

However, altering alloy composition and performing surface treatments also possess respective drawbacks. Aluminum and rare earth elements are often used as alloying elements to modify alloy composition; however, their long-term biocompatibility remains uncertain and may cause adverse effects in the human body.[127] Moreover, magnesium alloys do not form thermodynamically stable passive layers comparable to those of stainless steel.[128] While implant surface treatments can reduce the degradation rate to some extent, it is challenging to achieve a good match between the degradation rate and bone repair rate.[127] Furthermore, there is a risk of corrosive components penetrating the metal/polymer interface and a decrease in coating adhesion.[126] In contrast, porous structure design offers comprehensive control over the mechanical properties, degradation behavior, and biocompatibility of magnesium/magnesium alloy biodegradable implants, allowing for more efficient simultaneous modulation of multiple properties.

3.3. Influences of porous structural parameters on the degradation behavior of magnesium/magnesium alloy orthopedic implants

Porous structures play critical roles in regulating mechanical properties, bearing and transmitting physiological loads, and establishing a localized mechanical microenvironment for magnesium/magnesium alloy orthopedic implants. The porous structures of magnesium/magnesium alloy orthopedic implants significantly influence the interactions among physiological loading, degradation behavior, and bone tissue regeneration. Orthopedic implants must withstand approximately 2 million cycles of complex physiological loading generated by the movements of the musculoskeletal system annually.[129] Under the complex physiological loading, porous microstructural features such as the unit cell shape, pore size, and porosity affect the implant's macroscopic mechanical properties, deformation and stress distributions, and contact with surrounding tissues, significantly influencing its degradation rate and uniformity.[130] The degradation of the implant causes dynamic changes in the porous structure and mechanical properties, further affecting its mechanical responses under the physiological loading[131] and continuously altering the local mechanical microenvironment of the surrounding bone tissues.[132] Thus, the porous structure is a critical factor in regulating the degradation behavior of magnesium/magnesium alloy orthopedic implants to achieve the dynamic adaptation between changes in mechanical properties and the rate of bone tissue repair (Figure 5). There are various porous structural parameters, including porosity, specific surface area, pore size, shape, and pore interconnectivity.[133,134] This section systematically analyzes the influence of these porous structural parameters on the degradation behavior of magnesium/magnesium alloy orthopedic implants.

3.3.1. Porosity and specific surface area

Porosity and specific surface area are critical factors governing the mechanical properties and degradation behavior of magnesium/magnesium alloy orthopedic implants. Increased porosity and specific surface area enhance the permeability within a unit volume of the orthopedic implant and augment the contact area with body fluids, thereby accelerating the degradation rate.[135] The porosity of orthopedic implants can be directly controlled by modifying the number and the pore size of interconnected pores,[136] while the specific surface area is directly influenced by the size and shape of the basic unit cells of the porous structure.[137,138] Md Saad *et al.*[95] modulated

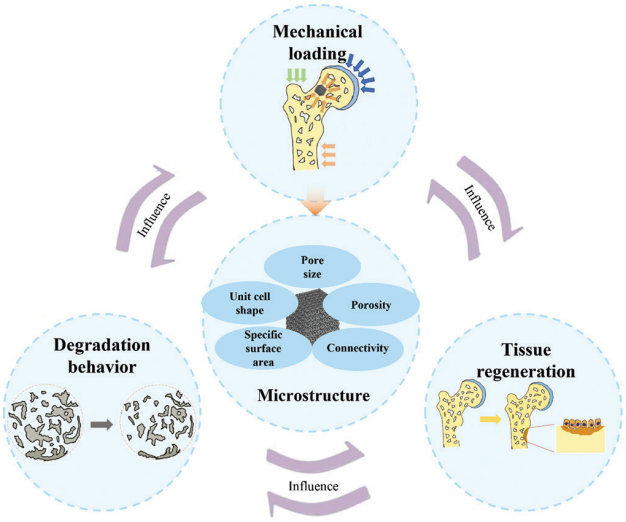

Figure 5. Interactions among porous structures, mechanical properties, degradation behavior, and tissue regeneration. Figure 5 was created with Microsoft PowerPoint 2021 (Microsoft Corporation) by Haoxuan Zeng (2025)

the porosity of bone scaffolds by altering the number of open pores on the surface. The degradation experiments demonstrated that the degradation rate increased with an increasing number of surface pores.[95] Similarly, Kopp *et al.*[77] varied the edge length of microstructures to modify the specific surface area of bone scaffolds and found that the degradation rate increased with increasing microstructure edge length.[77] Furthermore, Wang *et al.*[85] maintained a constant porosity of orthopedic implants while varying their specific surface areas by employing disordered, ordered, and lamellar porous unit cells.[85] According to degradation experiments, it was found that the degradation rate of orthopedic implants increased with increasing specific surface area under the same degradation mode.[85] Moreover, the porosity and specific surface area directly regulate structural permeability, which influences the nutrient/metabolic waste transport and cell adhesion/proliferation, thus regulating the osteogenic potential of orthopedic implants.[139] The permeability of orthopedic implants increased with increasing porosity and specific surface area.[137,140] However, an excessively high porosity will lead to a rapid decline in the mechanical properties of orthopedic implants during degradation, while insufficient porosity results in insufficient permeability, hindering the regeneration of surrounding tissues. Therefore, an appropriate porosity design is crucial to balance the mechanical performance and permeability of orthopedic implants.[137,141]

3.3.2. Pore size

The pore size of porous orthopedic implants not only influences cell and vascular ingrowth but also affects the surface area and strut thickness, thereby impacting degradation behavior. The influence of pore size on degradation behavior remains inconclusive in current research. Cheng *et al.*[142] found that, at a constant porosity, pore size variations had no significant effect on the average degradation rate of high-purity magnesium scaffolds *in vitro*.[142] However, scaffolds with larger pore sizes promoted early angiogenesis in newborn bone tissues, upregulated the expression of type I collagen and osteopontin, and effectively induced higher bone volume and more mature bone formation *in vivo*.[142] It was shown that, as long as porosity remains within an optimal range for tissue growth, appropriately increasing pore size can improve the osteogenic potential of scaffolds with minimal impact on their degradation rate. Conversely, Wang *et al.*[76] found that scaffolds with smaller pore sizes exhibited a larger specific surface area at a constant porosity, enabling the release of more magnesium ions during degradation, which promoted osteogenic differentiation of bone marrow mesenchymal stem cells and induced more new bone formation.[76] Jia *et al.*[136] modified the porosity of bone scaffolds by changing the interconnecting pore size and subsequently altered the specific surface area by changing the primary pore size.[136] They found that the permeability of the scaffolds increased as interconnectivity pore size and primary pore size increased.[136] Excessively small pore sizes resulted in an excessively large surface area of the orthopedic implant, potentially causing a rapid degradation in the initial implantation phase and hindering cell infiltration. In contrast, excessively large pore sizes reduced the specific surface area and mechanical strength of the scaffold, hindering magnesium ion release and failing to provide sufficient stable mechanical support for the newborn bone tissues.[143]

3.3.3. Shape and connectivity of unit cells

The shape and connectivity of unit cells influence stress distribution under physiological loading and fluid flow within the structure of porous orthopedic implants. Sharp-edged strut unit cells or sharp connections between adjacent units can act as stress and electrochemical corrosion concentration regions, leading to accelerated local degradation.[144] In contrast, curvature-based unit cells or smooth transitions at connections between adjacent units promote more uniform distributions of internal stress and flow fields of the structure, resulting in more homogeneous overall degradation.[144] Augustin *et al.*[145] demonstrated that the bone scaffolds based on regular circular unit cells exhibited a smoother surface after *in vivo* degradation, whereas scaffolds based on irregular unit cells displayed more pronounced, non-uniform degradation morphology accompanied by increased roughness.[145] Shi

et al.[146] compared the degradation behavior of magnesium alloy bone scaffolds based on strut unit cells and minimal surface unit cells, respectively, and pointed out that the shape of the unit cell affected the degradation mode of the scaffold.[146] During the degradation process, stagnant flow was generated as a result of the lower permeability within minimal surface scaffolds, causing the accumulation of degradation products that slowed the degradation rate and reduced the degradation uniformity of the structure.[146] The connectivity between unit cells in porous orthopedic implants affects the body fluid flow within the structure. Highly interconnected open-pore structures allow fluid to penetrate all surfaces within the structure, where degradation progresses gradually from the outer surface inward, forming a 3D "etching front" that promotes uniform degradation throughout the structure and avoids localized stress concentrations and sudden failure of local implant structures.[147] Conversely, closed cavities existing within the structure hinder fluid penetration and prevent degradation. The local closed cavities may form temporary self-passivation in adjacent regions due to the retention of degradation products. Although the self-passivation regions retard the degradation rate to a certain extent, it may lead to stress concentration and local failure of the structure, leaving isolated metal fragments that hinder the complete degradation of the implant.[147] The gradient design strategy of setting varying porosity or pore size in different regions of the implant has attracted increasing attention in recent years. For example, a structure with low porosity/pore size is arranged in the central region of the implant to provide stable mechanical support, while a structure with higher porosity/pore size is arranged at the bone-implant interface to promote osseointegration. Such designs theoretically enable slow degradation in the inner layer of the implant and rapid degradation in the outer layer, ensuring early mechanical stability and promoting surrounding bone tissue regeneration.[148] However, the precise fabrication of gradient porous structures remains challenging due to the limitations of magnesium alloy processing; therefore, the research on gradient porous magnesium alloy orthopedic implants is still in its early stage.

3.4. The structure-mechanics-biology interaction mechanisms in magnesium/magnesium alloy orthopedic implants degradation

The degradation of magnesium/magnesium alloy orthopedic implants in the physiological environment is a complex process influenced by multiple factors. This section reviews the "structure-mechanics-biology" interaction mechanisms in this process.

The cross-sectional area gradually decreases, and the pore size gradually increases with degradation of magnesium/magnesium alloy orthopedic implants, macroscopically manifesting as a decline in mechanical strength and stiffness. Although the degradation products can fill the pores partially and form a deposit layer on the surface of the structure to temporarily improve or maintain its mechanical strength in the early stages, this strengthening effect is limited. As the degree of degradation intensifies, the mechanical properties of the implant will continue to deteriorate.[149] Under cyclic physiological loading, the stress corrosion effect, caused by the coupling of cyclic stress and the body fluid environment, aggravates the local degradation of the magnesium scaffold. Guo *et al*.[150] found that the cyclic compressive loading can cause evident cracks in the protective film on the surface of high-purity magnesium scaffolds, thereby accelerating the degradation and failure of the structure.[150] The microstructural evolution during the degradation of magnesium/magnesium alloy orthopedic implants is closely related to the reduction of their macroscopic mechanical properties, which must be fully considered during structural design to ensure that the implant can maintain the necessary mechanical support throughout the critical period of bone healing. However, the relationship between microstructural evolution and macroscopic mechanical property degradation during the degradation of magnesium/magnesium alloy orthopedic implants has not yet been systematically revealed. Models that can quantitatively describe these relationships are necessary to provide a fundamental basis for the design of magnesium/magnesium alloy orthopedic implants.

The *in vivo* degradation behavior of magnesium/magnesium alloy orthopedic implants differs significantly from that observed *in vitro*. The high concentration of proteins and inorganic ions (such as phosphate and carbonate) in body fluids, combined with the magnesium ions released during magnesium degradation, form a phosphate/carbonate deposition layer on the surface of the implant.[151] This biomineralized layer, resembling the natural bone mineral to some extent, slows subsequent degradation and provides a favorable substrate for bone cell adhesion and proliferation.[152] Consequently, magnesium/magnesium alloy orthopedic implants often exhibit an initially rapid degradation rate *in vivo*, followed by surface passivation and degradation deceleration. Moreover, the *in vivo* immune response and degradation rate vary depending on the structures of the magnesium/magnesium alloy orthopedic implants. Structures with smaller pore sizes, due to the slower corrosion and smoother surfaces, tend to induce the formation of a fibrous capsule at the bone-implant interface, which isolates the implant from the surrounding bone tissues and results in a milder inflammatory response.[142] In contrast, structures with larger pore sizes initially exhibit greater infiltration of

macrophages and lymphocytes, which leads to a slightly stronger inflammatory response, with a simultaneous release of osteogenic factors promoting bone remodeling.[142] The *in vivo* degradation of magnesium/magnesium alloy orthopedic implants is accompanied by the regeneration of surrounding bone tissues. The formation and remodeling of new bone tissues are highly dependent on the mechanical microenvironment, that is, the "mechano-biological" coupling effect. Appropriate mechanical stimulation promotes osteoblast activation and matrix deposition, while excessive micromotion can lead to fibrous union or delayed healing.[152] Magnesium/magnesium alloy orthopedic implants should provide sufficient stiffness and mechanical stability to the damaged bone tissues in the early stage after implantation. Meanwhile, the gradual degradation of magnesium/magnesium alloy orthopedic implants should enable a progressive transfer of stress to the newborn bone tissues to provide a graded mechanical environment during the healing process. In addition to the local mechanical environment, the released ions and local pH changes during the degradation of magnesium/magnesium alloy orthopedic implants also affect cell behavior. The magnesium ions released during the degradation of magnesium/magnesium alloy orthopedic implants can promote osteogenesis-related processes, enhance osteoblast adhesion and migration, improve angiogenesis, and exert a certain immunomodulatory effect.[153] When perceived by surrounding osteogenesis-related cells, moderate magnesium ion concentrations can activate osteogenic pathways, promoting the deposition of new bone matrix. This combined chemical and mechanical stimulation is beneficial for bone remodeling.[154] However, if the degradation is too rapid, a dramatic accumulation of magnesium and hydroxide ions will occur locally, causing an increase in pH value and accompanied by the production of a large amount of hydrogen gas.[128] Excessive alkalinity leads to an abnormal mineralization of the extracellular matrix or stimulation of surrounding tissues.[128] The large amount of hydrogen gas retained in the tissues can form bubbles, hindering close contact between the newborn bone tissues and the implant and potentially inducing inflammation or delayed healing.[152] Therefore, the degradation rate of magnesium/magnesium alloy orthopedic implants should match the rate of bone repair to achieve complete degradation after the completion of bone tissue repair, but not be too rapid to cause excessive stimulation to the surrounding tissues.

The influences of the mechanical environment on the "structure-mechanics-biology" interactions during the degradation of magnesium/magnesium alloy orthopedic implants vary significantly at different implantation sites. The diaphysis of long bones (such as the femur and tibia) is typically a dominant load-bearing region with an abundant blood supply in the medullary cavity.[155] Studies have shown that magnesium implants degrade more rapidly in long bones than in non-load-bearing sites, such as subcutaneous tissues. Cyclic loads promote the generation of stress corrosion cracks, whereas fluid flow and higher oxygen content in the medullary cavity may accelerate electrochemical reactions.[152] The higher concentrations of calcium and phosphate ions in the bone tissues promote new bone formation, which will facilitate the formation of a protective mineralized layer on the magnesium surface to partially offset the negative effects of excessively rapid degradation. Non-load-bearing or low-load-bearing sites, such as craniofacial bones, experience relatively lower mechanical loads. The bone tissues in these regions primarily regenerate in the intramembranous osteogenesis mode, of which the rate is slower than that of long bones.[156] The catastrophic mechanical instability is less prone to occur during the degradation of magnesium/magnesium alloy orthopedic implants used for craniofacial repair. More attentions are focused on the precise reconstruction of geometry and biocompatibility of the magnesium/magnesium alloy implants used in craniofacial repair.[157] In addition, the biological environment at the skull is relatively closed, which may make it difficult for the released hydrogen gas to diffuse during the degradation process. Therefore, greater attention should be paid to the issue of gas release during degradation. Research on the application of magnesium/magnesium alloy orthopedic implants in craniofacial repair is relatively limited, as the effects of the region's complex anatomical structures on degradation behavior require further study. In the internal fixation of joint fractures, the high chloride ion concentration and relatively low fluidity of synovial fluid within the joint cavity can affect the degradation behavior of the magnesium/magnesium alloy orthopedic implants. The low buffering capacity and closed cavity of synovial fluid may lead to the local accumulation of degradation products, inducing synovitis or cartilage damage.[158] Conversely, joint movement promotes agitation of the synovial fluid, accelerating the dissipation of corrosion products and avoiding excessive local concentrations.[158] Therefore, for joint fixation applications, it is essential to carefully regulate the degradation rate and product release to promote bone healing without damaging joint tissues.

4. Key challenges and prospective future directions

The widely applied research methodologies in studying the degradation behavior of magnesium/magnesium alloy orthopedic implants include degradation experiments and numerical simulations, both of which possess

distinct advantages. Degradation experiments directly assess degradation morphologies, degradation rates, and mechanical properties of magnesium/magnesium alloy orthopedic implants, enabling the analysis of the regulations of porous structures on the degradation behavior and the corresponding mechanisms. In different degradation experiments, a diverse and inconsistent range of solutions is commonly employed to construct the simulated body fluid environments, with variations in both composition and concentration. This heterogeneity complicates the direct comparison of degradation rates across different studies. Moreover, most studies utilized static or semi-static immersion conditions in the degradation experiments, which could not precisely simulate the body fluid flow in the actual physiological environment of the human body. The dynamic immersion conditions with a flow rate of 2 mL/(100 mL/min) can more accurately simulate the body fluid flow in the musculoskeletal system. Significant discrepancies exist between the degradation rates of magnesium/magnesium alloy orthopedic implants observed *in vitro* and *in vivo*. Therefore, *in vivo* degradation experiments should be carried out preferentially to obtain more accurate data. In the numerical simulations of the degradation behavior of magnesium/magnesium alloy orthopedic implants, the influences of various factors can be simulated by adjusting model parameters and boundary conditions. Compared to degradation experiments, numerical simulations are more efficient and resource-saving. Moreover, stress/strain and fluid flow field distributions in the structure of the implant during the degradation process can be computed through the numerical simulations, facilitating the analysis of the "structure-mechanics-degradation" interaction mechanisms. However, current degradation numerical simulation models have limited consideration of the *in vivo* biological processes, such as the clearance of degradation products by tissues and the influences of surrounding bone remodeling on stress redistributions. Future research should focus on the development of more comprehensive multi-physics coupling models that integrate electrochemical corrosion, stress fields, and biological interactions to simulate the "structure-mechanics-degradation-biology" interactions during the dynamic degradation process of magnesium/magnesium alloy orthopedic implants more accurately.

The degradation mechanisms of magnesium and magnesium alloys in physiological environments are complex. At present, no single theory can fully explain all experimental observations. Therefore, the applications of more advanced surficial characterization, *in situ* analysis, and atomic modeling techniques are necessary to further clarify the degradation mechanisms of magnesium/magnesium alloy orthopedic implants.[144] Material composition modification, surface treatments, and structural optimization are three primary approaches to address the issue of excessively rapid degradation rates in magnesium/magnesium alloy orthopedic implants. Aluminum and rare earth elements are frequently applied as alloying elements to modify material composition; however, the long-term biocompatibility of these alloying elements remains a concern due to their potential negative effects on the human body. Although the surface treatments can reduce the degradation rates to a certain extent, achieving a satisfactory match between the degradation and bone repair rate remains challenging. Structural design of implant offers advantages over the abovementioned two approaches, but further research is needed to comprehensively compare the advantages and disadvantages of these three approaches to obtain more rigorous conclusions.[127] To improve the performance of magnesium/magnesium alloy orthopedic implants, the optimization of porous structural design parameters is crucial. However, the current challenge lies in the balance among various performance requirements, including mechanical strength and compatibility, fatigue resistance, and tissue regeneration performance. A comprehensive consideration of the multiple factors is necessary to identify the optimal balance in porous structure design. Therefore, further research is needed to develop novel structural design methods, which can offer greater flexibility and decouple the different performance requirements, ensuring that adjusting parameters related to one property does not cause a significant impact on the others.[159]

Future research should be focused on the following directions. First, standardization of simulated body fluid environments and immersion conditions in degradation experiments is essential, enabling the degradation experiment results to be more instructive and allowing direct comparisons among different studies. Second, to achieve a satisfactory match between bone repair and the degradation rate of magnesium/magnesium alloy orthopedic implants, a systematic investigation of the potential synergistic effects between different influencing factors is needed. Moreover, designing structural parameters and material composition of magnesium/magnesium alloy orthopedic implants is generally conducted independently in existing studies, without sufficient consideration of their coupled influences on degradation behavior and tissue regeneration processes. Quantitative models that systematically describe the "structural design variables-material composition-degradation behavior-tissue regeneration" relationships remain to be developed. The influences of the porous structures on the mechanical properties, degradation behavior, and tissue regeneration

performance of magnesium/magnesium alloy orthopedic implants are complex, exhibiting inconsistent or even contradictory trends that require careful trade-offs in the design. Combining generative techniques based on artificial intelligence[160,161] (including generative adversarial networks, variational autoencoders, deep learning, and reinforcement learning) and data-driven inverse design paradigms, it is possible to achieve efficient generation of structural parameters, accurate prediction of macroscopic performances, and effective trade-offs between multiple design objectives. These advanced design technologies can overcome the limitations of traditional design methods, such as cumbersome processes, insufficient flexibility, and low efficiency, and provide a new inspiration to optimize the design of magnesium/magnesium alloy orthopedic implants. These technologies will help achieve an optimal match between implant degradation rate and tissue regeneration, facilitating the development and clinical applications of magnesium/magnesium alloy orthopedic implants.

5. Conclusion

Porous magnesium/magnesium alloy orthopedic implants have attracted significant attention due to their favorable biocompatibility, biodegradability, and mechanical compatibility with bone tissues. Many studies have confirmed the application potential of porous magnesium/magnesium alloy orthopedic implants. However, uncontrollable degradation behavior, the mismatch between degradation-induced mechanical property changes, and tissue regeneration rates are the main bottlenecks currently hindering the clinical translation of porous magnesium/magnesium alloy orthopedic implants. The porous structure is a critical factor influencing the degradation behavior of magnesium/magnesium alloy orthopedic implants. This study summarized the widely applied methodologies in investigating the degradation behavior of porous magnesium/magnesium alloy orthopedic implants and their respective features. The influences of the porous structures of magnesium/magnesium alloy orthopedic implants on their degradation behavior and the corresponding "structure-mechanics-biology" interaction mechanisms during the degradation process were systematically analyzed. The main findings of this study include:

(i) AM technologies offer numerous advantages compared to traditional manufacturing methods. The specific selection of an AM technique and its corresponding process parameters is critically important, contingent on the particular requirements of the implant
(ii) Degradation experiments and numerical simulations each possess distinct emphases and advantages in characterizing and describing the degradation behavior of magnesium/magnesium alloy orthopedic implants. Their mutual validation provides a robust foundation for the optimized design of magnesium/magnesium alloy bone implants
(iii) Porous structures serve as a crucial vehicle for modulating the mechanical properties of magnesium/magnesium alloy orthopedic implants, bearing and transmitting mechanical loads, and establishing the local mechanical microenvironment. They exert a significant influence on the intricate interplay between physiological loading, implant degradation behavior, and bone tissue regeneration
(iv) The degradation of magnesium/magnesium alloy orthopedic implants within the human physiological environment is a complex process driven by multifactorial coupling. However, a quantitative description of the underlying "structure-mechanics-biology" interaction mechanisms remains presently unattainable.

This study provides a systematic understanding of the state-of-the-art research and future directions in the field of porous magnesium/magnesium alloy orthopedic implants to guide future development and applications.

Acknowledgments

None.

Funding

This work was supported by the National Natural Science Foundation of China (Nos. 12425209, 12402351, 12332019, 12172043), the Beijing Municipal Natural Science Foundation (No. L241067), and the Research Funding of Hangzhou International Innovation Institute of Beihang University (No. 2024KQ108).

Conflicts of interest

The authors declare that they have no known competing financial interests or personal relationships that could have appeared to influence the work reported in this paper.

Authors' contributions

Conceptualization: Haoxuan Zeng, Huiwen Huang
Funding acquisition: Lizhen Wang, Yubo Fan, Huiwen Huang, Qiao Li
Supervision: Huiwen Huang, Lizhen Wang, Yubo Fan, Chunli Song
Visualization: Haoxuan Zeng, Huiwen Huang
Writing – original draft: Haoxuan Zeng
Writing – review and *editing:* Huiwen Huang, Lizhen Wang

Ethics approval and consent to participate

Not applicable.

Consent for publication

Not applicable.

Availability of data

Not applicable.

References

1. Hu X, Lin Z, He J, *et al*. Recent progress in 3D printing degradable polylactic acid-based bone repair scaffold for the application of cancellous bone defect. *MedComm*. 2022;1(1):e14.

   doi: 10.1002/mba2.14

2. Habibovic P. Strategic directions in osteoinduction and biomimetics. *Tissue Eng*. 2017;23(23-24):1295-1296.

   doi: 10.1089/ten.tea.2017.0430

3. Yang Y, He C, Yang W, *et al*. Mg bone implant: Features, developments and perspectives. *Mater Des*. 2020;185:108259.

   doi: 10.1016/j.matdes.2019.108259

4. Wang W, Yeung KW. Bone grafts and biomaterials substitutes for bone defect repair: A review. *Bioact Mater*. 2017;2(4):224-247.

   doi: 10.1016/j.bioactmat.2017.05.007

5. Block MS, Kent JN. Sinus augmentation for dental implants: The use of autogenous bone. *J Oral Maxillofac Surg*. 1997;55(11):1281-1286.

   doi: 10.1016/S0278-2391(97)90185-3

6. Sakkas A, Wilde F, Heufelder M, Winter K, Schramm A. Autogenous bone grafts in oral implantology-is it still a "gold standard"? A consecutive review of 279 patients with 456 clinical procedures. *Int J Implant Dent*. 2017;3:1-17.

   doi: 10.1186/s40729-017-0084-4

7. Younger EM, Chapman MW. Morbidity at bone graft donor sites. *J Orthop Trauma*. 1989;3(3):192-195.

   doi: 10.1097/00005131-198909000-00002

8. Robinson PG, Abrams GD, Sherman SL, Safran MR, Murray IR. Autologous bone grafting. *Oper Techn Sport Med*. 2020;28(4):150780.

   doi: 10.1016/j.otsm.2020.150780

9. Sumner DR, Galante JO. Determinants of stress shielding: Design versus materials versus interface.*Clin Orthop Relat Res*. 1992;274:202-212.

10. Huiskes R, Weinans H, Van Rietbergen B. The relationship between stress shielding and bone resorption around total hip stems and the effects of flexible materials. *Clin Orthop Relat Res*. 1992;274:124-134.

11. Sundfeldt M, Carlsson LV, Johansson CB, Thomsen P, Gretzer C. Aseptic loosening, not only a question of wear: A review of different theories. *Acta Orthop*. 2006;77(2):177-197.

    doi: 10.1080/17453670610045902

12. Yaszemski MJ, Payne RG, Hayes WC, Langer R, Mikos AG. Evolution of bone transplantation: Molecular, cellular and tissue strategies to engineer human bone. *Biomaterials*. 1996;17(2):175-185.

    doi: 10.1016/0142-9612(96)85762-0

13. Roshan-Ghias A, Lambers FM, Gholam-Rezaee M, Müller R, Pioletti DP. *In vivo* loading increases mechanical properties of scaffold by affecting bone formation and bone resorption rates. *Bone*. 2011;49(6):1357-1364.

    doi: 10.1016/j.bone.2011.09.040

14. Kroeze RJ, Helder MN, Govaert LE, Smit TH. Biodegradable polymers in bone tissue engineering. *Materials*. 2009;2(3):833-856.

    doi: 10.3390/ma2030833

15. Giarmatzis G, Jonkers I, Wesseling M, Van Rossom S, Verschueren S. Loading of hip measured by hip contact forces at different speeds of walking and running. *J Bone Miner Res*. 2015;30(8):1431-1440.

    doi: 10.1002/jbmr.2483

16. Hart NH, Newton RU, Tan J, *et al*. Biological basis of bone strength: Anatomy, physiology and measurement. *J Musculoskelet Neuronal Interact*. 2020;20(3):347-371.

17. Bakhtiari H, Nouri A, Khakbiz M, Tolouei-Rad M. Fatigue behaviour of load-bearing polymeric bone scaffolds: A review. *Acta Biomater*. 2023;172:16-37.

    doi: 10.1016/j.actbio.2023.09.048

18. Bandyopadhyay A, Mitra I, Goodman SB, Kumar M, Bose S. Improving biocompatibility for next generation of metallic implants. *Prog Mater Sci*. 2023;133:101053.

    doi: 10.1016/j.pmatsci.2022.101053

19. Lee BH, Lee C, Kim DG, Choi K, Lee KH, Do Kim Y. Effect of surface structure on biomechanical properties and osseointegration. *Mater Sci Eng C*. 2008;28(8):1448-1461.

    doi: 10.1016/j.msec.2008.03.015

20. Shah FA, Thomsen P, Palmquist A. Osseointegration and current interpretations of the bone-implant interface. *Acta Biomater*. 2019;84:1-15.

    doi: 10.1016/j.actbio.2018.11.018

21. Heary RF, Parvathreddy N, Sampath S, Agarwal N. Elastic modulus in the selection of interbody implants. *J Spine Surg*. 2017;3(2):163.

    doi: 10.21037/jss.2017.05.01

22. Yang W, Chen H, Bai H, *et al*. Additive manufactured osseointegrated screws with hierarchical design. *Bio-Des Manuf.* 2024;7(2):206-235.

doi: 10.1007/s42242-024-00269-3

23. Agarwal R, Gupta V, Singh J. Additive manufacturing-based design approaches and challenges for orthopaedic bone screws: A state-of-the-art review. *J Braz Soc Mech Sci Eng*. 2022;44(1):37.

doi: 10.1007/s40430-021-03331-8

24. Wang X, Xu S, Zhou S, *et al*. Topological design and additive manufacturing of porous metals for bone scaffolds and orthopaedic implants: A review. *Biomaterials*. 2016;83:127-141.

doi: 10.1016/j.biomaterials.2016.01.012

25. Zhang J, Shen Y, Sun Y, *et al*. Design and mechanical testing of porous lattice structure with independent adjustment of pore size and porosity for bone implant. *J Mater Res Technol*. 2022;18:3240-3255.

doi: 10.1016/j.jmrt.2022.04.002

26. Mandal S, Das V, Debata M, *et al*. Study of pore morphology, microstructure, and cell adhesion behaviour in porous Ti-6Al-4V scaffolds. *Emergent Mater*. 2019;2:453-462.

doi: 10.1007/s42247-019-00055-3

27. Zhang Z, Jones D, Yue S, *et al*. Hierarchical tailoring of strut architecture to control permeability of additive manufactured titanium implants. *Mater Sci Eng C*. 2013;33(7):4055-4062.

doi: 10.1016/j.msec.2013.05.050

28. Chua C. The design of scaffolds for use in tissue engineering. Part I. Traditional factors. *Tissue Eng*. 2001;7:679-689.

doi: 10.1089/107632701753337645

29. Zhang Q, Zhou J, Zhi P, *et al*. 3D printing method for bone tissue engineering scaffold. *Med Novel Technol Devices*. 2023;17:100205.

doi: 10.1016/j.medntd.2022.100205

30. Ansari N, Alabtah FG, Albakri MI, Khraisheh M. Post processing of additive manufactured Mg alloys: Current status, challenges, and opportunities. *J Magnesium Alloys*. 2024;12(4):1283-1310.

doi: 10.1016/j.jma.2024.04.017

31. Guddati S, Kiran ASK, Leavy M, Ramakrishna S. Recent advancements in additive manufacturing technologies for porous material applications. *Int J Adv Manuf Tech*. 2019;105(1):193-215.

doi: 10.1007/s00170-019-04116-z

32. Prakash KS, Nancharaih T, Rao VS. Additive manufacturing techniques in manufacturing-an overview. *Mater Today Proc.* 2018;5(2):3873-3882.

doi: 10.1016/j.matpr.2017.11.642

33. Nahlieli O. Complications of sialendoscopy: Personal experience, literature analysis, and suggestions. *J Oral Maxillofac Surg*. 2015;73(1):75-80.

doi: 10.1016/j.joms.2014.07.028

34. Chen Y, Li W, Zhang C, Wu Z, Liu J. Recent developments of biomaterials for additive manufacturing of bone scaffolds. *Adv Healthcare Mater.* 2020;9(23): e2000724.

doi: 10.1002/adhm.202000724

35. Germaini MM, Belhabib S, Guessasma S, Deterre R, Corre P, Weiss P. Additive manufacturing of biomaterials for bone tissue engineering-A critical review of the state of the art and new concepts. *Prog Mater Sci.* 2022;130:100963.

doi: 10.1016/j.pmatsci.2022.100963

36. Cockerill I, Su Y, Sinha S, *et al*. Porous zinc scaffolds for bone tissue engineering applications: A novel additive manufacturing and casting approach. *Mater Sci Eng C*. 2020;110:110738.

doi: 10.1016/j.msec.2020.110738

37. Gartzke AK, Julmi S, Klose C, *et al*. A simulation model for the degradation of magnesium-based bone implants. *J Mech Behav Biomed Mater.* 2020;101:103411.

doi: 10.1016/j.jmbbm.2019.103411

38. Nasr Azadani M, Zahedi A, Bowoto OK, Oladapo BI. A review of current challenges and prospects of magnesium and its alloy for bone implant applications. *Prog Biomater*. 2022;11(1):1-26.

doi: 10.1007/s40204-022-00182-x

39. Cheng A, Schwartz Z, Kahn A, *et al*. Advances in porous scaffold design for bone and cartilage tissue engineering and regeneration. *Tissue Eng Part B Rev*. 2019;25(1):14-29.

doi: 10.1089/ten.teb.2018.0119

40. Garimella A, Ghosh SB, Bandyopadhyay-Ghosh S. A comprehensive study of the impact on the microstructure and corrosion behavior of magnesium alloy-based porous bone implants. *Mater Today Proc.* 2023;9(3):1249-1282.

doi: 10.1016/j.matpr.2023.04.027

41. Zhao D, Yu K, Sun T, *et al*. Material-structure-function integrated additive manufacturing of degradable metallic bone implants for load-bearing applications. *Adv Funct Mater*. 2023;33(16):2213128.

doi: 10.1002/adfm.202213128

42. Parai R, Bandyopadhyay-Ghosh S. Engineered bio-nanocomposite magnesium scaffold for bone tissue regeneration. *J Mech Behav Biomed Mater*. 2019;96:45-52.

doi: 10.1016/j.jmbbm.2019.04.019

43. Sarian MN, Iqbal N, Sotoudehbagha P, *et al*. Potential bioactive coating system for high-performance absorbable magnesium bone implants. *Bioact Mater.* 2022;12:42-63.

doi: 10.1016/j.bioactmat.2021.10.034

44. Krämer M, Schilling M, Eifler R, *et al*. Corrosion behavior, biocompatibility and biomechanical stability of a prototype magnesium-based biodegradable intramedullary nailing system. *Mater Sci Eng C Mater Biol Appl*. 2016;59:129-135.

doi: 10.1016/j.msec.2015.10.006

45. Ghazizadeh E, Jabbari A, Sedighi M. *In vitro* corrosion-fatigue behavior of biodegradable Mg/HA composite in simulated body fluid. *J Magnesium Alloys*. 2021;9(6):2169-2184.

doi: 10.1016/j.jma.2021.03.027

46. Jing X, Ding Q, Wu Q, *et al*. Magnesium-based materials in orthopaedics: Material properties and animal models. *Biomater Transl*. 2021;2(3):197-213.

doi: 10.12336/biomatertransl.2021.03.004

47. Saad APM, Syahrom A. Study of dynamic degradation behaviour of porous magnesium under physiological environment of human cancellous bone. *Corros Sci.* 2018;131:45-56.

doi: 10.1016/j.corsci.2017.10.026

48. Peng B, Xu H, Song F, Wen P, Tian Y, Zheng Y. Additive manufacturing of porous magnesium alloys for biodegradable orthopedic implants: Process, design, and modification. *J Mater Sci Technol*. 2024;182:79-110.

doi: 10.1016/j.jmst.2023.08.072

49. Bielik M, Neubauer E, Kitzmantel M, Neubauer I, Kozeschnik E. Numerical simulation and experimental characterization of a single-seam plasma wire arc additive manufacturing process for Ti-6Al-4V. *Mater Sci Addit Manuf.* 2025;4(3):025140021.

doi: 10.36922/MSAM025140021

50. Shahed KS, Groeneveld-Meijer W, Lear M, Schreiber J, Manogharan G. Powder spreading behavior of bimodal ceramics in the binder jetting process. *Mater Sci Addit Manuf.* 2025;4(2):025110016.

doi: 10.36922/MSAM025110016

51. Chen J, Chen B. Progress in additive manufacturing of magnesium alloys: A review. *Materials*. 2024;17(15):3851.

doi: 10.3390/ma17153851

52. Zaitceva M, Borisov A, Popovich A, Sufiiarov V. Selective laser melting of ferritic/martensitic oxide dispersion-strengthened steel: Processing, microstructure, and mechanical properties. *Mater Sci Addit Manuf.* 2025;4(1):025060004.

doi: 10.36922/MSAM025060004

53. Li X, Fang X, Zhang M, Wang B, Huang K. Enhanced strength-ductility synergy of magnesium alloy fabricated by ultrasound assisted directed energy deposition. *J Mater Sci Technol*. 2024;178:247-261.

doi: 10.1016/j.jmst.2023.09.021

54. Cheng S, Liu F, Xu Y, *et al*. Effects of arc oscillation on microstructure and mechanical properties of AZ31 magnesium alloy prepared by CMT wire-arc directed energy deposition. *Mater Sci Eng A*. 2023;864:144539.

doi: 10.1016/j.msea.2022.144539

55. Gieseke M, Noelke C, Kaierle S, Wesling V, Haferkamp H. Selective laser melting of magnesium and magnesium alloys. *Magnes Technol*. 2013:65-68.

doi: 10.1007/978-3-319-48150-0_11

56. Prashanth KG, Scudino S, Klauss HJ, *et al*. Microstructure and mechanical properties of Al-12Si produced by selective laser melting: Effect of heat treatment. *Mater Sci Eng A*. 2014;590:153-160.

doi: 10.1016/j.msea.2013.10.023

57. Allavikutty R, Gupta P, Santra TS, Rengaswamy J. Additive manufacturing of Mg alloys for biomedical applications: Current status and challenges. *Curr Opin Biomed Eng.* 2021;18:100276.

doi: 10.1016/j.cobme.2021.100276

58. Gao C, Wang C, Jin H, *et al*. Additive manufacturing technique-designed metallic porous implants for clinical application in orthopedics. *RSC Adv.* 2018;8(44):25210-25227.

doi: 10.1039/c8ra04815k

59. Dong J, Li Y, Lin P, *et al*. Solvent-cast 3D printing of magnesium scaffolds. *Acta Biomater.* 2020;114:497-514.

doi: 10.1016/j.actbio.2020.08.002

60. Takagi H, Sasahara H, Abe T, *et al*. Material-property evaluation of magnesium alloys fabricated using wire-and-arc-based additive manufacturing. *Addit Manuf.* 2018;24:498-507.

doi: 10.1016/j.addma.2018.10.026

61. Karunakaran R, Ortgies S, Tamayol A, Bobaru F, Sealy MP. Additive manufacturing of magnesium alloys. *Bioact Mater.* 2020;5(1):44-54.

doi: 10.1016/j.bioactmat.2019.12.004

62. Manjhi SK, Sekar P, Bontha S, Balan A. Additive manufacturing of magnesium alloys: Characterization and post-processing. *Int J Lightweight Mater Manuf*. 2024;7(1):184-213.

doi: 10.1016/j.ijlmm.2023.06.004

63. Kleger N, Cihova M, Masania K, Studart AR, Löffler JF. 3D printing of salt as a template for magnesium with structured porosity. *Adv Mater*. 2019;31(37):1903783.

doi: 10.1002/adma.201903783

64. Wolff M, Mesterknecht T, Bals A, Ebel T, Willumeit-Römer R. FFF of Mg-alloys for biomedical application. *Magnes Technol*. 2019:43-49.

doi: 10.1007/978-3-030-05789-3_8

65. Farag M, Yun HS. Effect of gelatin addition on fabrication of magnesium phosphate-based scaffolds prepared by additive manufacturing system. *Mater Lett.* 2014;132:111-115.

doi: 10.1016/j.matlet.2014.06.055

66. Wei D, Anniyaer A, Koizumi Y, *et al*. On microstructural homogenization and mechanical properties optimization of biomedical Co-Cr-Mo alloy additively manufactured by using electron beam melting. *Addit Manuf.* 2019;28:215-227.

doi: 10.1016/j.addma.2019.05.010

67. Badkoobeh F, Mostaan H, Rafiei M, Bakhsheshi-Rad HR, RamaKrishna S, Chen X. Additive manufacturing of biodegradable magnesium-based materials: Design strategies, properties, and biomedical applications. *J Magnesium Alloys*. 2023;11(3):801-839.

doi: 10.1016/j.jma.2022.12.001

68. Zhang WN, Wang LZ, Feng ZX, Chen YM. Research progress on selective laser melting (SLM) of magnesium alloys: A review. *Optik*. 2020;207:163842.

doi: 10.1016/j.ijleo.2019.163842

69. Zumdick NA, Jauer L, Kersting LC, Kutz TN, Schleifenbaum JH, Zander D. Additive manufactured WE43 magnesium: A comparative study of the microstructure and mechanical properties with those of powder extruded and as-cast WE43. *Mater Charact.* 2019;147:384-397.

doi: 10.1016/j.matchar.2018.11.011

70. Guo Y, Quan G, Jiang Y, Ren L, Fan L, Pan H. Formability, microstructure evolution and mechanical properties of wire arc additively manufactured AZ80M magnesium alloy using gas tungsten arc welding. *J Magnesium Alloys*. 2021;9(1):192-201.

doi: 10.1016/j.jma.2020.01.003

71. Juan C. Microstructure and mechanical properties of high strength Mg-15Gd-1Zn-0.4 Zr alloy additive-manufactured by selective laser melting process. *T Nonferr Metal Soc*. 2021;31(7):1969-1978.

doi: 10.1016/S1003-6326(21)65630-3

72. Zhang XL, Zhang ZT. Influence of sub-rapid solidification on microstructure and mechanical properties of AZ61A magnesium alloy. *T Nonferr Metal Soc*. 2008;18:S86-S90.

doi: 10.1016/s1003-6326(10)60180-x

73. Kokubo T, Ito S, Shigematsu M, Sanka S, Yamamuro T. Fatigue and life-time of bioactive glass-ceramic AW containing apatite and wollastonite. *J Mater Sci.* 1987;22:4067-4070.

doi: 10.1007/BF01133359

74. Dutta S, Devi KB, Roy M. Processing and degradation behavior of porous magnesium scaffold for biomedical applications. *Adv Powder Technol*. 2017;28(12):3204-3212.

doi: 10.1016/j.apt.2017.09.024

75. Zhuang H, Han Y, Feng A. Preparation, mechanical properties and *in vitro* biodegradation of porous magnesium scaffolds. *Mater Sci Eng C*. 2008;28(8):1462-1466.

doi: 10.1016/j.msec.2008.04.001

76. Wang C, Liu J, Min S, *et al*. The effect of pore size on the mechanical properties, biodegradation and osteogenic effects of additively manufactured magnesium scaffolds after high temperature oxidation: An *in vitro* and *in vivo* study. *Bioact Mater*. 2023;28:537-548.

doi: 10.1016/j.bioactmat.2023.06.009

77. Kopp A, Derra T, Müther M, *et al*. Influence of design and postprocessing parameters on the degradation behavior and mechanical properties of additively manufactured magnesium scaffolds. *Acta Biomater.* 2019;98:23-35.

doi: 10.1016/j.actbio.2019.04.012

78. Zhen Z, Xi TF, Zheng YF. A review on *in vitro* corrosion performance test of biodegradable metallic materials. *T Nonferr Metal Soc*. 2013;23(8):2283-2293.

doi: 10.1016/s1003-6326(13)62730-2

79. Abidin NIZ, Rolfe B, Owen H, *et al*. The *in vivo* and *in vitro* corrosion of high-purity magnesium and magnesium alloys WZ21 and AZ91. *Corros Sci*. 2013;75:354-366.

doi: 10.1016/j.corsci.2013.06.019

80. Hou R, Feyerabend F, Helmholz H, Garamus VM, Willumeit-Römer R. Effects of proteins on magnesium degradation-static vs. dynamic conditions. *J Magnesium Alloys*. 2023;11(4):1332-1342.

doi: 10.1016/j.jma.2021.07.021

81. Ng W, Chiu K, Cheng F. Effect of pH on the *in vitro* corrosion rate of magnesium degradable implant material. *Mater Sci Eng C*. 2010;30(6):898-903.

doi: 10.1016/j.msec.2010.04.003

82. Marco I, Feyerabend F, Willumeit-Römer R, Van der Biest O. Degradation testing of Mg alloys in Dulbecco's modified eagle medium: Influence of medium sterilization. *Mater Sci Eng C Mater Biol Appl*. 2016;62:68-78.

doi: 10.1016/j.msec.2016.01.039

83. Jia G, Chen C, Zhang J, *et al*. *In vitro* degradation behavior of Mg scaffolds with three-dimensional interconnected porous structures for bone tissue engineering. *Corros Sci.* 2018;144:301-312.

doi: 10.1016/j.corsci.2018.09.001

84. Saad APM, Jasmawati N, Harun MN, *et al*. Dynamic degradation of porous magnesium under a simulated environment of human cancellous bone. *Corros Sci.* 2016;112:495-506.

doi: 10.1016/j.corsci.2016.08.017

85. Wang Y, Huang H, Jia G, Zeng H, Yuan G. Fatigue and

dynamic biodegradation behavior of additively manufactured Mg scaffolds. *Acta Biomater.* 2021;135:705-722.

doi: 10.1016/j.actbio.2021.08.040

86. Zhao F, Vaughan TJ, Mcnamara LM. Multiscale fluid-structure interaction modelling to determine the mechanical stimulation of bone cells in a tissue engineered scaffold. *Biomech Model Mechanobiol.* 2015;14:231-243.

doi: 10.1007/s10237-014-0599-z

87. Witte F, Fischer J, Nellesen J, *et al*. *In vitro* and *in vivo* corrosion measurements of magnesium alloys. *Biomaterials*. 2006;27(7):1013-1018.

doi: 10.1016/j.biomaterials.2005.07.037

88. Kleer-Reiter N, Julmi S, Feichtner F, *et al.* Biocompatibility and degradation of the open-pored magnesium scaffolds LAE442 and La2. *Materials.* 2021;16(3):035037.

doi: 10.1088/1748-605x/abf5c5

89. Li Y, Zhou J, Pavanram P, *et al*. Additively manufactured biodegradable porous magnesium. *Acta Biomater.* 2018;67:378-392.

doi: 10.1016/j.actbio.2017.12.008

90. Yin Yee Chin P, Cheok Q, Glowacz A, Caesarendra W. A review of *in-vivo* and *in-vitro* real-time corrosion monitoring systems of biodegradable metal implants. *Appl Sci.* 2020;10(9):3141.

doi: 10.3390/app10093141

91. Bobe K, Willbold E, Morgenthal I, *et al*. *In vitro* and *in vivo* evaluation of biodegradable, open-porous scaffolds made of sintered magnesium W4 short fibres. *Acta Biomater.* 2013;9(10):8611-8623.

doi: 10.1016/j.actbio.2013.03.035

92. Kim JA, Lim J, Naren R, Yun HS, Park EK. Effect of the biodegradation rate controlled by pore structures in magnesium phosphate ceramic scaffolds on bone tissue regeneration *in vivo*. *Acta Biomater.* 2016;44:155-167.

doi: 10.1016/j.actbio.2016.08.039

93. Feyerabend F. *In vitro* analysis of magnesium corrosion in orthopaedic biomaterials. *Biomater Bone Regener*. 2014: 225-269.

doi: 10.1533/9780857098104.2.225

94. Kirkland N, Birbilis N, Staiger M. Assessing the corrosion of biodegradable magnesium implants: A critical review of current methodologies and their limitations. *Acta Biomater.* 2012;8(3):925-936.

doi: 10.1016/j.actbio.2011.11.014

95. Saad AP, Prakoso AT, Sulong M, Basri H, Wahjuningrum DA, Syahrom A. Impacts of dynamic degradation on the morphological and mechanical characterisation of porous magnesium scaffold. *Biomech Model Mechanobiol.* 2019;18:797-811.

doi: 10.1007/s10237-018-01115-z

96. Liu Y, Yang Z, Tan L, Li H, Zhang Y. An animal experimental study of porous magnesium scaffold degradation and osteogenesis. *Braz J Med Biol Res*. 2014;47(8):715-720.

doi: 10.1590/1414-431x20144009

97. Zhao D, Wang T, Nahan K, *et al*. *In vivo* characterization of magnesium alloy biodegradation using electrochemical H2 monitoring, ICP-MS, and XPS. *Acta Biomater*. 2017;50:556-565.

doi: 10.1016/j.actbio.2017.01.024

98. Zhao D, Wang T, Hoagland W, *et al*. Visual H2 sensor for monitoring biodegradation of magnesium implants *in vivo*. *Acta Biomater.* 2016;45:399-409.

doi: 10.1016/j.actbio.2016.08.049

99. Abdalla M, Joplin A, Elahinia M, Ibrahim H. Corrosion modeling of magnesium and its alloys for biomedical applications. *Corros Mater Degrad*. 2020;1(2):11.

doi: 10.3390/cmd1020011

100. Barzegari M, Mei D, Lamaka SV, Geris L. Computational modeling of degradation process of biodegradable magnesium biomaterials. *Corros Sci.* 2021;190:109674.

doi: 10.1016/j.corsci.2021.109674

101. Grogan JA, Leen SB, McHugh PE. A physical corrosion model for bioabsorbable metal stents. *Acta Biomater.* 2014;10(5):2313-2322.

doi: 10.1016/j.actbio.2013.12.059

102. Bajger P, Ashbourn J, Manhas V, Guyot Y, Lietaert K, Geris L. Mathematical modelling of the degradation behaviour of biodegradable metals. *Biomech Model Mechanobiol.* 2017;16:227-238.

doi: 10.1007/s10237-016-0812-3

103. Grogan J, O'Brien B, Leen S, McHugh P. A corrosion model for bioabsorbable metallic stents. *Acta Biomater.* 2011;7(9):3523-3533.

doi: 10.1016/j.actbio.2011.05.032

104. Grogan JA, Leen SB, McHugh PE. Optimizing the design of a bioabsorbable metal stent using computer simulation methods. *Biomaterials*. 2013;34(33):8049-8060.

doi: 10.1016/j.biomaterials.2013.07.010

105. Gastaldi D, Sassi V, Petrini L, Vedani M, Trasatti S, Migliavacca F. Continuum damage model for bioresorbable magnesium alloy devices-Application to coronary stents. *J Mech Behav Biomed Mater.* 2011;4(3):352-365.

doi: 10.1016/j.jmbbm.2010.11.003

106. Wilder JW, Clemons C, Golovaty D, Kreider KL, Young GW, Lillard RS. An adaptive level set approach for modeling damage due to galvanic corrosion. *J Eng Math.* 2015;91:121-142.

doi: 10.1007/s10665-014-9732-3

107. Gao Y, Wang L, Gu X, Chu Z, Guo M, Fan Y. A quantitative study on magnesium alloy stent biodegradation. *J Biomech.* 2018;74:98-105.

doi: 10.1016/j.jbiomech.2018.04.027

108. Duddu R. Numerical modeling of corrosion pit propagation using the combined extended finite element and level set method. *Comput Mech.* 2014;54(3):613-627.

doi: 10.1007/s00466-014-1010-8

109. Vijayaraghavan V, Garg A, Gao L, Vijayaraghavan R. Finite element based physical chemical modeling of corrosion in magnesium alloys. *Metals*. 2017;7(3):83.

doi: 10.3390/met7030083

110. Quinn C, Van Gaalen K, McHugh PE, Kopp A, Vaughan TJ. An enhanced phenomenological model to predict surface-based localised corrosion of magnesium alloys for medical use. *J Mech Behav Biomed Mater.* 2023;138:105637.

doi: 10.1016/j.jmbbm.2022.105637

111. Boland EL, Shirazi RN, Grogan JA, McHugh PE. Mechanical and corrosion testing of magnesium WE43 specimens for pitting corrosion model calibration. *Adv Eng Mater.* 2018;20(10):1800656.

doi: 10.1002/adem.201800656

112. Sanz-Herrera JA, Reina-Romo E, Boccaccini AR. *In silico* design of magnesium implants: Macroscopic modeling. *J Mech Behav Biomed Mater.* 2018;79:181-188.

doi: 10.1016/j.jmbbm.2017.12.016

113. Amerinatanzi A, Mehrabi R, Ibrahim H, Dehghan A, Shayesteh Moghaddam N, Elahinia M. Predicting the biodegradation of magnesium alloy implants: Modeling, parameter identification, and validation. *Bioengineering*. 2018;5(4):105.

doi: 10.3390/bioengineering5040105

114. Shen Z, Zhao M, Bian D, *et al*. Predicting the degradation behavior of magnesium alloys with a diffusion-based theoretical model and *in vitro* corrosion testing. *J Mater Sci Technol*. 2019;35(7):1393-1402.

doi: 10.1016/j.jmst.2019.02.004

115. Putra RU, Basri H, Prakoso AT, *et al*. Level of activity changes increases the fatigue life of the porous magnesium scaffold, as observed in dynamic immersion tests, over time. *Sustainability*. 2023;15(1):823.

doi: 10.3390/su15010823

116. Sanz-Herrera JA, Reina-Romo E. Continuum modeling and simulation in bone tissue engineering. *Appl Sci.* 2019;9(18):3674.

doi: 10.3390/app9183674

117. Ahmed H, Bedding-Tyrrell M, Deganello D, Xia Z, Xiong Y, Zhao F. Efficient calculation of fluid-induced wall shear stress within tissue engineering scaffolds by an empirical model. *Med Novel Technol Devices*. 2023;18:100223.

doi: 10.1016/j.medntd.2023.100223

118. Chalisgaonkar R. Insight in applications, manufacturing and corrosion behaviour of magnesium and its alloys-A review. *Mater Today Proc.* 2020;26:1060-1071.

doi: 10.1016/j.matpr.2020.02.211

119. Dong J, Lin T, Shao H, *et al*. Advances in degradation behavior of biomedical magnesium alloys: A review. *J Alloys Compd*. 2022;908:164600.

doi: 10.1016/j.jallcom.2022.164600

120. Chen J, Tan L, Yu X, Etim IP, Ibrahim M, Yang K. Mechanical properties of magnesium alloys for medical application: A review. *J Mech Behav Biomed Mater.* 2018;87:68-79.

doi: 10.1016/j.jmbbm.2018.07.022

121. Erdmann N, Angrisani N, Reifenrath J, *et al*. Biomechanical testing and degradation analysis of MgCa0. 8 alloy screws: A comparative *in vivo* study in rabbits. *Acta Biomater.* 2011;7(3):1421-1428.

doi: 10.1016/j.actbio.2010.10.031

122. Singh S, Manoj Kumar R, Kuntal KK, *et al*. Sol-gel derived hydroxyapatite coating on Mg-3Zn alloy for orthopedic application. *JOM*. 2015;67(4):702-712.

doi: 10.1007/s11837-015-1364-1

123. Gu X, Xie X, Li N, Zheng Y, Qin L. *In vitro* and *in vivo* studies on a Mg-Sr binary alloy system developed as a new kind of biodegradable metal. *Acta Biomater.* 2012;8(6):2360-2374.

doi: 10.1016/j.actbio.2012.02.018

124. Niu J, Xiong M, Guan X, *et al*. The *in vivo* degradation and bone-implant interface of Mg-Nd-Zn-Zr alloy screws: 18 months post-operation results. *Corros Sci.* 2016;113:183-187.

doi: 10.1016/j.corsci.2016.10.009

125. Gawlik MM, Wiese B, Desharnais V, Ebel T, Willumeit-Römer R. The effect of surface treatments on the degradation of biomedical Mg alloys-a review paper. *Materials*. 2018;11(12):2561.

doi: 10.3390/ma11122561

126. Saket M, Amini R, Kardar P, Ganjaee M. The chemical treatment of the AZ31-Magnesium alloy surface by a high-performance corrosion protective praseodymium (III)-based film. *Mater Chem Phys*. 2021;260:124113.

doi: 10.1016/j.matchemphys.2020.124113

127. Riaz U, Shabib I, Haider W. The current trends of Mg alloys in biomedical applications-A review. *J Biomed Mater Res B Appl Biomater*. 2019;107(6):1970-1996.

doi: 10.1002/jbm.b.34290

128. Esmaily M, Svensson J, Fajardo S, *et al*. Fundamentals and advances in magnesium alloy corrosion. *Prog Mater Sci*. 2017;89:92-193.

doi: 10.1016/j.pmatsci.2017.04.011

129. Bergmann G, Graichen F, Rohlmann A, *et al*. Realistic loads for testing hip implants. *Biomed Mater Eng.* 2010;20(2):65-75.

doi: 10.3233/bme-2010-0616

130. Li X, Chu C, Chu PK. Effects of external stress on biodegradable orthopedic materials: A review. *Bioact Mater*. 2016;1(1):77-84.

doi: 10.1016/j.bioactmat.2016.09.002

131. Wu H, Wang X, Wang G, *et al*. Advancing scaffold-assisted modality for *in situ* osteochondral regeneration: A shift from biodegradable to bioadaptable. *Adv Mater.* 2024;36(47):2407040.

doi: 10.1002/adma.202407040

132. Callens SJ, Fan D, van Hengel IA, *et al*. Emergent collective organization of bone cells in complex curvature fields. *Nat Commun.* 2023;14(1):855.

doi: 10.1038/s41467-023-36436-w

133. Otsuki B, Takemoto M, Fujibayashi S, Neo M, Kokubo T, Nakamura T. Pore throat size and connectivity determine bone and tissue ingrowth into porous implants: Three-dimensional micro-CT based structural analyses of porous bioactive titanium implants. *Biomaterials*. 2006;27(35):5892-5900.

doi: 10.1016/j.biomaterials.2006.08.013

134. Egan PF, Gonella VC, Engensperger M, Ferguson SJ, Shea K. Computationally designed lattices with tuned properties for tissue engineering using 3D printing. *PLoS One*. 2017;12(8):e0182902.

doi: 10.1371/journal.pone.0182902

135. Aghion E, Perez Y. Effects of porosity on corrosion resistance of Mg alloy foam produced by powder metallurgy technology. *Mater Charact*. 2014;96:78-83.

doi: 10.1016/j.matchar.2014.07.012

136. Jia G, Huang H, Niu J, *et al*. Exploring the interconnectivity of biomimetic hierarchical porous Mg scaffolds for bone tissue engineering: Effects of pore size distribution on mechanical properties, degradation behavior and cell migration ability. *J Magn Alloys*. 2021;9(6):1954-1966.

doi: 10.1016/j.jma.2021.02.001

137. Li Z, Chen Z, Chen X, Zhao R. Multi-objective optimization for designing porous scaffolds with controllable mechanics and permeability: A case study on triply periodic minimal surface scaffolds. *Compos Struct.* 2024;333:117923.

doi: 10.1016/j.compstruct.2024.117923

138. Chen Y, Zhou S, Li Q. Microstructure design of biodegradable scaffold and its effect on tissue regeneration. *Biomaterials*. 2011;32(22):5003-5014.

doi: 10.1016/j.biomaterials.2011.03.064

139. Truscello S, Kerckhofs G, Van Bael S, Pyka G, Schrooten J, Van Oosterwyck H. Prediction of permeability of regular scaffolds for skeletal tissue engineering: A combined computational and experimental study. *Acta Biomater.* 2012;8(4):1648-1658.

doi: 10.1016/j.actbio.2011.12.021

140. Jeong CG, Hollister SJ. Mechanical, permeability, and degradation properties of 3D designed poly (1, 8 octanediol-co-citrate) scaffolds for soft tissue engineering. *J Biomed Mater Res B Appl Biomater*. 2010;93(1):141-149.

doi: 10.1002/jbm.b.31568

141. Guo X, Zheng X, Yang Y, Yang X, Yi Y. Mechanical behavior of TPMS-based scaffolds: A comparison between minimal surfaces and their lattice structures. *SN Appl Sci.* 2019;1(10):1145.

doi: 10.1007/s42452-019-1167-z

142. Cheng MQ, Wahafu T, Jiang GF, *et al*. A novel open-porous magnesium scaffold with controllable microstructures and properties for bone regeneration. *Sci Rep.* 2016;6(1):24134.

doi: 10.1038/srep24134

143. Yan Y, Kang Y, Li D, *et al*. Microstructure, mechanical properties and corrosion behavior of porous Mg-6 wt.% Zn scaffolds for bone tissue engineering. *J Mater Eng Perform*. 2018;27:970-984.

doi: 10.1007/s11665-018-3189-x

144. Wang C, Min S, Liu J, *et al*. Effect of pore geometry on properties of high-temperature oxidized additively manufactured magnesium scaffolds. *J Magn Alloys*. 2023;12(11):4509-4520.

doi: 10.1016/j.jma.2023.08.016

145. Augustin J, Feichtner F, Waselau AC, *et al*. Effect of pore size on tissue ingrowth and osteoconductivity in biodegradable Mg alloy scaffolds. *J Appl Biomater Funct Mater.* 2022;20:22808000221078168.

doi: 10.1177/22808000221078168

146. Shi Y, Xu W, Che H, *et al*. The effect of topological design on the degradation behavior of additively manufactured porous zinc alloy. *NPJ Mater Degrad.* 2024;8(1):42.

doi: 10.21203/rs.3.rs-3460164/v1

147. Motaharinia A, Drelich JW, Sharif S, *et al*. Overview of porous magnesium-based scaffolds: development, properties and biomedical applications. *Mater Futures*. 2025;4(1):012401.

doi: 10.1088/2752-5724/ad9493

148. Antoniac I, Manescu V, Paltanea G, *et al*. Additive

manufactured magnesium-based scaffolds for tissue engineering. *Materials*. 2022;15(23):8693.

doi: 10.3390/ma15238693

149. Bonithon R, Lupton C, Roldo M, *et al*. Open-porous magnesium-based scaffolds withstand *in vitro* corrosion under cyclic loading: A mechanistic study. *Bioact Mater.* 2023;19:406-417.

doi: 10.1016/j.bioactmat.2022.04.012

150. Guo L, Zhang X, Zhang Z, Hao Z. Degradation characteristics of high-purity magnesium implants under single static and cyclic compressive loads *in vivo* and *in vitro*. *J Magn Alloys*. 2025;13:1480-1494.

doi: 10.1016/j.jma.2024.12.014

151. Schmidt M, Waselau AC, Feichtner F, *et al*. *In vivo* investigation of open-pored magnesium scaffolds LAE442 with different coatings in an open wedge defect. *J Appl Biomater Funct Mater.* 2022;20:22808000221142679.

doi: 10.1177/22808000221142679

152. Ye J, Miao B, Xiong Y, *et al*. 3D printed porous magnesium metal scaffolds with bioactive coating for bone defect repair: Enhancing angiogenesis and osteogenesis. *J Nanobiotechnol.* 2025;23(1):160.

doi: 10.1186/s12951-025-03222-3

153. Zhang Y, Ding Y, Wang J, *et al*. Study on degradation behavior of porous magnesium alloy scaffold loaded with rhBMP-2 and repair of bone defects. *J Mater Res Technol.* 2024;30:6498-6507.

doi: 10.1016/j.jmrt.2024.04.227

154. Lv Z, Peng B, Ye Y, *et al*. Bolstered bone regeneration by multiscale customized magnesium scaffolds with hierarchical structures and tempered degradation. *Bioact Mater.* 2025;46:457-475.

doi: 10.1016/j.bioactmat.2024.12.002

155. Gong T, Lu Y, Cheng L. Comparison of the biomechanical performance of three spinal implants for treating the wedge-shaped burst fractures. *Med Novel Technol Devices*. 2022;13:100109.

doi: 10.1016/j.medntd.2021.100109

156. Lei B, Gao X, Zhang R, Yi X, Zhou Q. *In situ* magnesium phosphate/polycaprolactone 3D-printed scaffold induce bone regeneration in rabbit maxillofacial bone defect model. *Mater Des.* 2022;215:110477.

doi: 10.1016/j.matdes.2022.110477

157. Huang X, Lou Y, Duan Y, *et al*. Biomaterial scaffolds in maxillofacial bone tissue engineering: A review of recent advances. *Bioact Mater.* 2024;33:129-156.

doi: 10.1016/j.bioactmat.2023.10.031

158. Koo Y, Lee HB, Dong Z, *et al*. The effects of static and dynamic loading on biodegradable magnesium pins *in vitro* and *in vivo*. *Sci Rep.* 2017;7(1):14710.

doi: 10.1038/s41598-017-14836-5

159. Foroughi AH, Valeri C, Razavi MJ. A review of computational optimization of bone scaffold architecture: Methods, challenges, and perspectives. *Prog Biomed Eng.* 2024;12:212.

doi: 10.1088/2516-1091/ad879a

160. Bonfanti S, Hiemer S, Zulkarnain R, Guerra R, Zaiser M, Zapperi S. Computational design of mechanical metamaterials. *Nat Comput Sci.* 2024;4(8):574-583.

doi: 10.1038/s43588-024-00672-x

161. Qian C, Kaminer I, Chen H. A guidance to intelligent metamaterials and metamaterials intelligence. *Nat Commun.* 2025;16(1):1154.

doi: 10.1038/s41467-025-56122-3

ACCSCIENCE PUBLISHING

Materials Science in Additive Manufacturing

REVIEW ARTICLE

Laser additive manufacturing of nickel-based superalloys: A review

Yunlong Hu[1]*, Zihong Wang[1]*, Qiang Zhang[1], Shan Li[1], Xin Zhang[2], and Weidong Huang[2]

[1]Department of Structural Materials Research, Suzhou Laboratory, Suzhou, Jiangsu, China

[2]State Key Laboratory of Solidification Processing, Northwestern Polytechnical University, Xi'an, Shaanxi, China

(This article belongs to the *Special Issue*: *Additive Manufacturing of Materials for Extreme Environments*)

Abstract

Nickel-based superalloys are critical materials for high-temperature components in core equipment, such as aerospace engines and gas turbines. In recent years, with the rapid advancement of metal additive manufacturing (AM) technologies, the fabrication of complex geometries using nickel-based superalloys has been successfully applied in modern engines and gas turbines. These components demonstrate significant advantages in integration, weight reduction, multifunctionality, and performance enhancement. However, due to the complex alloy composition and multiphase microstructure of nickel-based superalloys, the AM process is accompanied by intricate phase transformations and high thermal stresses. This often leads to defects, such as hot cracking—particularly in the vicinity of the molten pool. In addition, the rapid non-equilibrium solidification and repeated thermal cycles from layer-by-layer deposition result in complex microstructural evolution and phase transformations during both solidification and subsequent solid-state reactions. These factors significantly influence the strengthening and toughening behavior of the superalloys. Consequently, the comprehensive mechanical properties of additively manufactured nickel-based superalloys still lag behind those of their traditionally forged counterparts. This article reviews recent domestic and international research progress on the mechanisms of crack formation and control strategies in AM of nickel-based superalloys, as well as the evolution of microstructure and the associated strengthening and toughening mechanisms. Furthermore, it discusses the design of nickel-based superalloys tailored specifically for AM, and offers insights and future perspectives on the development of advanced strengthening strategies and alloy design methodologies for AM applications.

Keywords: Additive manufacturing; Nickel-based superalloy; Cracking mechanism; Microstructural evolution; Strengthening mechanism; Alloy design

***Corresponding authors:**
Yunlong Hu
(huyl@szlab.ac.cn)
Zihong Wang
(wangzh@szlab.ac.cn)

Citation: Hu Y, Wang Z, Zhang Q, Li S, Zhang X, Huang W. Laser additive manufacturing of nickel-based superalloys: A review. *Mater Sci Add Manuf*. 2026;5(1):025240051. doi: 10.36922/MSAM025240051

Received: June 14, 2025

Revised: August 07, 2025

Accepted: August 11, 2025

Published online: October 31, 2025

1. Introduction

High-temperature alloys refer to materials capable of maintaining long-term structural stability and operational performance at temperatures above 600°C. They exhibit excellent mechanical properties at both room and elevated temperatures, including high

static mechanical strength, creep resistance at elevated temperatures, and fatigue performance. In addition, they possess good oxidation and corrosion resistance, as well as exceptional microstructural stability under harsh service conditions. As a result, they are extensively employed in aerospace engines, gas turbines, and petrochemical industries.[1] Based on their matrix composition, high-temperature alloys can be classified into iron-based, nickel-based, and cobalt-based alloys. Compared to iron-based and cobalt-based superalloys, nickel-based superalloys feature a single-phase crystal structure (face-centered cubic [FCC] structure) and do not undergo allotropic transformations at high temperatures, which enhance their structural stability. Moreover, the nickel matrix can dissolve a large quantity of strengthening elements, such as aluminum, molybdenum, niobium, tungsten, and titanium, allowing for a high degree of alloying and the formation of multiple strengthening phases within the matrix. Consequently, nickel-based superalloys demonstrate superior mechanical performance. In addition, nickel has a high melting point and excellent chemical stability, which endows these alloys with remarkable oxidation and corrosion resistance. For these reasons, nickel-based superalloys are the most widely used and extensively developed class of high-temperature alloys.[2]

In recent years, with the rapid advancement of technologies in modern aero-engines and gas turbines, increasingly stringent requirements have been placed on the structure, performance, and functionality of their hot-section components. The integrated structural and functional design of complex components in aero-engines and gas turbines can significantly improve lightweight characteristics, functional performance, and mechanical properties, and has gradually become a key direction in the design and manufacturing of high-performance complex components in this field. However, currently, 30–45% of hot-section components in aero-engines and gas turbines are manufactured from high-temperature alloys using forging processes, followed by subtractive machining, which often results in substantial material waste. Moreover, high-temperature alloys generally exhibit poor formability and machinability, making the production of complex structural components even more challenging. As a result, in actual component design and manufacturing processes, design compromises are frequently made regarding functionality and lightweight features due to limitations in current machining technologies,[2,3] which severely restrict innovation and development in aero-engine and gas turbine technologies.

Metal additive manufacturing (AM), also known as 3D printing, is an advanced, freeform digital manufacturing method that has created a transformative pathway for the integrated structural-functional manufacturing of complex components in aero-engines and gas turbines. Meanwhile, it can also strengthen metallic materials, thereby improving their mechanical properties. At present, the mainstream high-performance laser AM (LAM) technologies for metals are primarily categorized into two types: laser-directed energy deposition (LDED) and laser powder bed fusion (LPBF). LDED enables efficient fabrication of complex, high-performance components, with virtually no size limitation of the final part. Moreover, LDED features *in situ* material feeding (using metal powders or wires), which allows for arbitrary multi-material integration and the creation of functionally graded structures within a single component, providing a technological foundation for multifunctional design. In contrast, although LPBF has relatively lower build efficiency, it offers superior dimensional accuracy and surface finish, making it particularly suitable for producing intricate and highly detailed geometries.[3-7] With the rapid development of AM technologies, numerous companies have successfully implemented metal AM in the production of critical high-performance components for aero-engines and gas turbines. It has been demonstrated that metal AM can: (i) achieve near-net shaping of complex components with significantly improved material utilization; (ii) enhance lightweight design and overall performance; and (iii) shorten research and production cycles, thereby reducing manufacturing costs. For example, General Electric (GE) in the United States (U.S.) optimized the design of the fuel nozzle for the LEAP-1A engine and utilized AM to fabricate a previously unachievable complex internal channel structure using conventional manufacturing methods.[7,8] This innovation enabled the integration of over 20 individual components into a single, monolithic part, which was manufactured in a single process step. As a result, fuel efficiency and nozzle durability were significantly improved. The redesigned nozzle is expected to reduce fuel consumption and emissions of the LEAP engine by approximately 15%. At present, LEAP engines equipped with additively manufactured fuel nozzles have been installed on the Airbus A320neo aircraft, with the first successful flight completed on May 19, 2015. The engine has been certified by both the European Aviation Safety Agency and the U.S. Federal Aviation Administration. At the 2017 Paris Air Show, GE announced that LEAP engines containing additively manufactured components had generated $31 billion in orders for the company.[9]

At present, the number of nickel-based superalloy components fabricated through AM for commercial applications remains relatively limited, and the range of nickel-based superalloys suitable for AM is also quite

narrow. This limitation primarily stems from the complex alloy composition and phase structure of nickel-based superalloys, as well as the intricate metallurgical behaviors and high thermal stresses that occur during the AM process, making them highly susceptible to defects such as hot cracking. The near-rapid, non-equilibrium solidification within the melt pool, coupled with repeated thermal cycling and associated solid-state phase transformations, further complicates microstructural evolution. Moreover, the diverse strengthening and toughening mechanisms inherent to nickel-based superalloys introduce additional challenges in achieving consistent control over mechanical properties. Although the mechanical performance of additively manufactured nickel-based superalloys has, in some cases, exceeded that of their forged counterparts, the available data often exhibit significant variability, with notable differences observed between different batches. As a result, research on the AM of nickel-based superalloys remains predominantly at the laboratory scale, hindering their widespread adoption in commercial applications.[10]

In addition, most of the nickel-based superalloys currently studied for AM are conventional commercial alloys, including cast superalloys (such as K465, IN738, DZ125, and CM247LC), wrought superalloys (such as Inconel 718, Inconel 625, and Hastelloy X [HX]), and powder metallurgy superalloys (such as IN100, Rene95, Rene88DT, and FGH4096). A review of the development history of superalloys reveals that alloy composition is closely tied to the processing method. To enhance mechanical properties, cast nickel-based superalloys typically contain relatively high levels of aluminum and titanium, resulting in a higher volume fraction of strengthening phases. However, this also makes them prone to macro- and micro-segregation during solidification, as well as the formation of coarse eutectic phases at the end of solidification, which negatively affects their weldability. In single-crystal superalloys, to avoid the formation of stray grains and low-angle grain boundaries, the content of grain boundary strengthening elements, such as carbon, boron, zirconium, and magnesium, is typically kept very low or even eliminated. In wrought superalloys, to reduce deformation resistance during plastic forming and to prevent cracking during forging, the aluminum and titanium contents are relatively low, and the volume fraction of strengthening phases is generally below 40%, which limits the extent of performance improvement achievable. In contrast, powder metallurgy superalloys completely avoid the solidification process, thereby minimizing elemental segregation. These alloys typically exhibit a higher volume fraction of strengthening phases (usually above 45%), leading to superior mechanical properties compared to wrought superalloys. This analysis highlights that the composition design of nickel-based superalloys has traditionally been optimized to align with the specific characteristics of their respective manufacturing processes. Since the processing characteristics of AM differ significantly from those of conventional methods, traditional commercial nickel-based superalloys may not be well-suited. Therefore, it is essential to develop novel nickel-based superalloys specifically tailored for AM to meet its unique requirements and promote the industrial application of additively manufactured nickel-based superalloys.[10]

The present review focuses on nickel-based superalloys, which are widely used as high-temperature structural materials for hot-section components in aerospace engines and gas turbines. It provides a comprehensive assessment of recent research progress, both domestically and internationally, in cracking mechanisms and crack prevention strategies in additively manufactured nickel-based superalloys, microstructural evolution, and underlying strengthening-toughening mechanisms, as well as alloy composition design specifically tailored for AM. Furthermore, this review presents insights and forward-looking perspectives on the future development of additively manufactured nickel-based superalloys.

2. Cracking mechanisms and crack control in additively manufactured nickel-based superalloys

Cracking is a prevalent issue in additively manufactured nickel-based superalloys. It has been observed not only in cast superalloys with poor weldability (such as K465,[11,12] DZ125,[13,14] CM247LC,[15,16] and IN738[17,18]) but also in powder metallurgy superalloys with good weldability (such as Rene 104,[19,20] Rene 88DT,[21,22] and IN100[23]), and even in wrought superalloys with relatively low crack sensitivity (such as Inconel 718[24-27], Inconel 625[28-30], and HX[31-37]). The presence of cracks significantly degrades the mechanical properties of the material, rendering it unsuitable for service applications. Therefore, understanding the cracking mechanisms and developing effective crack control strategies are critical priorities in the AM of nickel-based superalloys.

The metallurgical processes occurring in the melt pool during AM are comparable to those in welding. Therefore, established principles from welding metallurgy can be referenced to investigate the cracking mechanisms in additively manufactured nickel-based superalloys. According to well-established knowledge in the welding metallurgy of nickel-based superalloys, hot cracking is a prevalent metallurgical defect, and the primary types of cracks include solidification cracking (SC), liquation

cracking (LC), ductility dip cracking (DDC), and strain-age cracking (SAC).[38] SC occurs during the final stage of solidification when a low-melting-point eutectic liquid film forms between dendrites. Under the influence of shrinkage and thermal stresses, this film ruptures. Due to the closure of feeding channels, insufficient compensation for shrinkage leads to crack formation, typically located between dendrites and along grain boundaries. The key metallurgical factors influencing the SC susceptibility of nickel-based superalloys include the solidification temperature range, the amount and distribution of interdendritic liquid during late-stage solidification, and the morphology and size of grains. In general, the larger the solidification temperature range, the higher the susceptibility to SC.[39]

LC occurs in the heat-affected zone (HAZ) near the deposited layer during AM, where the material remains within the temperature range between the solidus and liquidus for an extended period. Within this range, some low-melting-point eutectic phases may partially remelt, forming liquid films that cannot withstand the applied stress, leading to crack initiation—most commonly along grain boundaries. DDC typically occurs in pure metals or single-phase austenitic alloys. Within the temperature range of $0.5T_S$ to T_S (where T_S is the solidus temperature), the material's ductility experiences a sharp decline. When localized deformation exceeds the critical strain limit under stress, cracks may form. As this type of cracking occurs in the solid state, it is also referred to as solid-state cracking. DDC is closely associated with grain boundary migration and is frequently observed at grain boundaries. SAC develops during reheating or subsequent heat treatment and is specific to precipitation-strengthened nickel-based superalloys. When the temperature range for precipitate formation overlaps with the stress relaxation range during heating, high local stresses can develop at grain boundaries. If the local stress exceeds a critical threshold, grain boundary failure occurs, resulting in SAC. The volume fraction of precipitates is the main factor affecting SAC susceptibility; the higher the aluminum and titanium content, the greater the cracking susceptibility.[40] The main types of cracking and their characteristics in additively manufactured nickel-based superalloys are displayed in Figure 1.

The AM process of nickel-based superalloys involves rapid cooling of small melt pools and repeated thermal cycling of the fabricated part, which leads to the development of significant thermal and residual stresses.[43-46] Although the near-rapid solidification in the melt pool during AM can effectively prevent macroscopic segregation, microscopic segregation still occurs—and in some cases, it may be even more severe than that observed in conventional casting. During solidification, alloying elements with equilibrium partition coefficients <1 tend to segregate into the interdendritic regions. This microsegregation results in a wider solidification temperature range and facilitates the formation of low-melting-point eutectic liquid phases between dendrites in nickel-based superalloys,[47-51] thereby promoting liquid film formation and further increasing susceptibility to SC and LC. Furthermore, repeated thermal cycling can expose already-deposited material to elevated temperatures that fall within the brittle temperature range of the alloy. At such temperatures, the alloy exhibits reduced ductility, making it more susceptible to DDC under thermal stress. In the case of precipitation-strengthened nickel-based superalloys, precipitate phases may form during thermal cycling, increasing the risk of SAC. Ojo *et al.*,[52,53] in their study of the welding of IN-738 alloy, observed that cracks primarily formed at grain boundaries within the HAZ, a characteristic feature of LC. They attributed this phenomenon to the rapid heating during welding, which prevented the complete dissolution of coarse γ' particles located at grain boundaries. The residual γ' then underwent a eutectic reaction with the surrounding γ matrix ($\gamma + \gamma' \rightarrow L$), resulting in the formation of a liquid film. In addition, grain-boundary M(Ti, Mo, W)C (MC) carbides, borides, and carbon-sulfide inclusions were found to experience similar liquation reactions, further promoting liquid film formation and crack initiation under stress. Other researchers have proposed that the liquid film in the HAZ may also arise from the direct melting of low-melting-point eutectic phases at grain boundaries.[54] Xu *et al.*,[41] in a study on laser solid-formed IN738LC superalloys, found that liquation cracks in the HAZ were predominantly located along grain boundaries. The primary cause of this liquation was the melting of low-melting γ–γ' eutectic at grain boundaries during processing, leading to continuous or semi-continuous liquid films. Moreover, boron enrichment at grain boundaries was found to lower the local melting temperature. It was, further, clarified that the liquation observed in laser solid-formed IN738LC was primarily due to direct eutectic melting rather than compositional liquation. This observation was supported by the fine size (~100 nm) and coherent nature of the γ' particles with the γ matrix, which implied that their dissolution was interface-controlled, resulting in a slow increase in solute concentration at the γ/γ' interface and thereby suppressing compositional liquation during rapid heating. In multilayer, multipass specimens, the overlapping regions exhibited the most severe cracking, with both liquation and solidification cracks present. Solidification cracks in the melt pool of the

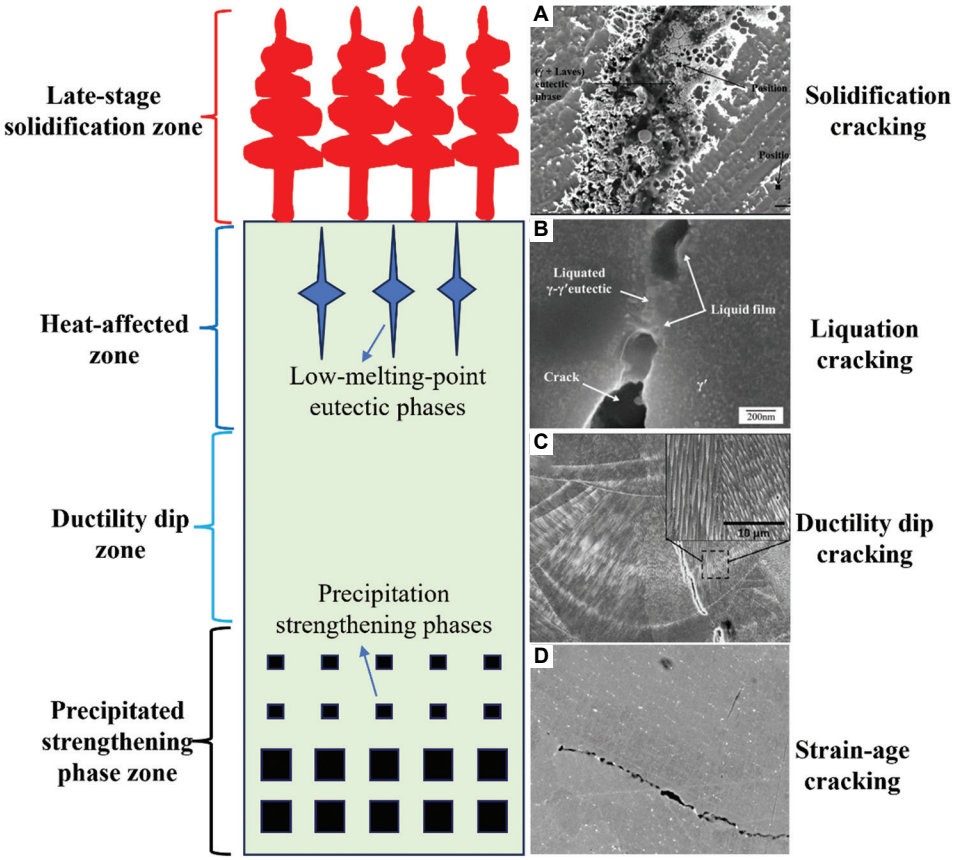

Figure 1. Cracking types and the characteristics of additively manufactured nickel-based superalloys. (A) Solidification cracking. Adapted with permission from Hu *et al.*[39] Copyright © 2017 Elsevier Ltd. (B) Liquation cracking. Adapted with permission from Xu *et al.*[41] Copyright © 2018 Elsevier Ltd. (C) Ductility dip cracking. Adapted with permission from Cloots *et al.*[42] Copyright © 2016 Elsevier Ltd. (D) Strain-age cracking. Adapted with permission from Li *et al.*[14] Copyright © 2018 Elsevier Ltd

overlay layer were observed to propagate directly from pre-existing liquation cracks in the HAZ. This crack linkage was attributed to a mismatch in thermal flow direction on either side of the overlap region, promoting the formation of high-angle grain boundaries. These boundaries have a lower complete solidification temperature and higher wettability compared to low-angle grain boundaries, making them more susceptible to liquid film spreading and, consequently, to crack initiation and propagation. Residual stress analysis of these specimens revealed that stress in the overlap zones was 300 MPa higher than in the bead interiors, providing a strong driving force for crack formation.

In the laser solid-forming process of Inconel 625, the present authors observed the segregation of alloying elements, such as Nb and Mo, into the interdendritic regions during solidification. This promoted the formation of Laves phases, which increased the alloy's solidification temperature range from 90°C to 210°C and significantly raised its susceptibility to SC.[39] In addition, the high thermal gradients inherent in the laser-forming process induced large thermal stresses in the deposited layers. These stresses acted on the thin, continuous liquid films present between dendrites at the end of solidification, leading to crack initiation. The mushy zone in Inconel 625 was found to be relatively wide, yet with a low liquid phase volume fraction. As a result, feeding channels became blocked, and the liquid phase could not adequately compensate for solidification shrinkage, allowing cracks to persist in the deposited layers. Chen *et al.*,[55] in their investigation of the cracking mechanisms in laser-additively manufactured Inconel 718, observed both solidification and liquation cracks in as-deposited specimens. However, he emphasized that liquation cracks had a more detrimental effect on mechanical properties. Hot cracks mainly propagated along Laves phases near grain boundaries, attributed to significant elemental segregation at grain boundaries, which promoted the formation of additional low-melting-point eutectics. This segregation enhanced constitutional supercooling, lowered the local solidification temperature,

and widened the solidification temperature range—factors that collectively contributed to increased stress concentration and greater susceptibility to liquation or partially liquated hot cracking. Cloots *et al.*,[42] in their study of selective laser melting (SLM)-formed IN738LC, employed focused ion beam slicing and atom-probe tomography to perform 3D reconstructions around cracks and found that Zr segregation was a primary cause of SC. Simulation results indicated a solidification temperature of 670°C for IN738LC, with pronounced Zr enrichment in the residual liquid phase, increasing crack susceptibility. Harrison *et al.*[56] concluded that cracks in SLM-formed HX were predominantly of solid-state origin, specifically ductility dip cracks. Similarly, Zhong *et al.*[57] reported multiple cracking modes in laser-cladded IN-738, including not only LC but also non-liquation DDC and SC. SAC commonly occurs in precipitation-strengthened superalloys, with γ' phase-strengthened superalloys exhibiting higher sensitivity. There is a positive correlation between SAC sensitivity and both the volume fraction and precipitation kinetics of the strengthening precipitates.

From the above studies, it can be seen that cracking in additively manufactured nickel-based superalloys is highly complex, often involving the coexistence of two or more crack types. To address this complexity, researchers have conducted extensive studies on crack control from multiple perspectives, including process parameter optimization, substrate pre-treatment, and alloy composition modification. A common strategy involves optimizing process parameters to suppress crack formation by adjusting heat input, modifying the solidification behavior of the melt pool, or tailoring the thermal history during deposition. Such adjustments help control the size and distribution of phases and mitigate thermal stresses generated during the build process. Zhao *et al.*[58] found that adjusting the overlap ratio between adjacent deposition tracks can effectively suppress crack formation in laser solid-formed Rene88DT superalloy. When the overlap ratio is too small, a "V"-shaped depression forms between tracks, where the fraction of low-melting (γ + γ') eutectic phases is relatively high and stress concentration is more pronounced, increasing the likelihood of crack initiation. Conversely, an excessive overlap ratio leads to sloped surfaces on the deposited layers, compromising dimensional accuracy. The study identified an optimal overlap ratio of 40%, which effectively avoids both cracking and surface distortion. Furthermore, post-process hot isostatic pressing (HIP) of the as-deposited components has been demonstrated to heal small internal cracks, thereby improving structural integrity. Chen *et al.*[55] found that optimizing processing parameters during LAM of Inconel 718—specifically, using lower scan speeds and laser power—effectively reduced cracking. Moreover, a clockwise rotation of the laser beam along the scanning direction was observed to further suppress crack formation. This was attributed to the concentration of more laser energy at the front of the melt pool, which enhanced lateral heat dissipation. As a result, secondary dendrite arm growth was promoted, leading to a regular, interlocking banded microstructure that inhibited the formation of continuous, low-melting Laves phases and improved interdendritic connectivity, thereby enhancing crack resistance. In addition, this approach reduced the size of the HAZ, helping to suppress thermal cracking. In a follow-up study, carbon nanotubes (CNTs) were incorporated into Inconel 718 to evaluate their effectiveness in crack suppression. The results demonstrated that CNT addition significantly reduced cracking. This was attributed to an increased elastic modulus of the alloy, which lowered overall strain. CNTs also facilitated thermal stress transfer between dendrites, alleviating local stress concentration. Furthermore, the CNTs themselves absorbed part of the applied stress, increasing resistance to crack propagation and thus effectively suppressing crack initiation. Nematzadeh *et al.*[59] and Zhong *et al.*[57] reported that reducing heat input during welding significantly alleviated cracking. However, Idowu *et al.*[60] reached the opposite conclusion: when grain boundary liquation is sufficiently severe, higher heat input can enhance grain boundary ductility and consequently reduce cracking. Similarly, Bian *et al.*[61] found that moderately increasing heat input could effectively suppress crack formation during laser-forming repair of DZ125 superalloy. This is because higher heat input reduces thermal stress to some extent and increases the amount of eutectic liquid phase, promoting better feeding and enabling *in situ* healing of incipient cracks during solidification. Ebrahimnia *et al.*[62] employed a grain refinement strategy to suppress the formation of coarse γ' phases, MC carbides, and γ–γ' eutectics, successfully reducing cracking in welded IN-738LC alloy. Xu *et al.*[41] investigated the influence of induction preheating on the microstructure and cracking behavior of laser solid-formed IN738LC. The results indicated that preheating the substrate significantly reduced thermal stresses during deposition, thereby decreasing crack density in as-deposited samples. In contrast, Chen *et al.*[55] demonstrated that bottom-side directional cooling of the substrate was an effective approach for inhibiting the initiation and propagation of thermal cracks. Directional cooling enhanced the directionality of heat flow during solidification, reduced grain boundary misorientation, destabilized interdendritic liquid films, and alleviated local stress concentration. In summary, while optimization of process parameters and substrate pretreatment can both

contribute significantly to crack mitigation, they have inherent limitations and are often insufficient to eliminate cracking. Moreover, conflicting requirements among different control strategies frequently arise, resulting in an extremely narrow processing window for nickel-based superalloys.

In recent years, alloy design has emerged as an increasingly recognized and widely investigated strategy for mitigating cracking in metallic materials. A substantial body of research has been devoted to this approach. To suppress SC in laser solid-formed Inconel 625, the authors of this study implemented a hybrid alloying strategy by incorporating varying amounts of titanium (Ti).[39] The results revealed that when the Ti content in Inconel 625 was below 2 wt.%, the solidification temperature range remained relatively constant at approximately 210°C. However, with further increases in Ti content, the solidification temperature range significantly decreased. At a Ti content of 5 wt.%, the range dropped to 149°C—a reduction of 30% compared to that of the base Inconel 625 alloy. This led to a marked improvement in crack resistance; cracks were eliminated in the as-deposited samples when the Ti content exceeded 3 wt.%. This enhancement is primarily attributed to the narrowed solidification temperature range, which reduces the alloy's susceptibility to SC. In addition, the volume fraction of (γ + Laves) eutectic phases increased significantly with Ti addition, resulting in the formation of thicker interdendritic liquid films during the later stages of solidification. These thicker films enhance feeding capability and reduce the likelihood of crack initiation. When the volume fraction of interdendritic liquid exceeds 7%, the feeding channels become more continuous, enabling sufficient liquid to backfill and heal incipient cracks during solidification. It has been found that reducing the contents of minor alloying elements manganese (Mn) and silicon (Si) significantly decreased cracking in laser-additively manufactured HX superalloy.[35,36] The primary mechanism is that lowering the levels of these elements narrows the solidification temperature range, thereby reducing its propensity for SC during processing. Chen *et al.*[63] successfully reduced cracking in laser-cladded IN-738 alloy layers by incorporating small amounts of rare earth oxide (Y_2O_3). Han *et al.*[64] found that the addition of nano-sized TiC particles to HX effectively suppressed crack formation. This was primarily attributed to an increased volume fraction of low-angle grain boundaries and subgrain boundaries, as well as the enhanced yield strength (YS) of the alloy, which collectively improved resistance to solid-state cracking. Harrison *et al.*[56] proposed an alloy redesign strategy to mitigate microcrack formation in nickel-based superalloys during AM. Their approach focused on increasing the concentration of solid-solution strengthening elements to enhance the high-temperature strength of HX. As a result, the thermal stresses generated during fabrication were no longer sufficient to exceed the alloy's strength, thereby effectively preventing crack initiation. These studies collectively demonstrate that compositional optimization is a highly effective strategy for minimizing cracking in laser-additively manufactured components. Moreover, this approach provides a promising pathway for the future design of nickel-based superalloys specifically tailored for AM applications.

3. Microstructural evolution and strengthening-toughening mechanisms of nickel-based superalloys fabricated by AM

The microstructure and mechanical properties of nickel-based superalloys fabricated by AM are primarily determined by the near-rapid solidification process within the molten pool during deposition, as well as by the solid-state phase transformations occurring during subsequent thermal cycles and post-processing heat treatments. Therefore, a clear understanding of microstructural evolution during fabrication and heat treatment is a prerequisite for achieving superior mechanical performance. Unlike traditional manufacturing processes (*e.g.*, casting, forging, and powder metallurgy), AM is characterized by rapid solidification in a small molten pool and repeated thermal cycling. During solidification, the molten pool exhibits a high temperature gradient (approximately 10^6 K/m) and a high cooling rate (10^3–10^6 K/s). Due to the heat transfer characteristics within the molten pool, the temperature gradient decreases from the bottom to the top, while the solidification rate increases, as illustrated in Figure 2C. In addition, the direction of the temperature gradient evolves from being nearly perpendicular to the scanning direction at the pool bottom to nearly parallel at the top. The growth direction of columnar grains is governed by the local heat flow direction and the crystallographic preferred orientation. Consequently, the columnar grain growth direction—perpendicular to the local temperature gradient at the pool top—shifts from perpendicular to parallel relative to the scanning direction, resulting in the formation of misoriented dendrites in the upper region of the molten pool. Furthermore, according to the columnar-to-equiaxed transition diagram for nickel-based superalloys (Figure 2D), as the temperature gradient decreases and the solidification rate increases, a transition from columnar to equiaxed grains occurs, leading to the formation of equiaxed grains in the upper region of the molten pool. When the subsequent layer is deposited, the equiaxed grain region at the top of the previous layer is remelted. Since the matrix phase of nickel-based superalloys is the γ-phase with an FCC structure, which exhibits a strong

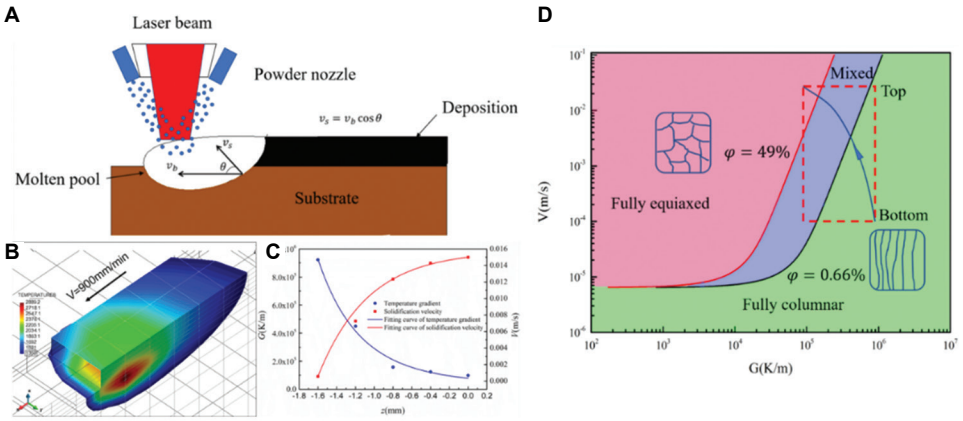

Figure 2. Solidification conditions of the molten pool and structure selection map for laser solid-formed Inconel 625 alloy. (A) Schematic of laser-directed energy deposition processing.[66] (B) The molten pool morphology and temperature filed of single-track; (C) Evolution of the local solidification variables G and V as the depth z for the 1st layer; (D) Microstructure selection map for Inconel 625 superalloy under the experiment conditions. Adapted with permission from Hu *et al.*[65] Copyright © 2018 Elsevier Limited

<001> crystallographic growth preference, columnar grains with non-<001> orientations are progressively eliminated during competitive growth. This enables the epitaxial growth of <001>-oriented grains across multiple deposited layers, ultimately resulting in a pronounced <001> solidification texture in the as-deposited material.[65]

The high cooling rate inherent in AM results in extremely fine dendritic substructures within the grains, and in some cases, even cellular structures may form. Although macrosegregation is generally absent in AM-processed materials, microsegregation remains significant. The segregation of alloying elements promotes the formation of interdendritic eutectic phases, which can be either dispersed or continuously distributed (Figure 3).[39] In addition, the rapid, localized heating, and cooling cycles during AM introduce substantial thermal stresses within the deposited layers. On cooling, significant residual stresses are retained, and the as-deposited samples exhibit high dislocation densities (Figure 4).[64] Therefore, the microstructure of nickel-based superalloys fabricated by AM is characterized by coarse, epitaxially grown columnar grains, containing fine dendritic or cellular substructures and high dislocation density within the grains. Eutectic phases form in the interdendritic regions to a certain volume fraction, and the material develops a strong solidification texture. Consequently, AM-fabricated nickel-based superalloys exhibit pronounced microstructural and mechanical anisotropy.[10]

The size and distribution of interdendritic eutectic phases significantly influence the strength and ductility of nickel-based superalloys. On one hand, the elements that segregate during solidification—such as Nb, Ti, and Al—are often the primary strengthening elements. The formation of interdendritic eutectic phases depletes these elements from the γ-matrix, thereby reducing the solute concentration available for precipitation hardening and ultimately lowering the alloy's overall strength. On the other hand, interdendritic eutectic phases are typically hard and brittle, acting as preferential sites for crack initiation or serving as easy paths for crack propagation under applied stress. This behavior severely compromises the alloy's fracture toughness and ductility. To achieve superior mechanical properties, precise control over the microstructure of laser-based additively manufactured nickel-based superalloys is essential. Current strategies primarily focus on optimizing processing parameters to tailor solidification conditions within the molten pool and suppress the formation of continuously networked eutectic phases. These process optimizations are typically followed by post-processing heat treatments, which further refine grain morphology and size, as well as the morphology, volume fraction, and spatial distribution of secondary precipitated phases.[65]

Extensive research has been conducted by numerous domestic and international institutions on the microstructural evolution and mechanical properties of laser-additively manufactured nickel-based superalloys with relatively good weldability, such as Inconel 718, Inconel 625, and HX.[65-77] Some additively manufactured components made from these alloys have already been successfully implemented in aerospace engines and gas turbines. Among these alloys, Inconel 625 and HX are solid-solution-strengthened superalloys, whose microstructural evolution, phase composition, and strengthening-toughening mechanisms are relatively straightforward. In contrast, Inconel 718 is a precipitation-strengthened superalloy characterized by more complex

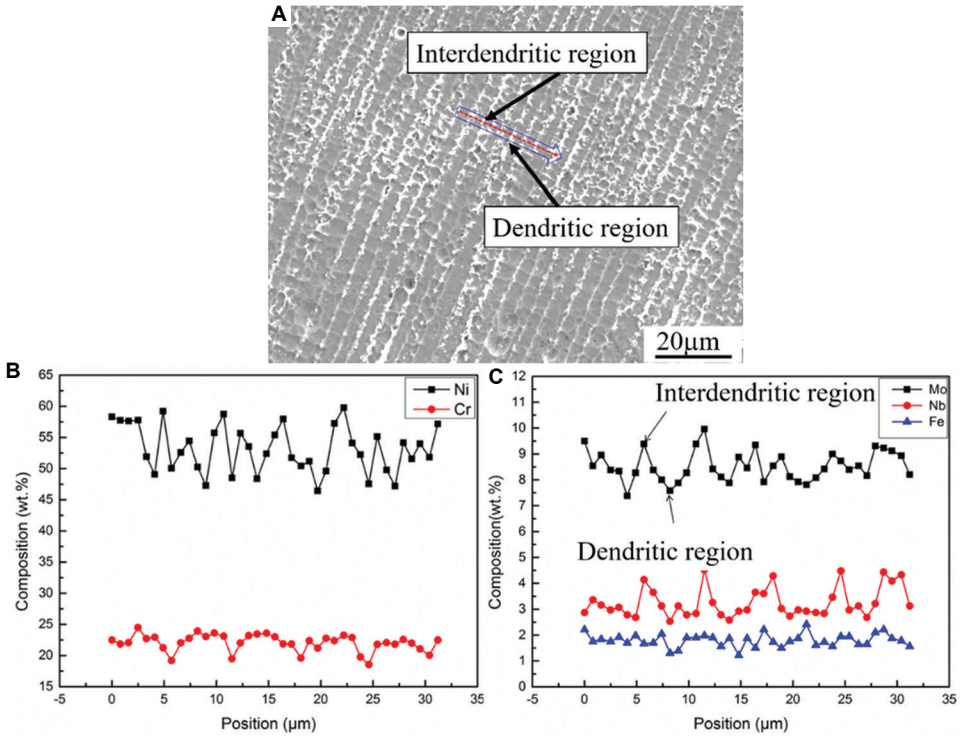

Figure 3. Microscale elemental segregation in the as-deposited sample of laser solid-formed Inconel 625 alloy. (A) Distribution of elements in dendritic and interdendritic region. (B) The distribution of Ni and Cr elements in the interdendritic regions and dendritic arms. (C) The distribution of Mo, Nb, and Fe elements in the interdendritic regions and dendritic arms. Adapted with permission from Hu *et al.*[39] Copyright © 2017 Elsevier Limited

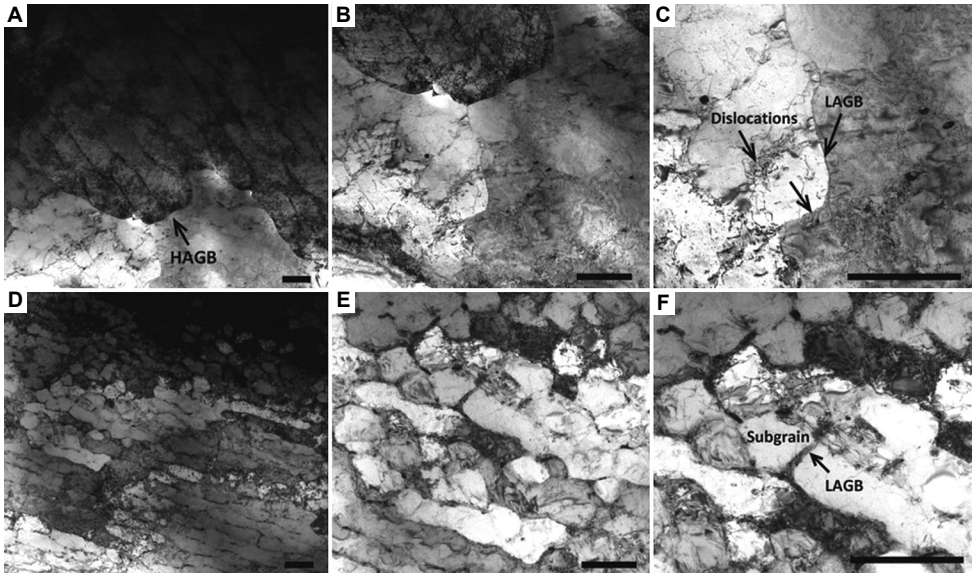

Figure 4. Dislocation configurations in laser-additively manufactured Hastelloy X (HX) alloy. (A-C) Transmission electron microscopy (TEM) images of the as-built HX alloy at different magnifications: Characteristic structure of high-angle grain boundaries (A), subgrain structure (B), and characteristic structure of dislocations and low-angle grain boundaries (LAGBs) (C). (D-F) TEM images of TiC nanoparticles enhanced HX sample, displaying increased dislocation density and the presence of LAGBs: Subgrain structure (D), dislocation cell (E), and characteristic structure of subgrain and LAGBs (F). Scale bars: 1 μm. Adapted with permission from Han *et al.*[64] Copyright © 2019 Elsevier Limited

phase assemblages and multi-faceted strengthening mechanisms. Despite significant progress, several critical challenges in the AM of nickel-based superalloys remain unresolved:

(i) Non-equilibrium phases, such as Laves phases, carbides, and γ–γ' eutectic phases, formed during rapid solidification in the molten pool can significantly degrade the mechanical properties of the material.
(ii) AM- fabricated nickel-based superalloys typically exhibit mechanical anisotropy and a combination of high strength with low ductility. Although post-processing heat treatments can eliminate or reduce microstructural anisotropy, anisotropic mechanical behavior often persists. Compared to their wrought counterparts, AM superalloys generally display inferior tensile ductility even after heat treatment, failing to meet stringent requirements for structural stability and operational safety.
(iii) Fatigue, creep, and long-term durability data for AM nickel-based superalloys remain limited. These materials also suffer from poor long-term plasticity, and the underlying deformation mechanisms under creep or sustained loading conditions are not yet fully understood. Consequently, the full application potential of AM nickel-based superalloys has not been fully realized.

Dinda *et al.*[78] found that the laser scanning strategy is a key factor influencing the crystallographic texture of laser-additively manufactured Inconel 718 alloy. Unidirectional laser scanning tends to promote the formation of a fiber texture, whereas bidirectional scanning results in a rotated cube texture. The difference in texture type is primarily attributed to the significant variation in temperature gradients within the melt pool induced by different scanning strategies. Ma *et al.*[79] investigated the texture of as-deposited Inconel 625 fabricated by LAM and found that it is dominated by a strong Goss texture ({011}<100>), with a weaker cube texture ({001}<100>) component. This specific texture type leads to a lower work hardening rate in the additively manufactured alloy compared to its wrought counterpart. The observed texture in Inconel 625 differs from that reported by Dinda *et al.*[78] for Inconel 718. Analysis indicates that, at a constant scanning speed, increasing the laser power and the material's absorptivity enhances the heat input, resulting in a deeper molten pool. Consequently, the temperature gradient along the deposition (z) direction decreases, and the maximum heat flow direction becomes increasingly aligned with the laser scanning direction. As a result, <100>-oriented grains are favored to grow along the scanning path, promoting the formation of a Goss texture. These findings demonstrate that process parameters—such as laser power, scanning speed, scanning strategy, and material absorptivity—exert a significant influence on texture development in laser-additively manufactured nickel-based superalloys, which, in turn, affects their mechanical anisotropy and overall performance.

For Nb-containing nickel-based superalloys, such as Inconel 625 and Inconel 718, the segregation of Nb and Mo during solidification is the primary driver for the formation of topologically close-packed (TCP) Laves phases. The presence of Laves phases significantly degrades the mechanical properties of these alloys. Studies have demonstrated that needle-like or plate-like Laves phases often act as preferential sites for crack initiation and propagation pathways, thereby substantially reducing the creep strength and room-temperature ductility of the superalloys.[80,81] When Laves phases precipitate as continuous films along grain boundaries, they can severely embrittle the interfaces and drastically reduce the creep life of the alloy.[82] In the GH2135 alloy, a small amount of fine, granular Laves phases at the grain boundaries did not significantly affect the strength or ductility. However, as the volume fraction of Laves phases increased, pronounced mechanical degradation became evident.[83] Li *et al.*,[84] in their study of the K4169 alloy, found that a large volume of coarse, blocky Laves phases led to a 20% reduction in room-temperature tensile strength and a 60% reduction in ductility. Under creep testing conditions of 650°C and 620 MPa, the alloy exhibited a 60% decrease in both creep life and creep elongation. Similarly, Sullivan *et al.*[85] reported that in Inconel 718, even a small Laves phase volume fraction of just 2–3% can lead to a significant deterioration in both strength and ductility.

Therefore, in the AM of Nb-containing nickel-based superalloys, it is essential to strictly control the size, morphology, and distribution of Laves phases. Studies have demonstrated that in laser-additively manufactured Inconel 625 alloys, as the deposition height increases, the accumulated heat in successive layers is not effectively dissipated, leading to a gradual rise in baseplate temperature. Consequently, the temperature gradient within the molten pool decreases during solidification, primary dendrite arm spacing increases, and secondary dendrite arms become more developed. This provides greater interdendritic space and longer solidification time for Laves phase formation. As a result, the size of Laves phases gradually increases from the bottom to the top of the deposited structure. This indicates that controlling the solidification conditions in the molten pool is critical to avoiding coarse and continuously distributed Laves phases in interdendritic regions. Ling *et al.*[86] found that increasing the cooling rate during solidification reduces secondary dendrite arm spacing, which effectively suppresses both the size and volume fraction of Laves phases in Inconel 718 alloys. The laser AM process inherently features high cooling rates, resulting in finer Laves phases compared to those formed during conventional casting. Xiao *et al.*[87,88] investigated the influence of quasi-continuous wave (QCW) pulsed laser

and continuous wave (CW) laser on Nb segregation, Laves phase characteristics, and mechanical properties in laser-additively manufactured Inconel 718. The results indicated that compared to continuous laser, pulsed laser operation provides higher peak cooling rates during solidification, which more effectively suppresses Nb microsegregation, reduces Laves phase size, and enhances overall mechanical performance. In addition, high-temperature solution treatment significantly affects the content, morphology, and size of Laves phases in AM Inconel 625 and Inconel 718 alloys. During solution treatment of laser-additively manufactured Inconel 625, substantial dissolution of Laves phases is observed. As the solution temperature increased, both the size and volume fraction of Laves phases decreased progressively. The dissolution kinetics of Laves phases are primarily governed by the long-range diffusion of alloying elements, such as Nb and Mo. With increasing solution temperature, the diffusion coefficients of these elements increase considerably, greatly accelerating the dissolution process. Chlebus *et al.*[68] reported that after solution treatment at 980°C and 1040°C for 1 h, Nb- and Mo-rich granular Laves phases, a small amount of MC-type carbides, and δ-phases were still present at the grain boundaries of as-built Inconel 718 samples. However, after solution treatment at 1100°C for 1 h, the δ-phase completely dissolved, large Laves phases nearly disappeared, and noticeable grain growth occurred. Tucho *et al.*[89] reported that in SLM-manufactured Inconel 718, Laves phases did not fully dissolve even after heat treatment at 1250°C for 7 h, with nanoscale remnants persisting within coarsened grains. Sui *et al.*[80] studied the effect of Laves phases on the room-temperature tensile properties of laser-additively manufactured Inconel 718 alloys. They found that Laves phases influence the YS primarily by altering the volume fraction and morphology of strengthening phases. Moreover, compared to elongated or network-like Laves phases, spherical or isolated morphologies are more favorable for plastic deformation and ductility. Therefore, by optimizing the solidification conditions in the molten pool and applying tailored solution heat treatments, it is possible to effectively regulate the morphology, size, and spatial distribution of Laves phases, thereby enhancing the mechanical properties of the alloy.

During the solution treatment of additively manufactured nickel-based superalloys, in addition to the dissolution of eutectic phases, significant microstructural evolution occurs in the morphology and size of the initial grains due to static recrystallization.[65] Studies have demonstrated that after solution treatment above 900°C, the coarse, epitaxially grown columnar grains in laser-additively manufactured Inconel 625 are gradually replaced by finer equiaxed grains. As the solution temperature increases, the volume fraction of recrystallized grains also increases. When the temperature reaches 1200°C, complete static recrystallization is achieved. Concurrently, the texture strength of the alloy decreases significantly with increasing temperature, the original <100> solidification texture formed during deposition weakens, and grain orientation becomes increasingly random. Compared with the recrystallization temperature range of conventionally forged Inconel 625 (930–1040 °C), AM Inconel 625 exhibits a higher recrystallization temperature onset. This behavior can be attributed to several factors[66]:

(i) The grain size in AM alloys is relatively large, and the grain boundary area fraction is low, resulting in fewer nucleation sites for recrystallization.
(ii) The plastic strain introduced during laser AM is generally less than 5%, which is significantly lower than the 30% strain typically experienced in forging, leading to reduced stored energy and a weaker driving force for recrystallization.
(iii) A considerable amount of Laves phase remains in the as-built microstructure, which can act as pinning points that hinder grain boundary migration during recrystallization, thereby further suppressing recrystallization kinetics.

Dinda *et al.*,[90] in their study on the microstructural evolution and thermal stability of laser-additively manufactured Inconel 625, observed that when the heat treatment temperature is below 1000°C (~3/4 T_m), the dendritic structures formed during the AM process remain stable. Full recrystallization only occurred at around 1200°C, indicating that AM Inconel 625 possesses high thermal stability. Kreitcberg *et al.*[91] investigated the effects of different heat treatment regimens and HIP on the microstructure and mechanical properties of selective laser-melted Inconel 625. Their results demonstrated that recrystallization occurred after post-processing and HIP, leading to the formation of equiaxed grains. In AM Inconel 625, interdendritic Laves phases were significantly dissolved during solution treatment, and the grain morphology transitioned from epitaxial columnar grains to equiaxed grains, resulting in a marked improvement in ductility. However, due to the reduction in dislocation density after recrystallization, the contribution from dislocation strengthening is diminished, leading to a decrease in the alloy's YS.

For Inconel 718 alloys, the δ-, γ"-, and γ'-phases play a critical role in determining mechanical properties. Therefore, in addition to solution treatment, aging treatment is essential to achieve sufficient strength through controlled precipitation. Figure 5 displays the precipitation-temperature-time diagram for various precipitates in

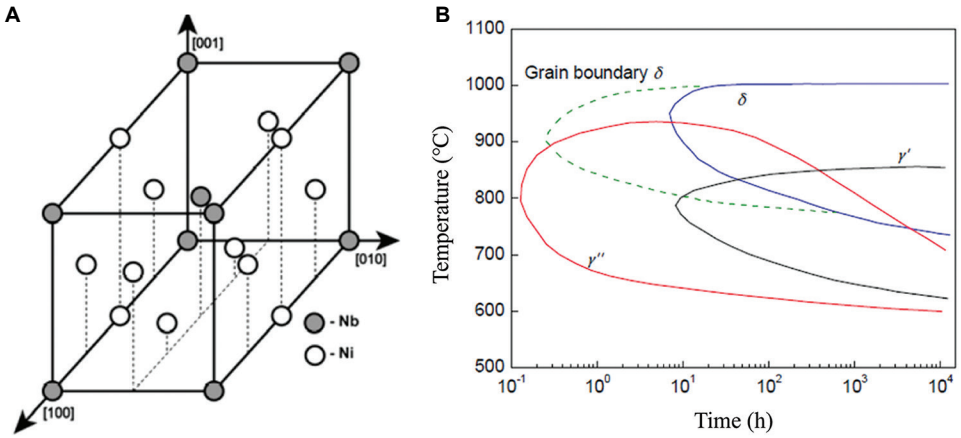

Figure 5. Lattice structure and precipitation kinetics curves of δ-phase. (A) Unit cell structure of the δ-phase. (B) Precipitation-temperature-time diagram of different phases in wrought Inconel 718 alloy. Adapted with permission from Thomas *et al.*[92] Copyright © 2006 Elsevier Limited

Inconel 718.[92] When the aging temperature (T_f) is between 870°C and 900°C, the δ phase precipitates as long needle-like particles, often continuously distributed along grain boundaries or within grains, and occasionally forming Widmanstätten structures. When 900°C < T_f < 930°C, the δ phase appears as granule particles located at grain boundaries or in intragranular regions. At 940°C < T_f < 960°C, it forms short rod-like morphologies preferentially along grain boundaries. At temperatures above 980°C, the δ phase is partially or completely dissolved. In laser-additively manufactured Inconel 718, the precipitation behavior of the δ-phase differs significantly from that in conventionally forged alloys. Liu *et al.*[93] investigated δ-phase precipitation in laser-additively manufactured Inconel 718 and found that, in the as-deposited condition, short needle-like or rod-like δ-phases precipitate within interdendritic regions during aging between 810°C and 950°C. After high-temperature solution treatment, elemental segregation in the interdendritic regions is substantially reduced or eliminated, and the δ-phase preferentially nucleates at high-angle grain boundaries and twin boundaries. Azadian *et al.*[94] demonstrated that both the nucleation and growth of δ-phases require a critical Nb concentration, and higher Nb content leads to an increased volume fraction of δ-phase. These studies collectively indicate that the morphology, size, and distribution of the δ-phase are strongly influenced by the degree of elemental segregation, as well as the temperature and duration of solution treatment. As presented in Table 1, the δ-phase morphology, size, and distribution vary significantly under different processing routes and heat treatment conditions.[92-97] Compared with wrought and cast alloys, the δ-phase in AM Inconel 718—under standard heat treatment—exhibits significantly finer precipitates at grain boundaries. In addition, the distribution of the δ-phase is closely correlated with the initial microstructural state of the material.

Table 1. Morphology, size, and distribution of the δ phase under different manufacturing methods and heat treatment conditions

Manufacturing method	Heat treatment	Grain boundary	Intragranular
Selective laser melting	δ aging	Length: 1–2 μm Width: 0.2–0.4 μm	Length: 0.5–1 μm Width: 50–90 nm
	Homogenization+ δ aging	Length: 0.2–0.4 μm Width: 10–20 nm	None
Wrought	δ aging	Length: 2–8 μm Width: 0.2–0.5 μm	None
Casting	Homogenization+ δ aging	Length: 2–8 μm Width: 0.5–0.9 μm	None

At present, there are two main perspectives regarding the influence of the δ-phase on the mechanical properties of Inconel 718 alloy. The first perspective holds that the presence of the δ-phase is beneficial to the mechanical performance of Inconel 718.[98] Li *et al.*[96] found that spheroidized δ-phases distributed along grain boundaries can inhibit crack initiation and propagation during high-temperature creep and fatigue processes, thereby improving the creep ductility of the alloy while maintaining creep life. Cai *et al.*[95] suggested that a moderate amount of δ-phase can reduce the notch sensitivity of Inconel 718. Yuan *et al.*[99] also reported that short rod-shaped δ-phases can enhance both the strength and ductility of Inconel 718 at elevated temperatures. The second perspective argues that the δ-phase degrades the mechanical properties of Inconel 718.[100] Hong *et al.*[101] pointed out that Nb-depleted

zones surrounding δ-phases can reduce the low-cycle fatigue performance. Zeng *et al.*[102] observed that the YS of Inconel 718 decreases significantly with increasing δ-phase content. Zhang *et al.*[103] identified the δ-phase as the preferential site for micropore nucleation during high-temperature tensile deformation in Inconel 718, and its presence reduces the alloy's high-temperature ductility. Wang *et al.*[104] also noted that δ-phases formed along Nb-rich grain boundaries consume a large amount of Nb atoms, resulting in local compositional deviations. An excessive volume fraction of δ-phase may impair the alloy's low-cycle fatigue performance at elevated temperatures. In fact, the influence of the δ-phase on mechanical properties is strongly dependent on its morphology and volume fraction. Needle-like δ-phases hinder lateral grain boundary migration and promote intergranular fracture, leading to reduced ductility. In contrast, granular δ-phases delay necking and inhibit crack propagation, thereby enhancing the mechanical performance of Inconel 718.[105] When short rod-shaped δ-phases are present, the alloy tends to exhibit superior ductility, whereas needle-like δ-phases are associated with higher strength.[106]

The disc-shaped γ"-phase (comprising three variants), which is coherent with the matrix, along with the spherical γ'-phase, acts as the primary and secondary strengthening phases, respectively, in Inconel 718 alloy.[107] Due to a significant lattice mismatch with the γ-matrix, the γ"-phase exerts strong coherent strengthening effects and is widely recognized as the principal contributor to strength in Inconel 718.[108] Consequently, current research predominantly focuses on the evolution of the γ"-phase and its influence on mechanical properties. A. Drexler *et al.*[109] reported that the coarsening behavior of the γ"-phase in Inconel 718 can be described by the Lifshitz-Slyozov-Wagner theory. Calculations indicate that γ"-phase coarsening is governed by bulk diffusion of Nb in the γ-matrix, with an activation energy of 272 kJ/mol. Liu *et al.*[93] found that, during aging at 720°C, the growth rate of γ" precipitates in solution-treated laser additive manufactured Inconel 718 is lower than that in wrought Inconel 718. This suggests that γ" precipitates in the AM alloy exhibit superior size stability. The dimensional stability of the γ"-phase has a significant impact on the alloy's high-temperature mechanical performance. As the size of the γ" precipitates increases, they may lose coherency with the matrix, and under mechanical stress, transform into δ-phase—a transformation that degrades mechanical performance. The size of strengthening precipitates plays a crucial role in precipitation hardening. Figure 6 illustrates the interaction between dislocations and precipitates.[110] It

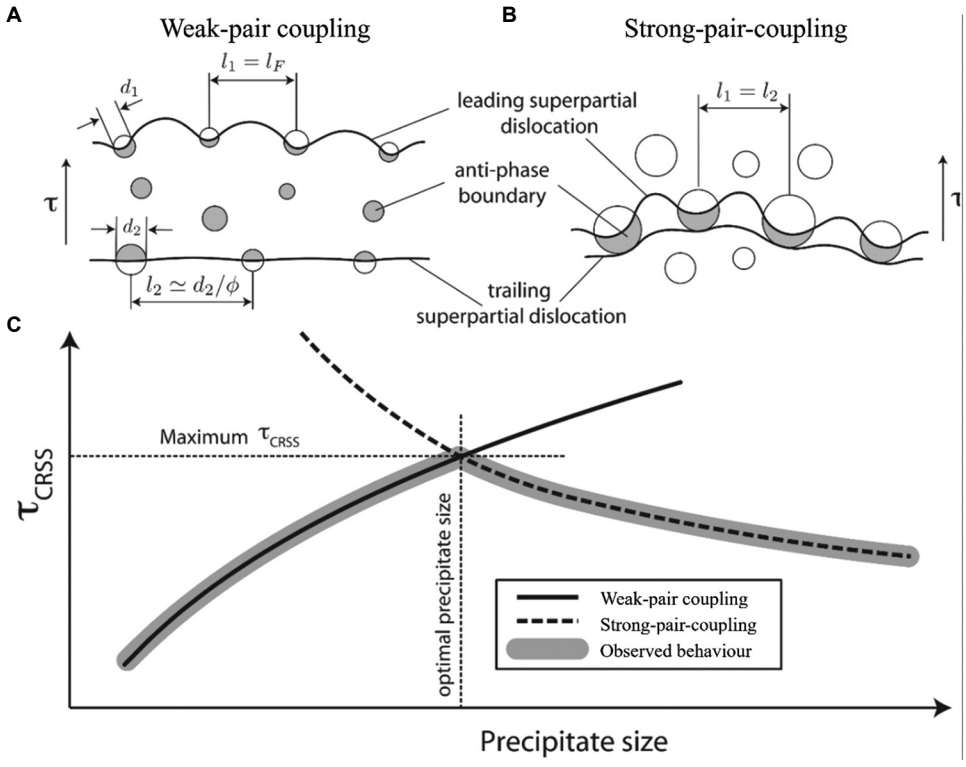

Figure 6. Interaction between dislocations and precipitates: (A) weak coupling; and (B) strong coupling. (C) Relationship between precipitate size and critical shear stress. Adapted with permission from Collins and Stone[110] Copyright © 2014 Elsevier Limited

can be seen that strong and weak coupling exists between dislocations and precipitates: weak coupling increases with precipitate size, while strong coupling decreases. Consequently, there exists a critical precipitate size at which the critical shear stress for dislocation cutting reaches a maximum. To determine the optimal precipitate size for strengthening in Inconel 718, numerous studies have investigated the interaction mechanisms between γ" precipitates of varying sizes and dislocations. Slama and Abdellaoui[111] suggested that the optimal γ" precipitate size in Inconel 718 is approximately 30 nm; beyond this size, the tetragonal distortion of γ" increases with particle size, leading to a reduction in strengthening efficiency. Srinivas *et al.*[112] reported that degradation in high-temperature creep resistance is closely related to the reduction of γ" size, from 23 nm to 16 nm. Ming *et al.*[113] studied the coarsening behavior of γ" precipitates in laser-additively manufactured Inconel 718 aged at 720°C for different durations and its influence on mechanical properties. The results indicated that hardness, room-temperature tensile strength, and high-temperature creep resistance of the alloy initially increase and then decrease with increasing γ" size. Chaturvedi and Han[114] indicated that the steady-state creep rate decreases as γ" particle size increases. However, once the size exceeds a critical threshold, the creep rate begins to rise again. Moreover, the particle size corresponding to the minimum creep rate is slightly smaller than that associated with peak tensile strength at room temperature. This difference arises from distinct deformation mechanisms: at room temperature, deformation is primarily governed by dislocation cutting through the precipitates, whereas at elevated temperatures, dislocation climb becomes the dominant mechanism.

From the above analysis, it is evident that the size and distribution of eutectic phases formed during the solidification of nickel-based superalloys, as well as the size, volume fraction, and spatial distribution of strengthening phases after heat treatment, all have a significant influence on the mechanical properties of the alloy. By optimizing processing parameters and subsequent heat treatment conditions, it is possible to tailor the microstructure and enhance mechanical performance. However, the selection of heat treatment procedures should fully account for the initial microstructural state of the alloy. At present, heat treatment processes for additively manufactured superalloys largely follow conventional procedures. For example, the heat treatment regime used to control the size of strengthening phases in Inconel 718 still follows the traditional two-step aging treatment developed for wrought alloys, without adequately considering the microstructural characteristics of the as-deposited condition. Liu *et al.*[93] have demonstrated that the growth kinetics of γ" precipitates differ between wrought and laser-additively manufactured Inconel 718 alloys under identical aging conditions. Furthermore, in-depth research and analysis remain limited regarding the optimization of strengthening phase size in AM nickel-based superalloys and their impact on deformation mechanisms.

Superalloy components serve for long periods under high-temperature, high-pressure, and oxidizing conditions. Their high-temperature fatigue performance, creep rupture life, creep properties, and oxidation resistance significantly influence their service life. Among these, defects, surface quality, and microstructure are key factors determining the high-temperature service performance of superalloys. Wan *et al.*[115] have investigated the effects of different thicknesses (1.3 and 3.3 mm) and surface states (as-formed and machined) on the fatigue performance of Inconel 718 alloys fabricated by LPBF. Combined with 3D high-resolution X-ray tomography (3D-XRT) and finite element analysis (FEA) simulations, the impact of surface defects on fatigue life was analyzed in depth. The results indicated that as wall thickness decreases, the material's microstructure and surface roughness undergo significant changes, leading to distinct thickness dependencies in its high-temperature fatigue strength: unmachined thin-walled samples exhibited longer fatigue life, while machined thick-walled samples exhibited the opposite trend, primarily attributed to differences in stress distribution, surface roughness, and thickness-dependent microstructure. In addition, FEA simulations revealed that the depth and shape of defects exert important effects on fatigue life; when defect sizes are small, the shape of defects reduces the material's fatigue limit more significantly than depth. Crack growth rates are significantly influenced by material microstructure, temperature, and loading direction. At 25°C, as crack length increases, the crack growth rates in different loading directions (X-, XZ-, and Z-axes) follow the order Z > X > XZ. At 650°C, this order changes to XZ > X > Z, with only a small difference between the X and XZ directions. Furthermore, crack growth rates under high-temperature conditions are significantly higher than those under low-temperature conditions, indicating a notable regulatory effect of temperature on crack propagation. The crack propagation process is accompanied by complex fracture mechanisms, including grain boundary blocking, slip activity, and secondary crack formation, all of which are closely related to the material's microstructural characteristics.[116] Yu *et al.*[117] studied the high-cycle fatigue (HCF) performance of Inconel 718 alloys fabricated by LDED at room temperature and 650°C, and explored the influence of heat treatment on the material's microstructure and mechanical properties. By adopting a specific heat treatment scheme—homogenization +

solution + aging (HSA)—the alloy's microstructure was optimized. Results indicated that Inconel 718 alloys treated with HSA exhibit a typical bimodal granular distribution, including coarse grains (CGs) and fine grains. Compared with Inconel 718 produced by traditional manufacturing methods, the fatigue limit (σ_a) of HSA-treated LDED Inconel 718 is approximately 385 MPa at room temperature and 280 MPa at 650°C, suggesting obvious temperature dependence. Further analysis indicated that as the test temperature increases, the fatigue crack initiation mode transitions from surface slip to fracture along large grain boundaries, and the presence of CGs significantly affects the material's fatigue strength.

Zhang *et al.*[118] conducted a comparative analysis of the microstructure and creep properties of Inconel 718 alloys fabricated by LPBF and forging. The results indicated that Inconel 718 fabricated by LPBF has a more complex microstructure, characterized by uneven grain size and shape, as well as the distribution of a small amount of second phases, while the forged alloy exhibits more regular grain shape and uniform grain size. This difference leads to lower average creep life, reduction of area, and uniform elongation of the LPBF alloy during the creep stage. Studies also found that in the steady creep stage, the LPBF alloy has fewer activated slip systems due to its irregular grain morphology, whereas the grains of the forged alloy can more easily activate slip systems to alleviate stress concentration. In addition, in the tertiary creep stage, the abnormal grain size distribution and shape in the LPBF alloy exacerbate stress concentration at grain boundaries, promoting the initiation and propagation of initial microcracks and thus accelerating material fracture. Subsequently, they further investigated the influence of grain boundary serration (GBS) on creep properties and its formation mechanism in Inconel 718 alloys fabricated by LPBF. By adjusting heat treatment conditions, such as intermediate solution temperature and cooling rate, different degrees of GBS were successfully achieved. Studies found that GBS significantly increases creep life by approximately 56%, increases creep strain by about 19%, and reduces creep strain rate by roughly 26%. Analysis of crack surface morphology and grain boundary dislocation density using Scanning Electron Microscopy and Electron Backscatter Diffraction confirmed that the main role of GBS in delaying crack initiation is its ability to effectively alleviate stress concentration. Further research revealed three GBS formation mechanisms: serration formation caused by the growth of δ phases along specific directions, inhibition of grain boundary migration by δ-phases larger than the critical size, and grain boundary distortion induced by element segregation.[119]

4. Alloy design for AM of nickel-based superalloys

There is a strong correlation among composition, processing, microstructure, and properties in materials science. In AM of nickel-based superalloys, the size and distribution of precipitates play a crucial role in determining the mechanical performance of the alloy. For instance, in laser-additively manufactured Inconel 718 and Inconel 625 alloys, the presence of chain-like Laves phases distributed in interdendritic regions not only increases the susceptibility to hot cracking but also serves as preferential sites for crack initiation and pathways for crack propagation under load, thereby significantly degrading the mechanical properties. Studies have demonstrated that during the AM process, reducing laser power, increasing scanning speed, applying active cooling to the substrate, and employing QCW laser modes can enhance the cooling rate, refine dendrite arm spacing, and promote a more uniform and dispersed distribution of precipitates within the interdendritic regions. Moreover, adjusting heat treatment temperature and holding time can modify the size and morphology of precipitates, thus improving the mechanical properties of nickel-based superalloys. However, an increase in cooling rate also leads to a significant rise in residual stress, which may induce plastic deformation or cracking and consequently compromise dimensional accuracy and structural integrity. In addition, excessively high heat treatment temperatures can result in grain coarsening, whereas overly low temperatures may prevent complete dissolution of secondary phases. These factors impose limitations on the extent to which microstructure and mechanical properties can be tailored through post-process heat treatments. Therefore, under the constraints of maintaining dimensional precision and forming quality, the potential for enhancing mechanical properties solely through optimization of processing and heat treatment parameters is inherently limited.[56]

In recent years, significant progress has been made in the AM of aluminum alloys. Researchers have developed Sc-modified Al-Mg-Sc-Zr alloy powders specifically tailored for laser-based AM, taking into account the unique thermal and solidification characteristics of AM processes. After SLM and subsequent heat treatment, these alloys exhibit excellent overall mechanical properties (with tensile strength exceeding 500 MPa and elongation surpassing 10%) and have been successfully applied in aerospace components.[120] This success demonstrates that alloy composition design aligned with the inherent characteristics of AM processes holds great potential for advancing the industrial application of nickel-based superalloys in AM.

From the above analysis, it is evident that current challenges in AM of nickel-based superalloys primarily lie in crack control during both the fabrication and post-processing stages, as well as in microstructural regulation and toughening strategies. Therefore, alloy design should first consider the influence of different alloying elements on crack initiation and propagation. Furthermore, to ensure the service performance, efforts should be made to maximize the volume fraction of strengthening phases. At present, compositional optimization of existing alloys through minor modifications has been demonstrated to reduce or even eliminate cracking to some extent, as discussed in detail in Section 2. However, there remains a lack of in-depth research on the mechanical properties of these modified alloys. Sreeramagiri *et al.*[121] combined laser AM with synchronized powder feeding, high-throughput compositional design, and phase diagram modeling to develop a novel nickel-based superalloy (WSU 150). By suppressing premature precipitation of strengthening phases during solidification, cracking was effectively avoided. A suitable heat treatment was then applied to fully precipitate the strengthening phases and enhance mechanical performance. Specifically, in the laser deposition process, two powder feeders were used to deliver Alloy A (with low γ' phase volume fraction) and Alloy B (with high γ' volume fraction) into the melt pool at a predetermined ratio, enabling *in situ* compositional synthesis. This created compositional gradients across different regions of the XY-plane in the deposited component, transitioning from Alloy A to Alloy B. Microstructural characterization and hardness testing of these gradient samples were performed to identify optimal compositions—those exhibiting no cracks and high microhardness. Through this high-throughput screening, the WSU 150 alloy (with a γ' phase volume fraction of 38%) was selected. In the as-deposited state, WSU 150 exhibited no cracking and a relatively high hardness of 375 HV. Subsequent optimization of laser deposition parameters and mechanical testing revealed that the as-deposited WSU 150 alloy achieved a YS of 867 MPa, ultimate tensile strength (UTS) of 1188 MPa, and an elongation of 27.9%. After aging at 760°C for 4 h, the yield and tensile strengths increased to 1114 MPa and 1396 MPa, respectively, while the elongation decreased to 16.1%. These room-temperature mechanical properties surpass those of Rene 88DT and indicate potential for service temperatures up to 800°C.

The alloy design strategy adopted in the study,[121] known as the element blending method, involved combining two well-established superalloys in controlled ratios for laser deposition. While this approach offers certain advantages, it also presents notable limitations. When blending two complex alloys, the concentration of multiple elements changes simultaneously, making it difficult to isolate the specific contributions of individual elements to improve cracking resistance or mechanical performance. As a result, the underlying mechanisms often remain unclear. Moreover, since nickel-based superalloys are typically employed in high-temperature environments, evaluation based solely on room-temperature tensile properties is insufficient for assessing practical applicability. More recently, Tang *et al.*[122] employed a physics-guided high-throughput computational alloy design approach to develop two AM-specific nickel-based superalloys: ABD-850AM (with ~3 wt.% Al and Ti) and ABD-900AM (with ~5 wt.% Al and Ti). These alloys were evaluated for both room- and high-temperature mechanical properties. Compared to commercial alloys, such as IN 939 and CM247LC, the newly developed alloys demonstrated superior printability and enhanced mechanical performance. The alloy design was guided by physically informed high-throughput computational models, which establish quantitative correlations between alloy composition and key mechanical properties. For AM applications, the primary design criterion is an alloy's resistance to cracking during solidification. Therefore, the Scheil non-equilibrium solidification model was used to calculate solidification temperature ranges, and the alloys' susceptibility to SAC during thermal cycling and heat treatment was also assessed. To ensure high mechanical performance and thermal stability, YS and creep resistance were predicted by considering key microstructural parameters, including anti-phase boundary energy, γ' phase volume fraction, and elemental interdiffusion coefficients. In addition, the tendency for TCP phase formation was evaluated using d-electron band theory. Based on these multi-objective criteria, two promising alloy compositions were identified, as displayed in Figure 7. The ABD-850AM alloy was selected for experimental validation and compared with IN 939 and CM247LC.[122]

Results indicated that ABD-850AM exhibited superior printability (*i.e.*, enhanced crack resistance) and reduced texture intensity. As illustrated in Figure 8, the ABD-850AM samples were free of cracks, whereas the other two alloys frequently exhibited SC, LC, and SAC. Research by Kou[123] on SC pointed out that evaluating crack susceptibility based solely on the solidification temperature range is limited, as it neglects the alloy's solidification path during the final stages. He proposed a new evaluation metric—Solidification Cracking Index—which integrates both the strain rate in the solid phase and the feeding capability of the residual liquid phase to assess the likelihood of SC. Tensile tests across a range of temperatures were conducted to evaluate the alloys' susceptibility to hot ductility loss and SAC. The high-temperature tensile and creep properties of ABD-900AM

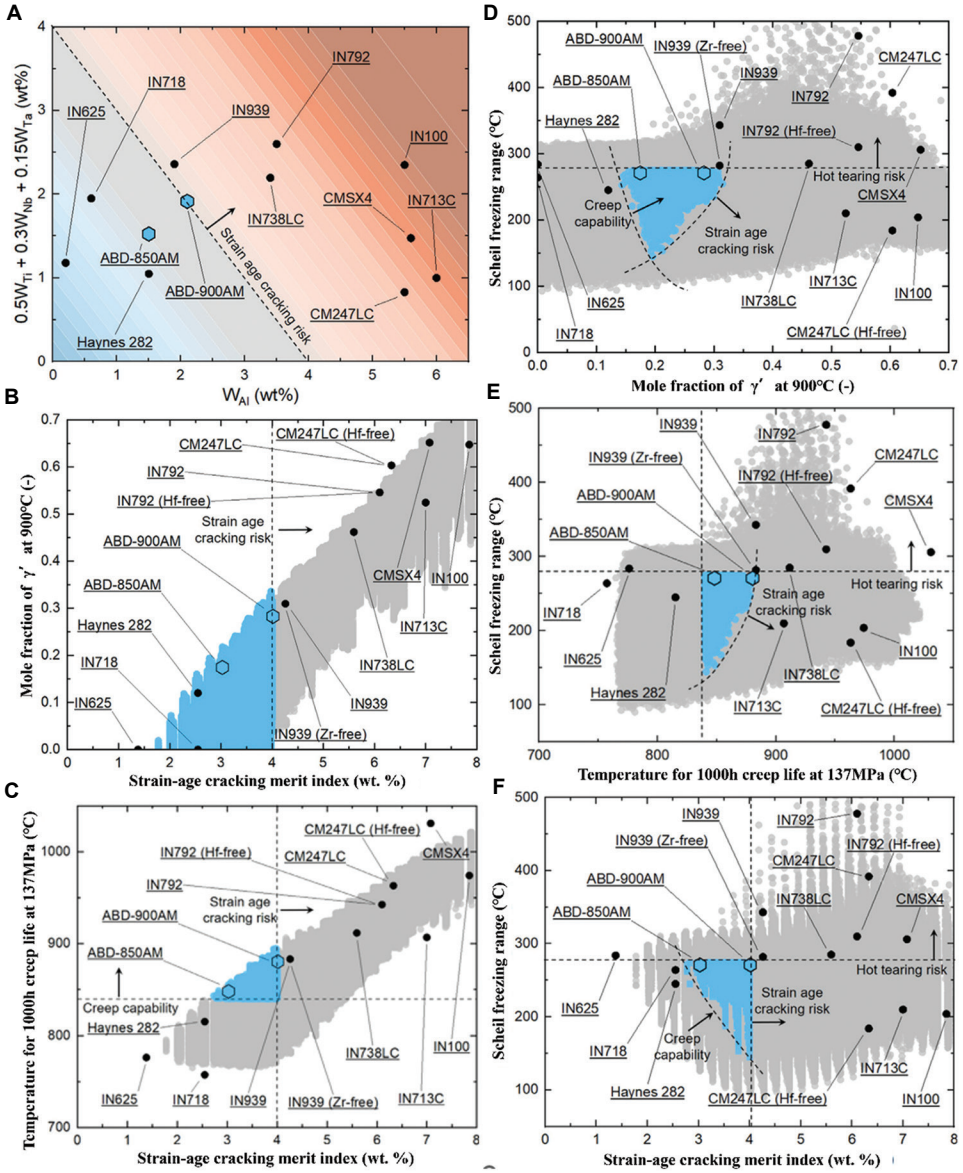

Figure 7. Composition screening of nickel-based superalloys. (A) Modified weldability diagram with maximum strain-age cracking index identified. (B and C) Strain-age cracking merit index and its relationship to γ' fraction (B) and creep merit index (C). (D and E) Magnitude of freezing range in relation to γ' fraction (D) and creep merit index (E), where strain-age cracking and creep merit contours are indicated. (F) Final design space used to isolate new grades of alloy based on freezing range, strain-age cracking index, and minimum required strength and creep. Adapted with permission from Tang *et al.*[122]

demonstrated excellent strength and ductility, with creep performance significantly surpassing that of IN 718 and approaching that of CM247LC. The study comprehensively evaluated the printability and mechanical performance of AM-specific nickel-based superalloys, providing valuable insights and strategic guidance for future design of alloy compositions tailored for AM.

Liang *et al.*[124] utilized coaxial powder-fed laser AM technology to develop a novel nickel-based superalloy (ZK401), characterized by low crack susceptibility, low density, and high strength, and obtained a corresponding patent. According to the patent, this alloy is primarily intended for the repair of high-temperature alloy components and for the AM of medium- and low-temperature nickel-based alloy parts. The alloy composition includes Al, Ti, and Nb as key precipitation-strengthening elements that promote γ' phase formation; Cr, Mo, and Co as solid-solution strengthening elements; and Si, C, and Hf as grain boundary-strengthening elements. Cr plays

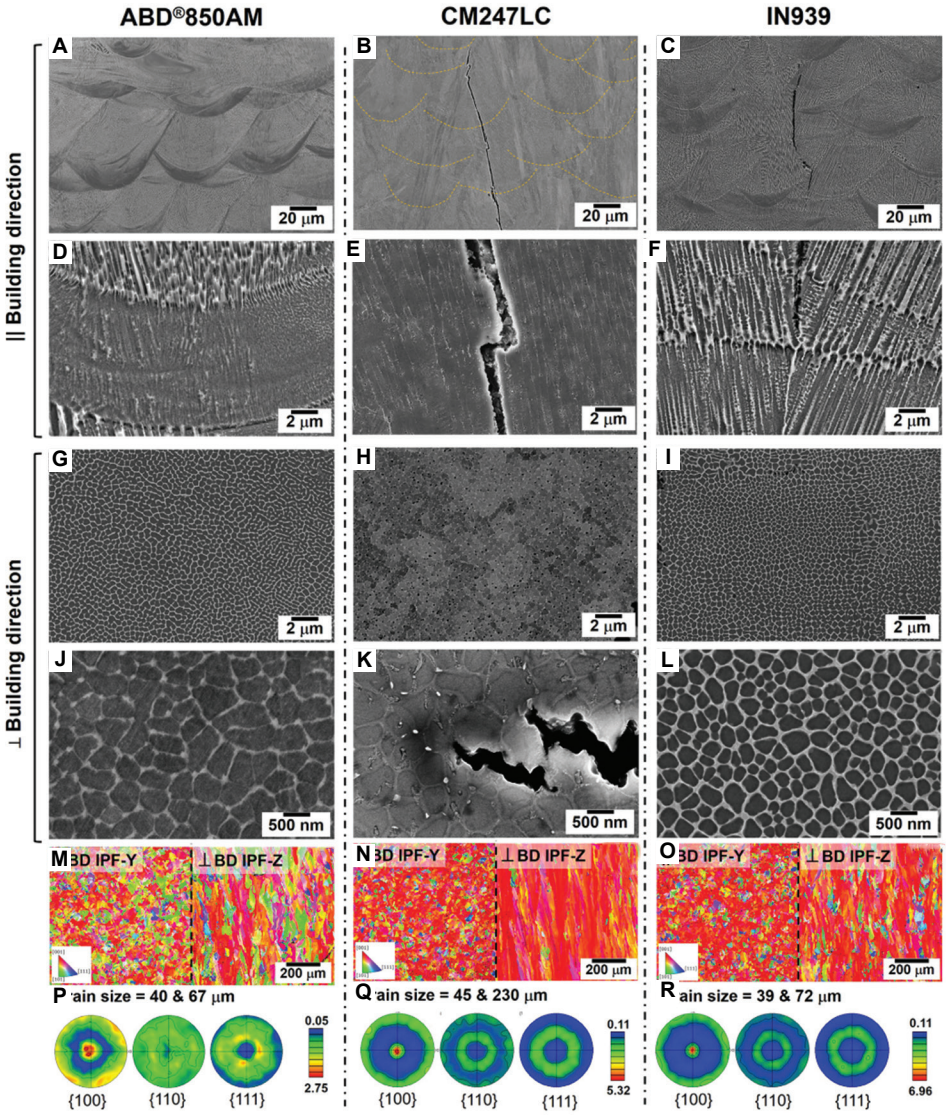

Figure 8. Microstructure comparison of additively manufactured ABD850AM, CM247LC, and IN939 alloys. (A-F) Microstructure of the XZ-plane at two magnifications (×100 and ×1000). (G-L) Microstructure of XY-plane at two magnifications. (M-O) Inverse pole figure of both planes along the building direction. (P-R) Bulk texture strength of {1 0 0}, {1 1 0}, and {1 1 1} poles. Adapted with permission from Tang *et al.*[122] Copyright © 2021 Elsevier Limited

a key role in oxidation resistance, corrosion resistance, and solid-solution strengthening. In addition, it can form carbides with C to enhance precipitation strengthening. To suppress the formation of TCP phases, the Cr content is controlled within the range of 9.0–11.0 wt.%. Mo increases the lattice misfit between the matrix and the strengthening phase, enhances atomic bonding strength, and promotes dislocation network formation, thereby improving both printability and mechanical performance.

However, excessive Mo promotes TCP phase formation, which is detrimental to oxidation and corrosion resistance. Therefore, its content is limited to 4.0–6.0 wt.%. Co contributes to solid-solution strengthening and reduces the stacking fault energy, thus improving the alloy's intermediate-temperature mechanical properties and structural stability. Its content is maintained between 9.0 and 11.0 wt.%. Nb acts as the primary strengthening element and also enhances oxidation and corrosion resistance. Nevertheless, excess Nb can promote TCP phase formation; thus, its content is controlled within 3.0–5.0 wt.%. Al is the main constituent of the γ' phase; its concentration directly determines the γ'-phase and improves oxidation resistance. However, excessive Al may lead to the formation of low-melting-point eutectic phases, which negatively affect printability. Thus, Al is maintained within 3.0–5.0 wt.%. Ti can substitute for Al in the γ'-phase

and serves as a major precipitation-strengthening element. It also enhances resistance to hot corrosion, though it may impair oxidation resistance. Its content is kept between 1.0 and 2.0 wt.%. Si improves oxidation and corrosion resistance but can form brittle Nb_3Si phases when combined with Nb, thereby reducing mechanical performance. Thus, its content is limited to 0.0–0.6 wt.%. C aids in deoxidation during melting, improves melt fluidity, and forms grain boundary-stabilizing carbides. However, excessive C increases crack susceptibility; thus, its content is strictly controlled within 0.0–0.02 wt.%. Sun *et al.*[125] have revealed that in the AM of IN738LC alloy, a moderate increase in C content can improve its mechanical properties to a certain extent, particularly in terms of hardness. Nevertheless, excessive C content will instead reduce the alloy's high-temperature performance and introduce new defects. Hf enhances precipitate strengthening, purifies grain boundaries, prevents sulfur-induced embrittlement, broadens the solidus-liquidus temperature range, improves melt fluidity, and reduces SC tendency, thereby significantly enhancing weldability. Hf content is maintained within 0.1–0.6 wt.%. This alloy exhibits superior room- and intermediate-temperature tensile properties compared to Inconel 625: at room temperature, tensile strength > 900 MPa, elongation>10.0%; at 650°C, tensile strength >800 MPa, elongation>10.0%; at 800°C: tensile strength >680 MPa, elongation>7.0%. In terms of creep performance, the alloy achieves: creep life >50 h at 650°C/690 MPa; and creep life >25 h at 800°C/400 MPa. Moreover, the alloy demonstrates excellent oxidation resistance at 800°C, with no observable weight gain or spallation after prolonged exposure.[125]

The aforementioned studies are based on alloying strategies for material design, whereby increasing the content of precipitation-strengthening elements, such as Al, Ti, and Nb—followed by appropriate heat treatment—can effectively enhance the volume fraction of γ'- and γ"-strengthening phases in the alloy, thereby improving its mechanical properties. However, when the Al and Ti contents exceed 6 wt.%, the weldability of the alloy deteriorates significantly. During the AM process, this leads to a marked susceptibility to hot cracking, which adversely affects the geometric fidelity and structural integrity of the fabricated components. Therefore, improvements in the mechanical performance of AM nickel-based superalloys through alloying approaches are inherently constrained by the alloy's processability limitations.[124] Studies have demonstrated that incorporating nanoscale reinforcements—such as metal oxides, ceramic particles, and carbon-based nanomaterials—into nickel-based superalloys to form metal matrix composites (MMCs) can significantly enhance strength while maintaining favorable processability.[126,127] This strategy offers an alternative and effective pathway for enhancing the mechanical performance of laser-additively manufactured nickel-based superalloys.

Research indicates that the addition of nanoparticles reduces the thermal conductivity of the melt pool, thereby inhibiting heat transfer to the substrate. Meanwhile, the nanoparticles increase the viscosity of the molten alloy and suppress thermocapillary flow, which, in turn, reduces thermal convection within the melt pool. As a result, the HAZ is minimized, while the fusion zone is enlarged.[126] Gu *et al.*[126-129] systematically investigated multi-phase reinforcement and gradient-interface synergistic toughening mechanisms in particle-reinforced nickel-based superalloys fabricated by LAM. Their studies revealed that the addition of nanoscale TiC particles to Inconel 625 refined the grain structure. The TiC nanoparticles effectively impeded dislocation motion, resulting in a notable increase in tensile strength without compromising ductility, and also improved the alloy's tribological performance. The incorporation of nanoscale TiB_2 particles into Inconel 625 effectively pinned grain boundaries and suppressed grain boundary migration during deformation, thereby enhancing mechanical properties.[130] Yang *et al.*[131] systematically investigated the effects of adding 10 vol.% micron-sized TiCN particles on the microstructure and mechanical properties of Inconel 718 matrix composites fabricated through LPBF and further analyzed the performance changes of the composites after heat treatment. The results indicated that the incorporation of TiCN particles significantly improved the hardness, tensile strength, and wear resistance of the composites. In addition, heat treatment further enhanced the mechanical properties of the composites, with the improvement in compressive strength being particularly prominent. Gruber *et al.*[132] revealed that the addition of an appropriate amount of micron-sized carbides and nitrides to Inconel 718 alloy can significantly alter its macro morphology and microstructure, resulting in finer grain sizes and uniformly distributed second-phase particles. By adjusting process parameters to precisely control the type, content of additives, and the processing procedure, the mechanical properties of the material can be significantly improved while ensuring good machinability, with particular enhancement in the balance between strength and ductility. The addition of CNTs into AM nickel-based superalloys also contributed to grain refinement and strength improvement. However, it was accompanied by a reduction in ductility. After appropriate heat treatment, the composites exhibited superior overall mechanical properties compared to their unreinforced counterparts.[133] Furthermore, in Inconel 718, CNTs provided dispersion

strengthening, reduced localized strain accumulation between dendrites during solidification, and enhanced resistance to thermal stress and strain in the interdendritic regions, thereby effectively suppressing crack formation.[55]

These findings suggest that nanoparticles, as reinforcing agents, can significantly enhance alloy strength. However, this often comes at the expense of ductility, which poses significant challenges for effective toughening strategies. Therefore, there is an urgent need to explore novel reinforcing agents capable of simultaneously enhancing both strength and ductility.[134,135] Graphene, as an emerging reinforcement in MMCs, offers a high aspect ratio (lateral dimension to thickness), an exceptionally large specific surface area, and outstanding intrinsic mechanical strength. Even at low volume fractions, graphene can dramatically improve the comprehensive performance of composites, resulting in high reinforcement efficiency. Its large surface area enables superior wettability with metallic matrices compared to CNTs, promoting stronger interfacial bonding. Moreover, graphene effectively suppresses grain growth in the matrix with minimal disruption to intergranular spacing, thereby enhancing stress transfer efficiency. The surface of graphene exhibits a unique wrinkled morphology, which flattens under applied stress, dissipating energy and contributing to simultaneous improvements in both strength and toughness.[134,135] Xiao *et al.*[135] employed laser cladding to fabricate graphene-reinforced Inconel 625 composites. The resulting material exhibited increased hardness, enhanced thermal conductivity, and improved tribological performance, attributed to the self-lubricating effect of the graphene interlayer. Xiao *et al.*[135] incorporated 1 wt.% graphene into AM Inconel 718 and reported that the YS and UTS increased by 42% and 53%, respectively, compared to the unreinforced alloy. In addition, the friction coefficient and wear rate were reduced by 22.4% and 66.8%, respectively. Therefore, graphene serves as a highly effective reinforcement, capable of significantly improving both the mechanical and tribological properties of additively manufactured nickel-based superalloys.

5. Conclusion

The development of AM technology has liberated design constraints, making it possible to realize complex, lightweight, and functional designs and the manufacturing of engine components. This advancement has significantly contributed to the development of next-generation aerospace engines and gas turbines. At present, certain AM-fabricated nickel-based superalloy components have already been successfully installed in engines or passed rigorous qualification tests, achieving remarkable results. These milestones demonstrate the tremendous potential of AM technology in the aerospace propulsion field. However, several critical challenges remain in the AM of nickel-based superalloys, including the mitigation of process-induced defects (such as porosity and hot cracking), the precise control of microstructure evolution and resultant mechanical properties, and the design of AM-specific alloy compositions tailored to the unique thermal and solidification conditions of AM processes. Looking ahead, several key research directions warrant focused investigation and development in the field of AM nickel-based superalloys:

(i) The innovative structural design of nickel-based superalloy components leveraging AM enables lightweight, functionally integrated architecture and the fabrication of highly complex engine parts, thereby enhancing their service performance and multifunctional capabilities. With the continuous advancement of AM technology, achieving structural-functional integration in high-temperature components—while simultaneously improving the mechanical properties and service temperature of nickel-based superalloys—has become a critical development trend for meeting the demanding operational requirements of aerospace engines and gas turbines. AM offers unparalleled advantages over conventional manufacturing methods in fabricating complex geometries and enabling multi-material integration. By integrating AM with advanced design methodologies—such as topology optimization, biomimetic structures, architected metamaterials, and hierarchical architectures—the structural efficiency and material performance of components can be maximized. Therefore, structural innovation, functional design, and precise process control through AM represent key research and development directions for achieving structural-functional integration in nickel-based superalloy components for aero-engine and gas turbine applications.

(ii) In integrated components of engines and gas turbines—such as compressor disks and turbine hubs—different regions are subject to markedly distinct service conditions (*e.g.*, temperature, loading), resulting in non-uniform distributions of thermal and mechanical stresses within the material. Traditional monolithic components are increasingly incapable of meeting the demanding performance requirements in such complex operational environments. Through functionally graded material (FGM) design, the blade section can be tailored to exhibit high ductility, excellent thermal stability, and superior HCF resistance at elevated temperatures, while the disk section can be engineered for high creep resistance, low-cycle fatigue strength, and enhanced fracture

toughness. By establishing a gradual transition in mechanical and thermal performance between the disk and blade regions—aligned with the spatial variations in temperature and mechanical load—the full material and structural potential of nickel-based superalloys can be exploited. This enables the fulfillment of region-specific thermal and mechanical demands, thereby improving overall engine efficiency and reliability. AM, with its layer-by-layer, point-by-point fabrication principle, offers a unique capability to produce complex-shaped components with spatially tailored property gradients. This is achieved through *in situ* feeding of multiple materials with varying compositions, coupled with real-time adjustment of processing parameters based on predefined material and performance specifications. As a result, components with precisely controllable gradients in compositions, microstructures, and mechanical properties can be manufactured. The integration of AM with functionally graded material design represents a highly promising pathway toward the development of next-generation, high-performance gradient material components for the hot sections of aerospace engines.

(iii) Traditional strengthening mechanisms, such as grain refinement, solid solution strengthening, precipitation strengthening through dispersed phases, and deformation strengthening, can effectively enhance the strength of metallic materials. However, these approaches often sacrifice ductility and toughness, making it challenging to achieve an optimal balance between strength and plasticity. In recent years, studies have demonstrated that heterogeneous composite architectures—such as those with hybrid, layered, gradient, bimodal, hierarchical, or harmonic structures—are more effective in harnessing the synergistic coupling effects among distinct microstructural constituents. This enables the simultaneous enhancement of both strength and ductility, thereby achieving a superior combination of mechanical properties. Metal AM provides a powerful platform for fabricating complex-shaped functionally graded components with spatially controlled gradients in compositions, microstructures, and properties. This capability greatly facilitates the design and realization of tailored composite architectures for concurrent strengthening and toughening. Without modifying the base alloy composition, AM can precisely control microstructural features, including grain morphology, size, crystallographic orientation, and substructures, across different regions of the component. This enables the construction of engineered "heterogeneous" architectures that fully exploit the performance potential of conventional structural metals to meet increasingly demanding industrial requirements. Such advancements are expected to accelerate the engineering deployment of laminated and architected metal composites in aerospace and related high-performance sectors. Therefore, composite-architecture-based strengthening and toughening of AM-fabricated nickel-based superalloys represents a significant and promising research direction.

(iv) Alloy composition design for AM-specific nickel-based superalloys and nickel-based composites presents a critical research frontier. First, suitable compositions and phase constituents must be carefully selected to suppress the formation of processing defects, such as solidification and LC during both the fabrication and post-processing stages. Concurrently, the alloy must meet stringent service performance requirements under high-temperature and high-stress conditions. By integrating computational materials design software—such as Thermo-Calc and JMatPro for thermodynamic calculations, and DICTRA for kinetic simulations—with high-throughput experimental approaches, it becomes feasible to quantitatively predict the influence of elemental additions on the processability and mechanical behavior of nickel-based superalloys. This integrated approach enables rapid screening and identification of promising alloy compositions with tailored properties, thereby accelerating the development of next-generation AM-specific superalloys. Likewise, the incorporation of secondary phase particles (such as ceramic particles, rare earth oxides, graphene, and CNTs) into nickel-based superalloys offers an alternative strategy for performance enhancement. Research in this domain focuses on elucidating how these reinforcing phases affect microstructural evolution and mechanical response. However, in composite materials, the dispersion homogeneity of the secondary phase and the integrity of interfacial bonding are critical factors that significantly influence overall mechanical performance. To address these challenges, *in situ* characterization techniques—such as high-speed synchrotron X-ray radiography and small-angle neutron scattering (SANS)—can be employed to probe the dynamic behavior and spatial distribution of reinforcing phases, the initiation and propagation of metallurgical defects, and the underlying mechanisms of microstructural evolution. Such real-time insights are essential for deepening the fundamental understanding of formation and performance optimization in AM-fabricated nickel-based

composites. Consequently, AM process engineering is fundamentally distinct from conventional material processing. Therefore, the development of nickel-based superalloys and composite materials specifically engineered to leverage the unique thermal and kinetic conditions of AM processes represents a pivotal direction for future research.

Acknowledgments

None.

Funding

This work was supported by the Advanced Materials-National Science and Technology Major Project (Grant No. 2024ZD0601000), National Natural Science Foundation of China (Grant No. 52105344), Natural Science Foundation of Guangdong Province (Grant No. 2021A1515010942), and Guangzhou Basic and Applied Basic Research (Grant No. 202201010365).

Conflicts of interest

The authors declare no financial or personal relationships with other people or organizations that can inappropriately influence the present work. There is no professional or other personal interest of any nature or kind in any product, service, or company that could be construed as influencing the work presented in, or the review of, the present article.

Authors' contributions

Conceptualization: Yunlong Hu
Investigation: Zihong Wang, Qiang Zhang, Shan Li
Methodology: Xin Zhang
Writing–original draft: Yunlong Hu, Zihong Wang, Qiang Zhang, Shan Li
Writing–review and editing: Xin Zhang Weidong Huang

Ethics approval and consent to participate

Not applicable.

Consent for publication

Not applicable.

Availability of data

Not applicable.

References

1. Zhang Z, Huang H, Zhang Z. A review of the microstructure and properties of superalloys regulated by magnetic field. *J Mater Res Technol*. 2024;30:9285-9317.

   doi: 10.1016/j.jmrt.2024.05.189

2. Gudivada G, Pandey AK. Recent developments in nickel-based superalloys for gas turbine applications: Review. *J Alloys Comp*. 2023;964:171128.

   doi: 10.1016/j.jallcom.2023.171128

3. Ding W, Miao Q, Li B, *et al*. Review on grinding technology of nickel-based superalloys used for aero-engine. *J Mech Eng*. 2019;55:189-215.

   doi: 10.3901/JME.2019.01.189

4. Su J, Ng WL, An J, Yeong WY, Chua CK, Sing SL. Achieving sustainability by additive manufacturing: A state-of-the-art review and perspectives. *Virtual Phys Prototyp*. 2024;19(1):2438899.

   doi: 10.1080/17452759.2024.2438899

5. Tan C, Li R, Su J, *et al*. Review on field assisted metal additive manufacturing. *Int J Mach Tools Manuf*. 2023;189:104032.

   doi: 10.1016/j.ijmachtools.2023.104032

6. Su J, Li Q, Teng J, *et al*. Programmable mechanical properties of additively manufactured novel steel. *Int J Extreme Manuf*. 2025;7:015001.

   doi: 10.1088/2631-7990/ad88bc

7. Pusateri V, Hauschild MZ, Kara S, Goulas C, Olsen SI. Quantitative sustainability assessment of metal additive manufacturing: A systematic review. *CIRP J Manuf Sci Technol*. 2024;49:95-110.

   doi: 10.1016/j.cirpj.2023.12.005

8. Sarac Yakupoglu T. The qualification of the additively manufactured parts in the aviation industry. *Am J Aerosp Eng*. 2019;6(1):1-10.

   doi: 10.11648/j.ajae.20190601.11

9. CFM International. *CFM International Celebrates $32 Billion in New Orders and Commitments at 2017 Paris Air Show*. United States: CFM International; 2017.

10. Mostafaei A, Ghiaasiaan R, Ho IT, *et al*. Additive manufacturing of nickel-based superalloys: A state-of-the-art review on process-structure-defect-property relationship. *Prog Mater Sci*. 2023;136:101108.

    doi: 10.1016/j.pmatsci.2023.101108

11. Shi F, Zhao J, Wang Z, *et al*. Research on processing technology of superalloy K465 via laser additive manufacturing. *Mech Sci Technol Aerospace Eng*. 2017;36:1298-1302.

    doi: 10.13433/j.cnki.1003-8728.2017.1298

12. Wang XH, Lin X, Yang HO, *et al*. Research on the crack predictions in K465 superalloy by laser remelting based on BP neural networks. *Yingyong Jiguang/Appl Laser Technol*. 2014;34(1):9-14.

13. He B, Li D, Zhang A, *et al*. Influence of oxidation on the cracks of DZ125L nickel-based superalloy thin-walled parts in laser metal direct forming. *Rapid Prototyp J*.

2013;19(6):446-451.

doi: 10.1108/RPJ-12-2011-0133

14. Li Y, Chen K, Tamura N. Mechanism of heat affected zone cracking in Ni-based superalloy DZ125L fabricated by laser 3D printing technique. *Mater Des*. 2018;150:171-181.

doi: 10.1016/j.matdes.2018.04.032

15. Boswell JH, Clark D, Li W, Attallah MM. Cracking during thermal post-processing of laser powder bed fabricated CM247LC Ni-superalloy. *Mater Des*. 2019;174:107793.

doi: 10.1016/j.matdes.2019.107793

16. Kalentics N, Farrokhpour N, Logé RE, *et al*. Healing cracks in selective laser melting by 3D laser shock peening. *Addit Manuf*. 2019;30:100881.

doi: 10.1016/j.addma.2019.100881

17. Chen M, Hua L, Hu Z, Dong K, Qin X. Cracking and suppression mechanisms of directed energy deposited IN738 superalloy revealed by microstructural characterization, *in-situ* thermal monitoring, and numerical simulations. *J Alloys Comp.* 2025;1020:179446.

doi: 10.1016/j.jallcom.2025.179446

18. Perevoshchikova N, Gharbi F, Audinot JN, *et al*. Optimisation of selective laser melting parameters for the Ni-based superalloy IN-738 LC using Doehlert's design. *Rapid Prototyp J*. 2017;23(5):881-892.

doi: 10.1108/RPJ-04-2016-0063

19. Duan RX, Huang BY, Liu ZM, Peng K, Lu XQ. Selective laser melting fabrication and cracking behavior of Rene104 nickel-based superalloy. *Trans Nonferrous Metals Soc China*. 2018;28(8):1568-1578.

doi: 10.19476/j.ysxb.1004.0609.2018.08.10

20. Yang J, Li F, Wang Z, Zeng X. Cracking behavior and control of Rene 104 superalloy produced by direct laser fabrication. *J Mater Process Technol*. 2015;225:229-239.

doi: 10.1016/j.jmatprotec.2015.06.002

21. Carter LN, Martin C, Withers PJ, Attallah MM. The influence of the laser scan strategy on grain structure and cracking behaviour in SLM powder-bed fabricated nickel superalloy. *J Alloys Comp.* 2014;615:338-347.

doi: 10.1016/j.jallcom.2014.06.172

22. Zhao X, Chen J, He F, Tan H, Huang W. Cracking mechanism of Rene88DT superalloy by laser rapid forming. *Rare Metal Mater Eng*. 2007;36(2):216-220.

23. Bi G, Sun CN, Chen HC, Ng FL, Ma CCK. Microstructure and tensile properties of superalloy IN100 fabricated by micro-laser aided additive manufacturing. *Mater Des*. 2014;60:401-408.

doi: 10.1016/j.matdes.2014.04.020

24. Chen Y, Zhang K, Huang J, Hosseini R, Li Z. Characterization of heat affected zone liquation cracking in laser additive manufacturing of Inconel 718. *Mater Des*. 2015;90:586-594.

doi: 10.1016/j.matdes.2015.10.155

25. Chen Y, Lu FG, Zhang K, *et al*. Dendritic microstructure and hot cracking of laser additive manufactured Inconel 718 under improved base cooling. *J Alloys Comp.* 2016;670:312-321.

doi: 10.1016/j.jallcom.2016.01.250

26. Lu YZ, Lei WN, Ren WB, Chen SX. Crack analysis and control of laser cladding Inconel 718 alloy. *Surf Technol*. 2020;49(9):233-243.

27. Zhang YC, Wang Z, Zhang YY, *et al*. Microstructure, mechanical properties and thermal crack behavior of laser cladded In718 alloy coating. *J Xihua Univ* (*Nat Sci Ed*). 2022;41(3):42-50.

28. Zhang J, Li S, Wei QS, Shi Y, Wang L, Guo L. Cracking behavior and inhibiting process of Inconel 625 alloy formed by selective laser melting. *Chin J Rare Metals*. 2015;39(11):961-966.

doi: 10.13373/j.cnki.cjrm.2015.11.001

29. Qiu C, Chen HX, Liu Q, Yue S, Wang HM. On the solidification behaviour and cracking origin of a nickel-based superalloy during selective laser melting. *Mater Character*. 2019;148:330-344.

doi: 10.1016/j.matchar.2018.12.032

30. Darabi R, Oliveira JP, Nemati N, Reis A, Cesar de Sá J. Benchmarking advanced multiphase field modeling of Inconel 625 in additive manufacturing: Correlating powder bed fusion with dendrite growth and crack formation. *Materialia*. 2025;40:102384.

doi: 10.1016/j.mtla.2025.102384

31. Pakniat M, Ghaini FM, Torkamany MJ. Hot cracking in laser welding of Hastelloy X with pulsed Nd: YAG and continuous wave fiber lasers. *Mater Des*. 2016;106:177-183.

doi: 10.1016/j.matdes.2016.05.124

32. Han Q, Gu Y, Soe S, Lacan F, Setchi R. Effect of hot cracking on the mechanical properties of Hastelloy X superalloy fabricated by laser powder bed fusion additive manufacturing. *Optics Laser Technol*. 2019;124:105984.

doi: 10.1016/j.optlastec.2019.105984

33. Hu J, Lin X, Hu Y. High wear resistance and strength of Hastelloy X reinforced with TiC fabricated by laser powder bed fusion additive manufacturing. *Appl Surf Sci*. 2024;648:159004.

doi: 10.1016/j.apsusc.2023.159004

34. Han Q, Mertens R, Montero-Sistiaga ML, *et al*. Laser powder bed fusion of Hastelloy X: Effects of hot isostatic pressing and the hot cracking mechanism. *Mater Sci Eng A*. 2018;732:228-239.

doi: 10.1016/j.msea.2018.07.008

35. Hu J, Hu Y, Lan C, *et al*. Cracking mechanism and control of Hastelloy X prepared by laser powder bed fusion. *J Mater Res Technol*. 2022;21:3526-3547.

    doi: 10.1016/j.jmrt.2022.10.164

36. Tomus D, Rometsch PA, Heilmaier M, Wu X. Effect of minor alloying elements on crack-formation characteristics of Hastelloy-X manufactured by selective laser melting. *Addit Manuf*. 2017;16:65-72.

    doi: 10.1016/j.addma.2017.05.006

37. Saarimäki J, Lundberg M, Moverare JJ, *et al*. Characterization of Hastelloy X produced by laser powder bed additive manufacturing. In: *Proceedings of the World Congress on Powder Metallurgy & Particulate Materials (World PM2016)*. Hamburg, Germany: European Powder Metallurgy Association (EPMA); 2016. p. 1-8.

38. Dupont JN, Lippold JC, Kiser SD. *Welding Metallurgy and Weldability of Nickel-Based Alloys*. Hoboken, NJ: John Wiley & Sons, Inc.; 2009.

39. Hu YL, Lin X, Yu XB, Xu JJ, Lei M, Huang WD. Effect of Ti addition on cracking and microhardness of Inconel 625 during the laser solid forming process. *J Alloys Comp*. 2017;711:267-277.

    doi: 10.1016/j.jallcom.2017.03.355

40. Sonar T, Balasubramanian V, Malarvizhi S, Venkateswaran T, Sivakumar D. An overview on welding of Inconel 718 alloy - Effect of welding processes on microstructural evolution and mechanical properties of joints. *Mater Character*. 2021;174:110997.

    doi: 10.1016/j.matchar.2021.110997

41. Xu JJ, Lin X, Guo PF, *et al.* The initiation and propagation mechanism of the overlapping zone cracking during laser solid forming of IN-738LC superalloy. *J Alloys Compd*. 2018;749:859-870.

    doi: 10.1016/j.jallcom.2018.03.366

42. Cloots M, Uggowitzer PJ, Wegener K. Investigations on the microstructure and crack formation of IN738LC samples processed by selective laser melting using Gaussian and doughnut profiles. *Mater Des*. 2016;89:770-784.

    doi: 10.1016/j.matdes.2015.10.027

43. Ci S, Liang J, Li J, *et al*. Microstructure and stress-rupture property of DD32 nickel-based single crystal superalloy fabricated by additive manufacturing. *J Alloys Compd*. 2021;854:157180.

    doi: 10.1016/j.jallcom.2020.157180

44. Zhou Z, Gill AS, Qian D, *et al*. A finite element study of thermal relaxation of residual stress in laser shock peened IN718 superalloy. *Int J Impact Eng*. 2011;38(7):590-596.

    doi: 10.1016/j.ijimpeng.2011.02.006

45. Moat RJ, Pinkerton AJ, Li L, Withers PJ, Preuss M. Residual stresses in laser direct metal deposited Waspaloy. *Mater Sci Eng A*. 2011;528(6):2288-2298.

    doi: 10.1016/j.msea.2010.12.010

46. Nadammal N, Cabeza S, Mishurova T, *et al*. Effect of hatch length on the development of microstructure, texture and residual stresses in selective laser melted superalloy Inconel 718. *Mater Des*. 2017;134:139-150.

    doi: 10.1016/j.matdes.2017.08.049

47. Mazumder J. Laser direct metal deposition technology and microstructure and composition segregation of Inconel 718 superalloy. *J Iron Steel Res Int*. 2011;18(4):73-78.

    doi: 10.1016/S1006-706X(11)60054-X

48. Wang F, Ma D, Buhrig-Polaczek A. Microsegregation behavior of alloying elements in single-crystal nickel-based superalloys with emphasis on dendritic structure. *Mater Charact*. 2017;127:311-316.

    doi: 10.1016/j.matchar.2017.02.030

49. Shi Z, Dong J, Zhang M, Zheng L. Solidification characteristics and segregation behavior of Ni-based superalloy K418 for auto turbocharger turbine. *J Alloys Compd*. 2013;571:168-177.

    doi: 10.1016/j.jallcom.2013.03.241

50. Feng S, Zhang N, Luo X. Influence of segregation on liquid density in the mushy zone of DZ483 Ni-based superalloy. *Acta Metall Sin*. 2012;48(5):541-546.

    doi: 10.3724/SP.J.1037.2012.00037

51. Liang YJ, Cheng X, Wang HM. A new microsegregation model for rapid solidification multicomponent alloys and its application to single-crystal nickel-base superalloys of laser rapid directional solidification. *Acta Mater*. 2016;118:17-27.

    doi: 10.1016/j.actamat.2016.07.008

52. Ojo OA, Chaturvedi MC. On the role of liquated γ′ precipitates in weld heat affected zone microfissuring of a nickel-based superalloy. *Mater Sci Eng A*. 2005;403(1-2):77-86.

    doi: 10.1016/j.msea.2005.04.034

53. Sidhu RK, Ojo OA, Chaturvedi MC. Microstructural response of directionally solidified Rene' 80 superalloy to gas-tungsten arc welding. *Metall Mater Trans A*. 2009;40(1):150-162.

    doi: 10.1007/s11661-008-9700-5

54. Rush MT, Colegrove PA, Zhang Z, Broad D. Liquation and post-weld heat treatment cracking in Rene 80 laser repair welds. *J Mater Process Technol*. 2012;212(1):188-197.

    doi: 10.1016/j.jmatprotec.2011.09.001

55. Chen Y, Lu FG, Zhang K, *et al.* Laser powder deposition of carbon nanotube reinforced nickel-based superalloy Inconel 718. *Carbon*. 2016;107:361-370.

    doi: 10.1016/j.carbon.2016.06.014

56. Harrison NJ, Todd I, Mumtaz K. Reduction of micro-cracking in nickel superalloys processed by selective laser melting: A fundamental alloy design approach. *Acta Mater*. 2015;94:59-68.

    doi: 10.1016/j.actamat.2015.04.035

57. Zhong M, Sun H, Liu W, Li J, Zhu X, He J. Boundary liquation and interface cracking characterization in laser deposition of Inconel 738 on directionally solidified Ni-based superalloy. *Scr Mater*. 2005;53(2):159-164.

    doi: 10.1016/j.scriptamat.2005.03.047

58. Zhao XM, Lin X, Chen J, Xue L, Huang WD. The effect of hot isostatic pressing on crack healing, microstructure, and mechanical properties of Rene88DT superalloy prepared by laser solid forming. *Mater Sci Eng A*. 2009;504:29-134.

    doi: 10.1016/j.msea.2008.12.024

59. Nematzadeh F, Akbarpour MR, Parvizi S, Kokabi AH, Sadrnezhaad SK. Effect of welding parameters on microstructure, mechanical properties and hot cracking phenomenon in Udimet 520 superalloy. *Mater Des*. 2012;36:94-99.

    doi: 10.1016/j.matdes.2011.10.020

60. Idowu OA, Ojo OA, Chaturvedi MC. Effect of heat input on heat affected zone cracking in laser welded ATI Allvac 718Plus superalloy. *Mater Sci Eng A*. 2007;454:389-397.

    doi:10.1016/j.msea.2006.11.054

61. Bian HY, Zhai XY, Wang SJ, Li Y, Wang W. Influence of heat input and thermal cycling on the crack and microstructure of laser deposition repair DZ125 alloy. *Rare Met Mater Eng*. 2020;49:1701-1706.

    doi: 10.12442/j.issn.1002-185X.20190156

62. Ebrahimnia M, Ghaini FM, Shahverdi HR. Hot cracking in pulsed laser processing of a nickel-based superalloy built up by electrospark deposition. *Sci Technol Weld Join*. 2014;19(1):25-29.

    doi: 10.1179/1362171813Y.0000000157

63. Chen ZJ, Zhang QL, Lou CH, Yao JH. Methods of crack control for inconel 738 laser cladding layer. *Appl Laser*. 2013;33(1):7-13.

64. Han Q, Gu Y, Setchi R, *et al*. Additive manufacturing of high-strength crack-free Ni-based Hastelloy X superalloy. *Addit Manuf*. 2019;30:100919.

    doi: 10.1016/j.addma.2019.100919

65. Hu YL, Lin X, Zhang SY, *et al*. Effect of solution heat treatment on the microstructure and mechanical properties of Inconel 625 superalloy fabricated by laser solid forming. *J Alloys Comp*. 2018;767:330-344.

    doi: 10.1016/j.jallcom.2018.07.087

66. Hu YL, Lin X, Lu XF, *et al*. Evolution of solidification microstructure and dynamic recrystallisation of Inconel 625 during laser solid forming process. *J Mater Sci*. 2018;53:15650-15666.

    doi: 10.1007/s10853-018-2701-x

67. Li X, Shi JJ, Wang CH, *et al*. Effect of heat treatment on microstructure evolution of Inconel 718 alloy fabricated by selective laser melting. *J Alloys Compd*. 2018;764:639-649.

    doi: 10.1016/j.jallcom.2018.06.112

68. Chlebus E, Gruber K, Kuźnicka B, Kwaśny W, Sałacinski T. Effect of heat treatment on the microstructure and mechanical properties of Inconel 718 processed by selective laser melting. *Mater Sci Eng A*. 2015;639:647-655.

    doi: 10.1016/j.msea.2015.05.035

69. Zhang H, Li C, Liu Y, *et al*. Effect of hot deformation on γ″ and δ phase precipitation of Inconel 718 alloy during deformation and isothermal treatment. *J Alloys Compd*. 2017;716:65-72.

    doi: 10.1016/j.jallcom.2017.05.042

70. Konečná R, Nicoletto G, Kunz L, Bača A. Microstructure and directional fatigue behavior of Inconel 718 produced by selective laser melting. *Procedia Struct Integr*. 2016;2: 2381-2388.

    doi: 10.1016/j.prostr.2016.06.298

71. Zhang F, Ilavsky J, Lindwall G, Stoudt M, Levine L, Allen A. Solid-state transformation of an additively manufactured Inconel 625 alloy at 700°C. *Appl Sci*. 2021;11:8643.

    doi: 10.3390/app11188643

72. Lass EA, Stoudt MR, Katz MB, Williams ME, Ghosh G, Levine LE. Precipitation and dissolution of δ and γ″ during heat treatment of a laser powder-bed fusion produced Ni-based superalloy. *Scr Mater.* 2018;154:83-86.

    doi: 10.1016/j.scriptamat.2018.05.025

73. Marchese G, Bassini E, Parizia S, *et al*. Role of the chemical homogenization on the microstructural and mechanical evolution of prolonged heat-treated laser powder bed fused Inconel 625. *Mater Sci Eng A*. 2020;796:140007.

    doi: 10.1016/j.msea.2020.140007

74. Lass EA, Stoudt MR, Williams ME, *et al*. Formation of the Ni_3Nb δ-phase in stress-relieved Inconel 625 produced via laser powder-bed fusion additive manufacturing. *Metall Mater Trans A Phys Metall Mater Sci*. 2017;48(11): 5547-5558.

    doi: 10.1007/s11661-017-4304-6

75. Luna V, Trujillo L, Gamon A, *et al*. Comprehensive and comparative heat treatment of additively manufactured Inconel 625 alloy and corresponding microstructures and mechanical properties. *J Manuf Mater Process*. 2022;6:107.

    doi: 10.3390/jmmp6050107

76. Rosenthal S, Platt S, Hoelker-Jaeger R. Forming properties of additively manufactured monolithic Hastelloy X sheets. *Mater Sci Eng A*. 2019;753:300-316.

    doi: 10.1016/j.msea.2019.03.035

77. Zhang F, Levine LE, Allen AJ, *et al*. Effect of heat treatment on the microstructural evolution of a nickel-based superalloy additive manufactured by laser powder bed fusion. *Acta Mater*. 2018;152:200-214.

    doi: 10.1016/j.actamat.2018.03.017

78. Dinda GP, Dasgupta AK, Mazumder J. Texture control during laser deposition of nickel-based superalloy. *Scr Mater*. 2012;67(5):503-506.

    doi: 10.1016/j.scriptamat.2012.12.028

79. Ma D, Stoica AD, Wang Z, Beese AM. Crystallographic texture in an additively manufactured nickel-base superalloy. *Mater Sci Eng A*. 2017;684:47-53.

    doi: 10.1016/j.msea.2016.11.110

80. Sui S, Tan H, Chen J, *et al.* The influence of Laves phases on the room temperature tensile properties of Inconel 718 fabricated by powder feeding laser additive manufacturing. *Acta Mater*. 2019;164:413-427.

    doi: 10.1016/j.actamat.2018.10.032

81. Sui S, Chen J, Fan E, Yang H, Lin X, Huang W. The influence of Laves phases on the high-cycle fatigue behavior of laser additive manufactured Inconel 718. *Mater Sci Eng A*. 2017;695:6-13.

    doi: 10.1016/j.msea.2017.03.098

82. Wu S, Peng HZ, Gao X, *et al*. Improving creep property of additively manufactured Inconel 718 through specifically designed post heat treatments. *Mater Sci Eng A*. 2022;857:144047.

    doi: 10.1016/j.msea.2022.144047

83. Guo J. The effect of aluminum and titanium on the microstructure and mechanical properties of an iron-base alloy. *Acta Metall Sin*. 1978;14(3):227-234.

84. Li X, Chen B, Xing W, *et al*. Effect of Si on solidification behavior and mechanical property of superalloy K4169. *Chin J Mater Res*. 2018;32(12):936-945.

    doi: 10.11901/1005.3093.2018.181

85. Sullivan CP, Donachie MJ. Microstructures and mechanical properties of iron-base (containing) superalloys. *Met Eng Q*. 1971;4(11):1.

86. Ling L, Han Y, Zhou W, *et al.* Study of microsegregation and Laves phase in Inconel 718 superalloy regarding cooling rate during solidification. *Metall Mater Trans A*. 2015;46(1):1-8.

    doi: 10.1007/s11661-014-2614-5

87. Xiao H, Li S, Han X, Mazumder J, Song L. Laves phase control of Inconel 718 alloy using quasi-continuous-wave laser additive manufacturing. *Mater Des*. 2017;122:330-339.

    doi: 10.1016/j.matdes.2017.03.004

88. Xiao H, Li SM, Xiao WJ, *et al.* Effects of laser modes on Nb segregation and Laves phase formation during laser additive manufacturing of nickel-based superalloy. *Mater Lett*. 2017;188:260-262.

    doi: 10.1016/j.matlet.2016.10.118

89. Tucho WM, Cuvillier P, Sjølst-Kverneland A, Hansen V. Microstructure and hardness studies of Inconel 718 manufactured by selective laser melting before and after solution heat treatment. *Mater Sci Eng A*. 2017;689:220-232.

    doi: 10.1016/j.msea.2017.02.062

90. Dinda GP, Dasgupta AK, Mazumder J. Laser aided direct metal deposition of Inconel 625 superalloy: Microstructural evolution and thermal stability. *Mater Sci Eng A*. 2009;509(1):98-104.

    doi: 10.1016/j.msea.2009.01.009

91. Kreitcberg A, Brailovski V, Turenne S. Effect of heat treatment and hot isostatic pressing on the microstructure and mechanical properties of Inconel 625 alloy processed by laser powder bed fusion. *Mater Sci Eng A*. 2017;689:1-10.

    doi: 10.1016/j.msea.2017.02.038

92. Thomas A, El-Wahabi M, Cabrera JM, Prado JM. High temperature deformation of Inconel 718. *J Mater Process Technol*. 2006;177(1-3):469-472.

    doi: 10.1016/j.jmatprotec.2006.04.072

93. Liu F, Lin X, Song M, *et al*. Effect of intermediate heat treatment temperature on microstructure and notch sensitivity of laser solid-formed Inconel 718 superalloy. *J Wuhan Univ Technol Mater Sci Ed*. 2011;26(5):908-913.

    doi: 10.1007/s11595-011-0335-9

94. Azadian S, Wei L, Warren R. Delta phase precipitation in Inconel 718. *Mater Charact*. 2004;53(1):7-16.

    doi: 10.1016/j.matchar.2004.07.004

95. Cai D, Zhang W, Nie P, Liu W, Yao M. Dissolution kinetics of δ phase and its influence on the notch sensitivity of Inconel 718. *Mater Charact*. 2007;58(3):220-225.

    doi: 10.1016/j.matchar.2006.04.020

96. Li S, Zhuang J, Yang J, *et al.* The effect of δ-phase on crack propagation under creep and fatigue conditions in Alloy 718. In: Loria EA, editor. *Superalloys 718, 625, 706 and Various Derivatives*. Warrendale, PA: TMS; 1994. p. 545-556.

97. Sundararaman M. Evolution of δ phase microstructure in Alloy 718. In: *Superalloy 718, 718+ and 907: Proceedings of the 7th International Symposium on Superalloy 718 and Derivatives*. United States: John Wiley & Sons; 2010. p. 139-152.

    doi: 10.1002/9781118762488.ch11

98. Ye N, Cheng M, Zhang S, Song HW, Zhou HW, Wang PB.

Effect of δ phase on mechanical properties of GH4169 alloy at room temperature. *J Iron Steel Res Int*. 2015;22(8):752-756.

doi: 10.1016/S1006-706X(15)30068-6

99. Yuan Z, Liu J, Zhang S. Research on precipitation kinetics of δ-phase in GH4169 alloy. *J Shenyang Ligong Univ*. 2010;29(2):23-26.

100. Deng G, Tu S, Zhang X, *et al.* Small fatigue crack initiation and growth mechanisms of nickel-based superalloy GH4169 at 650°C in air. *Eng Fract Mech*. 2016;153:35-49.

doi: 10.1016/j.engfracmech.2015.12.014

101. Hong B, Yi X, Meng QC. Effect of δ-Ni_3Nb on low-cycle fatigue fracture of Inconel 718. *Acta Metall Sin*. 1994;27(2):79-82.

102. Zhang XC, Li HC, Zeng X, Tu ST, Zhang CC, Wang CQ. Fatigue behavior and bilinear Coffin-Manson plots of Ni-based GH4169 alloy with different volume fractions of δ phase. *Mater Sci Eng A*. 2017;682:12-22.

doi: 10.1016/j.msea.2016.11.040

103. Zhang H, Zhang S, Cheng M. Effect of δ phase on the tensile deformation behavior of GH4169 alloy at high temperature. *Acta Metall Sin*. 2013;29(4):483-488.

doi: 10.3724/SP.J.1037.2012.00620

104. Wang RYZ, Zhang XC, Liu F, Yao LL, Tu ST. Fatigue and fracture behaviors of nickel-based forging GH4169 superalloy and optimization of model parameters. *Procedia Eng*. 2015;130:1088-1096.

doi: 10.1016/j.proeng.2015.12.270

105. Zhang H, Li C, Guo Q, *et al*. Hot tensile behavior of cold-rolled Inconel 718 alloy at 650°C: the role of δ phase. *Mater Sci Eng A*. 2018;722:136-146.

doi: 10.1016/j.msea.2018.02.093

106. Ning Y, Huang S, Fu MW, Dong J. Microstructural characterization, formation mechanism, and fracture behavior of the needle δ phase in Fe–Ni–Cr-type superalloys with high Nb content. *Mater Charact*. 2015;109:36-42.

doi: 10.1016/j.matchar.2015.09.011

107. Cao GH, Sun TY, Wang CH, *et al*. Investigations of γ′, γ″, and δ precipitates in heat-treated Inconel 718 alloy fabricated by selective laser melting. *Mater Charact.* 2018;136:398-406.

doi: 10.1016/j.matchar.2018.01.015

108. Tiley J, Viswanathan GB, Hwang JY, Srinivasan R, Lipsitt HA. Evaluation of gamma prime volume fractions and lattice misfits in a nickel-base superalloy using the external standard X-ray diffraction method. *Mater Sci Eng A*. 2010;528(1):32-36.

doi: 10.1016/j.msea.2010.07.036

109. Drexler A, Oberwinkler B, Primig S, *et al*. Experimental and numerical investigations of the γ″ and γ′ precipitation kinetics in Alloy 718. *Mater Sci Eng A*. 2018;723:314-323.

doi: 10.1016/j.msea.2018.03.013

110. Collins DM, Stone HJ. A modelling approach to yield strength optimisation in a nickel-base superalloy. *Int J Plast*. 2014;54:96-112.

doi: 10.1016/j.ijplas.2013.08.009

111. Slama C, Abdellaoui M. Structural characterization of the aged Inconel 718. *J Alloys Compd*. 2000;306(1-2):277-284.

doi: 10.1016/S0925-8388(00)00789-1

112. Srinivas S, Prasad KS, Gopikrishna D, Venugopal P. Stress rupture in hot-rolled superalloy 718: Property-microstructure correlation. *Mater Charact*. 1995;35(2):93-98.

doi: 10.1016/1044-5803(95)80108-1

113. Ming X, Chen J, Tan H, *et al*. Coarsening behavior of γ″ precipitates in GH4169 superalloy fabricated by laser solid forming. *J Mater Eng*. 2014;8:8-14.

114. Chaturvedi MC, Han Y. Effect of particle size on the creep rate of superalloy Inconel 718. *Mater Sci Eng*. 1987;89:7-10.

doi: 10.1016/0025-5416(87)90264-3

115. Wan HY, Luo YW, Zhang B, *et al*. Effects of surface roughness and build thickness on fatigue properties of selective laser melted Inconel 718 at 650°C. *Int J Fatigue*. 2020;137:105654.

doi: 10.1016/j.ijfatigue.2020.105654

116. Ma XF, Zhai HL, Zuo L, *et al*. Fatigue short crack propagation behavior of selective laser melted Inconel 718 alloy by *in-situ* SEM study: Influence of orientation and temperature. *Int J Fatigue*. 2020;139:105739.

doi: 10.1016/j.ijfatigue.2020.105739

117. Yu X, Lin X, Wang Z, *et al*. Room and high temperature high-cycle fatigue properties of Inconel 718 superalloy prepared using laser directed energy deposition. *Mater Sci Eng A*. 2021;825:141865.

doi: 10.1016/j.msea.2021.141865

118. Zhang S, Weng K, Guo C, *et al*. The creep behavior of IN718 alloy fabricated by selective laser melting compared to forging. *Appl Mater Today*. 2024;38:102252.

doi: 10.1016/j.apmt.2024.102252

119. Shi Q, Zhang S, Dong X, Wang H, Liu Y, Zhang X. Achieving superior resistance to high-temperature creep in laser powder bed fusion of Inconel 718 via grain boundary serration. *J Mater Res Technol*. 2024;33:7534-7545.

doi: 10.1016/j.jmrt.2024.11.038

120. Spierings AB, Dawson K, Kern K, Stanojevic A, Weber R. SLM-processed Sc- and Zr-modified Al-Mg alloy: Mechanical properties and microstructural effects of heat treatment. *Mater Sci Eng A*. 2017;701:264-273.

doi: 10.1016/j.msea.2017.06.089

121. Sreeramagiri P, Bhagavatam A, Ramakrishnan A, Alrehaili H, Dinda GP. Design and development of a high-performance Ni-based superalloy WSU 150 for additive manufacturing. *J Mater Sci Technol*. 2020;47:20-28.

doi: 10.1016/j.jmst.2020.01.041

122. Tang YT, Panwisawas C, Ghoussoub JN, *et al.* Alloys-by-design: application to new superalloys for additive manufacturing. *Acta Mater*. 2021;202:417-436.

doi: 10.1016/j.actamat.2020.09.023

123. Kou S. A criterion for cracking during solidification. *Acta Mater*. 2015;88:366-374.

doi: 10.1016/j.actamat.2015.01.034

124. Song W, Yang J, Liang J, *et al.* A new approach to design advanced superalloys for additive manufacturing. *Addit Manuf*. 2024;84:104098.

doi: 10.1016/j.addma.2024.104098

125. Sun Z, Soh V, Lee C, Tan MJ, Bi G, Zhou W. Effects of carbon content on precipitate evolution and crack susceptibility in additively manufactured IN738LC. *Mater Sci Addit Manuf*. 2024;3(1):2264.

doi: 10.36922/msam.2264

126. Hong C, Gu DD, Dai DH, Zhang D, Wen M. Laser additive manufacturing of ultrafine TiC particle reinforced Inconel 625 based composite parts: Tailored microstructures and enhanced performance. *Mater Sci Eng A*. 2015;635:118-128.

doi: 10.1016/j.msea.2015.03.043

127. Gu DD, Hong C, Jia Q, Dai DH, Zhang D. Combined strengthening of multi-phase and graded interface in laser additive manufactured TiC/Inconel 718 composites. *J Phys D Appl Phys*. 2014;47(4):045309.

doi: 10.1088/0022-3727/47/4/045309

128. Gu DD, Zhang HM, Dai DH, Zhang D, Wen M. Laser additive manufacturing of nano-TiC reinforced Ni-based nanocomposites with tailored microstructure and performance. *Compos Part B Eng*. 2019;163:585-597.

doi: 10.1016/j.compositesb.2018.12.146

129. Cao SN, Gu DD. Laser metal deposition additive manufacturing of TiC/Inconel 625 nanocomposites: Relation of densification, microstructures, and performance. *J Mater Res*. 2015;30(23):3616-3628.

doi: 10.1557/jmr.2015.358

130. Zhang BC, Bi GJ, Sun CN, Dong ZL, Bi J. Microstructure and mechanical properties of Inconel 625/nano-TiB_2 composite fabricated by LAAM. *Mater Des*. 2016;111:70-79.

doi: 10.1016/j.matdes.2016.08.078

131. Yang W, He W, Hu Z, Zhang X, Liu Y, Wang H. Fabrication of Inconel 718 composites reinforced with TiCN via laser powder bed fusion: Integration of triply periodic minimal surface lattice structures. *J Mater Res Technol*. 2024;32:2443-2458.

doi: 10.1016/j.jmrt.2024.08.102

132. Gruber K, Stopyra W, Kobiela K, Kurzynowski T, Skiba M, Szczepański T. Achieving high strength and ductility in Inconel 718: Tailoring grain structure through micron-sized carbide additives in PBF-LB/M additive manufacturing. *Virtual Phys Prototyp*. 2024;19(1):e2396064.

doi: 10.1080/17452759.2024.2396064

133. Wang P, Zhang BC, Liu J, Du X. Microstructural characteristics and mechanical properties of carbon nanotube reinforced Inconel 625 parts fabricated by selective laser melting. *Mater Des*. 2016;112:290-299.

doi: 10.1016/j.matdes.2016.09.080

134. Deng PS, Yao CW, Feng K, *et al.* Enhanced wear resistance of laser cladded graphene nanoplatelets reinforced Inconel 625 superalloy composite coating. *Surf Coat Technol*. 2018;335:334-344.

doi: 10.1016/j.surfcoat.2017.12.047

135. Xiao WH, Lu SQ, Wang YC, *et al.* Mechanical and tribological behaviors of graphene/Inconel 718 composites. *Trans Nonferrous Met Soc China*. 2018;28:1958-1969.

doi: 10.1016/S1003-6326(18)64841-1

ACCSCIENCE PUBLISHING

Materials Science in Additive Manufacturing

ORIGINAL RESEARCH ARTICLE

Personalized antimicrobial and soundproof earplugs through embedded-suspension 3D printing of polydimethylsiloxane-Ag composites for the prevention of swimmers' otitis externa

Lili Qin[1]*, Xinran Qian[1], Dengyun Xu[1], Jianming Yang[2], Junye Ren[1], Jialu Lu[2], Wenjia Zhang[1], Tianfeng Lu[1], Wenrui Wang[3]*, and Ai Du[2]*

[1]Sports and Health Research Center, Department of Physical Education, Tongji University, Shanghai, China

[2]Shanghai Key Laboratory of Special Artificial Microstructure Materials and Technology, School of Physics Science and Engineering, Tongji University, Shanghai, China

[3]Anhui Provincial Key Laboratory of Tumor Evolution and Intelligent Diagnosis and Treatment, School of Life Sciences, Anhui Engineering Research Center for Neural Regeneration Technology and Medical New Materials, Bengbu Medical University, Bengbu, Anhui, China

***Corresponding authors:**
Ai Du
(duai@tongji.edu.cn)
Wenrui Wang
(2015003@bbmu.edu.cn)
Lili Qin
(qinlili@tongji.edu.cn)

Citation: Qin L, Qian X, Xu D, *et al*. Personalized antimicrobial and soundproof earplugs through embedded-suspension 3D printing of polydimethylsiloxane-Ag composites for the prevention of swimmers' otitis externa. *Mater Sci Add Manuf*. 2026;5(1):025260054. doi: 10.36922/MSAM025260054

Received: June 27, 2025

Revised: July 22, 2025

Accepted: July 25, 2025

Published online: October 6, 2025

Abstract

Aquatic activities, particularly swimming, have been demonstrated to enhance physical conditioning and psychological well-being. However, the risk of water-induced otitis externa—caused by microbial colonization in the external auditory canal—often deters sustained participation in aquatic sports. Traditional swimming earplugs are typically limited in terms of comfort, water resistance, and antimicrobial protection, which can lead to potential ear canal infections and reduced effectiveness in preventing water ingress. In this study, we proposed using 3D scanning and printing technology to produce personally customized swimming earplugs to address these challenges. Embedded-suspension 3D printing technology was applied to fabricate structures using non-self-supporting Polydimethylsiloxane (PDMS) ink, printing hydrophobic ink in a hydrophilic system. The 3D-printed PDMS/Ag-3% composites exhibited an excellent inhibition rate (99.89%), good sound insulation performance (>30 dB, 1000–6300 Hz, 8 mm thickness), elasticity (elongation at break of 62.93%), and low modulus (0.85 MPa). We then recruited 60 beginner swimmers for a wear trial to demonstrate the effectiveness of personalized earplugs in preventing otitis externa and reducing ear canal irritation. This approach not only highlights the potential of 3D printing technology in sports equipment but also offers new insights for developing customized wearables.

Keywords: 3D printing; Swimming earplugs; Swimmer's ear prevention; Sports equipment; Sports injury prevention

1. Introduction

Swimming and aquatic activities are integral to public health promotion, improving physical fitness, mental well-being, and social cohesion. However, swimming-induced ear pain has emerged as a significant health burden,[1,2] which may affect vulnerable

populations and exacerbate health disparities.[3] When swimmers' ears are exposed to water, the moisture and water in the auditory canal can remove the protective lining and change the acidic environment of the ear canal to alkaline, thereby increasing susceptibility to infections.[4-9] Water safety is a critical public health priority. The Centers for Disease Control and Prevention highlights the importance of preventing swimming-related illnesses,[10] which not only compromise individual health but also impose substantial healthcare expenditure.[11,12] The economic burden extends beyond direct healthcare costs to include work and school absenteeism, as well as reduced participation in physical activities.[13,14] Therefore, it is vital to protect the health of swimmers when swimming in pools and public waters. Traditional swimming earplugs, typically made from silicone, wax, or foam, are designed for general use.[15] However, these earplugs often leave debris in the ear canal, increasing the risk of infection. In addition, traditional manufacturing processes restrict earplugs to standardized shapes, resulting in poor stability and limited antibacterial properties.[16]

In recent years, 3D printing technology has been increasingly applied in the modeling and preparation of new materials.[17] The flexibility of inks and materials, along with the ability to manipulate structures and functions, demonstrates great prospects across various fields.[18,19] Compared with traditional manufacturing processes, 3D printing technology demonstrates higher plasticity and flexibility, enabling the fabrication of complex structures.[20,21] Among the 3D printing techniques, embedded extrusion printing stands out as a promising method for fabricating complex 3D structures using low-modulus, low-viscosity, or slow-curing inks.[22-24] The suspension bath overcomes many limitations, including the dependence on support structures and nozzle clogging problems.[25-28] The application of 3D printing technology to fabricate swimming earplugs is not only cost-effective and easy to use but also allows for personalized designs tailored to the ear canal structures of swimmers and enthusiasts. Manufacturing earplugs that conform more closely to the auditory canal ensures enhanced stability and wearing comfort.

In terms of material selection, polydimethylsiloxane (PDMS) is a chemically stable, flexible, and biocompatible silicone macromolecular polymer material, which has a wide range of applications in flexible electronics,[29] medical devices,[30] and microfluidics.[31] Owing to the low elastic modulus of PDMS (≤1 MPa), it is often necessary to use support materials to maintain the stability of complex 3D structures.[32,33] Carbomer can be uniformly dispersed and stably suspended in liquid to form a high-viscosity gel,[34] which can provide a good supportive environment and ensure the uniform distribution of the printing material to enhance the printing accuracy and consistency. Concurrently, the gel strength and viscosity of carbomer can be precisely controlled by adjusting the concentration and pH to adapt to different printing requirements.[35] To further enhance the antimicrobial properties of the materials, silver (Ag), known for its antimicrobial effects, was incorporated to prepare novel PDMS-Ag composite inks. Ag is currently considered the most effective antibacterial metal. Silver ions (Ag^+) readily adsorb onto most bacterial biomolecules, disrupting their functions,[36] and this antimicrobial property is widely exploited in biomedicine, biomaterials, and medical implants.[37-39] The incorporation of Ag particles can significantly improve the mechanical properties of PDMS, complementing its inherent flexibility and elasticity. Slow sound propagation occurs in mixed structures, similar to aerogels.[40] High-density Ag particles combined with soft PDMS substrates may enhance the interaction between the material and sound waves, potentially improving sound insulation performance.[41]

In this study, we propose 3D-printed antimicrobial earplugs as both personal protective devices and scalable public health tools that provide an innovative solution to a common health issue faced by swimmers. The outer ear canal of each participant was modeled using an ear impression material and 3D scanning technology to create a personalized design. These custom swimming earplugs offer tailored protection during aquatic activities, reducing the risk of otitis externa. This aligns with the World Health Organization's (WHO) core principles of providing population-specific health solutions.[42] 3D-printed earplugs fabricated using suspension-embedded technology can be personalized and produced at a low cost, presenting an innovative solution aimed at preventing water-related ear infections and promoting safer aquatic activities. The key innovations in this study include (i) successful printing of hydrophobic PDMS ink within a hydrophilic support medium, enabling the creation of complex models without traditional molds and (ii) a dual-function design incorporating Ag, which imparts antibacterial properties to the composite material while enhancing its overall sound insulation performance.

2. Materials and methods

2.1. Materials

The PDMS material used was Sylgard 184 (Dow Corning), which was purchased from Merck Chemical Technology Co., Ltd. (China). Ag nanoparticles (200 nm), Carbomer 940, sodium hydroxide (NaOH), sodium chloride

(NaCl), and deionized water (DW) were purchased from Sinopharm Chemical Reagent Co., Ltd. (China); NaOH, NaCl, and DW were of analytical grade purity and used without further purification. LB broth and LB nutrient agar for biological experiments were purchased from Hope Biotechnology Co., Ltd. (China).

2.2. 3D printing of models

The earplug mold was first created using ear impression material, which was injected into the subject's external ear canal and quickly cured to obtain a personalized earplug size. This physical mold was then digitized using a 3D scanner, and the resulting model was optimized and styled using Rhino software (Figure 1). The 3D models, saved as Standard Triangle Language files, were converted to G-code and sliced into thick layers using Slic3r software integrated within the printing software (Cura Wiiboox). The resulting X3G file was then transferred to the 3D printer through an SD card.

2.3. Inks and support medium preparation

Pure PDMS ink is in a liquid state when extruded and requires prolonged curing at high temperatures (Figure 2A). Therefore, traditional direct-write 3D printing technology cannot produce complex structures using pure PDMS. The PDMS ink was prepared by mixing Sylgard 184 at a 10:1 base-to-curing-agent ratio. This mixture was stirred for 30 min using a mechanical mixer and then vacuum degassed for 20 min. The PDMS-Ag inks were prepared by mixing PDMS ink with Ag nanoparticles at different mass concentrations of 1%, 3%, 5%, and 10% relative to the total mass. Compared to pure PDMS ink, the PDMS-Ag ink requires ultrasonic dispersion for 30 min to evenly disperse the Ag nanoparticles before degassing. In preliminary experiments, we studied different carbomer formulations to optimize the NaOH concentration. Carbomer gels were prepared with 0, 0.40, and 0.60 g NaOH per 100 mL DW, while keeping Carbomer 940 fixed at 1.20 g. Pure carbomer has low yield stress and strong intermolecular forces, resulting in rheological properties unsuitable for printing. After adding NaOH, the carbomer molecular chains undergo stretching and crosslinking (Figure 2B), increasing the yield stress of the system to a suitable range for printing. The prepared mixture was then loaded into a sealed syringe for extrusion. The carbomer support bath was poured into a square container (side length = 4 cm) to hold the earplug construct during 3D printing and secured on the build platform.

2.4. Extrusion printing process

Figure 3A displays the 3D printing process for the personalized earplugs. A commercial fused deposition modeling 3D printer (One Mini, Wiiboox, China) was modified by incorporating an additional pressure-controlled regulator to precisely control the ink extrusion rate. Initially, when PDMS ink was injected into the pure

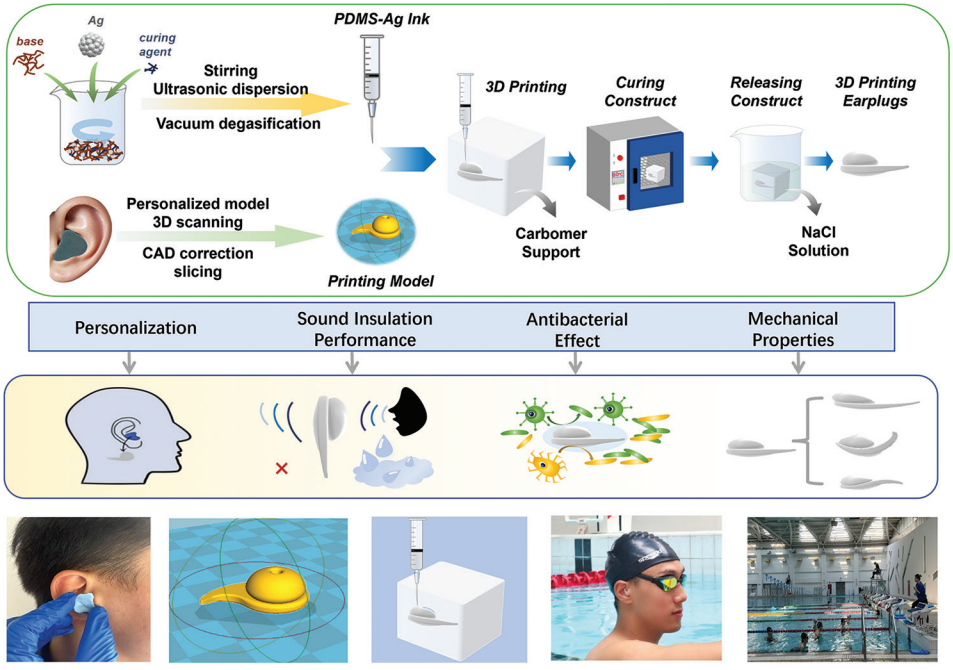

Figure 1. Synthesis and application of 3D-printed personalized earplugs
Abbreviations: CAD: Computer-aided design; PDMS: Polydimethylsiloxane

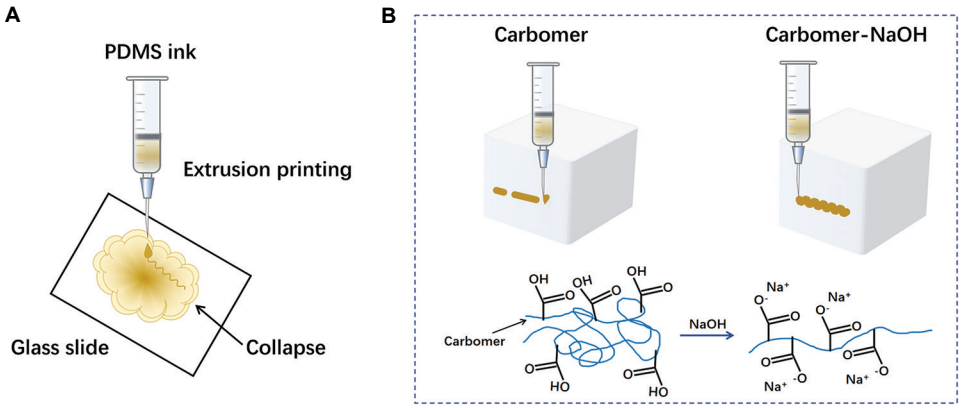

Figure 2. 3D printing with PDMS ink. (A) Polydimethylsiloxane (PDMS) ink in direct-write 3D printing. (B) PDMS ink in embedded-suspension 3D printing

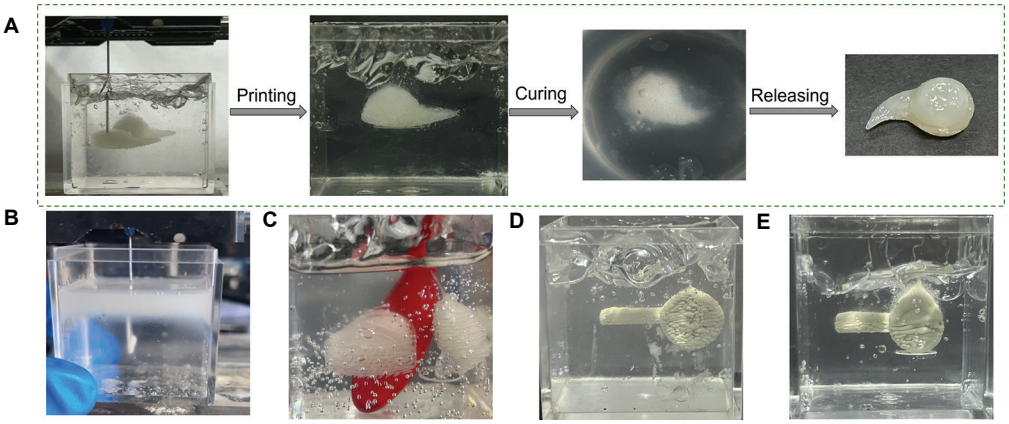

Figure 3. 3D printing process. (A) 3D-printed earplug process. (B) Extrusion in pure carbomer solution. (C) Curing of Polydimethylsiloxane (PDMS) in carbomer. (D and E) Print structure under different printing parameters: Printing with 80% fill density (D); and with other parameters unchanged, the upper layer: 0.15 mm layer height, and the lower layer: 0.20 mm layer height (E)

carbomer solution, it formed droplets near the needle tip and adhered to the needle surface (Figure 3B). After parameter adjustment, PDMS ink was successfully extruded as smooth, continuous, fine filaments within the carbomer matrix (Figure 3C), establishing the foundation for subsequent 3D structure printing. Figure 3D illustrates the outcome of suboptimal print parameters, specifically high layer height (>0.15 mm), low pressure (<40 psi), and low fill density (<80%), which lead to discontinuous ink deposition in the support structure. This results in an unstable printed form that fails to solidify properly and cannot be successfully removed. In contrast, the upper half of the features structure (Figure 3E) was printed with optimized parameters: layer height of 0.15 mm, 85% infill density, 25 mm/s print speed, and 50 psi extrusion pressure; these settings yielded dense, continuous filaments. However, when the layer height was reduced to 0.02 mm while keeping the other parameters constant, the resulting structure was sparse and poorly fused. These observations highlight how careful adjustment of printing parameters significantly enhances printing fidelity, improving both layer-to-layer bonding and structural integrity.

2.5. Curing and releasing the construct from the support medium

The construct, embedded within the carbomer support gel, was cured in a vacuum oven at 80°C for 24 h to ensure complete polymerization and formation of a stable elastomer. A flush solution was prepared by dissolving 2.338 g NaCl in 200 mL DW. After cooling, the construct was immersed in the flush solution for 20 min to remove the carbomer support. The remaining support material was easily removed through gentle rinsing, leaving behind the printed structure with high fidelity and minimal residual material.

2.6. Characterization

The rheological behaviors of the inks and the support medium were analyzed using a rotational rheometer

(HAAKE MARS 40, Thermo Scientific, Germany). Apparent viscosity was measured under shear rate sweep mode, with the shear rate increasing from 0.001 to 1000 s^{-1}. Stress sweep tests were performed at a constant frequency of 1 Hz to determine the storage modulus (G′) and loss modulus (G″) as functions of shear stress from 1 to 1000 Pa. All experiments were conducted at 25°C, within the instrument's Peltier temperature control range of −40–200°C. Triplicate measurements were performed for each ink formulation, and the initial data points were discarded to eliminate artifacts due to sample loading. The microscopic morphology and elemental distribution of the printed constructs were analyzed using scanning electron microscopy (SEM) (Sigma 300, ZEISS, Germany). The crystal structure and phase composition were measured using X-ray diffraction (XRD) (Ultima IV, Rigaku, Japan). The mechanical properties of PDMS-Ag composites were assessed using a universal mechanical testing machine (5982, INSTRON, United States of America [USA]). The acoustic insulation properties of the 3D-printed materials were determined using an impedance tube (Type-4206, Brüel & Kjær, Denmark), covering a frequency range from 500 to 6300 Hz. The contact angle was measured by contact angle analysis (DSA25, KRUSS, Germany). The antimicrobial effects of the materials were tested using the spread plate method, with *Staphylococcus aureus* as the test organism, incubated in contact with the materials.

2.7. Applications of the 3D-printed earplugs in swimming

2.7.1. Participants and sampling

Participants in this study were recruited from a junior swimming class and a swimming club at Tongji University, China. Baseline data were collected from 60 participants, including height, weight, swimming level, swimming frequency, ear health status, and physical fitness. A total of 60 young adults (34 males and 26 females) aged 18–24 years participated in this study. The mean age of males was 20.15 ± 1.28 years, while that of the females was 20.12 ± 1.24 years. From this pool, 32 participants were selected for a 7-week experimental study based on the following criteria: no prior swimming experience, good physical health, and a normal body mass index. This subgroup included 16 males (age: 20.3 ± 1.40 years; height: 1.76 ± 0.43 m; mass: 65.6 ± 6.4 kg) and 16 females (age: 20.3 ± 1.4 years; height: 1.65 ± 0.38 m; mass: 53.5 ± 4.9 kg), with all values presented as mean ± standard deviation.

Ethical approval for this study was obtained from the Ethics Committee of Tongji University (approval number: tjdxsr2025061). All procedures were conducted in accordance with the Declaration of Helsinki and relevant institutional guidelines.

2.7.2. Personalized earplug wearing experiment

A total of 60 participants were selected for the earplugs-wearing experiment. Following ear impression molding, 3D scanning, and 3D printing, each participant received a custom-fitted pair of earplugs tailored to the unique shape of their ear canal (Figure S1). All participants were instructed to wear the earplugs during a 1-h swimming session. Afterward, user satisfaction was assessed using a structured questionnaire based on a Likert scale. The questionnaire consisted of 8 questions, each rated on a 5-point scale: strongly agree (5), agree (4), neither agree nor disagree (3), disagree (2), and strongly disagree (1).

2.7.3. Seven-week swimming exercise with earplugs

A total of 32 screened participants were randomly divided into two gender-balanced groups: an earplug-wearing group and a non-wearing control group. Both groups completed a 1-h swimming session once a week over 7 weeks. During this period, the Likert scale questionnaire was administered to both groups in weeks 1, 4, and 7. The questionnaire was designed to assess the participants' physical and psychological safety experience.

2.7.4. Statistical analysis

Data collected from the questionnaires were analyzed using the Statistical Package for Social Sciences® Version 29 (IBM Corp., USA). Continuous variables were reported as mean ± standard deviation or as median with interquartile range (IQR; 25^{th}–75^{th} percentiles), depending on data distribution. The Mann-Whitney U test was used to analyze the differences between groups for continuous variables. The Friedman test was used to analyze the data differences at different time points. A two-tailed $p<0.05$ was considered statistically significant.

3. Results

3.1. Ink matrix and carbomer formulation

Inks containing 1% and 3% Ag exhibited good fluidity and uniform Ag distribution. However, at concentrations of 5% and above, the inks experienced rapid nanoparticle agglomeration, leading to heterogeneous Ag distribution and compromised print fidelity. PDMS could not be extruded smoothly in the pure carbomer solution, and excessive NaOH addition reduced the transparency of the carbomer solution and introduced numerous bubbles. To address this, the NaOH concentration was fixed at 0.01 M to ensure adequate neutralization of the carbomer and sufficient yield stress, while preventing viscosity loss and

bubble defects caused by excessive alkali. The viscous colloidal gel support medium was prepared by mixing 0.04 g NaOH and 1.2 g carbomer in 100 mL DW. The mixture was stirred for 2 h using a mechanical mixer and subsequently stored at 2°C for 48 h to reduce bubble formation. Through systematic optimization of the carbomer formulation, we mitigated critical challenges, including compromised interfacial adhesion and delamination propensity, arising from hydrophilic-hydrophobic repulsion between the ink matrix and the support structure.

3.2. Printing parameters

The printing parameters were carefully optimized to accommodate the specific requirements of the PDMS-Ag composite ink and the carbomer support gel system. Printing was conducted at a controlled temperature of 25°C. The syringe needles used had an inner diameter (d) and length (l) of 410 and 13 mm, respectively. The extrusion pressure was maintained within the range of 40–60 psi, and the print speed was set at 25 mm/s to ensure smooth and consistent ink flow without causing excessive shear stress on the ink. Based on preliminary experiments and ink rheological behavior, a layer height of 0.15 mm and an infill density of 85% were adopted to provide structural support while minimizing material usage and print time.

3.3. Rheological behavior

The viscosity of the PDMS ink displayed three distinct regimens across the shear rate range (Figure 4A): an initial shear-thickening region characterized by increasing viscosity with shear rate, followed by a Newtonian plateau where viscosity remained relatively constant, and a shear-thinning region in which viscosity decreased with increasing shear rate. In contrast, the PDMS-Ag inks exhibited shear-thinning properties at the initial stage, transitioning to Newtonian fluid and later displaying shear-thinning properties similar to the pure PDMS ink. Notably, all inks used in this study demonstrated low static viscosities (<60 Pa·s).

All inks exhibited a loss modulus (G″) greater than the storage modulus (G′) (Figure 4B). Overall, the incorporation of Ag particles increased the viscosity of the system compared to pure PDMS inks. However, when the amount of Ag particles was low (*i.e.*, PDMS/Ag-1%), the interparticle interactions were weak, resulting in minimal reinforcement of the matrix. In addition, the incorporation

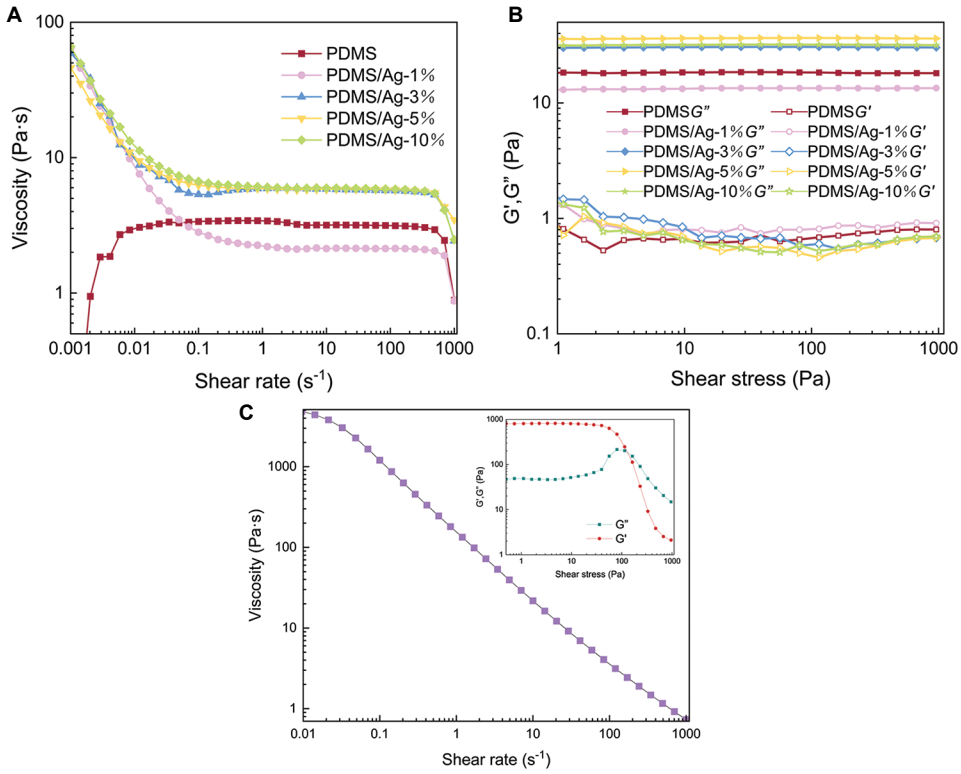

Figure 4. Rheological behaviors of the inks. (A) Apparent viscosity as a function of shear rate. (B) Storage (G′) and loss (G″) moduli as a function of shear stress. (C) Rheological behavior of the carbomer solution
Abbreviation: PDMS: Polydimethylsiloxane

of Ag particles may have disrupted the original molecular chain mobility of the matrix, leading to a slight decrease in both modulus and viscosity. The differences in viscosity, G′, and G″ of several other inks were relatively minor. Nevertheless, during the printing process, PDMS/Ag-5% and PDMS/Ag-10% exhibited poor stability due to the high concentration of Ag particles, which led to agglomeration, nozzle clogging, and the formation of intermittent filaments. Considering the overall rheological behavior and print performance, PDMS/Ag-3% was selected as the optimal ink formulation for 3D printing earplugs.

Carbomer solutions (Figure 4C) exhibited shear-thinning properties and rapid self-healing capabilities. Localized fluidization occurred when a needle applied stress while tracing across the supporting microgel, which rapidly returned to its original state when the needle was withdrawn. The viscosity of the carbomer support gel was modulated by adjusting its pH. We conducted several experiments to determine the optimal NaOH concentration, ensuring that the ink can spread effectively within the gel matrix for deposition, adhesion, and curing.

3.4. 3D-printed construct

3.4.1. Microstructural analysis

The SEM images of the samples (Figure 5A) indicated that the Ag nanoparticles have relatively smooth surfaces and are dispersed within the PDMS matrix as small-sized nanoparticles. The XRD spectra of Ag, PDMS-Ag, and PDMS are presented in Figure 5B. Ag exhibited characteristic diffraction peaks, suggesting that Ag has a face-centered cubic structure. Meanwhile, PDMS exhibited no distinct peaks, confirming it as a non-crystalline material.

3.4.2. Mechanical properties

Three independent samples (n = 3) were tested for tensile fracture and cyclic loading. To enhance clarity, representative curves from one sample are presented in Figure 6. The construct was stretched to fracture at a fixed rate of 10 mm/min, and the composites displayed approximately linear elastic behavior, with a maximum tensile strength of 0.52 ± 0.06 MPa and an elongation at break of 62.93 ± 3.8% (Figure 6A). The material exhibited good mechanical stability even after multiple stretch and compression cycles. The Mullins effect is most pronounced in the first loading cycle, with progressive stabilization after 3–5 cycles.[43] Accordingly, five consecutive loading-unloading cycles were applied to each PDMS-Ag sample to ensure that the material had reached a repeatable steady state. While the material exhibited plastic deformation in the first cycle, subsequent cycles demonstrated good elastic recovery (Figure 6B and C), indicating that the material possessed both elasticity and plasticity, enabling partial recovery of its original state, though some permanent deformation remains.

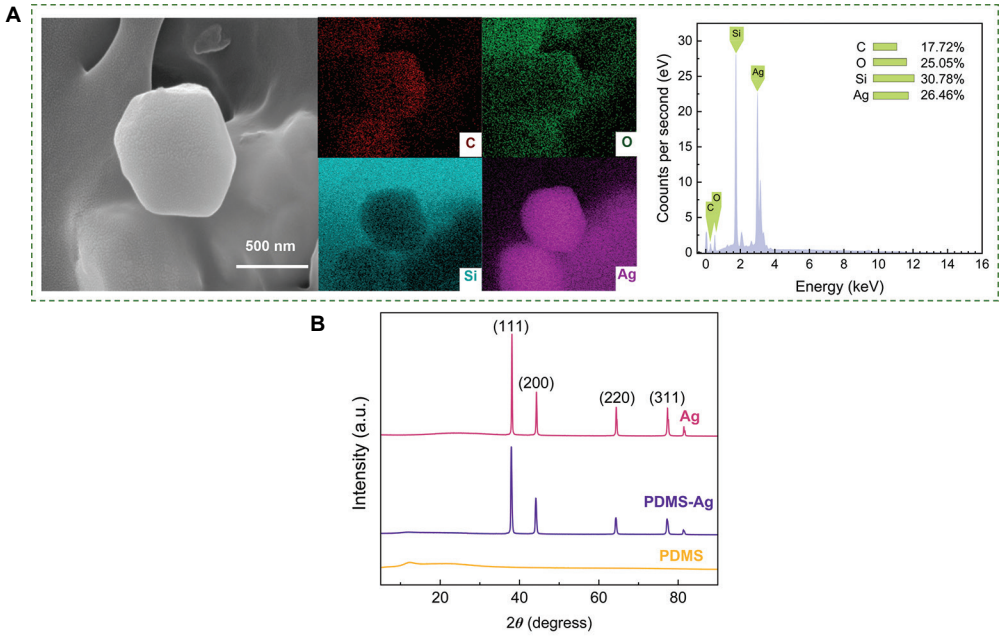

Figure 5. Microscopic morphology of the sample. (A) SEM images and EDS of the sample. (B) XRD patterns for Ag, PDMS-Ag, and PDMS. Scale bar: 500 nm (A)
Abbreviations: EDS: Energy dispersive spectroscopy; PDMS: Polydimethylsiloxane; SEM: Scanning electron microscope; XRD: X-ray diffraction

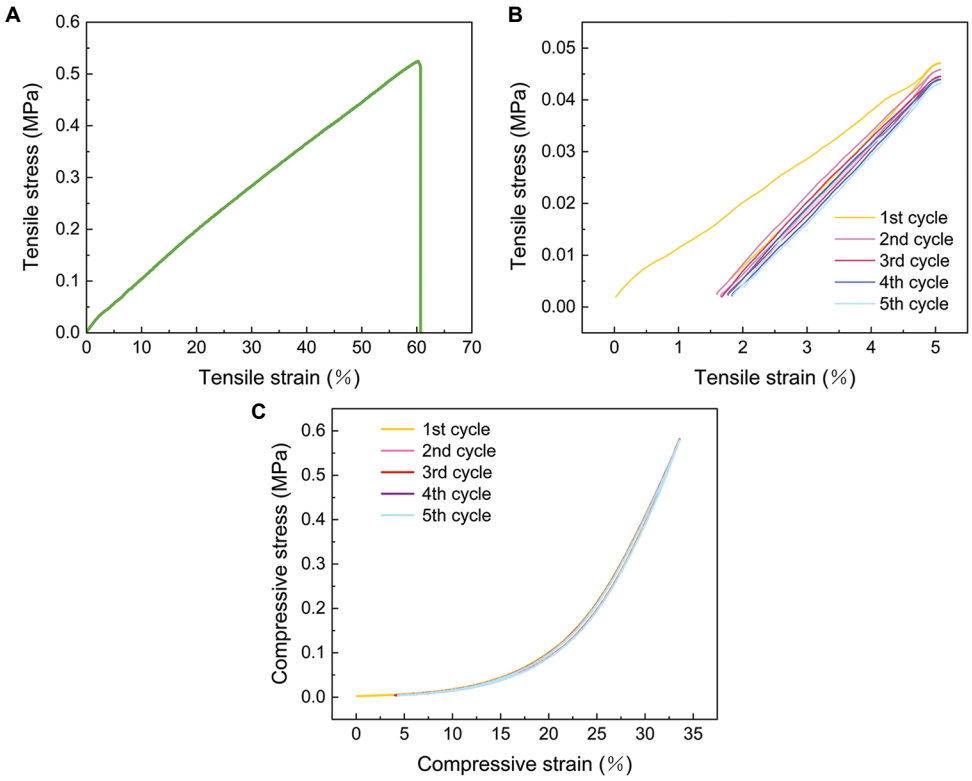

Figure 6. Mechanical properties of composites. (A) Tensile stress-strain of composites. (B) Tensile stress-strain curves of composites. (C) Compressive stress-strain curves of composites

3.4.3. Acoustic properties

Three independent PDMS-Ag earplugs were fabricated and tested. Figure 7 presents a representative sound insulation curve. The acoustic performance of PDMS-Ag composite samples (8 mm thickness; 29 mm diameter) was evaluated at a frequency range of 500–6300 Hz (Figure 7). The earplugs demonstrated excellent sound isolation at 1000–6300 Hz, achieving over 30 dB of sound insulation. Notably, at 4000 Hz, sound insulation ranged from 35.03 to 37.58 dB. Although the earplugs were less effective at blocking out low-frequency noises—such as human speech, which typically ranges from 85 and 255 Hz[44]—they outperformed most commercial swimming and sleeping earplugs. For comparison, typical silicone putty plugs offer ≈ 22 dB, wax plugs ≈ 25 dB, and polyurethane (PU)-foam plugs 29–32 dB. Compared to more airtight earplugs, the 3D-printed earplugs increase the swimmer's awareness of external warning sounds, further enhancing swimming safety.

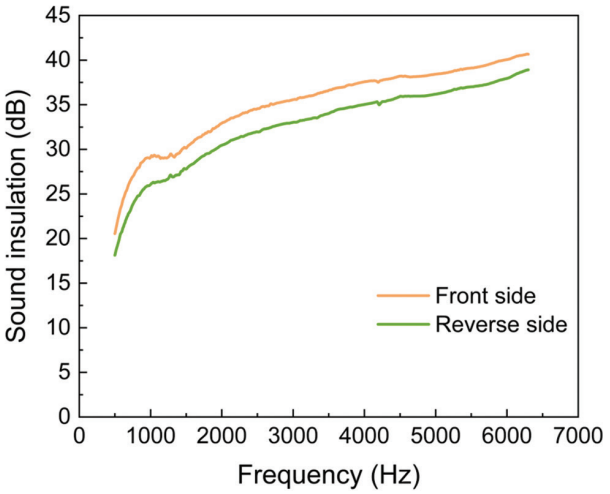

Figure 7. Sound insulation properties of polydimethylsiloxane-Ag composites. Front side refers to the upper surface; reverse side refers to the lower surface

The PDMS-Ag composite offers advantages in terms of mid- to high-frequency sound insulation and thickness efficiency, making it suitable for applications that require lightweight, flexible materials with wide-frequency noise reduction capabilities. These features may be attributed to the high impedance of Ag, which enhances interface reflection and inhibits sound wave transmission, thereby improving the sound insulation performance of PDMS-Ag composites. Table 1 presents the sound insulation values for various materials with different thicknesses reported in

Table 1. Sound insulation effects of different materials

Material	Sample thickness (mm)	Sound frequency (Hz)	Sound insulation capacity (dB)	References
PDMS-Ag	8	500–6300	−26–−38	This work
PDMS	5.08	1000	−29	45
PDMS-HGMs	5.08	1000	−26	45
Composite sound insulation structure	>50	1000	−35.1	46
Mineral wool panel	23	500–8000	−24–−30	47
Polyurethane foam panel	23	500–8000	−11–−30	47
	48	500–8000	−11–−32	48

Abbreviations: HGMs: Hollow glass microspheres; PDMS: Polydimethylsiloxane.

other studies. Although PDMS/HGM composite materials reduce thermal conductivity, they exhibit decreased sound insulation performance. In contrast, PU rubber focuses on low-frequency vibration reduction, while elastomer foam requires greater thickness to achieve broadband noise reduction.

3.4.4. Contact angle

The contact angle was measured at three distinct spots on a representative sample and averaged. As displayed in Figure 8, the droplet is fully absorbed by the material even after 100 s, and a higher receding contact angle of 95.64° was observed. In the context of swimming—where earplugs are used intermittently and are not exposed to water for prolonged periods—these properties indicate that the earplugs can maintain effective water resistance during typical swimming activities. In addition, the water droplets are less likely to stick to the surface, minimizing the scattering and absorption of sound waves, thereby allowing sound to be transmitted more clearly into the ear canal.

3.5. Antimicrobial performance of earplugs

The PDMS/Ag-1% formulation displayed no statistically significant antibacterial efficacy compared to the control group. In addition, further increasing the Ag content may increase material costs without significantly enhancing antibacterial efficacy. Therefore, the PDMS/Ag-3% formulation offered the best balance among antibacterial efficacy, printability, and cost effectiveness, and was selected as the representative composition. For each material type, three separate batches were produced, obtaining a total of nine samples. Each sample was co-cultured in LB broth, spread on three plates, and the average colony count was calculated (Figure 9A). Error bars in Figure 9B represent the standard deviation among the three averaged values per group. PDMS alone displayed no antibacterial activity and, in fact, slightly promoted bacterial growth compared to the LB blank control. Between pure PDMS and Ag, a highly significant difference was observed (***$p<0.001$), highlighting that pure Ag exhibits strong antibacterial effects. In repeated experiments, the colony-forming unit count for Ag was zero, with no significant variation across tests. However, the antibacterial effect of Ag was superior to that of PDMS-Ag, likely due to the encapsulation of Ag within PDMS reducing its antibacterial effect (Figure 9B). In summary, the PDMS/Ag-3% composite exhibited effective antimicrobial properties and meets the requirements for use in swimming earplugs.

3.6. User feedback on earplug wearability

Survey results (Figure 10) from 60 participants indicate that the 3D-printed swimming earplugs received high ratings across multiple dimensions, with average scores exceeding 4.0 for all questions. The mean score for satisfaction with appearance was 4.2, indicating that most respondents were satisfied with the earplugs' styling. High scores for non-allergic reaction (4.8) and comfort (4.1) emphasize the biocompatibility and safety of the material. Functional performance ratings focused on waterproofness (4.2) and acoustic isolation (4.0) further highlight the earplugs' effectiveness. The average score for no interference with swimming (4.0) and ear canal fit (4.1) highlights the benefits of personalized design. Notably, willingness to continue using the earplugs in the future scored 4.0, demonstrating a high level of user acceptance. Overall, these results validate that the 3D-printed swimming earplugs are a promising alternative to traditional earplugs, offering enhanced comfort and customization.

3.7. Effect of prolonged earplug use on swimmers over 7 weeks

The data analysis of 32 beginner swimmers (Table S1) revealed that the frequency of water entering the ear canal decreased in the group wearing earplugs compared to the non-wearing group starting from the 1st week. Significant differences were observed in weeks 4 and 7, indicating that the 3D-printed earplugs effectively reduce ear water ingress. In terms of underwater hearing, both groups had similar scores in recognizing external safety warning sounds, suggesting that the earplugs provide moderate isolation of the human voice and maintain good safety during swimming. In terms of concern about ear health, the wearing group exhibited a significant decrease after 7 weeks compared to the non-wearing group. In addition, the wearing group demonstrated better swimming

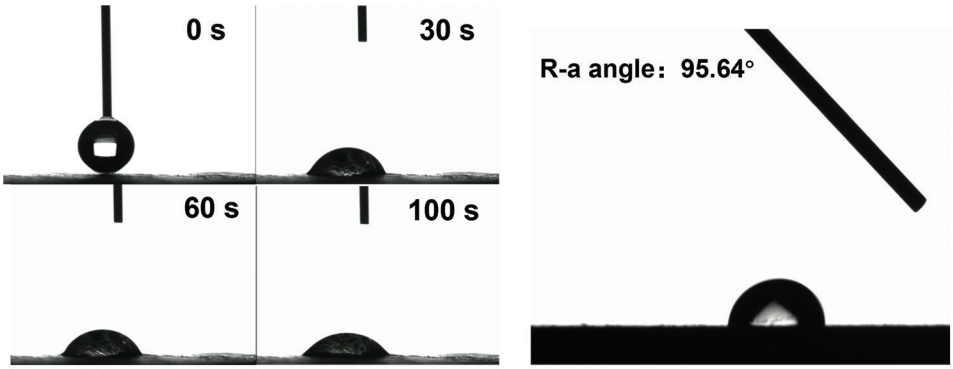

Figure 8. Water contact angle measurement of the construct
Abbreviation: R-a: Receding contact angle

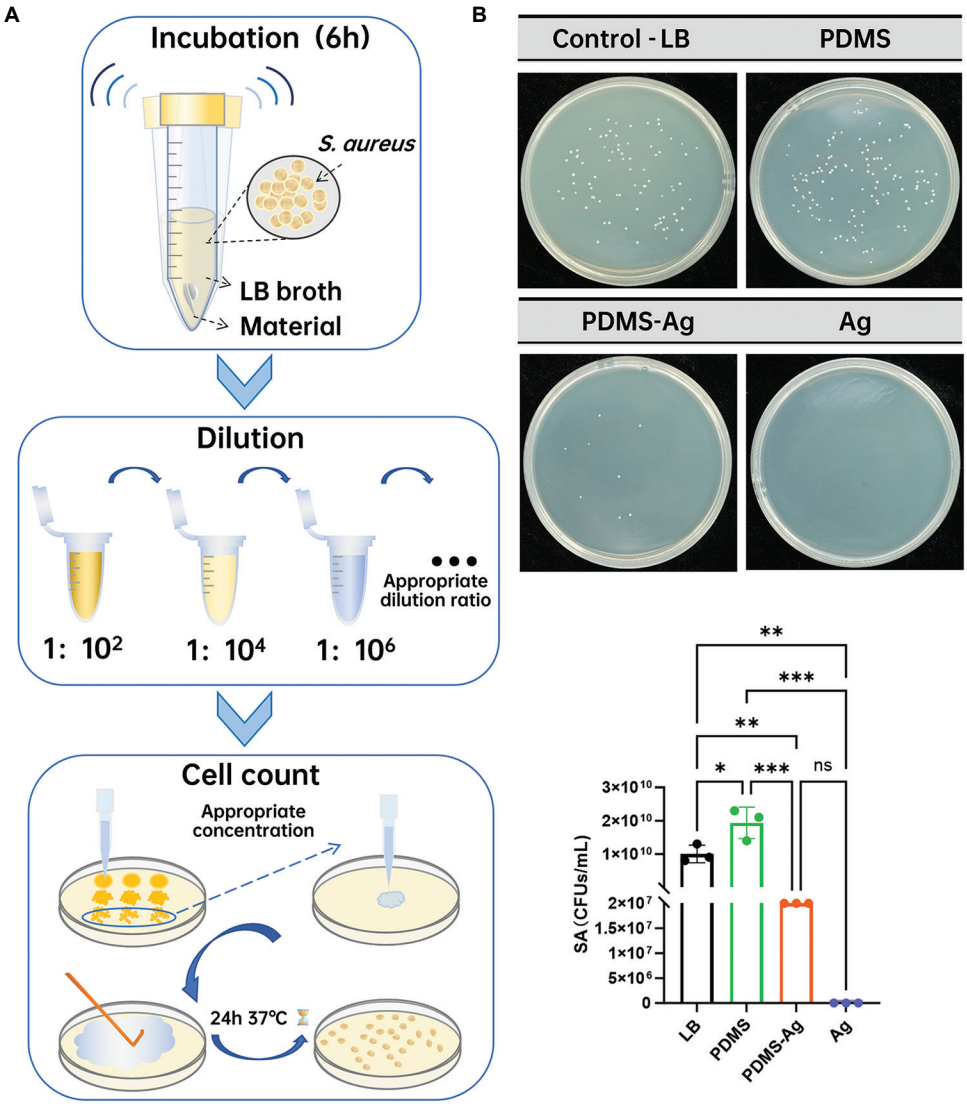

Figure 9. Antibacterial experiment on swimming earplugs. (A) Schematic workflow of the antibacterial activity test. (B) Antibacterial effects of different materials on *Staphylococcus aureus*; *$p<0.05$, **$p<0.01$, ***$p<0.001$, ns: $p>0.05$
Abbreviations: PDMS: Polydimethylsiloxane; SA: *Staphylococcus aureus*; CFU: Colony-forming Unit; LB: Luria-Bertani

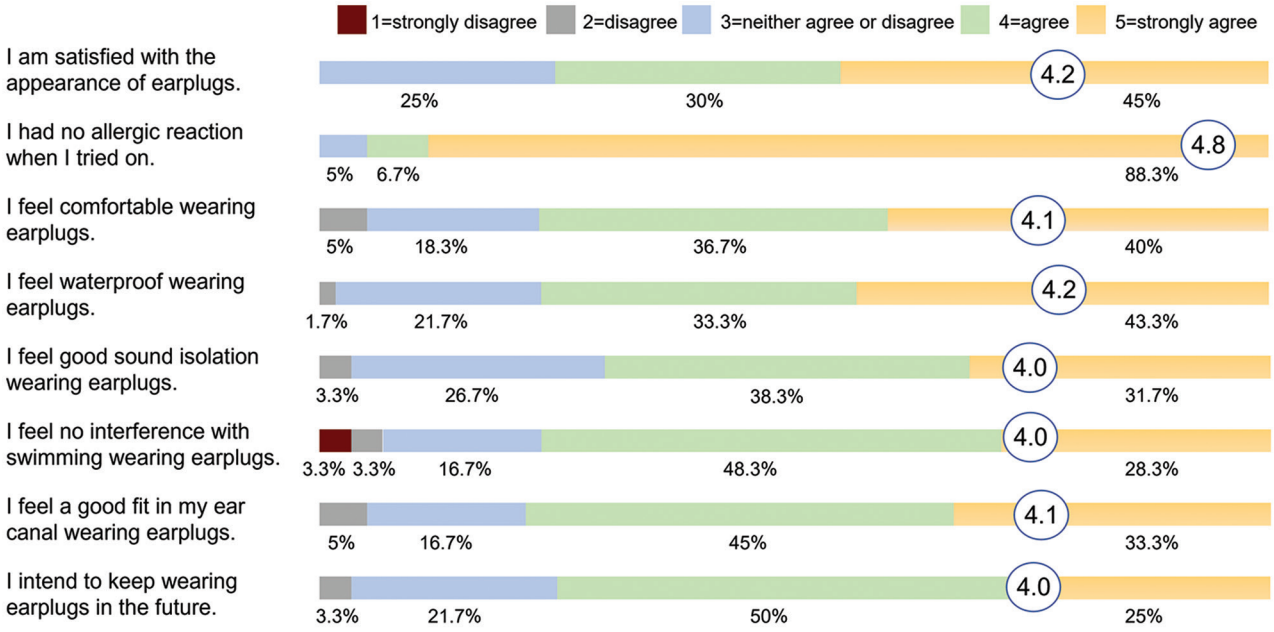

Figure 10. Likert scale for user feedback on earplug wearability (n = 60)

concentration than the non-wearing group during the 1st week of use.

4. Discussion

4.1. Superior performance of 3D-printed earplugs

The SEM, EDS, and XRD results collectively confirm that the PDMS-Ag composites were successfully fabricated, with Ag nanoparticles evenly distributed within the PDMS matrix. The overlapping curves (Figure 6B and C) after multiple cycles demonstrate good durability. For swimming earplugs, the resilience and durability of the material allow it to maintain a secure seal and comfort during repeated use while withstanding underwater pressure changes. Compared to soft silicone earplugs, these 3D-printed earplugs leave almost no debris in the ear canal after swimming. These earplugs performed well in insulating against medium- and high-frequency sounds but are less effective at blocking out low-frequency noises. In swimming environments, sounds such as splashing and underwater bubbles primarily occur above 1000 Hz, while human speech ranges between 85 and 255 Hz. These earplugs also effectively isolate underwater noise, providing swimmers with a comfortable swimming environment. Thus, the 3D-printed earplugs can increase the swimmer's awareness of external warning sounds, further enhancing swimming safety. In addition, the water droplets are less likely to stick to the surface of the earplugs, minimizing the scattering and absorption of sound waves to allow clearer sound transmission into the ear canal. Most literature addresses acoustic insulation and antimicrobial activity separately; however, our PDMS-Ag composite provides both effective sound insulation and broad-spectrum antibacterial effects, demonstrating a dual-function design ideal for swimming earplugs. Overall, users benefit from enhanced auditory clarity, which is especially important for underwater activities like swimming, where clear sound transmission is crucial for safety and communication.

4.2. Health promotion for swimmers wearing 3D-printed earplugs

The results for the non-wearing group revealed several improvements over the swimming period. Water comfort during swimming increased notably by weeks 4 and 7 compared to the initial week, indicating a growing adaptation to swimming activities. There was also a marked reduction in the incidence of water entering the ear canal by week 7, demonstrating an improvement in preventing water ingress over time. Underwater hearing, particularly in recognizing external safety warning sounds, significantly improved by week 7. Concerns regarding ear canal health decreased significantly at weeks 4 and 7, suggesting reduced anxiety about ear-related issues with continued swimming. This may be attributed to beginners' increasing adaptation to water exposure, leading to less frequent water ingress. Likewise, swimmers' anxiety levels decreased significantly by week 7, indicating greater overall comfort and confidence in the water. Furthermore, participants demonstrated improved concentration during swimming, with higher focus levels at weeks 4 and 7

compared to week 1, suggesting enhanced engagement and immersion as the swimming experience accumulated.

Over the 7-week experiment, the wearing group demonstrated significant improvements in water comfort and reduced ear canal water ingress (Table S2). Specifically, the frequency of water entering the ear canal decreased significantly during swimming. Concerns about ear canal health decreased significantly at weeks 4 and 7 compared to the initial week. Swimming anxiety also reduced over time, suggesting that wearing earplugs has a positive psychological impact on beginner swimmers. While overall swimming concentration remained relatively stable in the wearing group, participants wearing 3D-printed earplugs reported significantly higher concentration levels in the 1st week compared to the non-wearing group. These results highlight the positive impact of 3D-printed earplugs on swimmer comfort, ear protection, and psychological well-being over time.

4.3. Promotion of earplugs for swimming

Wearing personalized antibacterial earplugs can enhance public awareness of self-protection and increase enjoyment during aquatic activities. Through the 7-week experiment, participants in the wearing group demonstrated improved swimming safety awareness and developed long-term, effective health management habits. The promotion of swimming earplugs has significantly aided the public in learning the correct use of earplugs and other sports equipment. This has effectively prevented water ingress and ear infections, fostered awareness of safety and health, optimized swimming habits, and strengthened ear health protection. The promotion of earplugs also plays a valuable role in health monitoring and disease prevention. In future research, we envisage implanting smart sensors into 3D-printed structures to monitor vital signs, such as heart rate, ear health, and motion status.[48,49] By tracking physiological parameters, these devices can provide early warnings of potential health issues, such as infections and other illnesses, enabling timely medical intervention. Traditional silicone earplugs rely on injection molding,[16] which has limitations in terms of customizing the geometry of the individual ear canals. In contrast, we used embedded-suspension 3D printing technology to produce personalized earplugs that fit the user's ear canal without the need for molds. This innovation not only enhances personal health management but also contributes to safer and healthier swimming activities for the public in the future.

5. Conclusion

This study demonstrates the successful application of embedded 3D printing technology in developing personalized antimicrobial earplugs for swimming. The PDMS-Ag composite exhibited excellent rheological properties, inhibition rate (99.89%), and mechanical durability (elongation at break of 62.93%), enabling precise customization with high accuracy. The earplugs effectively block water ingress (water contact angle: 95.64°) while maintaining sound transmission in the 600–1000 Hz range, ensuring user safety and environmental awareness. Overall, this study highlights the feasibility and advantages of 3D printing technology for producing functional swimming accessories and offers innovative solutions for enhancing ear health protection in aquatic activities.

Acknowledgments

The authors would like to thank the Shanghai Key Laboratory of Special Artificial Microstructure Materials and Technology for providing the experimental conditions, as well as the students of the swimming class at Tongji University for their cooperation and support. The authors would like to acknowledge financial support from the Open Project of Anhui Engineering Research Center for Neural Regeneration Technology and Medical New Materials (AHNR2024Z002).

Funding

This work was supported in part by the Open Project of Anhui Engineering Research Center for Neural Regeneration Technology and Medical New Materials (AHNR2024Z002).

Conflict of interest

The authors declare that they have no competing interests.

Author contributions

Conceptualization: Lili Qin, Xinran Qian, Junye Ren
Data curation: Xinran Qian, Dengyun Xu, Junye Ren, Jianming Yang
Formal analysis: Xinran Qian, Jianming Yang, Junye Ren, Jialu Lu
Funding acquisition: Lili Qin
Investigation: Xinran Qian, Dengyun Xu, Jianming Yang, Junye Ren, Jialu Lu
Methodology: Wenrui Wang, Jianming Yang, Jialu Lu
Project administration: Wenjia Zhang, Tianfeng Lu
Supervision: Wenjia Zhang, Tianfeng Lu, Lili Qin
Writing–original draft: Lili Qin, Xinran Qian, Dengyun Xu
Writing–review & editing: Lili Qin, Ai Du, Wenrui Wang

Ethics approval and consent to participate

The study was conducted in accordance with the Declaration of Helsinki and approved by the Ethics Committee of

Tongji University (approval no. tjdxsr2025061; March 31, 2025).

Consent for publication

All participants agreed to participate in this study and provided verbal consent for the use of their data and images in publications.

Availability of data

All data generated or analyzed in this study are included in this article. Further inquiries can be directed to the corresponding authors.

References

1. DeFlorio-Barker S, Wing C, Jones RM, Dorevitch S. Estimate of incidence and cost of recreational waterborne illness on United States surface waters. *Environ Health.* 2018;17(1):3.

   doi: 10.1186/s12940-017-0347-9

2. Lipska J, Hamerska J, Hamerska L, *et al*. Swimmer's ear: Prevention, diagnosis, treatment, and management strategies for athletes. *Qual Sport.* 2024;18:53330.

   doi: 10.12775/QS.2024.18.53330

3. Perez-Stable EJ, Sayre MH. Reducing health disparities to promote health equity through policy research. *Ethn Dis*. 2019;29(S2):321-322.

   doi: 10.18865/ed.29.S2.321

4. Caramia G, Serafini V, Loggi A. The swimmer's otitis. An up to date and prevention options. *Pediatr Med Chir.* 2013;35(3):177-182.

   doi: 10.4081/pmc.2013.38

5. Strauss MB, Dierker RL. Otitis externa associated with aquatic activities (swimmer's ear). *Clin Dermatol.* 1987;5(3):103-111.

   doi: 10.1016/S0738-081X(87)80016-0

6. Beers SL, Abramo TJ. Otitis externa review. *Pediatr Emerg Care.* 2004;20(4):250-256.

   doi: 10.1097/01.pec.0000121246.99242.f5

7. Wang MC, Liu CY, Shiao AS, Wang T. Ear problems in swimmers. *J Chin Med Assoc.* 2005;68(7):347-352.

   doi: 10.1016/S1726-4901(09)70174-1

8. Kanagamuthu P, Dhanasekaran B, Karthika SR, Raghavan VK. To determine the pH of external auditory canal in otitis externa: A prospective observational study in a tertiary health care centre. *Indian J Otolaryngol Head Neck Surg.* 2023;75(1):502-506.

   doi: 10.1007/s12070-023-03591-x

9. Ellis J, De La Lis A, Rosen E, Simpson MTW, Beyea MM, Beyea JA. Approach to otitis externa. *Can Fam Physician.* 70(6):617-623.

   doi: 10.46747/cfp.7010617

10. World Health Organization. *Precision Public Health Strategy*. Brazzaville: WHO African Region; 2025. p. 2024-2030.

11. Wade TJ, Sams EA, Beach MJ, Collier SA, Dufour AP. The incidence and health burden of earaches attributable to recreational swimming in natural waters: A prospective cohort study. *Environ Health.* 2013;12(1):67.

    doi: 10.1186/1476-069X-12-67

12. Kumpel E, Delaire C, Peletz R, *et al*. Measuring the impacts of water safety plans in the Asia-Pacific region. *Int J Environ Res Public Health.* 2018,15(6):1223.

    doi: 10.3390/ijerph15061223

13. Bhatia R, Chauhan A, Rana M, Kaur K, Pradhan P, Singh M. Economic burden of otitis media globally and an overview of the current scenario to alleviate the disease burden: A systematic review. *Int Arch Otorhinolaryngol.* 2024;28(3):e552-e558.

    doi: 10.1055/s-0043-1767802

14. Graydon K, Waterworth C, Miller H, Gunasekera H. Global burden of hearing impairment and ear disease. *J Laryngol Otol.* 2019;133(1):18-25.

    doi: 10.1017/S0022215118001275

15. Mahboubi H, Lee A, Kiumehr S, Zardouz S, Shahriari S, Djalilian HR. Efficacy of commercial earplugs in preventing water intrusion during swimming. *Otolaryngol Head Neck Surg.* 2013;148(3):415-419.

    doi: 10.1177/0194599812471798

16. Chisholm EJ, Kuchai R, McPartlin D. An objective evaluation of the waterproofing qualities, ease of insertion and comfort of commonly available earplugs. *Clin Otolaryngol Allied Sci.* 2004;29(2):128-132.

    doi: 10.1111/j.1365-2273.2004.00795.x

17. Yang J, Lu J, Han D, Zhou B, Du A. Direct ink writing of aerogels: Fundamentals, strategies, applications, and perspectives. *Prog Mater Sci*. 2025;152:101462.

    doi: 10.1016/j.pmatsci.2025.101462

18. Yang J, Lu J, Xi S, *et al*. Direct 3D print polyimide aerogels for synergy management of thermal insulation, gas permeability and light absorption. *J Mater Chem A Mater Energy Sustain*. 2023;11(39):13.

    doi: 10.1039/D3TA02928J

19. Han D, Yang J, Wang H, *et al*. 3D-printed hybrid zirconia hydrogels for ultrahigh-efficiency phosphate adsorption. *Adv Compos Hybrid Mater*. 2024;7(4):1-14.

    doi: 10.1007/s42114-024-00941-3

20. Saadi M, Maguire A, Pottackal NT, *et al*. Direct ink writing: A 3D printing technology for diverse materials. *Adv Mater.*

2022;34(3):e2108855.

doi: 10.1002/adma.202108855

21. Walker DA, Hedrick JL, Mirkin CA. Rapid, large-volume, thermally controlled 3D printing using a mobile liquid interface. *Science.* 2019;366(6463):360-364.

doi: 10.1126/science.aax1562

22. Wu Q, Song K, Zhang D, *et al*. Embedded extrusion printing in yield-stress-fluid baths. *Matter.* 2022;5(11):3775-3806.

doi: 10.1016/j.matt.2022.09.003

23. Yang J, Qian X, Yang J, *et al*. Additive-free aerogel 3D printing using ultra-low storage modulus inks. *Adv Funct Mater.* 2024:2423739.

doi: 10.1002/adfm.202423739

24. McCormack A, Highley CB, Leslie NR, Melchels FPW. 3D printing in suspension baths: Keeping the promises of bioprinting afloat. *Trends Biotechnol.* 2020;38(6):584-593.

doi: 10.1016/j.tibtech.2019.12.020

25. Lee A, Hudson AR, Shiwarski DJ, *et al*. 3D bioprinting of collagen to rebuild components of the human heart. *Science.* 2019;365(6452):482-487.

doi: 10.1126/science.aav9051

26. Croom BP, Abbott A, Kemp JW, *et al*. Mechanics of nozzle clogging during direct ink writing of fiber-reinforced composites. *Addit Manuf.* 2021;37:101701.

doi: 10.1016/j.addma.2020.101701

27. Altıparmak SC, Yardley VA, Shi Z, Lin J. Extrusion-based additive manufacturing technologies: State of the art and future perspectives. *J Manuf Process.* 2022;83:607-636.

doi: 10.1016/j.jmapro.2022.09.032

28. Billiet T, Gevaert E, De Schryver T, Cornelissen M, Dubruel P. The 3D printing of gelatin methacrylamide cell-laden tissue-engineered constructs with high cell viability. *Biomaterials.* 2014;35(1):49-62.

doi: 10.1016/j.biomaterials.2013.09.078

29. Nathan A, Ahnood A, Cole M, *et al*. Flexible electronics: The next ubiquitous platform. *Proc IEEE.* 2012;100(SI):1486-1517.

doi: 10.1109/JPROC.2012.2190168

30. Gondil VS, Ashcraft M, Ghalei S, *et al*. Anti-infective bacteriophage immobilized nitric oxide-releasing surface for prevention of thrombosis and device-associated infections. *ACS Appl Bio Mater.* 2025;8(3):1362-1376.

doi: 10.1021/acsabm.4c01638

31. Wolf MP, Salieb-Beugelaar GB, Hunziker P. PDMS with designer functionalities-properties, modifications strategies, and applications. *Prog Polym Sci.* 2018;83:97-134.

doi: 10.1016/j.progpolymsci.2018.06.001

32. Duraivel S, Laurent D, Rajon DA, *et al*. A silicone-based support material eliminates interfacial instabilities in 3D silicone printing. *Science.* 2023;379(6638):1248-1252.

doi: 10.1126/science.ade4441

33. O'Bryan CS, Bhattacharjee T, Hart S, *et al*. Self-assembled micro-organogels for 3D printing silicone structures. *Sci Adv.* 2017;3(5):e1602800.

doi: 10.1126/sciadv.1602800

34. Hinton TJ, Hudson A, Pusch K, Lee A, Feinberg AW. 3D printing PDMS elastomer in a hydrophilic support bath via freeform reversible embedding. *ACS Biomater Sci Eng.* 2016;2(10):1781-1786.

doi: 10.1021/acsbiomaterials.6b00170

35. Fenny Indah S, Desy N, Dina F. Overview: Application of Carbopol 940 in Gel. In: *Proceedings of the International Conference on Health and Medical Sciences (AHMS 2020)*. Netherlands: Atlantis Press; 2021. p. 80-4.

36. Prasad SR, Teli SB, Ghosh J, *et al*. A review on bio-inspired synthesis of silver nanoparticles: Their antimicrobial efficacy and toxicity. *Eng Sci*. 2021;16:90-128.

doi: 10.30919/es8d479

37. Bhattacharjee T, Zehnder SM, Rowe KG, *et al*. Writing in the granular gel medium. *Sci Adv.* 2015;1(8):e1500655.

doi: 10.1126/sciadv.1500655

38. Mo F, Zhou Q, He Y. Nano-Ag: Environmental applications and perspectives. *Sci Total Environ*. 2022;829:154644.

doi: 10.1016/j.scitotenv.2022.154644

39. Yin IX, Zhang J, Zhao IS, Mei ML, Li Q, Chu CH. The antibacterial mechanism of silver nanoparticles and its application in dentistry. *Int J Nanomedicine.* 2020;15:2555-2562.

doi: 10.2147/IJN.S246764

40. Xie Y, Zhou B, Du A. Slow-sound propagation in aerogel-inspired hybrid structure with backbone and dangling branch. *Adv Compos Hybrid Mater*. 2021;4(8):248-256.

doi: 10.1007/s42114-021-00234-z

41. Borah B, Dash RK. Improved dielectric properties of rGO/PDMS composites by incorporation of Ag nanoparticles. *J Mater Sci Mater Electron*. 2022;33(15):12334-12350.

doi: 10.1007/s10854-022-08191-z

42. Centers for Disease Control and Prevention. *Preventing Swimming-Related Illnesses*; 2025. Available from: https://www.cdc.gov/healthy-swimming/prevention/index.html [Last accessed on 2024 Jul [20].

43. Mullins L. Softening of rubber by deformation. *Rubber Chem Technol*. 2012;42(1):339-362.

doi: 10.5254/1.3539210

44. Keating P, Kuo G. Comparison of speaking fundamental

frequency in English and Mandarin. *J Acoust Soc Am*. 2012;132(2):1050.

doi: 10.1121/1.4730893

45. Vlassov S, Oras S, Timusk M, *et al*. Thermal, mechanical, and acoustic properties of polydimethylsiloxane filled with hollow glass microspheres. *Materials (Basel)*. 2022;15(5):1652.

doi: 10.3390/ma15051652

46. Xia Z, Wu X, Yang Q, *et al*. Analysis and test of sound insulation performance of multilayer structures. *Noise Vibr Control*. 2023;43:129-34.

doi: 10.3969/j.issn.1006-1355.2023.06.020

47. Vortice. *Air Handling Unit Catalog*. Vortice. Available from: https://www.vortice.com/media2/export/inglese/doc_pubblicita_catalog_air_handling_unit_122215.pdf [Last accessed on 2020 Jun 27].

48. Xu Y, De la Paz E, Paul A, *et al*. In-ear integrated sensor array for the continuous monitoring of brain activity and of lactate in sweat. *Nat Biomed Eng*. 2023;7(10):1307-1320.

doi: 10.1038/s41551-023-01095-1

49. Burgos CP, Gärtner L, Ballester MAG, *et al*. In-ear accelerometer-based sensor for gait classification. *IEEE Sens J*. 2020;20(21):12895-12902.

doi: 10.1109/jsen.2020.3002589

ACCSCIENCE PUBLISHING

Materials Science in Additive Manufacturing

ORIGINAL RESEARCH ARTICLE

Optimizing 3D printing parameters for lightweight and high-strength unmanned aerial vehicle parts

Saleem Ramadan[1†*] and Mohammad Abu-Shams[2†]

[1]Department of Industrial Engineering, School of Engineering Technology, Al Hussein Technical University, Amman, Jordan

[2]Department of Industrial Engineering, School of Applied Technical Sciences, German Jordanian University, Amman, Jordan

Abstract

Additive manufacturing, particularly fused deposition modelling (FDM), has gained increasing attention in aerospace applications due to its capability to produce complex geometries with reduced material usage, making it a promising approach for manufacturing lightweight yet strong unmanned aerial vehicle (UAV) parts. In this study, an integrated framework was developed to optimize FDM parameters for producing UAV parts that are both lightweight and high in strength. A response surface methodology was used to analyze the effects of infill percentage, layer height, number of walls, and build plate temperature on the mass and tensile strength of the printed parts. Two regression models with high predictive accuracy were constructed (R^2 = 98.2% for mass, R^2 = 88.5% for tensile strength). A multi-objective optimization approach was applied, using the non-dominated sorting genetic algorithm II Pareto front analysis in combination with Minitab's Response Optimizer tool, to identify the optimal combination of parameters. The results showed that layer height, number of walls, and infill percentage, along with their interaction effects and quadratic effects, had the most significant effects on both mass and tensile strength, whereas build plate temperature had negligible effects. The results from the Pareto front analysis revealed the trade-off between minimizing mass and maximizing tensile strength for the parts. The optimal parameter settings (e.g., 58.26% infill percentage, 0.1635-mm layer height, 4 walls, and 65°C build plate temperature) achieved a tensile strength of 47.08 MPa and a mass of 1.60 g, offering a well-balanced strength-to-weight ratio suitable for UAV applications.

Keywords: Fused deposition modeling; Unmanned aerial vehicle parts; Multi-objective optimization; Response surface methodology; Tensile strength; 3D printing parameters

1. Introduction

Unmanned aerial vehicles (UAVs) are important tools in the energy field due to their ability to access places that are inaccessible to humans. In renewable energy applications, UAVs are extensively used to monitor photovoltaic arrays and to assess weather conditions that can affect energy production and grid stability, among other applications. With the use of high-resolution cameras and thermal sensors, UAVs can

†These authors contributed equally to this work.

***Corresponding author:**
Saleem Ramadan
(saleem.ramadan@htu.edu.jo)

Citation: Ramadan S, Abu-Shams M. Optimizing 3D printing parameters for lightweight and high-strength unmanned aerial vehicle parts. *Mater Sci Add Manuf*. 2026;5(1):025290065.
doi: 10.36922/MSAM025290065

Received: July 18, 2025

Revised: August 4, 2025

Accepted: August 14, 2025

Published Online: October 8, 2025

efficiently inspect photovoltaic arrays, detect faults, dirt buildup, and hotspots without the need for manual work, and shut down the system.[1] Moreover, UAVs can also be used as mobile weather stations to collect real-time data on temperature, humidity, and wind. This is important for improving energy forecasting and grid management.[2] For UAVs to perform well and have long flight times, they need to be designed with a high strength-to-weight ratio. Reducing the mass helps save battery and increases flight duration, allowing UAVs to cover larger areas and complete inspections more efficiently. Therefore, UAVs favor parts that are extremely lightweight but also strong enough to support flight efficiency and payload capacity.[3]

In recent years, additive manufacturing (AM) has played a significant and revolutionary role in applications across fields, including automotive, aerospace, medical, goods, food, and construction.[4-7] In complex and specialized industries, such as aviation, aerospace, and automotive, AM has been used to produce tools, parts, and components, as well as being involved in repair and restoration processes.[8-11] For example, fused deposition modeling (FDM) is a low-cost AM process, offering good flexibility for adjusting parameters such as layer height, raster orientation, and extrusion temperature, all of which directly affect the tensile strength of printed parts.[12,13] In addition, techniques such as design of experiments (DoE), including Taguchi method and response surface methodology (RSM), have been successfully used in literature to study the relationships between parameters and desired properties.[12,14,15] Moreover, multi-objective optimization methods, such as gray relational analysis and genetic algorithms, were used to compromise among tensile strength, elastic modulus, and strain at maximum stress for the printed parts.[16] Taguchi-based studies have shown that build orientation, raster angle, layer height, and extrusion temperature strongly affect the tensile properties of polylactic acid (PLA).[17,18] The mechanical properties of FDM-printed UAV parts are highly sensitive to process parameters.[19]

Recent achievements in composite filament materials, such as carbon fiber-reinforced PLA, enable the production of UAV parts with high strength-to-weight ratios and enhanced vibration stability.[1,20] AM techniques can increase the structural and aerodynamic efficiency of UAVs. With on-site/demand production capabilities, AM can effectively address supply chain issues and minimize operational costs.[21] For example, Huang *et al.*[22] developed a framework to design and produce topologically optimized, continuous carbon fiber-reinforced composites with both high manufacturing efficiency and manufacturability, and experimentally validated via material extrusion for a UAV wing spar that exceeded 1 m. They used 3D printing to produce the internal wing structure, while experimental tests and numerical analyses were conducted to validate the load-carrying capability. Similarly, Goh *et al.*[23] investigated the ability of the fused filament fabrication technique to fabricate geometrically hard-to-manufacture parts with continuous carbon fiber-reinforced thermoplastic. They found that the technique has a strong capability to print geometrically complex, high-performance structural parts for manufacturing a topology-optimized UAV landing gear.

To further enhance component performance, recent research has been using multi-objective optimization methods. For example, Grey–Taguchi techniques have been employed to optimize tensile strength, flexural strength, and shrinkage in PLA parts,[24,25] while genetic algorithms combined with RSM are effective in enhancing both mechanical strength and surface quality of FDM.[26] Meanwhile, advanced design methods, such as topology optimization and finite element analysis, have been used to create high-strength, lightweight UAV frames made from PLA and acrylonitrile butadiene styrene,[12,13] while composite filament materials can further enhance structural performance compared to traditional metals.[27]

Although progress has been made in understanding how FDM parameters affect PLA's mechanical properties, there is still a lack of integrated DoE frameworks that combine RSM with optimization, especially for the design of UAV parts. Limited studies focus on minimizing mass and maximizing tensile strength for UAV parts simultaneously. Therefore, this study filled this gap by using an RSM to systematically adjust FDM parameters, aiming to minimize mass while maximizing tensile strength of PLA parts for UAV applications. Then, the non-dominated sorting genetic algorithm II (NSGA-II) Pareto front analysis (using Python) and the Response Optimizer in Minitab were used to identify the optimal set of parameters to achieve the optimal strength-to-weight ratio.

2. Materials and methods

In this study, eight printing parameters were considered: Infill percentage, layer height, number of walls, nozzle temperature, printing speed, build plate temperature, number of bottom and upper layers, and infill pattern. When using the Taguchi L16 orthogonal design, four printing parameters were identified as the most influential factors: Infill percentage, layer height, number of walls, and build plate temperature. These four printing factors were selected and systematically varied using an RSM framework to study their influence on two response variables: Mass and tensile strength. RSM was chosen because it is a robust

statistical method for modeling and optimizing complex processes affected by multiple variables. It allows for the exploration of how process parameters affect responses, considering both linear and interactional effects, making it well-suited for processes such as FDM, where several parameters interact simultaneously.

The experimental results were then used to develop two regression models, one for mass and the other for tensile strength of a specimen. These models show how the four parameters affect their corresponding response variable. To identify the optimal combination of printing parameters that can both maximize the tensile strength and minimize the mass of the printed parts, two optimization methods were used simultaneously: NSGA-II Pareto front analysis (performed in Python) and the Response Optimizer tool in Minitab.

The test specimens were first designed using SolidWorks 3D CAD (SolidWorks®, United States [US]), adopting the geometry, as shown in Figure 1A, and then exported in STL format to be processed in ideaMaker® software (version 2023, US). To ensure the specimen had good adhesion to the build plate, the first layer of each print was made with a 0.3-mm layer height and with a brim. All printing was conducted at room temperature, and each print was started only after both the nozzle and the build plate reached a temperature of 25°C.

The fabrication process was carried out on the E2 3D printer (Raise3D, China; Figure 1B) equipped with a 0.4-mm nozzle, using 1.75-mm PLA filament (tensile strength: 46.6 MPa, modulus of elasticity: 2,636 MPa, elongation: 1.9%). The mass of each printed specimen was measured using the FX-200i digital scale (capacity: 220 g; readability: 0.001 g; A&D Company, Limited, Japan; Figure 1C), allowing precise detection of small differences between test samples. The tensile strength was tested using the FS300CT universal testing machine (Testometric, United Kingdom; Figure 1D), equipped with a 2,500 kg load cell.

The NSGA-II, a popular evolutionary algorithm for multi-objective optimization, was used in this study to generate a Pareto front. Instead of yielding a single optimal solution, NSGA-II generates a group of solutions in which improving one goal (e.g., mass) usually entails a trade-off in another (e.g., tensile strength). As there is an inherent conflict between reducing mass and increasing strength—lighter UAV parts often lose structural strength, whereas stronger parts tend to weigh more and thus reduce flight time—NSGA-II is an excellent method to study these trade-offs. In this research, NSGA-II was applied to analyze the combined effects of infill percentage, layer height, number of walls, and build plate temperature on the mass and tensile strength of UAV frame parts. Using regression models derived from the RSM data, the algorithm tested hundreds of parameter combinations and generated a Pareto front that shows the optimal trade-offs between the two goals. This approach enables data-driven optimization of 3D-printed UAV parts, enhancing both flight efficiency and mechanical durability.

In addition, the Response Optimizer tool in Minitab was used to identify the optimal combination of input settings based on the response surface models derived

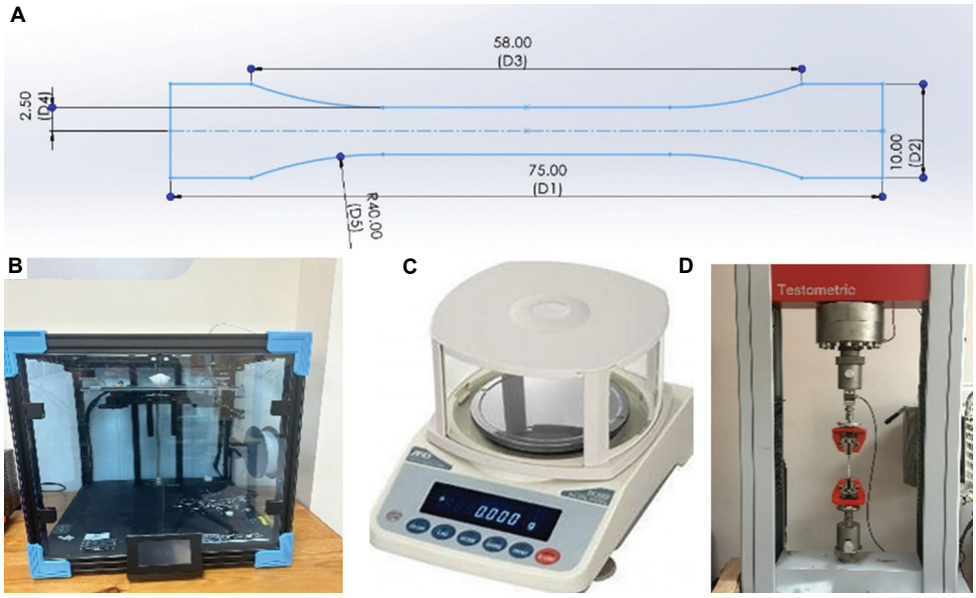

Figure 1. Specimen design and equipment used in the study. (A) Design of the test specimen (units in mm). (B) Fused deposition modeling 3D printer. (C) Digital weighing scale. (D) FS300CT testing machine

from RSM. It visualizes how input factors affect predicted outcomes and allows users to set goals (e.g., maximize tensile strength and minimize mass) and explore different combinations of input factors interactively. In this study, after modeling tensile strength and mass as functions of layer height, number of walls, infill percentage, and build plate temperature, the Response Optimizer was used to refine the selection of parameters—identifying combinations that achieve a balanced trade-off between high tensile strength and low mass for 3D-printed UAV parts.

This study presented an integrated method that combines RSM, NSGA-II Pareto front optimization, and Minitab's Response Optimizer to optimize FDM printing parameters for UAV parts. By modeling the effects of infill percentage, layer height, number of walls, and build plate temperature on both mass and tensile strength, and using multi-objective optimization, this research enables data-driven selection of printing parameters that balance lightweight design with mechanical performance. The resulting Pareto front and optimized parameter sets provide practical guidance for producing high-performance, lightweight UAV parts, enhancing flight endurance, energy efficiency, and structural strength in future drone designs. The flowchart of this study is shown in Figure 2.

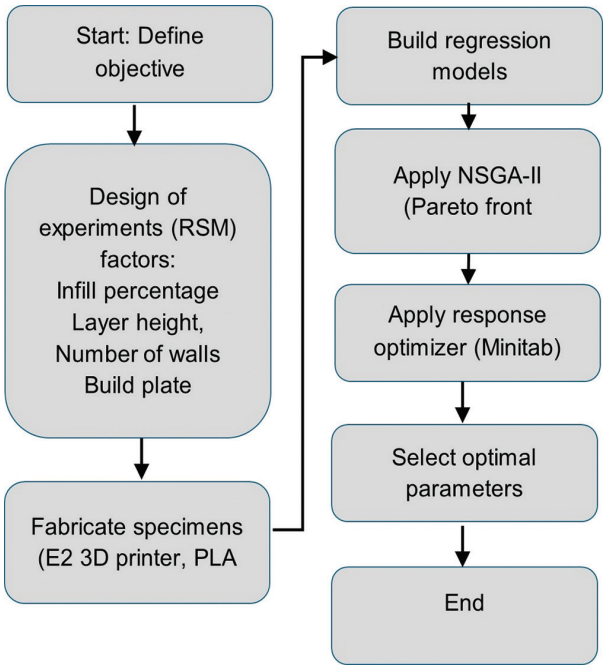

Figure 2. Methodology flowchart
Abbreviations: NSGA-II: Non-dominated sorting genetic algorithm II; PLA: Polylactic acid; RSM: Response surface methodology

3. Results

3.1. Analysis

In this study, RSM was employed to study the effects of four important FDM parameters on two response variables: Mass (g) and tensile strength (MPa). The selected parameters and their levels were: Infill percentage (40, 60, and 80%), which controls internal density; layer height (0.150, 0.175, and 0.250 mm), which affects bonding and surface finish; number of walls (2, 3, and 4), which impacts outer shell strength; and build plate temperature (45, 55, and 65°C), which influences adhesion and bonding between layers, such that if the temperature is too low, the material may shrink or warp, resulting in weak layer bonding (Table 1). These parameter ranges were selected to reflect practical process variations and to support the optimization of UAV parts for both high strength and low weight.

Table 2 presents the estimated regression coefficients for the mass of the designed UAV part. The analysis was conducted using uncoded units. RSM was employed instead of a full factorial design because the goals were not only to study the main effects and interactions between the factors but also to capture curvature in the responses (The design matrix for the RSM is provided in Supplementary Table S1). The squared terms—such as layer height × layer height—in Tables 2 and 3 indicate that the experiment was designed to model nonlinear relationships, which full factorial designs alone cannot model effectively without multiple levels. RSM allows for a more efficient exploration of the design space with fewer runs than a full factorial design, particularly when estimating second-order (quadratic) effects is important for optimization.

The model achieved a standard error of 0.01453, indicating a minimal difference between the observed values and the predicted regression line. The coefficient of determination (R^2) was 98.2%, and the adjusted R^2 was 98.0%. The high R^2, together with the minimal difference between R^2 and adjusted R^2, implies that the model explains nearly all of the variation in the response without evidence of overfitting. These results suggest that the predictors included in the model are important and that the model has strong and reliable predictive capability.

Table 1. Parameter ranges

Parameter	Min	Max
Infill percentage (%)	40	80
Layer height (mm)	0.15	0.25
Number of walls	2	4
Build plate temperature (°C)	45	65

Table 2. Regression coefficients for mass

Term	Coefficient	SE	*t*	*p*-value
Constant	0.67991	0.108492	6.267	<0.001*
Infill percentage	0.00999	0.001329	7.522	<0.001*
Layer height	0.65440	0.293337	2.231	0.027*
Number of perimeters	0.20984	0.026571	7.897	<0.001*
Build plate temperature	−0.00245	0.004509	−0.543	0.588
Infill percentage × infill percentage	−0.00000	0.000010	−0.270	0.788
Layer height × layer height	7.62339	0.717095	10.631	<0.001*
Number of walls × number of walls	−0.00815	0.004034	−2.020	0.045*
Build plate temperature × build plate temperature	0.00004	0.000040	0.890	0.375
Infill percentage × layer height	−0.01770	0.001083	−16.339	<0.001*
Infill percentage × number of walls	−0.00082	0.000081	−10.086	<0.001*
Infill percentage × build plate temperature	−0.00001	0.000008	−1.176	0.242
Layer height × number of walls	−0.28399	0.021660	−13.111	<0.001*
Layer height × build plate temperature	−0.00441	0.002166	−2.037	0.044*
Number of perimeters × build plate temperature	−0.00014	0.000162	−0.870	0.386

Notes: Significance level is set at p=0.05, *indicates p<0.05.

Table 3. Regression coefficients for tensile strength

Term	Coefficient	SE	t	*p*-value
Constant	−0.830	10.3567	−0.080	0.936
Infill percentage	0.357	0.1268	2.815	0.006*
Layer height	104.608	28.0020	3.736	0.000*
Number of walls	11.915	2.5365	4.698	0.000*
Build plate temperature	−0.185	0.4304	−0.429	0.669
Infill percentage × infill percentage	−0.002	0.0010	−1.561	0.121
Layer height × layer height	20.605	68.4540	0.301	0.764
Number of walls × number of walls	−0.902	0.3851	−2.343	0.021*
Build plate temperature × build plate temperature	0.003	0.0039	0.764	0.446
Infill percentage × layer height	−0.602	0.1034	−5.825	0.000*
Infill percentage × number of walls	−0.007	0.0078	−0.896	0.372
Infill percentage × build plate temperature	0.001	0.0008	0.699	0.485
Layer height × number of walls	−8.912	2.0677	−4.310	0.000*
Layer height × build plate temperature	−0.299	0.2068	−1.446	0.150
Number of walls × build plate temperature	−0.018	0.0155	−1.192	0.235

Notes: Significance level is set at p=0.05, *indicates p<0.05.

Figure 3 presents the normal probability plot for mass, where most residuals lie close to the reference line, with only minor deviations at the tails, indicating that the assumption of normally distributed residuals is largely met. Figure 4 shows the histogram of residuals, which is nearly symmetric and bell-shaped, centered around zero. Together, these plots suggest that the regression model for mass fits the data well, with no serious violations of the normality assumption, thereby confirming the reliability of the statistical results.

The regression results presented in Table 2 show that infill percentage, layer height, and number of walls have significant positive effects on mass (p<0.05), meaning that increasing any of these parameters raises mass. In contrast, build plate temperature showed no significant effect (p=0.588). Several interaction terms were highly significant, especially infill percentage × layer height, infill percentage × number of walls, and layer height × number of walls (all p<0.001), suggesting that combinations of these parameters strongly influence mass. The significant squared terms for layer height and number of walls also indicate that their relationships with mass are nonlinear, where the effect of increasing these parameters is not

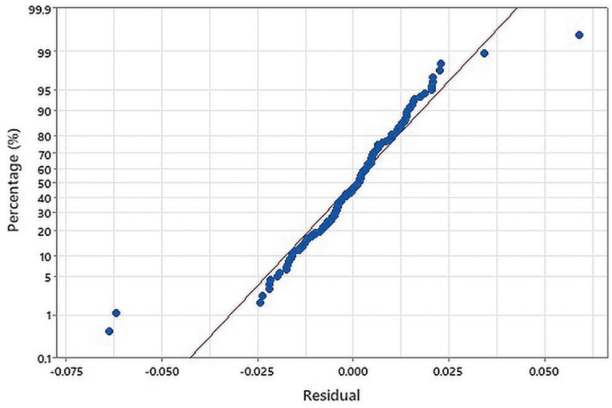

Figure 3. Normal probability plot for mass

constant across all levels. Meanwhile, terms involving the build plate temperature were mostly not significant. Overall, the findings suggest that controlling the mass of printed parts mainly depends on adjusting infill percentage, layer height, and number of walls, along with their interactions, while build plate temperature has minimal impact. This result is also illustrated in the Pareto chart of standardized effects for mass (Figure 5), using a reference line of 1.98.

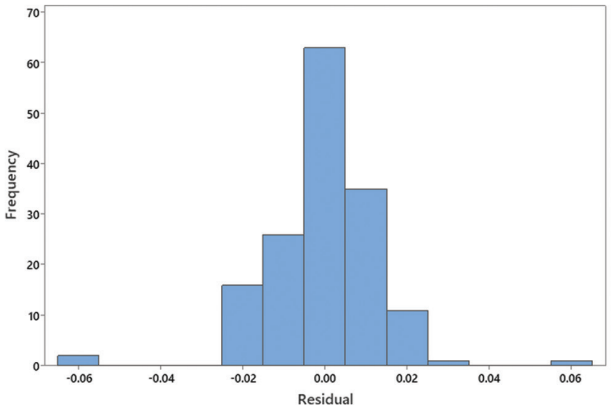

Figure 4. Histogram of residuals for mass

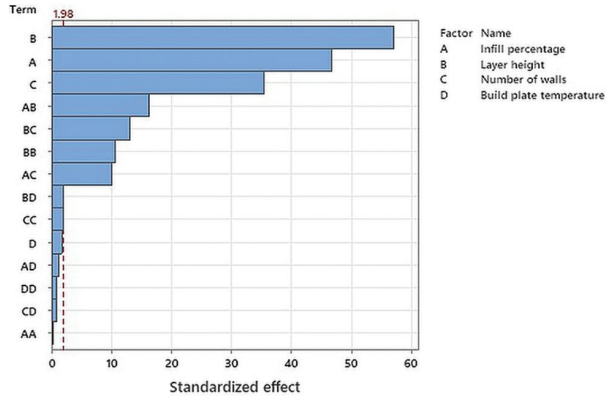

Figure 5. Pareto chart of standardized effects for mass

Figure 6A shows the main effects of the selected parameters on the average mass of the printed parts, indicating that infill percentage, layer height, and number of walls each have a strong positive effect on mass—when these parameters increase, the mass of the part also increases. In contrast, the build plate temperature has minimal effect. Figure 6B presents the interaction effects, confirming that mass increases even further when a higher layer height is combined with a higher number of walls. The interactions between infill percentage and either layer height or number of walls also show a clear increasing trend. In general, these results demonstrate that infill percentage, layer height, and number of walls are the primary factors influencing mass, both individually and in combination, whereas build plate temperature has minimal influence.

Figure 7 shows the contour plots for mass, illustrating the interaction effects of the selected parameters on the mass of the printed parts. Each plot presents how pairs of parameters—layer height, infill percentage, number of walls, and build plate temperature—interact to affect mass, with the other factors held constant. The results show that increasing layer height and number of walls leads to a clear increase in mass, while infill percentage has a smaller but noticeable effect. Build plate temperature, in contrast, has minimal impact on mass across its range. These findings suggest that careful adjustment of layer height and number of walls is important when aiming to reduce the mass of UAV parts.

Figure 8 presents the surface plots for mass, illustrating how the selected parameters jointly affect the mass of the printed parts. The surfaces demonstrate that increasing layer height and number of walls leads to substantial increases in mass, with a pronounced nonlinear trend—particularly for the number of walls. Infill percentage also increases the mass, but the effect is more gradual and mostly linear. Build plate temperature, in contrast, shows minimal influence, as indicated by the nearly flat surfaces in its plots. Overall, these results confirm that layer height and number of walls are the most important parameters to control when aiming to reduce the mass of UAV parts, and they must be adjusted carefully to achieve lightweight designs.

The regression equation (Equation I) for mass supports the trends observed in the main effects and interaction plots. The positive coefficients for infill percentage, layer height, and number of walls indicate that increasing any of these parameters increases the mass of the part, consistent with the strong upward trends in the main effects plots. The coefficient for the build plate temperature was close to zero, consistent with its minimal influence shown in earlier results. The significant squared terms for layer height and number of walls also reflect the curvature seen in their plots. The negative interaction terms (such as infill percentage × layer height and layer height × number of walls) suggest that when both these parameters are set to higher levels, the increase in mass is smaller than would be expected from simply adding their individual effects—this pattern is also visible in the interaction plots. In general, the regression equation provides a clear mathematical summary of the findings: layer height, number of walls, and infill percentage are the primary factors affecting mass, while build plate temperature has little effect.

$$\text{Mass} = 0.679909 + 0.00999339 \times IP + 0.654401 \times LH + 0.209838 \times NW - 0.00244999 \times BT - 2.72106E - 6 \times IP^2 + 7.62339 \times LH^2 - 0.00814842 \times NW^2 + 3.59158E - 5 \times BT^2 - 0.0176952 \times IP \times LH - 8.19231E - 4 \times IP \times NW - 9.54812E - 6 \times IP \times BT - 0.283995 \times LH \times NW - 0.00441283 \times LH \times BT - 1.41288E - 4 \times NW \times BT \quad \text{(I)}$$

where:

- IP = Infill percentage
- LH = Layer height (mm)
- NW = Number of walls
- BT = Build plate temperature (°C).

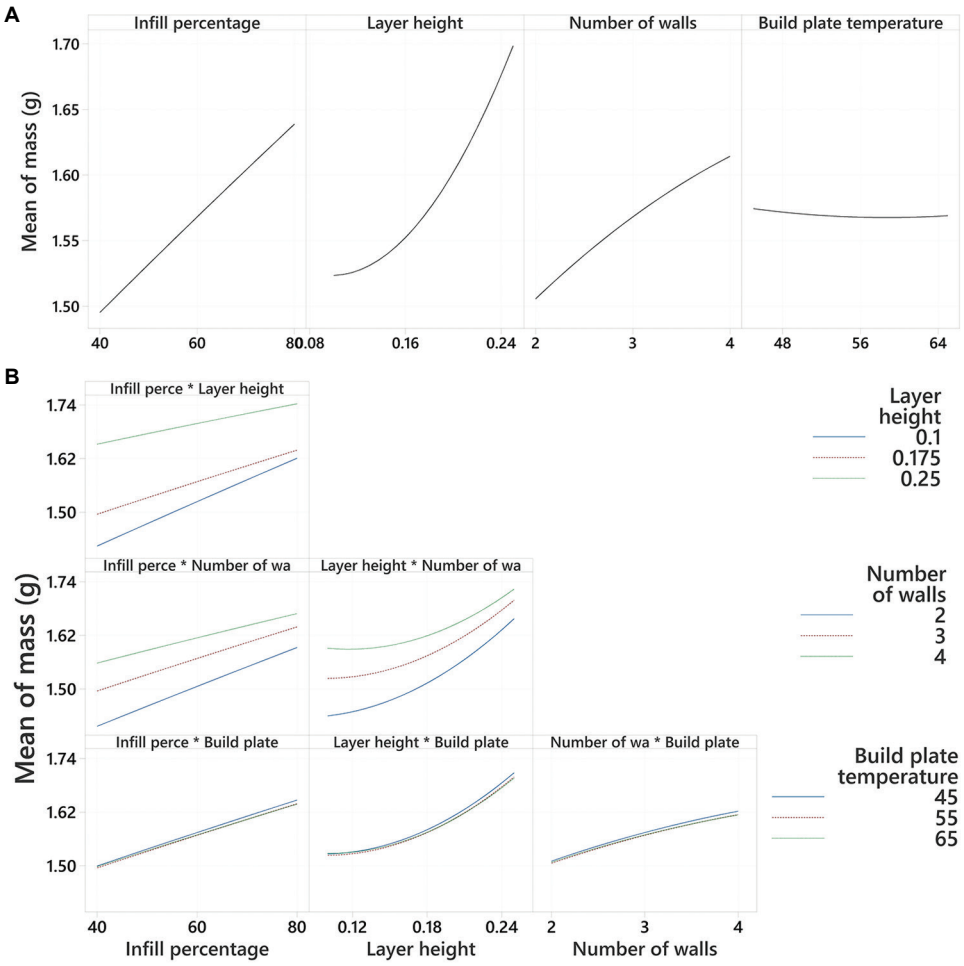

Figure 6. Factorial plots for mass. (A) Plots for individual parameters. (B) Plots for interaction effects

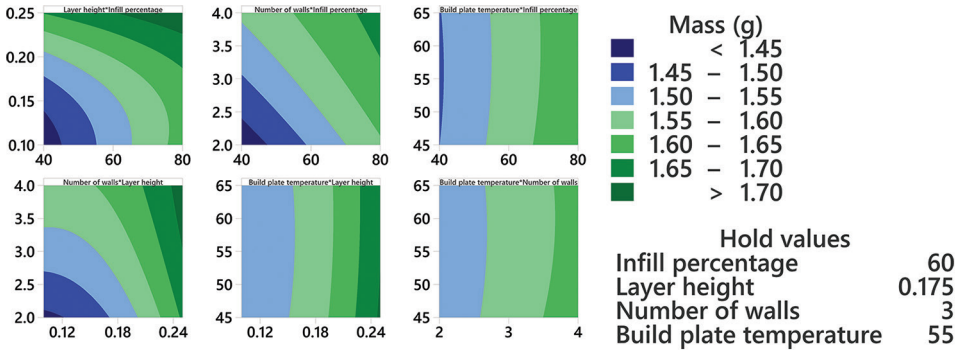

Figure 7. Contour plots for mass
Notes: Darker blue areas represent lower mass; Darker green areas represent higher mass

Table 3 presents the estimated regression coefficients for the tensile strength of the designed UAV part. The analysis was performed using uncoded units. The model produced a standard error of 1.387, indicating a minimal difference between the observed values and the predicted regression line. The R^2 showed that 88.5% of the variation

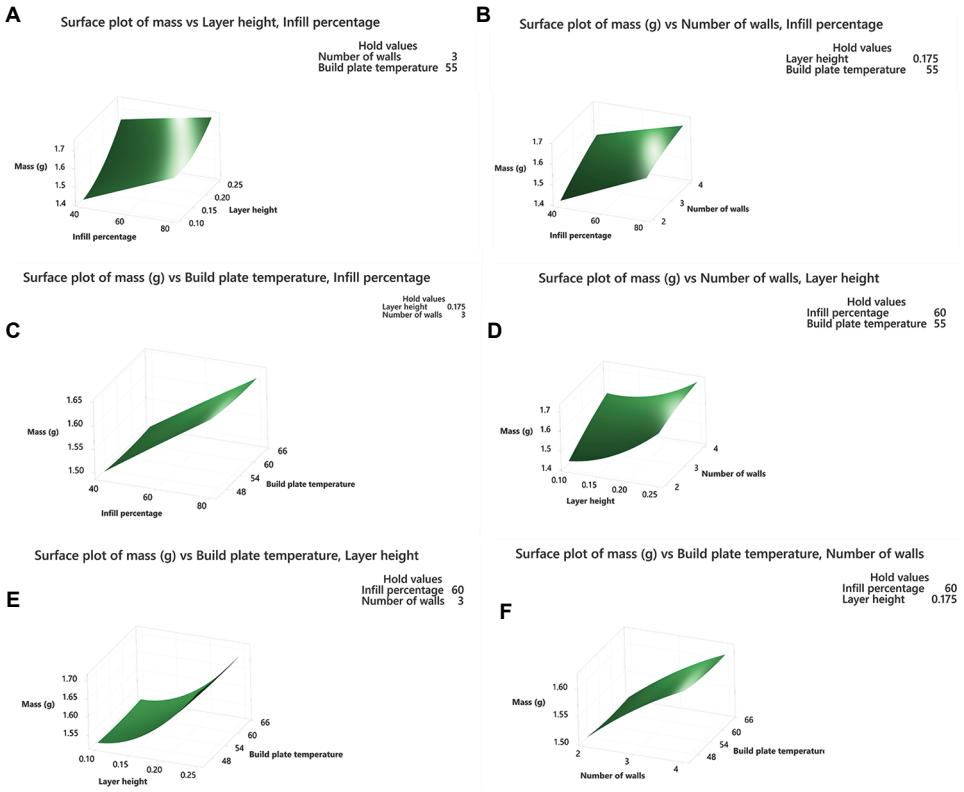

Figure 8. Surface plots for mass. (A) Mass versus LH versus IP. (B) Mass versus NW versus IP. (C) Mass versus BT versus IP. (D) Mass versus BT versus LH. (E) Mass versus NW versus LH. (F) Mass versus BT versus NW
Abbreviations: BT: Build plate temperature; IP: Infill percentage; LH: Layer height; NW: Number of walls.

in the response variable is explained by the model, while the adjusted R^2 of 87.3% was closely aligned, suggesting a good balance between explanatory power and simplicity without evidence of overfitting. The normal probability plot of residuals (Figure 9) shows that the residuals closely follow the reference line, indicating they are approximately normally distributed. The histogram of residuals (Figure 10) displays a roughly bell-shaped curve centered near zero, further supporting normality. Together, these results suggest that the assumptions of normality and homoscedasticity are reasonably met, reinforcing the reliability of the regression model for tensile strength.

The regression analysis results (Table 3) show that infill percentage, layer height, and number of walls have significant effects on tensile strength (p<0.05), whereas build plate temperature has no significant effect (p=0.669). Among the interaction terms, infill percentage × layer height and layer height × number of walls showed strong negative effects with high significance (p<0.001), meaning that combinations of these parameters strongly influence tensile strength. In addition, the term number of walls × number of walls was also significant (p=0.021), while other

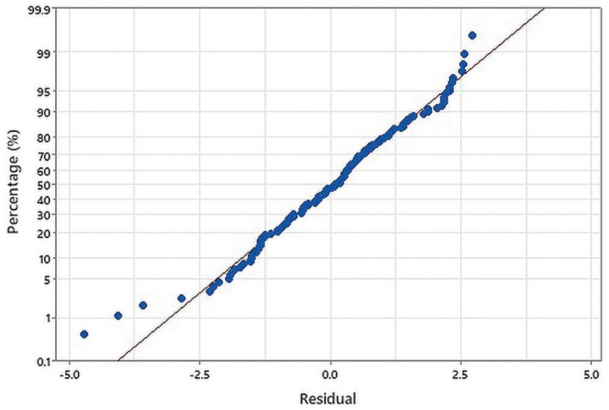

Figure 9. Normal probability plot for tensile strength

higher-order terms showed weaker or non-significant effects. Overall, the findings suggest that tensile strength is primarily affected by layer height, number of walls, infill percentage, and certain key interactions between these parameters. This result is also illustrated in the Pareto chart of standardized effects for tensile strength (Figure 11), using a reference line of 1.98.

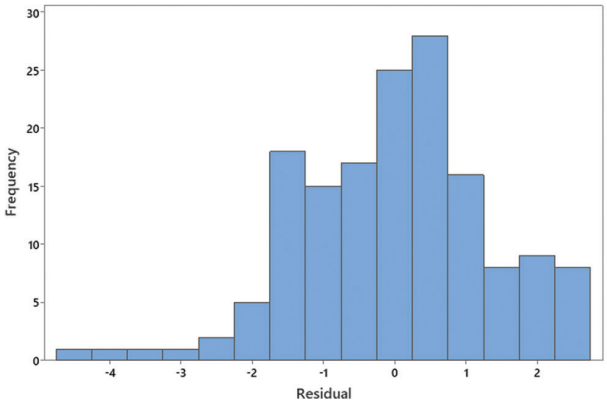

Figure 10. Histogram for tensile strength

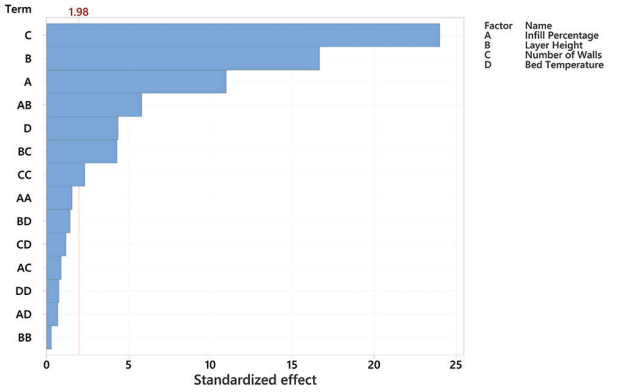

Figure 11. Pareto chart of standardized effects for tensile strength
Abbreviations: BT: Build plate temperature; IP: Infill percentage; LH: Layer height; NW: Number of walls

Figure 12A shows the main effects plots for tensile strength, indicating that increasing infill percentage, layer height, and number of walls all lead to higher tensile strength, whereas build plate temperature has only a smaller positive effect. Figure 12B presents the interaction effects between the primary parameters. Notably, there were strong interactions between infill percentage and layer height, as well as between layer height and number of walls, where higher combinations of these parameters result in greater tensile strength. The interactions between other factors were comparatively weak. In general, these results indicate that optimizing tensile strength requires careful adjustment of both the primary effects and the key interactions among the primary parameters.

The contour plots (Figure 13) show the interaction effects of the key parameters on tensile strength. Across the combinations of layer height, infill percentage, number of walls, and build plate temperature, higher tensile strength occurs when both layer height and number of walls are increased, as well as when infill percentage is higher. The plots also highlight the importance of interactions—particularly between layer height and infill percentage, and between number of walls and layer height—in achieving higher tensile strength. These visual trends reinforce that optimizing combinations of parameters, rather than adjusting individual factors in isolation, is necessary for producing high-performance printed parts.

Figure 14 presents the 3D surface plots, demonstrating the combined effects of the key FDM process parameters on tensile strength. The surfaces indicate that increasing layer height, infill percentage, and number of walls generally results in higher tensile strength. The curvature in the surfaces demonstrates that these relationships are not purely linear, confirming the presence of significant interaction and quadratic effects. This curvature reflects the complex interplay between parameters and underscores the need for multi-parameter optimization strategies to achieve superior mechanical performance in 3D-printed parts. The squared and interaction terms in the regression model account for this nonlinear behavior, explaining why the surfaces bend rather than remain flat, highlighting that optimal performance requires coordinated adjustment of parameters rather than isolated changes.

While the tensile strength tests were carried out on specific, individual samples, the smooth curves, as shown in Figure 14, were generated from the regression model developed through RSM. This model uses the experimental data to predict values across the entire range of input settings, effectively "connecting the dots" between the tested points. As a result, it is possible to visualize a continuous surface, even though the actual tests were conducted at discrete parameter combinations. The model fills in these gaps, providing a clearer picture of how the parameters interact across the design space.

The regression equation (Equation II) for tensile strength indicates that layer height and number of walls have the largest positive linear effects, with layer height contributing the most, consistent with the trends observed in the main-effects plot. Infill percentage also has a positive effect on strength, but with a smaller impact. The small negative linear effect of build plate temperature suggests a limited influence, aligning with the patterns shown in the main effects and interaction plots. The negative quadratic terms for infill percentage (IP^2) and number of walls (NW^2) indicate diminishing returns at higher values, while the positive quadratic term for layer height (LH^2) suggests a strong nonlinear increase in strength as layer height rises. The significant interaction terms, particularly

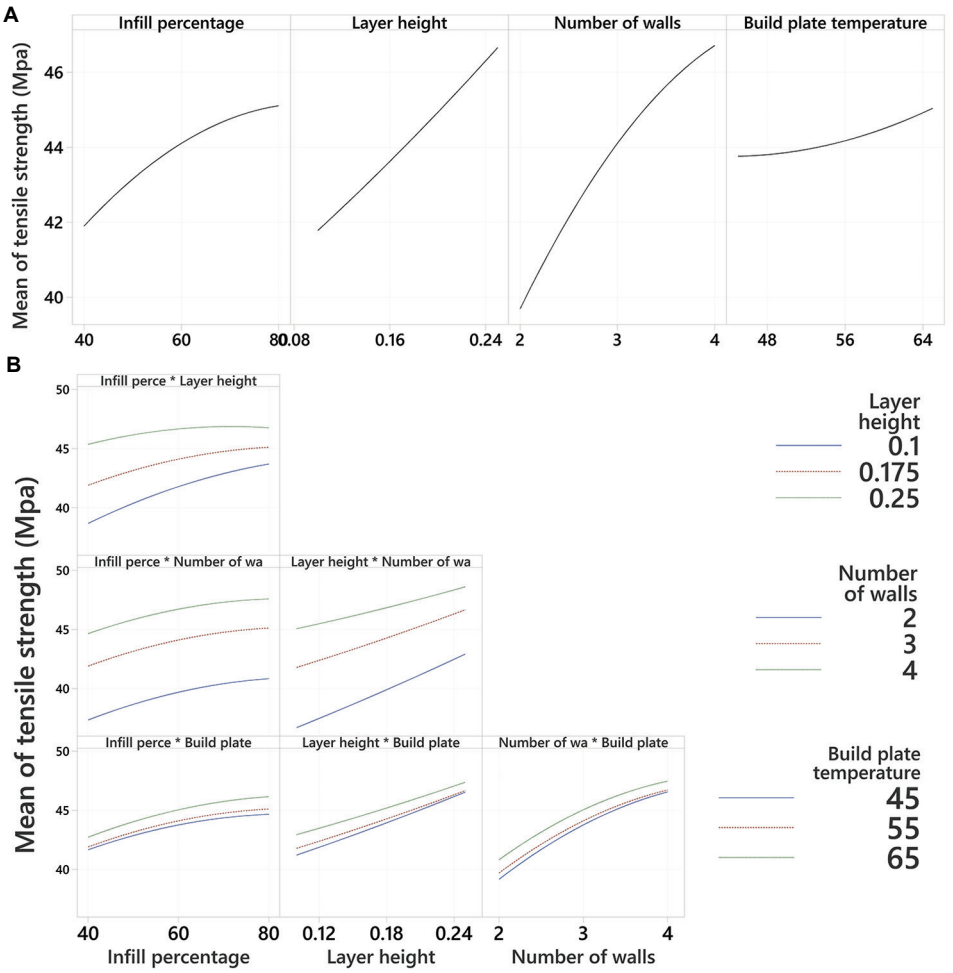

Figure 12. Factorial plots for tensile strength. (A) Plots for individual parameters. (B) Plots for interaction effects
Abbreviations: BT: Build plate temperature; IP: Infill percentage; LH: Layer height; NW: Number of walls

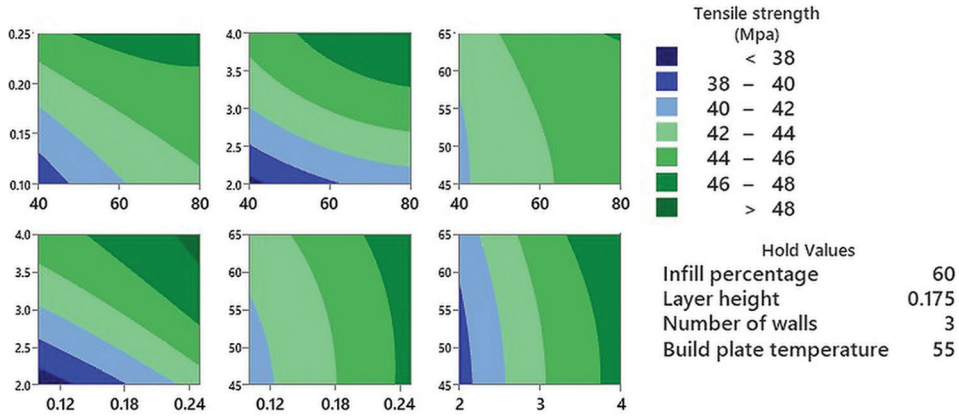

Figure 13. Contour plots for tensile strength
Notes: Darker blue areas represent lower mass; Darker green areas represent higher mass

layer height × number of walls and infill percentage × layer height, highlight the importance of combined parameter effects in achieving optimal tensile strength, as further confirmed by the interaction and contour plots. Overall,

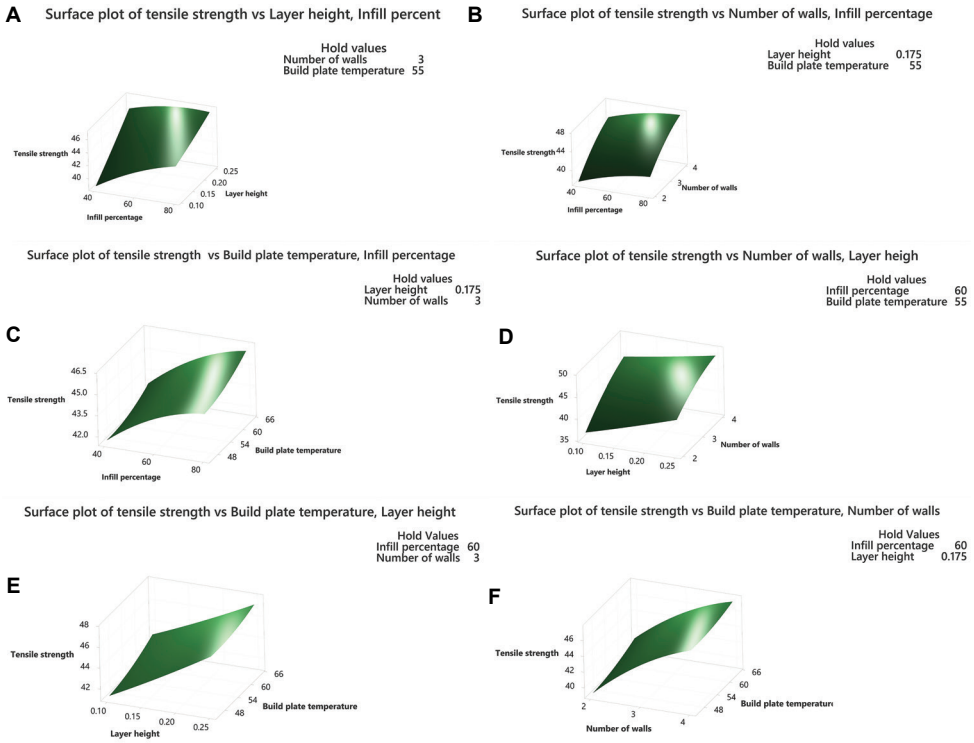

Figure 14. Surface plots for tensile strength. (A) Tensile strength versus LH versus IP. (B) Tensile strength versus NW versus LH. (C) Tensile strength versus NW versus IP. (D) Tensile strength versus BT versus LH. (E) Tensile strength versus BT versus IP. (F) Tensile strength versus BT versus NW
Abbreviations: BT: Build plate temperature; IP: Infill percentage; LH: Layer height; NW: Number of walls

the model identifies layer height, number of walls, and their interactions as the most important factors in optimizing tensile strength for the printed parts.

$$\text{Tensile strength} = -0.830244 + 0.356997 \times IP + 104.608 \times LH + 11.9154 \times NW - 0.184526 \times BT - 0.00150299 \times IP^2 + 20.6051 \times LH^2 - 0.901996 \times NW^2 + 0.00294304 \times BT^2 - 0.602183 \times IP \times LH - 0.00695 \times IP \times NW + 0.000542375 \times IP \times BT - 8.912 \times LH \times NW - 0.299033 \times LH \times BT - 0.01849 \times NW \times BT \quad \text{(II)}$$

Where:

- *IP* = Infill percentage
- *LH* = Layer height (mm)
- *NW* = Number of walls
- *BT* = Build plate temperature (°C).

After building the regression models for mass and tensile strength, these models were used to generate a Pareto front (Figure 15) to illustrate the trade-off between the two objectives: As tensile strength increases, mass also tends to increase. Each point on the curve represents an optimal combination of process parameters, where improving one objective (e.g., increasing strength) compromises the other (e.g., higher mass). The curve shows a smooth trade-off, with diminishing returns at the higher end of tensile strength, meaning that further gains in strength require disproportionately large increases in mass. When designing UAV parts, it is crucial to strike a balance between low weight and sufficient strength. Overemphasis on one aspect often comes at the cost of the other. Based on experience with FDM optimization in aerospace settings, the most reliable outcomes are typically achieved with parameter settings positioned in the mid-range rather than at the extremes. In this case, aiming for a tensile strength of 46 to 48 MPa and a mass of 1.5 to 1.6 g has proven to be an effective middle ground, delivering structural performance while supporting longer flight durations.

The response optimizer plot from Minitab (Figure 16) provides a visual summary of how each process parameter affects the two target responses—tensile strength (to be maximized) and mass (to be minimized). The optimizer identified the optimal combination of parameters as: Infill percentage of 58.26%, layer height of 0.1635 mm, number of walls of 4, and build plate temperature of 65°C. Under these settings, the model predicted a tensile strength of 47.08 MPa and an actual mass of 1.60 g, with a high composite desirability score of 0.9149. The individual desirability values indicate that mass was minimized almost perfectly (0.99944), while tensile strength reached a high value (0.83756), slightly below the target of 50

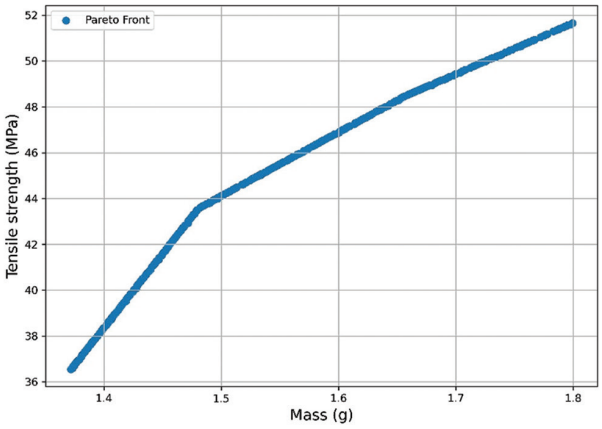

Figure 15. Pareto front analysis of mass versus tensile strength

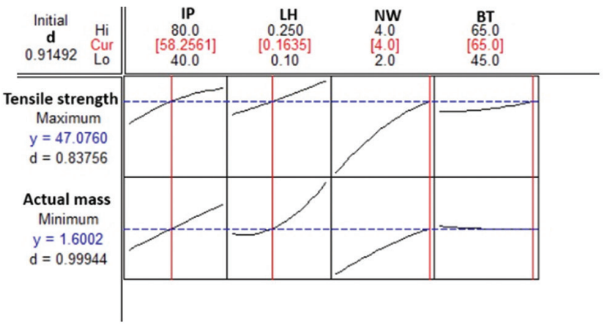

Figure 16. Response optimizer plot
Abbreviations: BT: Build plate temperature; IP: Infill percentage; LH: Layer height; NW: Number of walls

MPa. In the optimizer plot, the curves for each parameter illustrate the sensitivity of the responses to changes in the parameters:

- An increase in the number of walls and layer height substantially enhances tensile strength (as also seen in the Pareto front and interaction plots), but also increases mass.
- Infill percentage has a positive but smaller effect on strength and increases mass.
- Build plate temperature has a smaller but still positive influence on tensile strength at higher values.

The red vertical lines in the plot indicate the parameter settings selected by the optimizer, representing a balance between the two responses rather than maximizing one at the cost of the other. The balance was reflected in the high composite desirability of 0.91, very close to 1, meaning that both objectives were well satisfied simultaneously. Compared with the Pareto front results, this solution was located near the "knee" of the curve, the ideal area where further gains in tensile strength would require a disproportionately large increase in mass, thereby reducing flight efficiency. As such, the optimized configuration achieved an excellent balance between strength and weight, making it highly suitable for UAV applications where both mechanical performance and lightweight design are critical.

3.2. Validation

To verify the selected parameters, five specimens were produced using these exact settings. Their tensile strength and mass were then measured and compared with the values predicted by Equations I and II. The results are summarized in Table 4. The tensile strength showed a percentage error of less than 4.5%, while the error for mass was below 2.5%. These findings demonstrate that tensile strength and mass are highly affected by infill percentage, layer height, number of walls, and build plate temperature. With accurate control of these parameters, the tensile strength and mass of 3D-printed UAV parts can be reliably predicted.

4. Discussion

This work developed and validated an integrated optimization framework for producing lightweight and high-strength UAV parts through FDM. Through a detailed analysis of the effects of infill percentage, layer height, number of walls, and build plate temperature on both mass and tensile strength, and by applying RSM, NSGA-II Pareto optimization, and Minitab's Response Optimizer, the study offers valuable guidance for optimizing FDM parameters for UAV applications.

The regression models demonstrated strong predictive accuracy for both response variables (R^2 = 98.2% for mass; R^2 = 88.5% for tensile strength), confirming that infill percentage, layer height, and number of walls are the most significant factors, whereas build plate temperature has minimal direct influence. The findings also revealed clear trade-offs: Increasing layer height and number of walls enhances tensile strength but also increases mass. By carefully adjusting infill percentage, it is possible to balance both targets effectively.

The Pareto front analysis provided a clear visualization of this trade-off and identified a "knee" region where further increases in strength would come at the cost of greater mass. The Response Optimizer tool recommended an optimal parameter set: Infill percentage of 58.26%, layer height of 0.1635 mm, number of walls of 4, and build plate temperature of 65°C. Using these settings, the model predicted a tensile strength of 47.08 MPa and mass of 1.60 g, with a composite desirability of 0.9149. The validation phase, which involved fabricating test specimens with the optimal parameters, confirmed the effectiveness of this method. The percentage error for tensile strength

Table 4. Predicted versus actual tensile strength (TS) and mass

No.	Actual TS (Mpa)	Predicted TS (Mpa)	Predicted error (%)	Actual mass (g)	Predicted mass (g)	Predicted error (%)
1	47.803	47.080	−1.54	1.594	1.606	−0.93
2	45.0113		4.39	1.583		1.43
3	45.083		4.24	1.605		0.06
4	48.656		−3.35	1.642		−2.24
5	45.018		4.38	1.591		0.93

TS: Tensile strength

was below 4.5%, and for mass below 2.5%, demonstrating that infill percentage, layer height, number of walls, and build plate temperature strongly influence both properties in FDM-based printed parts. This optimized configuration offers a practical balance for UAV applications, where flight efficiency and structural strength are equally important.

5. Conclusion

In summary, this study presents a reliable, data-driven approach for optimizing FDM-based printed UAV parts. The same methodology can be extended to other lightweight structural or aerial applications where strength and low mass are key requirements. Future work can explore the use of advanced materials (such as carbon fiber-reinforced filaments), test larger UAV designs, and further refine the optimization models through validation under actual flight conditions.

Acknowledgments

None.

Funding

None.

Conflict of interest

The authors declare they have no competing interests.

Author contributions

Conceptualization: Saleem Ramadan
Formal analysis: Saleem Ramadan, Mohammad Abu-Shams
Investigation: Saleem Ramadan, Mohammad Abu-Shams
Methodology: Mohammad Abu-Shams, Saleem Ramadan
Writing–original draft: Saleem Ramadan, Mohammad Abu-Shams
Writing–review & editing: Mohammad Abu-Shams, Saleem Ramadan

Ethics approval and consent to participate

Not applicable.

Consent for publication

Not applicable.

Availability of data

The data supporting the findings of this study are available from the corresponding author upon reasonable request.

References

1. Barua A, Singha S. *Simulation Studies for Structural Optimization of A 3D Printable Quadcopter*. *Conference: 6th International Conference on Mechanical Industrial and Materials Engineering*; 2024.
2. Chodorek A, Chodorek R, Yastrebov A. Weather sensing in an urban environment with the use of a UAV and WebRTC-based platform: A pilot study. *Sensors (Basel)*. 2021;21:7113.
   doi: 10.3390/s21217113
3. Laghari AA, Jumani AK, Laghari RA, Nawaz H. Unmanned aerial vehicles: A review. *Cogn Robotics*. 2023;3:8-22.
   doi: 10.1016/J.COGR.2022.12.004
4. Praveena BA, Lokesh N, Buradi A, Santhosh N, Praveena BL, Vignesh R. A comprehensive review of emerging additive manufacturing (3D printing technology): Methods, materials, applications, challenges, trends and future potential. *Mater Today Proc*. 2022;52:1309-1313.
   doi: 10.1016/J.MATPR.2021.11.059
5. Shoeb M, Kumar L, Haleem A, Javaid M. Trends in additive manufacturing: An exploratory study. In: *Advances in Additive Manufacturing: Artificial Intelligence, Nature-Inspired, and Biomanufacturing*. Netherlands: Elsevier; 2023. p. 15-25.
   doi: 10.1016/B978-0-323-91834-3.00027-2
6. Klenam DEP, McBagonluri F, Asumadu TK, *et al.* Additive manufacturing: Shaping the future of the manufacturing industry - overview of trends, challenges and opportunities. *Appl Eng Sci*. 2025;22:100224.
   doi: 10.1016/J.APPLES.2025.100224
7. Kanishka K, Acherjee B. Revolutionizing manufacturing: A comprehensive overview of additive manufacturing processes, materials, developments, and challenges. *J Manuf Process*. 2023;107:574-619.

doi: 10.1016/J.JMAPRO.2023.10.024

8. Blakey-Milner B, Gradl P, Snedden G, *et al.* Metal additive manufacturing in aerospace: A review. *Mater Des*. 2021;209:110008.

   doi: 10.1016/J.MATDES.2021.110008

9. Khan N, Riccio A. A systematic review of design for additive manufacturing of aerospace lattice structures: Current trends and future directions. *Prog Aerospace Sci*. 2024;149:101021.

   doi: 10.1016/J.PAEROSCI.2024.101021

10. Alami AH, Ghani Olabi A, Alashkar A, *et al.* Additive manufacturing in the aerospace and automotive industries: Recent trends and role in achieving sustainable development goals. *Ain Shams Eng J*. 2023;14(11):102516.

    doi: 10.1016/J.ASEJ.2023.102516

11. Espadinha-Cruz P, Reboredo E. A fuzzy system to measure additive manufacturing maturity: A case study in the automotive industry. *Procedia Comput Sci*. 2025;253:1402-1411.

    doi: 10.1016/J.PROCS.2025.01.202

12. Zaman UK, Boesch E, Siadat A, Rivette M, Baqai AA. Impact of fused deposition modeling (FDM) process parameters on strength of built parts using Taguchi's design of experiments. *Int J Adv Manuf Technol*. 2019;101(5):1215-1226.

    doi: 10.1007/s00170-018-3014-6

13. Heidari-Rarani M, Ezati N, Sadeghi P, Badrossamay MR. Optimization of FDM process parameters for tensile properties of polylactic acid specimens using Taguchi design of experiment method. *J Thermoplast Compos Mater*. 2020;35(12):2435-2452.

    doi: 10.1177/0892705720964560

14. Kumar MS, Farooq MU, Ross NS, Yang CH, Kavimani V, Adediran AA. Achieving effective interlayer bonding of PLA parts during the material extrusion process with enhanced mechanical properties. *Sci Rep.* 2023;13(1):6800.

    doi: 10.1038/s41598-023-33510-7

15. Ramadan S, Altwarah Q, Abu-Shams M, Alkurdi D. Optimizing tensile strength and energy consumption for FDM through mixed-integer nonlinear multi-objective optimization and design of experiments. *Heliyon*. 2024;10(9):e30164.

    doi: 10.1016/J.HELIYON.2024.E30164

16. Panico A, Corvi A, Collini L, Sciancalepore C. Multi objective optimization of FDM 3D printing parameters set via design of experiments and machine learning algorithms. *Sci Rep.* 2025;15(1):16753.

    doi: 10.1038/s41598-025-01016-z

17. Medibew T. A comprehensive review on the optimization of the fused deposition modeling process parameter for better tensile strength of PLA-printed parts. *Adv Mater Sci Eng*. 2022;2022:1-11.

    doi: 10.1155/2022/5490831

18. Hamid RA, Husni S, Ito T. Effect of printing orientation and layer thickness on microstructure and mechanical properties of PLA parts. *Malays J Compos Sci Manuf*. 2022;8:11-23.

    doi: 10.37934/mjcsm.8.1.1123

19. Ahmed NA, Page JR. Manufacture of an unmanned aerial vehicle (UAV) for advanced project design using 3D printing technology. *Appl Mech Mater*. 2013;397-400:970-980.

    doi: 10.4028/www.scientific.net/AMM.397-400.970

20. Kantaros A, Drosos C, Papoutsidakis M, Pallis E, Ganetsos T. Composite filament materials for 3D-printed drone parts: Advancements in mechanical strength, weight optimization and embedded electronics. *Materials (Basel)*. 2025;18(11):2465.

    doi: 10.3390/ma18112465

21. Goh GD, Agarwala S, Goh GL, Dikshit V, Sing SL, Yeong WY. Additive manufacturing in unmanned aerial vehicles (UAVs): Challenges and potential. *Aerosp Sci Technol*. 2017;63:140-151.

    doi: 10.1016/J.AST.2016.12.019

22. Huang Y, Tian X, Li W, *et al.* 3D printing of topologically optimized wing spar with continuous carbon fiber reinforced composites. *Compos B Eng*. 2024;272:111166.

    doi: 10.1016/J.COMPOSITESB.2023.111166

23. Goh GD, Toh W, Yap YL, Ng TY, Yeong WY. Additively manufactured continuous carbon fiber-reinforced thermoplastic for topology optimized unmanned aerial vehicle structures. *Compos B Eng*. 2021;216:108840.

    doi: 10.1016/J.COMPOSITESB.2021.108840

24. Syed B, Rhaman Q, Shahriar H, Khan MMA. *Grey-Taguchi Approach for Optimizing Fused Deposition Modeling Process in Terms of Mechanical Properties and Dimensional Accuracy*. In: *Conference: International Conference on Engineering Research and Education School of Applied Science and Technology,* SUST, Sylhet; 2021.

25. Kumar K, Singh H. Multi-objective optimization of fused deposition modeling for mechanical properties of biopolymer parts using the grey-taguchi method. *Chinese J Mech Eng*. 2023;36(1):30.

    doi: 10.1186/s10033-023-00847-z

26. Chinchanikar S, Shinde S, Shaikh A, Gaikwad V, Ambhore NH. Multi-objective Optimization of FDM using hybrid genetic algorithm-based multi-criteria decision-making (MCDM) techniques. *J Institut Eng Ser D*. 2024;105(1):49-63.

    doi: 10.1007/s40033-023-00459-w

27. Kaptan A, Kartal F. A critical review of composite filaments for fused deposition modeling: Material properties, applications, and future directions. *Eur Mech Sci*. 2024;8:199-209.

    doi: 10.26701/ems.1451829

ACCSCIENCE PUBLISHING

Materials Science in Additive Manufacturing

ORIGINAL RESEARCH ARTICLE

Effect of hot isostatic pressing on the microstructure and mechanical properties of porous Ti-6Al-4V alloy manufactured by laser powder bed fusion

Marketa Strakova[1]*, Jiri Kubasek[1], Jonas Divin[1], Jan Pinc[2], and Dalibor Vojtech[1]

[1]Department of Metals and Corrosion Engineering, University of Chemistry and Technology, Prague, Czech Republic

[2]FZU - Institute of Physics of the Czech Academy of Sciences, Prague, Czech Republic

Abstract

Laser powder bed fusion (LPBF) enables the production of Ti-6Al-4V alloys with tailored porous structures, which are beneficial for biomedical applications due to their reduced elastic modulus and enhanced bone integration potential. This study examines the effect of hot isostatic pressing (HIP) on the microstructure and mechanical properties of diamond and gyroid porous structures fabricated by LPBF. Solid tensile specimens served as reference materials. HIP significantly reduced porosity, decreased ultimate tensile strength and hardness, but markedly increased ductility (from 6% to 17%). Compressive strengths reached approximately 100 MPa (diamond) and 240 MPa (gyroid), with HIP causing only a slight increase in strain. However, HIP notably improved bending performance, raising the flexural strength of gyroid structures from 280 MPa (as-printed) to 340 MPa (post-HIP). The strength of LPBF-fabricated Ti-6Al-4V porous structures is reduced by HIP, but their ductility and bending performance are enhanced, making them more suitable for biomedical applications.

Keywords: Ti-6Al-4V; Laser powder bed fusion; Hot isostatic pressing; Porous material; Mechanical properties; Lattice structures

***Corresponding author:**
Marketa Strakova
(strakovm@vscht.cz)

Citation: Strakova M, Kubasek J, Divin J, Pinc J, Vojtech D. Effect of hot isostatic pressing on microstructure and mechanical properties of porous Ti-6Al-4V alloy manufactured by laser powder bed fusion. *Mater Sci Add Manuf*. 2026;5(1):025260055. doi: 10.36922/MSAM025260055

Received: June 27, 2025

Revised: July 25, 2025

Accepted: August 11, 2025

Published online: October 13, 2025

1. Introduction

The aerospace, sporting goods, and petrochemical industries widely use titanium and its alloys, especially Ti-6Al-4V, due to their relatively low density, high strength, and good corrosion resistance.[1-4] Furthermore, this alloy is of particular importance in biomedical engineering because of its great mechanical performance. It also has a high strength-to-weight ratio, low modulus, high fatigue strength, and biocompatibility.[5] Ti-6Al-4V is particularly useful in the manufacture of artificial joints, bone implants, prosthetics, and surgical instruments, offering a good balance of strength, flexibility, and toughness. Aluminum makes the alloy stronger and lighter, while vanadium adds flexibility and stability. The applicability of Ti-6Al-4V alloy in biomedicine, as well as its potential modification to improve surface properties, has been a major topic in scientific research.[1,2,6]

The production process of titanium is so challenging that it makes it more valuable than steel or aluminum. Given the high material costs, it is advantageous to make parts that need very little post-processing.[3] Ti-6Al-4V is also an ideal candidate for innovative production methods, such as powder-based additive manufacturing (AM). In AM, components are fabricated in a net-shape process by fusing successive layers of metallic raw material to a base material using a pre-programmed scanning pattern of a focused laser or electron beam.[5,7,8] The powder can be applied either through powder bed fusion (PBF), which involves spreading and selectively melting individual layers of powder, or through direct energy deposition, which delivers powder continuously to the melt pool through coaxial jets.[9,10] In theory, AM can produce completely dense, three-dimensional components with highly intricate geometries.[11,12] However, AM-fabricated alloy often exhibits relatively high porosity.[12] The rapid melting and solidification inherent to AM vary with part geometry and path planning, and the layered nature of the process introduces non-fusion defects at layer and laser pass interfaces. Consequently, it becomes challenging to manufacture fully dense, defect-free components with consistent mechanical properties across multiple batches. A number of researchers have used hot isostatic pressing (HIP) to reduce pore size and homogenize microstructural properties through post-processing heat treatment.[12,13] Vilaro *et al.*[14] reported that the mechanical behavior of AM Ti-6Al-4V is strongly influenced by its high porosity, with macroscopic ductility strongly affected by pore orientation and shape.

Advances in AM technologies have been rapid, with laser PBF (LPBF) emerging as one of the key PBF techniques for producing the demanding $\alpha + \beta$ Ti-6Al-4V alloy.[15,16] Recent studies highlight LPBF's potential for fabricating multi-material parts with graded layers, significantly affecting interfacial bonding and mechanical integrity.[17] LPBF builds three-dimensional metal parts by melting metallic powders layer by layer with a laser, and the high cooling rate promotes rapid solidification and phase transformations. This method produces parts in the desired shape and size directly, minimizing the need for additional machining.[5,18,19] Its capability to produce complex 3D medical parts with high precision has driven demand for LPBF in biomedical applications.[6] LPBF can also create porous implant models, which can reduce the Young's modulus, mitigate stress shielding, and improve osseointegration.[20] The mechanical response of LPBF-fabricated porous structures can be tuned by varying unit cell geometry and orientation, significantly influencing impact resistance and energy absorption.[21] The porous part helps to avoid stress shielding and provides biological fixation by allowing tissue ingrowth. In addition, porous structures can act as efficient drug delivery reservoirs to suppress post-surgical inflammatory reactions. Thus, incorporating porous parts into implants can help mimic the behavior of human bone.[22] Significant research efforts have been devoted to optimizing both the manufacturing process and surface modification of porous titanium alloys to enhance their performance in medical applications.[23] In a study by Gao *et al.*,[24] porous titanium implants with a gradient modulus were found to increase femoral surface deformation by 17.1%, reducing the stress shield effect, bone loss, and aseptic loosening. Verma *et al.*[25] confirmed that the porous architecture reduced the effective modulus of elasticity by more than 95%, thereby reducing the stress-shielding effect.

Monotonic tensile properties superior to those of conventionally fabricated alloys have been reported for Ti-6Al-4V manufactured by LPBF. However, its fatigue resistance decreases during cyclic loading due to internal porosity.[15,16] Even with optimized parameters, it is not possible to achieve fully dense parts.[6,26] Recent studies have shown that this issue can be addressed by optimizing the microstructure through precise thermal annealing, which can be especially effective in balancing strength and ductility when performed near the β-transus temperature, typically between 700°C (stress-relieved state) and 1080°C (solution-treated state).[14,27-29] In stress-relieved samples, only minimal changes in grain size are observed; however, complete dissolution of martensitic phases occurs during solution treatment, leading to the formation of an equilibrium ($\alpha + \beta$) microstructure.[19] A comprehensive review of additively manufactured titanium alloys confirms that their microstructure, defect distribution, and mechanical properties are highly dependent on the AM technique employed and the subsequent post-processing conditions.[30] Thermal annealing also produces the expected grain refinement.[19] With increasing annealing temperature, tensile strength initially increases and then decreases, with a similar trend observed in elongation data.[16]

Thermomechanical HIP has also been demonstrated to be effective in minimizing defects associated with porosity in LPBF-printed components.[31] HIP is a process that applies high pressure and temperature evenly to materials in a high-pressure container, which helps to remove internal porosity, improve material density, and enhance mechanical properties.[32-34] Increasing HIP pressure promotes the formation of the β phase, while higher HIP temperatures lead to a reduction in the amount of α and β phases. Simultaneously, the tensile strength and yield strength of LPBF-produced Ti-6Al-4V

decrease as the HIP temperature rises.[35] HIP treatment is also known to eliminate microstructural differences across layers in Ti-6Al-4V, resulting in α + β layered structures that enhance energy uptake through plasticity induced by phase transformation.[36] Following HIP treatment, the fatigue strength at 8×10^6 cycles has been reported to attain 355 MPa, which is on par with that of conventional heat-treated materials.[29] Therefore, this study used post-processing involving both heat treatment and HIP to examine the differences in structure and material properties of the Ti-6Al-4V alloy manufactured by LPBF in three configurations: As-built compact structure, diamond structure, and gyroid porous structure.

While most reported studies deal with HIP processing of dense AM Ti-6Al-4V alloys, the present study focused on testing HIPed porous structures, which hold promise for use in medical implants. To the best of our knowledge, there is limited information on the HIP processing of porous AM-processed Ti-Al-V alloy. Specifically, diamond and gyroid structures were selected for investigation because they are widely utilized in the medical field. These two types of porous structures differ primarily in the size, shape, and arrangement of struts and in the geometry of interconnected pores between them. Mechanical characterization performed in this study included tensile, compressive, flexural, and hardness testing, accompanied by a detailed structural analysis.

2. Materials and methods

2.1. Materials and processing

For this work, Ti-6Al-4V flat bulk tensile samples (70 × 5 × 3 mm; Figure 1) prepared by the LPBF method were used as reference materials (Table 1). The samples were printed vertically in the LPBF chamber and examined in both the as-printed and HIPed states. The conditions for HIP process (950°C, 2 h, 150 MPa, Argon) were selected according to our preliminary experiments and literature,[37] with the temperature chosen to promote transformation of the martensitic phases to the equilibrium (α + β) structure while limiting grain coarsening.

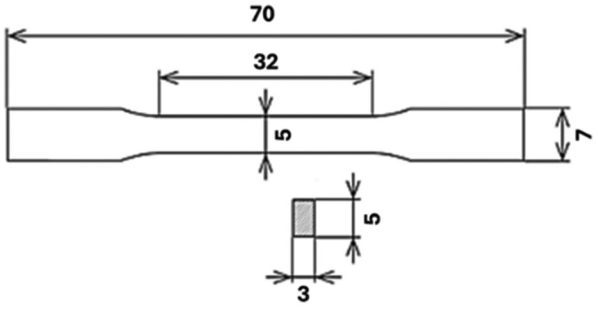

Figure 1. Drawing of printed samples for tensile tests (dimensions given in mm). Reprinted from Strakosova *et al.*[18]

The focus of our research was on the porous structure fabricated by LPBF in two types of structural lattices—diamond and gyroid—which belong to the class of triple periodic minimal surfaces (TPMS). All samples were built on a thin, non-porous substrate. Models of these structures, including elementary cells and larger structures, were generated using the MSLattice program[38] (Figure 2). The computer-aided design (CAD)-generated porosity was set to 70% for both diamond and gyroid types.

The experimental macro-scale porosity was evaluated using the gravimetric method to determine the percentage of free space in the porous structures. The base was removed before weighing, and the sample volume was calculated from measured dimensions. Porosity was determined according to Equation (I):

$$Porosity = 1 - \frac{\rho_{real}}{\rho_{theoretical}} \quad \text{(I)}$$

Where the theoretical density corresponds to the intrinsic material density of Ti-6Al-4V, and the actual density is calculated from the sample's measured mass and geometrical volume.

Using this method, the macroporosity values of 69% (diamond) and 67% (gyroid) were obtained, both of which are in good agreement with the designed value of 70%. Any minor deviations are attributed to imperfections in

Table 1. Supplementary data on the mechanical properties of as-printed and HIPed bulk samples, and porous Ti-6Al-4V samples

Sample	YS (MPa)	UTS (MPa)	E (GPa)	ε (%)	HV1	Micro-porosity (%)
P_AP	1190±8	1283±19	108±7	3±1	353±11	3.62
P_HIP	930±4	1024±3	110±6	17±1	323±7	0.02
Sample	**CYS (MPa)**	**UCS (MPa)**	**CD max (%)**	**UBS (MPa)**	**HV0.5**	**Macro-porosity (%)**
D_AP	81±6	99±1	13±1	164±9	395±18	69
D_HIP	68±2	102±2	16±2	214±35	362±7	66
G_AP	162±5	249±3	23±1	261±10	415±14	67
G_HIP	128±13	222±5	34±1	315±15	316±6	63

Abbreviations: AP: As-printed; CYS: Compressive yield strength; CD max: Maximum compressive deformation; D: Diamond structure; E: Young's modulus; G: Gyroid structure; HIP: Hot isostatic pressing; HV0.5: Vickers hardness (500 g load); HV1: Vickers hardness (1 kg load); UCS: Ultimate compressive strength; UBS: Ultimate bending strength; UTS: Ultimate tensile strength; YS: Yield strength; ε: Elongation.

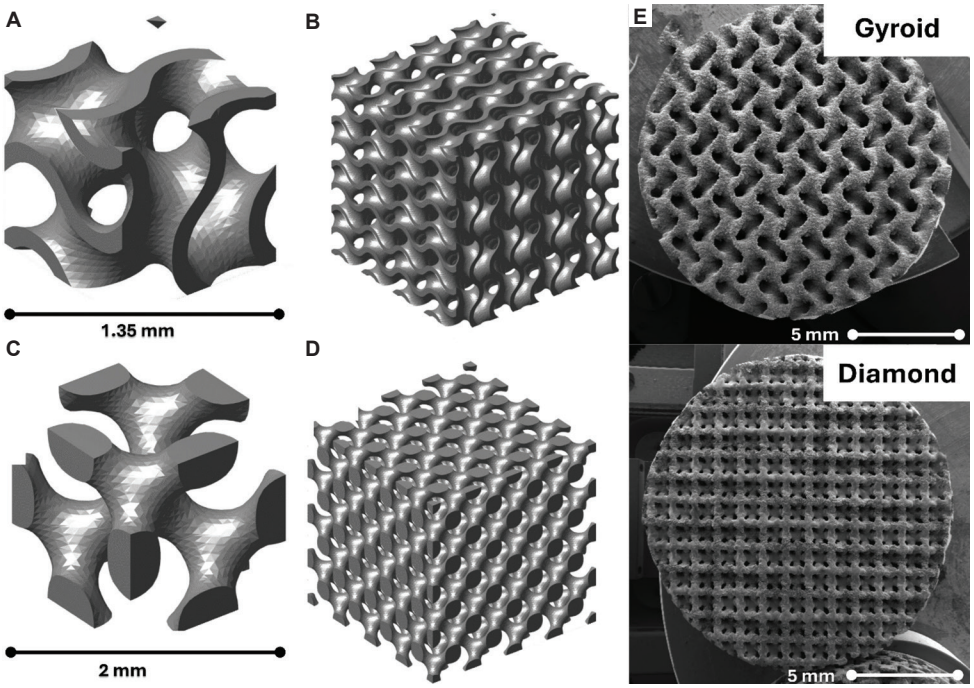

Figure 2. Porous gyroid and diamond structures. (A) Elementary of the cell gyroid structure. (B) Elementary of the diamond cell structure. (C) Gyroid model with multiple elementary cells. (D) Diamond model with multiple elementary cells. (E) Scanning electron microscopy images of diamond and gyroid structures in their as-printed condition. Reprinted from Školáková *et al.*[39]

the LPBF manufacturing process, such as partial melting or powder adhesion.

Both compact and porous samples were printed using a ConceptLaser M2 Cusing printer (ProSpon, Czech Republic) equipped with a 200 W Yb: YAG fiber laser. The printer has a working area of 250 × 250 × 280 mm^3 and operates under a protective argon atmosphere with an oxygen content of up to 0.5% by volume. Continuous mode was used for printing. The scanning speed was 1250 mm/s, the layer thickness was 30 μm, and the hatch spacing was 80 μm.

2.2. Microstructure and porosity

Phase composition of the given samples was determined by X-ray diffraction (XRD) using PANalytical X'Pert PRO system (PANanalytical, Holland) equipped with a copper tube (Kα radiation, λ = 0.15406 nm), Scans were performed over a 2θ range of 5–89° with a step size of 0.039° and a generator setting of 30 mA and 40 kV.

To examine the microstructure, we used a light optical microscope (Nicon, Czech Republic) and scanning electron microscopes (SEM; Tescan Mira, Czech Republic) equipped with energy dispersive spectroscopy (EDS). Metallographic preparation of samples (Figure 3A) included: (i) Sectioning with a cut-off machine (Q-ATM, Germany); (ii) grinding with SiC abrasive sandpapers (P400–P2500, Q-ATM, Germany); (iii) final polishing with a colloidal silica suspension (Eposil F, 0.1 μm; Q-ATM, Germany); LabTest 5.250SP1-VM universal testing machine (LABORTECH s.r.o., Czech Republic) mixed with 4 parts hydrogen peroxide and 1 part water; and (iv) chemical etching with a Croll's solution (2 mL HNO_3 + 98 mL H_2O; Penta, Jersey).

Samples for the measurement of volume porosity were cut from the center of the printed discs, with dimensions of 2.5 × 3 × 15 mm. These dimensions were selected for the resolution and the ability to detect small pores within the matrix. The volume porosity of the samples was determined using micro-computed tomography (μCT; Zeiss Xradia 610 Versa, Carl Zeiss Microscopy, Germany) at a resolution of 4.5 μm/pixel, and the results were analyzed using Dragonfly software (version 2022.1.0.1249).[36] Matrix material, pores within the matrix (matrix pores), and pores intentionally created by TPMS geometry (structural pores) were identified using histogram segmentation (based on pixel intensity) and classified according to pore size. The volume fractions (vol %) of each phase were determined, and mean Feret diameters were calculated for matrix pores.

2.3. Mechanical properties

Mechanical characterization included Vickers hardness (HV1, HV0.5), tensile, compression, and bending tests.

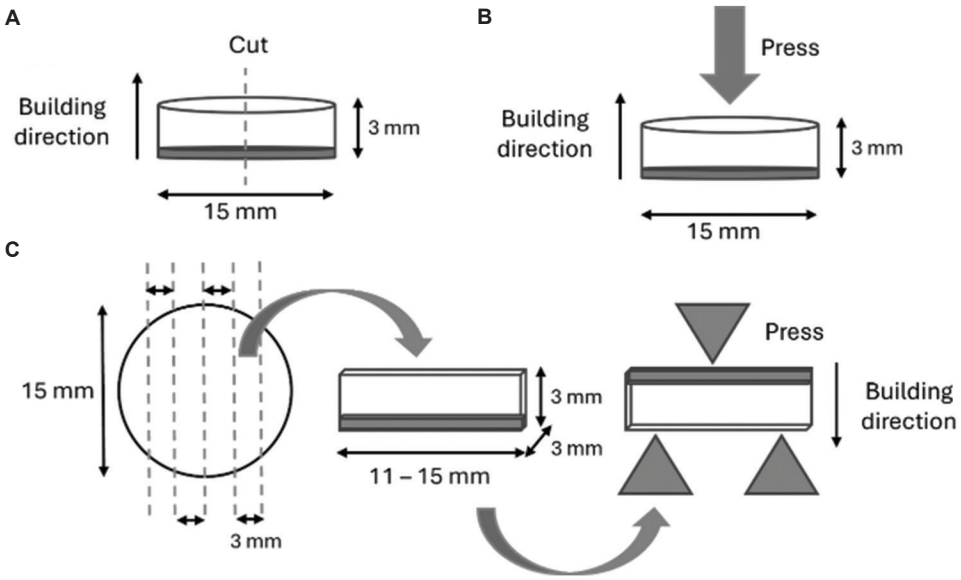

Figure 3. Schematic representations of the test setups. (A) Cutting a sample to create a metallographic cross-section. (B) Uniaxial compression test setup. (C) Specimen preparation for three-point bending tests

These tests were used to evaluate the influence of processing conditions and resulting structure on mechanical performance. For hardness measurements, a minimum of twenty indentations were made on the cross-sections of bulk samples (aligned with the build direction) at various points on a polished surface (P2500 finish). Measurements were taken both on the surface and in cross-section.

An Instron 5882 universal testing machine (Instron Corporation, Germany) with a ±100 kN load cell was used to perform three tensile tests at room temperature for each bulk material. Deformation testing was performed using an MFL 800B extensometer (MF Mess- und Feinwerktechnik GmbH, Velbert, Germany). The specimens were loaded incrementally at a rate of 5 mm/min until failure, after which fracture surfaces were examined using SEM.

Compression and bending tests were carried out on porous diamond and gyroid structures using a LabTest 5.250SP1-VM universal testing machine (Eposil F, 0.1 µm; Q-ATM, Germany); LabTest 5.250SP1-VM universal testing machine (LABORTECH s.r.o., Czech Republic) at room temperature. For each geometry, three compression tests (Figure 3B) and three bending tests (Figure 3C) were performed. Compression properties were evaluated at a constant loading rate of 5 mm/min. Bending tests were conducted using a three-point setup, where two support pins were inserted through the porous section and a third loading pin applied force vertically through the base of the sample (Figure 3C).

The bending test specimens were cut from printed discs into beams with approximate dimensions of 11–15 mm (length) × 3 mm (width) × 3 mm (height). Due to the limited number and small size of samples, a specific ASTM C1161 standard could not be followed for flexural testing. The dense base remained attached and was placed on the compression side (top) during testing. In all cases, the fracture occurred in the porous structure rather than at the base, indicating that the porous region governed the mechanical behavior. The presence of the base may have influenced the stress distribution, which is acknowledged as a limitation of the present test setup.

3. Results

3.1. Microstructure

XRD analysis was performed to analyze the phase composition of the samples (Figure 4). In the as-built condition, all samples exhibited the same phase composition, consisting exclusively of the α′-Ti phase—hexagonal martensite formed during rapid cooling from β-Ti. Following HIP, the α′ phase decomposed into α-Ti and β-Ti phases in both bulk samples and the diamond and gyroid structures. The α-Ti phase corresponds to the hcp allotropic modification of Ti and is difficult to distinguish from α′-Ti due to the near coincidence of their diffraction peaks.

The alloy's initial martensitic microstructure after LPBF is shown in Figure 5A. The fine martensite is characterized by a typical needle-like structure and is accompanied by a high porosity. For the bulk reference material in the as-printed state, the porosity, determined by the gravimetric method, was 3.62 vol % (Table 1), which is

in agreement with literature-reported values for standard LPBF parameters. This porosity likely contributed to the reduced ductility observed in mechanical testing.

After the application of the HIP process, the microstructure underwent significant changes. The martensite phase transformed into a dual-phase α + β titanium structure (Figure 5B).

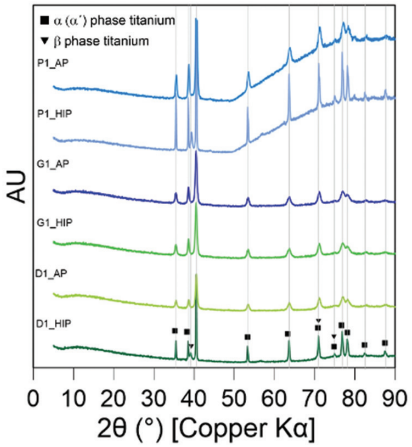

Figure 4. X-ray diffraction (XRD) analysis of the porous samples shows their phase composition
Abbreviations: D_AP: Diamond as-printed sample; D_HIP: Diamond hot isostatically pressed sample; G_AP: Gyroid as-printed sample; G_HIP: Gyroid hot isostatically pressed sample; P_AP: Porous as-printed sample; P_HIP: Porous hot isostatically pressed

Figure 6 shows microstructures of the porous diamond and gyroid structures in the as-printed and HIPed states. In both cross-sections, numerous small internal matrix pores (visible as dark spots) are present within individual struts. HIP transformed the martensite phase into α + β titanium structure and significantly reduced internal porosity to <0.01 vol %.

Figure 7 summarizes the quantitative μCT analysis of pores within the metallic matrix. The analysis focused exclusively on pores fully enclosed by the metallic matrix, excluding the designed macroporosity of the TPMS structures. As shown in Figure 7A, the median Feret diameter of matrix pores decreased after HIP by 38% (from 30.7 μm to 19.0 μm) in the gyroid structure and by 46% (from 30.6 μm to 16.3 μm) in the diamond structure. The total pore count was also markedly reduced—from ~4,400 to ~400. These conclusions are consistent with the volume ratios of pores shown in Figure 7B, illustrating the quantitative description of pores and their mutual relations with the matrix. This comparison is especially important due to potential errors caused by cropping slightly different areas during analysis. For the TPMS structures, the designed macroporosity constituted the largest proportion of sample volume, with minimal impact of the HIP process on this value. In contrast, the matrix pores identified by μCT accounted for up to 1 vol % of the sample volume. These unintended pores were significantly reduced after

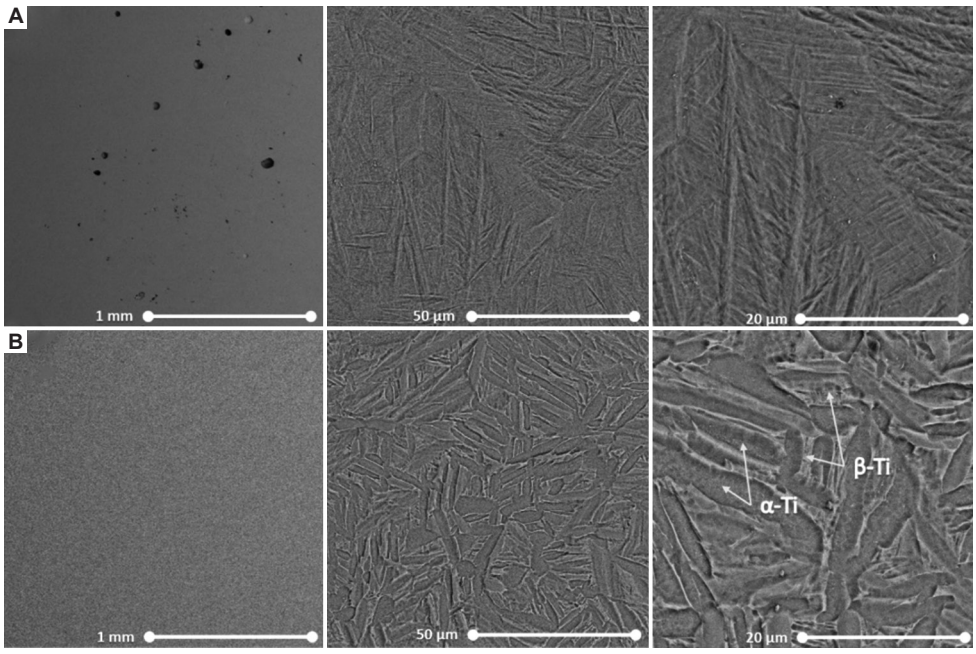

Figure 5. Ti-6Al-4V LPBF microstructure (SEM backscatter). (A) LPBF samples with a needle-like martensitic structure in their as-printed condition. (B) LPBF samples after the HIP process at 950°C and 200 MPa
Abbreviations: α-Ti: α phase titanium; β: β phase titanium; HIP: Hot isostatic pressing; LPBF: laser powder bed fusion; SEM: Scanning electron microscopy

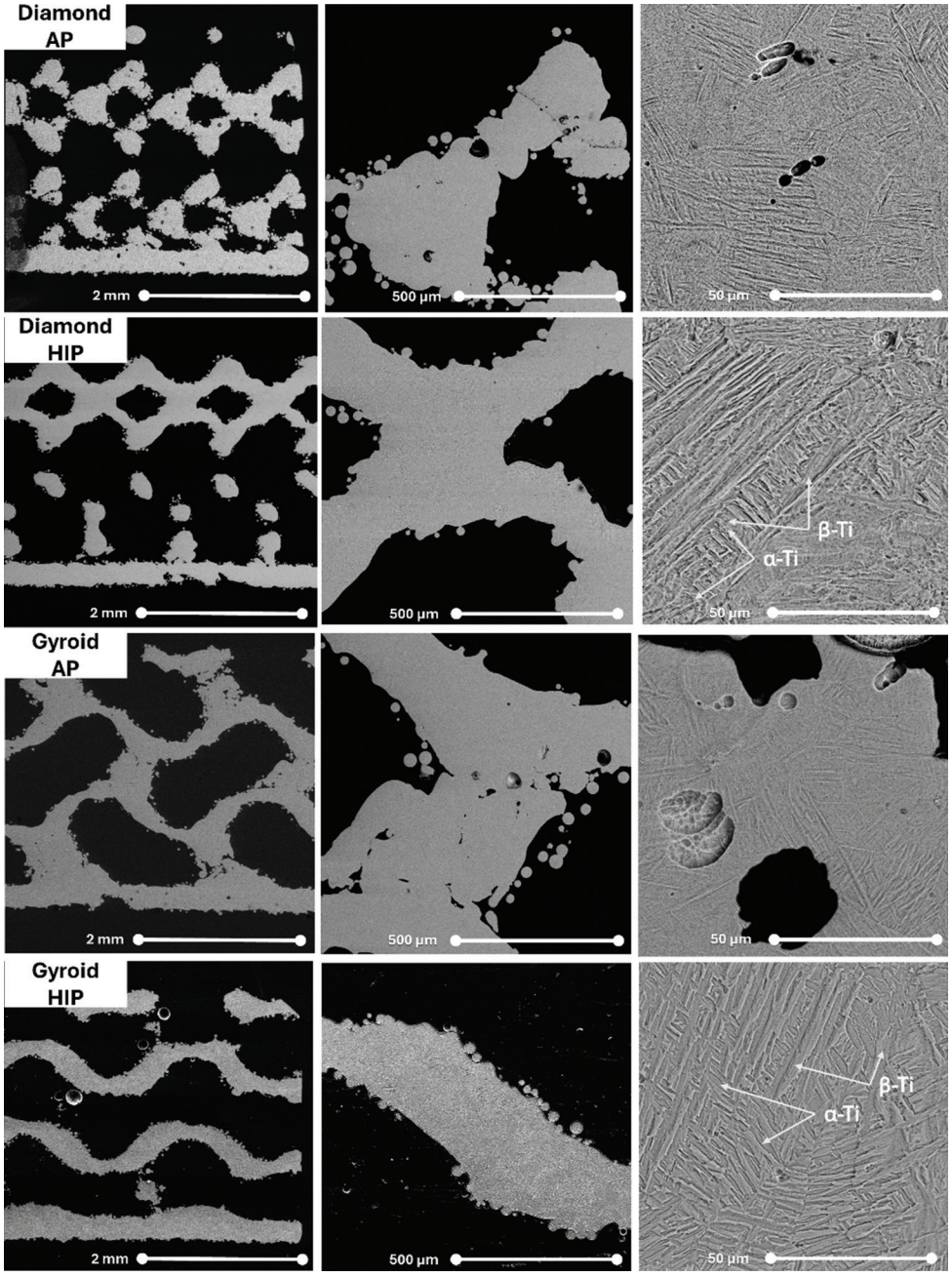

Figure 6. Ti-6Al-4V LPBF porous diamond and gyroid microstructure (SEM back-scattered). Needle-like martensitic structures in the as-printed condition and the corresponding microstructure after HIP at 950°C and 200 MPa

Abbreviations: HIP: Hot isostatic pressing; LPBF: Laser powder bed fusion; SEM: Scanning electron microscopy; α-Ti: α phase titanium; β: β phase titanium

HIP, indicating a strong link to improved mechanical properties. However, μCT was not used to evaluate overall macroporosity in bulk samples.

3.2. Mechanical properties

It is well established that HIP significantly influences the microstructural evolution of Ti-6Al-4V components, particularly by eliminating internal porosity and transforming the martensitic phase into an α + β equilibrium structure. Since the same HIP process was applied to the additively manufactured porous gyroid and diamond scaffolds, it is methodologically sound to first evaluate its effect on the bulk material. Although tensile testing cannot be directly applied to porous samples due

to their complex geometry and limitations in gripping the sample without causing structural damage, testing the bulk material provides an essential reference. The underlying microstructural mechanisms—porosity closure and phase transformation—are shared between the bulk material and the struts of the porous structures. Therefore, testing the mechanical properties of the bulk material is a relevant indicator of the changes in the mechanical response of the scaffold struts post-HIP.

A range of tests was carried out on reference bulk specimens at room temperature to characterize these changes, with the results expressed in terms of hardness measurements (HV1) and uniaxial tensile properties (Figure 8A and Table 1). The HIP-treated samples exhibited a reduction in hardness from 353 HV1 to 323 HV1, reflecting a phase transformation from a fine martensitic microstructure to a more stable α + β configuration. This transformation was also evident in the tensile properties: The as-built condition exhibited high strength (Ultimate tensile strength [UTS] ≈ 1300 MPa) but limited ductility (elongation ≈ 3%), whereas the HIPed samples displayed reduced strength (UTS ≈ 1024 MPa) and substantially improved ductility (elongation ≈ 17%). The results obtained are in line with the microstructural observations and the hardness trend.

Fractographic analysis of the tensile specimens corroborates this interpretation. The fracture surface of the as-built sample exhibited ductile dimples alongside visible, process-induced porosity. In contrast, the HIPed specimen showed uniform ductile fracture morphology with no observable porosity, indicating successful densification of the material (Figure 9).

The mechanical performance of porous gyroid and diamond structures under compressive and flexural loading is summarized in Figure 8B and C, Table 1. The gyroid structure demonstrated superior mechanical behavior compared to the diamond structure, due to its continuous curvature and more uniform stress distribution. HIP treatment enhanced both the compressive strength

A

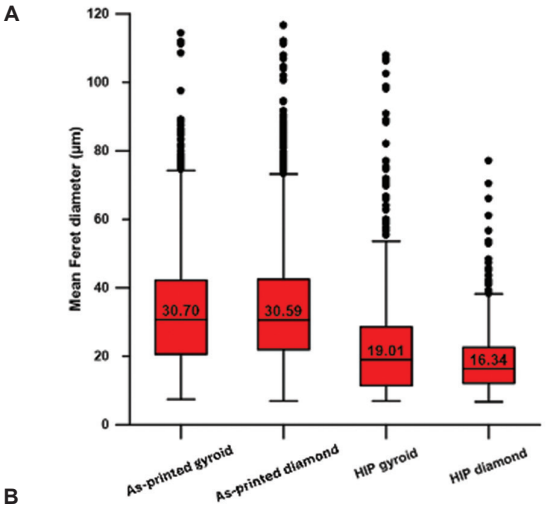

B

Type of ratio	As-printed gyroid	As-printed diamond	HIP gyroid	HIP diamond
	(vol. %)			
Matrix : Matrix pores	0.5	1.0	0.02	0.02
Triply periodic structure pores : Matrix	48.4	42.9	51.2	41.5
Matrix : Triply periodic structures pores	208.6	233.0	186.2	241.0
Triply periodic structure pores : Matrix pores	0.2	0.4	0.01	0.01

Figure 7. Effect of hot isostatic pressing (HIP) on pore size distribution and phase composition in 3D-printed TPMS structures, highlighting changes in Feret diameter and relative fractions of matrix and pores. (A) Box-whisker plot showing the mean Feret diameter of as-printed and HIPed samples. (B) Relative proportions of the matrix, matrix pores, and the intentionally created pores within the printed TPMS structures
Abbreviations: HIP: Hot isostatic pressing; TPMS: Triply periodic minimal surface

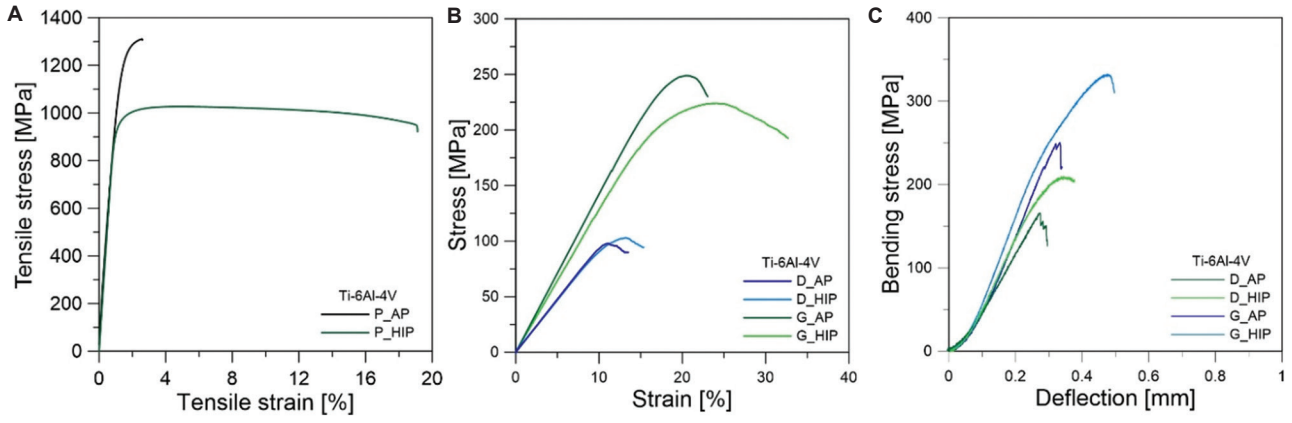

Figure 8. Mechanical properties of the Ti-6Al-4V alloy. (A) Typical stress-strain curves of bulk LPBF samples. (B) Compressive stress-strain curves of the porous samples. (C) Bending stress-strain curves of the porous samples
Abbreviations: D_AP: Diamond as-printed sample; D_HIP: Diamond hot isostatically pressed sample; G_AP: Gyroid as-printed sample; G_HIP: Gyroid hot isostatically pressed sample; LPBF: Laser powder bed fusion; P_AP: Porous as-printed sample; P_HIP: Porous hot isostatically pressed

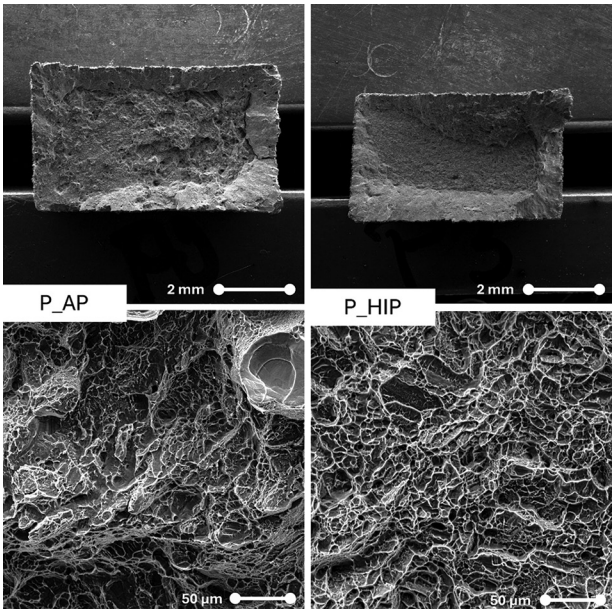

Figure 9. Fracture surfaces of LPBF-produced porous samples before and after HIP treatment. Corresponding high-magnification details of the fracture surfaces are shown below each main image, demonstrating the typical differences in fracture morphology, pore distribution, and surface roughness caused by the HIP
Abbreviations: HIP: Hot isostatically pressed; LPBF: Laser powder bed fusion; P_AP: Porous as-printed sample; P_HIP: Porous hot isostatically pressed

and the plastic deformation capacity of both topologies. For example, the compressive strain of failure increased from 23% to 34% in the gyroid structure. Although there was a slight reduction in ultimate compressive strength (from 249 MPa to 222 MPa), which is likely due to reduced dislocation density and stress relaxation, the increase in ductility is important for applications requiring mechanical reliability under cyclic or impact loading. This is particularly important for biomedical implants, where structural integrity and damage tolerance are essential.

Differences in elastic modulus were also observed between the two types of scaffolds. The gyroid structure exhibited an elastic modulus approximately 1.6 times higher than the diamond structure in the as-built condition and 1.4 times higher after HIP treatment. This reflects the influence of geometric design on stiffness and mechanical anisotropy.

Three-point bending tests (Figure 8C) confirmed the superior flexural performance of gyroid architecture. HIP processing resulted in a ~30% increase in maximum bending stress for both geometries. However, due to progressive micro-fracturing during loading, the stress-strain curves did not display a distinct linear region, which makes precise modulus determination impractical.

SEM of fractured porous samples (Figure 10) revealed residual porosity and unmelted particles in the LPBF condition, primarily in the cores of the struts. After HIP, these defects were eliminated, and the fracture surfaces exhibited fully ductile morphologies dominated by equiaxed dimples. Although macroscopic plastic deformation was not visible during the bending test, the higher fracture strain observed in the HIPed samples compared to the as-built ones is consistent with the tensile test data.

4. Discussion

4.1. Microstructure

The thermal history of Ti-6Al-4V has a significant impact on its microstructure, which in turn is influenced by the applied temperature and cooling rates.[4,40] The LPBF process involves subjecting powdered material to extreme cooling rates (10^3–10^6 K/s). This is achieved by rapidly melting the material with a highly energetic laser beam. This induces a fine acicular martensitic α′ microstructure (Figures 5 and 6) and results in the material having a relatively high residual stress. Directional solidification and repeated thermal cycling during layer formation also lead to pronounced anisotropy.[37-39]

To address these limitations, post-processing methods, such as HIP are commonly employed. HIP simultaneously applies high pressure (>100 MPa) and an elevated temperature (≈920°C for Ti-6Al-4V), which promotes phase transformation (α' → α + β), heals internal defects, and homogenizes the microstructure.[28-30] As demonstrated in previous studies, this process improves ductility and fatigue resistance while reducing anisotropy.[31,41] Although grain coarsening during HIP can cause a slight decrease in tensile and yield strength, the process generally produces a more balanced set of mechanical properties compared to as-built LPBF parts.[42]

However, in the context of porous structures, HIP introduces an additional dimension of complexity: Dimensional stability and structural integrity. Under multiaxial compressive stress and at an elevated temperature, internal pores collapse and surface-connected defects gradually close, leading to a redistribution of material volume. This localized densification can induce slight but significant dimensional changes, particularly in complex porous architectures, such as lattice structures. These changes can affect the geometric fidelity and mechanical response of the final part.

Since pore volume and connectivity vary according to unit cell topology (e.g., gyroid vs. diamond), the magnitude of structural shrinkage may also differ. For

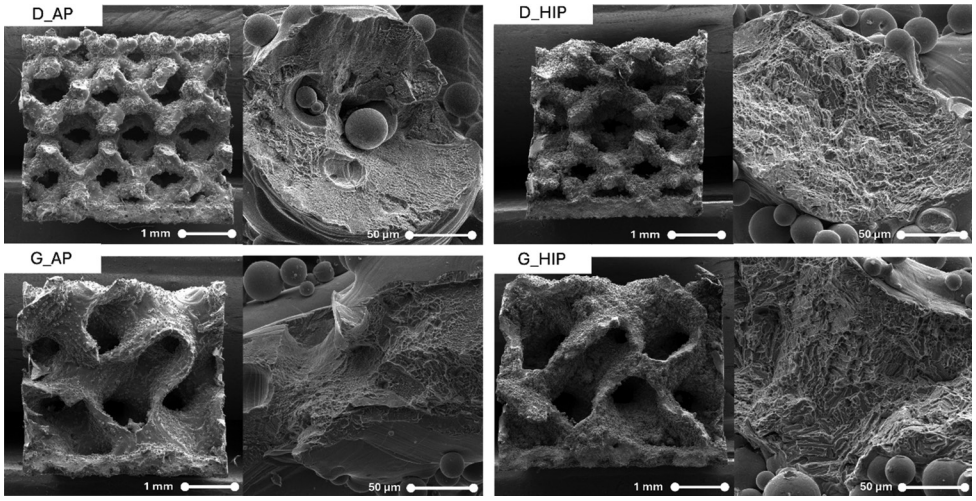

Figure 10. Fracture surfaces of LPBF-fabricated porous structures with diamond and gyroid geometries in the as-printed and HIP-treated states. Corresponding high-magnification details of the fracture surfaces are shown on the right side of each main image
Abbreviations: D_AP: Diamond as-printed sample; D_HIP: Diamond hot isostatically pressed sample; G_AP: Gyroid as-printed sample; G_HIP: Gyroid hot isostatically pressed sample; HIP: Hot isostatically pressed; LPBF: Laser powder bed fusion

example, if the initial pore volume fraction in a diamond scaffold is known from image-based quantification, the change in cross-sectional area or total volume after HIP can be theoretically estimated by subtracting the eliminated porosity from the original scaffold geometry. In practice, however, such changes may lead to a reduction in strut cross-section, alterations in relative density, and deviations from nominal CAD dimensions. Furthermore, the phase transformation from martensite to $\alpha + \beta$ can be accompanied by volumetric contraction. Though this is generally minor in bulk alloys, it can become significant in thin, highly curved features of porous architecture.

Thus, a comprehensive understanding of HIP-induced dimensional evolution is critical for applications requiring high-dimensional precision (e.g., patient-specific implants or load-bearing structures). Future studies may benefit from integrating *in situ* or *ex situ* digital volume correlation or high-resolution μCT to precisely quantify these changes, enabling predictive compensation during the design stage.

4.2. Mechanical properties

As shown in Table 1 and Figure 8, the application of HIP reduces the yield strength, UTS, strain to fracture, and Vickers hardness (HV1) compared with the as-built condition. This reduction is primarily associated with the transformation of the fine martensitic α' structure into a coarser two-phase $\alpha + \beta$ structure during high-temperature exposure in the dissolution annealing region.[35,41] HIP also eliminates internal defects (Figures 5 and 6), but the residual porosity of the material remains a factor influencing the final mechanical response. Porosity affects tensile and bending test performance much more than microhardness and compressive measurements. Therefore, hardness measurements in this study mainly reflect microstructure changes rather than porosity effects.[22] For example, HV1 values in the as-printed state were 395 ± 18 HV0.5 (diamond) and 415 ± 18 HV0.5 (gyroid), compared with 353 ± 11 HV1 for the HIP-treated bulk LPBF specimen (P1_AP) and about 331 ± 7 HV1 for commercial Ti-6Al-4V.[22] The P1_as-built sample is noticeably harder due to the finer lamellar microstructure produced by LPBF rapid cooling. While higher porosity typically reduces strength, pore arrangement and distribution can locally influence hardness. For instance, a fractal-like pore distribution may alter crack initiation and propagation, occasionally increasing local hardness.[42] Processing-induced phase transformations—such as crystallization of initially amorphous powders—can also enhance hardness.[43]

For biomedical Ti-6Al-4V alloy, achieving a UTS between 860 MPa and 1330 MPa and elongation between 10% and 25% is considered acceptable.[44-46] These properties are influenced by microstructure, alloying elements, and precise heat treatment processes, which together ensure the alloy's suitability for medical use. The LPBF as-built specimens in this study achieved UTS of ~1283 MPa, exceeding the lower bound, but with reduced ductility (~6%). After HIP, the UTS decreased to ~1024 MPa, while elongation improved to ~17%, comparable to the as-annealed condition after conventional heat treatment.[4] This strength–ductility trade-off is consistent with other reports showing that laser-based AM parts exhibit strengths comparable to age-hardened Ti-6Al-4V due to

their fine microstructure,[3,47] while HIP shifts properties toward a more ductile profile through microstructural coarsening.

Testing of porous structures was not possible due to their dimensions; therefore, compressive testing was carried out. The reported compressive strength of Ti-6Al-4V implants varies between 186 MPa and 462 MPa, depending on the design and porosity.[48] As shown in Figure 8 and Table 1, the diamond structure exhibited a linear elastic response up to approximately 80 MPa, which corresponds to its compressive yield strength. By contrast, the gyroid structure maintained a linear response up to around 160 MPa, which is also consistent with its measured yield strength. Beyond these points, both structures entered a non-linear deformation associated with plastic collapse. These results align with previous findings, such as Barui *et al.*,[49] who reported approximately 200 MPa compressive strength for microporous cylinders (Young's modulus ~4 GPa), and Li *et al.*,[50] who showed a compressive strength of 194.6 MPa for a porous Ti-6Al-4V implant—comparable to the gyroid structure here. The present porous specimens exhibited strengths of 47.0 ± 12.1 MPa (diamond) and 90.0 ± 4.0 MPa (gyroid).

The designed porosity for both diamond and gyroid structures was 64–72%, depending on lattice geometry (Figures 5 and 6). Such controlled porosity reduces stress shielding and promotes osseointegration, with the target of approximating natural bone stiffness for long-term implant stability.[53,54] HIP treatment reduced microporosity—potential crack initiation sites—thereby improving material integrity. However, this densification also slightly reduced UCS by modifying load distribution within the lattice. As expected, the compressive performance of porous lattices remains substantially below that of dense Ti-6Al-4V,[23] even though hardness values between porous and bulk specimens were comparable.

The study also included three-point bending tests to assess the stiffness and flexural strength of the porous implant. The results showed the same trend as the compressive tests, with the porous diamond structure exhibiting lower performance compared to the gyroid structure (Figure 8), which achieved a higher UBS (Table 1). For both structures, the HIP treatment led to an improvement in the UBS value (diamond: 164–214 MPa; gyroid: 261–315 MPa). The results of Suresh *et al.*[51] similarly showed that LPBF-produced porous Ti-6Al-4V implants have low stiffness and high porosity, favorable for biomedical applications, with reduced stiffness (80 GPa) and increased cell proliferation. Compared to Li *et al.*[50] (max bending strength 126.3 MPa), both porous structures in this study achieved higher bending strength in both the as-built and HIP conditions.

Interestingly, the improvement in mechanical performance following HIP is not uniform across all loading modes and scaffold geometries. For instance, gyroid structures demonstrated a substantial increase in flexural strength, whereas diamond structures exhibited only modest enhancement. This divergence may be attributed to differences in stress distribution under bending, influenced by unit cell design and load-bearing pathways. Furthermore, localized densification effects induced by HIP may benefit certain geometries more than others, depending on their internal curvature and pore connectivity.

Previous work highlights further distinctions in failure modes: Diamond lattices tend to fail abruptly through sudden strut buckling, whereas gyroid lattices fail more gradually through progressive wall collapse.[52] Thus, scaffold geometry strongly influences mechanical behavior and overall performance. Although a full mechanistic analysis was beyond the scope of this work, these observations underscore the importance of tailoring post-processing strategies, such as HIP, to both geometry and loading conditions.

5. Conclusion

This study examined the effect of HIP post-processing on the microstructure and mechanical properties of Ti-6Al-4V manufactured by LPBF. The key findings are: (1) HIP at 950°C transformed martensite α' into a two-phase α + β structure; (2) Pores produced during LPBF were reduced in volume; (3) Microstructural changes reduced mechanical properties but increased ductility; and (4) The applied post-processing treatment effectively reduced microporosity not only in bulk samples but also in porous scaffold structures, leading to improved mechanical properties. While further optimization of AM parameters may enhance the quality of porous structures, the present results demonstrate HIP's significant positive impact on both types of samples.

Acknowledgments

We gratefully acknowledge Jan Drahokoupil for his assistance with the micro-CT measurements.

Funding

This work was supported by the project "Mechanical Engineering of Biological and Bioinspired Systems" (Project No. CZ.02.01.01/00/22_008/0004634) funded

by "Programme Johannes Amos Commenius," Excellent Research Call. It was also supported by the Ministry of Health of the Czech Republic in cooperation with the Czech Health Research Council (Project No. NW25-08-00044). The authors also acknowledge the grant of Specific University Research (Grant No. A1_FCHT_2025_011).

Conflicts of interest

The authors declare that they have no competing interests.

Author contributions

Conceptualization: Dalibor Vojtech and Marketa Strakova
Investigation: Marketa Strakova, Jonas Divin, and Jan Drahokoupil
Methodology: Marketa Strakova, Jiri Kubasek, and Jan Pinc
Writing – original draft: Marketa Strakova
Writing – review and editing: Jiri Kubasek, Jan Pinc, and Dalibor Vojtech

Ethics approval and consent to participate

Not applicable.

Consent for publication

Not applicable.

Availability of data

The data are accessible through the Zenodo repository: https://doi.org/10.5281/zenodo.16794521

References

1. Pushp P, Dasharath SM, Arati C. Classification and applications of titanium and its alloys. *Mater Today Proc*. 2022;54(2):537-542.

   doi: 10.1016/j.matpr.2022.01.008

2. Elitzer D, Jäger S, Höll C, *et al*. Development of microstructure and mechanical properties of TiAl6V4 processed by wire and arc additive manufacturing. *Adv Eng Mater*. 2022;25:2201025.

   doi: 10.1002/adem.202201025

3. Carroll BE, Palmer TA, Beese AM. Anisotropic tensile behavior of Ti-6Al-4V components fabricated with directed energy deposition additive manufacturing. *Acta Mater*. 2015;87:309-320.

   doi: 10.1016/j.actamat.2014.12.054

4. Donachie MJ. *Titanium: A Technical Guide*. United States: ASM International; 2000. p. 369.

5. Etesami SA, Fotovvati B, Asadi E. Heat treatment of Ti-6Al-4V alloy manufactured by laser-based powder-bed fusion: Process, microstructures, and mechanical properties correlations. *J Alloys Compds*. 2022;895:162618.

   doi: 10.1016/j.jallcom.2021.162618

6. Mohammed MT. Mechanical properties of SLM-titanium materials for biomedical applications: A review. *Mater Today Proc*. 2018;5(Pt 3):17906-17913.

   doi: 10.1016/j.matpr.2018.06.119

7. Gu DD, Shen Y, Popovich VA, Wissenbach K. Laser additive manufacturing of metallic components: Materials, processes and mechanisms. *Int Mater Rev*. 2012;57(3):133-164.

   doi: 10.1179/1743280411Y.0000000014

8. Mueller B. Additive manufacturing technologies-rapid prototyping to direct digital manufacturing. *Assembly Automat*. 2012;32(2).

   doi: 10.1108/aa.2012.03332baa.010

9. Frazier WE. Metal additive manufacturing: A review. *J Mater Eng Perform*. 2014;23(6):1917-1928.

   doi: 10.1007/s11665-014-0958-z

10. Dutta B, Froes FH. Additive manufacturing of titanium alloys. *AMP Tech Artic*. 2014;172(2):18-23.

11. Hollander DA, Perez MC, Brinkmann M, *et al*. Structural, mechanical and *in vitro* characterization of individually structured Ti-6Al-4V produced by direct laser forming. *Biomaterials*. 2006;27(7):955-963.

    doi: 10.1016/j.biomaterials.2005.07.041

12. Leuders S, Thone M, Riemer A, *et al*. On the mechanical behavior of titanium alloy TiAl6V4 manufactured by selective laser melting: Fatigue resistance and crack growth performance. *Int J Fatigue*. 2013;48:300-307.

    doi: 10.1016/j.ijfatigue.2012.11.011

13. Das S, Zhang GD, Li H, *et al*. Processing of titanium net shapes by SLS/HIP. *Mater Design*. 1999;20(2):115-121.

14. Vilaro T, Colin C, Bartout JD. As-fabricated and heat-treated microstructures of the Ti-6Al-4V alloy processed by selective laser melting. *Metall Mater Trans A*. 2011;42(10):3190-3199.

    doi: 10.1007/s11661-011-0731-y

15. Bai L, Chen Y, Cheng N, *et al*. Effects of heat treatment and hot isostatic pressing on microstructure and fatigue improvements in Ti-6Al-4V alloy fabricated by selective laser melting. *Mater Lett*. 2024;367:136641.

    doi: 10.1016/j.matlet.2024.136641

16. Yadav BN, Lin DW, Lin MC, *et al*. Implemented *in-situ* heat treatment process for controlling the residual thermal stresses during the fabrication of Ti-6Al-4V titanium alloy through additive manufacturing. *Mater Lett*. 2024;356:135580.

    doi: 10.1016/j.matlet.2023.135580

17. Huang G, Gu D, Liu H, Lin K, Wang R, Sun H. The role of graded layers in interfacial characteristics and mechanical properties of Ti6Al4V/AlMgScZr-graded multi-material parts fabricated using laser powder bed fusion. *Mater Sci*

Addit Manuf. 2024;3(2):3088.

doi: 10.36922/msam.3088

18. Strakosova A, Kubásek J, Michalcová A, Průša F, Vojtěch D, Dvorský D. High strength X3NiCoMoTi 18-9-5 maraging steel prepared by selective laser melting from atomized powder. *Materials* (*Basel*). 2019;12:4174.

    doi: 10.3390/ma12244174

19. Herzog D, Seyda V, Wycisk E, Emmelmann C. Additive manufacturing of metals. *Acta Mater*. 2016;117:371-392.

    doi: 10.1016/j.actamat.2016.07.019

20. Shi J, Liang H, Jiang J, Tang W, Yang J. Design and performance evaluation of porous titanium alloy structures for bone implantation. *Math Problems Eng*. 2019;2019:5268280.

    doi: 10.1155/2019/5268280

21. Yue X, Tang H, Lu S, *et al*. Impact behavior of AlSi10Mg porous structures with varying single-unit cell rotation angles fabricated via laser powder bed fusion. *MSAM*. 2025;4(2):025130019.

    doi: 10.36922/MSAM025130019

22. Fousová M, Vojtěch D, Kubásek J, Jablonská E, Fojt F. Promising characteristics of gradient porosity Ti-6Al-4V alloy prepared by SLM process. *J Mech Behav Biomed Mater*. 2017;69:368-376.

    doi: 10.1016/j.jmbbm.2017.01.043

23. Wang B, Luo M, Shi Z, *et al*. Porous titanium alloys for medical application: Progress in preparation process and surface modification research. *MSAM*. 2024;3(1):2753.

    doi: 10.36922/msam.2753

24. Gao X, Zhao Y, Wang M, Liu Z, Liu C. Parametric design of hip implant with gradient porous structure. *Front Bioeng Biotechnol*. 2022;10:850184.

    doi: 10.3389/fbioe.2022.850184

25. Verma R, Kumar J, Singh N, *et al*. Low elastic modulus and highly porous triply periodic minimal surfaces architectured implant for orthopedic applications. *Proc Instit Mech Eng E J Process Mech Eng*. 2022;239(4):1553-1561.

    doi: 10.1177/09544089221111258

26. Roudnicka M, Mertova K, Vojtech D. Influence of hot isostatic pressing on mechanical response of as-built SLM titanium alloy. *IOP Conf Ser Mater Sci Eng*. 2019;629(1):012034.

    doi: 10.1088/1757-899X/629/1/012034

27. Alcisto J, Enriquez A, Garcia H, *et al*. Tensile properties and microstructures of laser-formed Ti-6Al-4V. *J Mater Eng Perform*. 2011;20:203-212.

    doi: 10.1007/s11665-010-9670-9

28. Amsterdam E, Kool G. High cycle fatigue of laser beam deposited Ti-6Al-4V and Inconel 718. In: *Proceedings of the 25th Symposium of the International Committee on Aeronautical Fatigue (ICAF)*. Rotterdam, The Netherlands: Springer; 2009.

29. Alegre JM, Díaz A, García R, Peral LB, Cuesta II. Effect of HIP post-processing at 850 °C/200 MPa in the fatigue behavior of Ti-6Al-4V alloy fabricated by selective laser melting. *Int J Fatigue*. 2022;163:107097.

    doi: 10.1016/j.ijfatigue.2022.107097

30. Ma HY, Wang JC, Qin P, *et al*. Advances in additively manufactured titanium alloys by powder bed fusion and directed energy deposition: Microstructure, defects, and mechanical behavior. *J Mater Sci Technol*. 2024;183:32-62.

    doi: 10.1016/j.jmst.2023.11.003

31. Wang Y, Liu X, Zhang X, *et al*. Cell-size graded sandwich enhances additive manufacturing fidelity and energy absorption. *Int J Mech Sci*. 2021;211:106798.

    doi: 10.1016/j.ijmecsci.2021.106798

32. Wu MW, Lai PH. The positive effect of hot isostatic pressing on improving the anisotropies of bending and impact properties in selective laser melted Ti-6Al-4V alloy. *Mater Sci Eng A*. 2016;658:429-438.

    doi: 10.1016/j.msea.2016.02.023

33. Wu MW, Chen JK, Lin BH, Chiang PH. Improved fatigue endurance ratio of additive manufactured Ti-6Al-4V lattice by hot isostatic pressing. *Mater Design*. 2017;134:163-170.

    doi: 10.1016/j.matdes.2017.08.048

34. Lee J, Ha H, Seol JB, *et al*. Reverse effect of hot isostatic pressing on high-speed selective laser melted Ti-6Al-4V alloy. *Mater Sci Eng A*. 2021;807:140880.

    doi: 10.1016/j.msea.2021.140880

35. Lv Z, Li H, Che L, *et al*. Effects of HIP process parameters on microstructure and mechanical properties of Ti-6Al-4V fabricated by SLM. *Metals*. 2023;13:991.

    doi: 10.3390/met13050991

36. Yan X, Yue S, Ge J, Chen C, Lupoi R, Yin S. Microstructural and mechanical optimization of selective laser melted Ti6Al4V lattices: Effect of hot isostatic pressing. *J Manuf Process*. 2022;77:151-162.

    doi: 10.1016/j.jmapro.2022.02.024

37. Xu Q, Chen B, Bai Q, *et al*. Effects of hot isostatic pressing temperature on casting shrinkage densification and microstructure of Ti6Al4V alloy. *China Foundry*. 2017;14(5):429-434.

    doi: 10.1007/s41230-017-7178-8

38. Alketan O, Abu Al-Rub RK. MSLattice: A free software for generating uniform and graded lattices based on triply periodic minimal surfaces. *Mater Design Process Commun*. 2020;3:e205.

39. Školáková A, Pinc J, Kubik R, *et al*. The effect of pulsed laser on the surface state of 3D-printed triply periodic structures in TiAl6V4 alloy. *Prog Addit Manuf*. 2025.

doi: 10.1007/s40964-025-01254-7

40. Technologies Canada Inc. *DragonflyComet*. Montreal, Canada: Technologies Canada Inc.; 2022.

41. Su C, Yu H, Wang Z, Yang J, Zeng X. Controlling the tensile and fatigue properties of selective laser melted Ti-6Al-4V alloy by post treatment. *J Alloys Compds*. 2021;857:157552.

doi: 10.1016/j.jallcom.2020.157552

42. Kuang DM, Long ZL, Ogwu I, Kuang FL, Yang LM. DEM study on the effect of pore characteristic on single particle crushing behavior of porous particles. *Comput Geotechnics*. 2024;165:105919.

doi: 10.1016/j.compgeo.2023.105919

43. Pilliar RM, Filiaggi MJ, Wells JD, Grynpas MD, Kandel RA. Porous calcium polyphosphate scaffolds for bone substitute applications -- *in vitro* characterization. *Biomaterials*. 2001;22(9):963-972.

doi: 10.1016/s0142-9612(00)00261-1

44. Ji R, Zhang H, Chen L, Cheng L, Luo H, Mao J. Improving the strength and maintaining good ductility of as-forged Ti6Al4V alloy by regulating the microstructural defects. *Mater Sci Eng A*. 2024;911:146913.

doi: 10.1016/j.msea.2024.146913

45. Li J, Liu X, Luo X, *et al*. Overcoming the strength-ductility trade-off and anisotropy of mechanical properties of Ti6Al4V with electron beam powder bed fusion. *Mater Sci Eng A*. 2023;879:145301.

doi: 10.1016/j.msea.2023.145301

46. Liu J, Sun Q, Zhou C, *et al.* Achieving Ti6Al4V alloys with both high strength and ductility via selective laser melting. *Mater Sci Eng A*. 2019;766:138319.

doi: 10.1016/j.msea.2019.138319

47. Vrancken B, Thijs L, Kruth JP, Van Humbeeck J. Heat treatment of Ti6Al4V produced by selective laser melting: Microstructure and mechanical properties. *J Alloys Compds*. 2012;541:177-185.

doi: 10.1016/j.jallcom.2012.07.022

48. Gain AK, Cui Y, Zhang L. Pore-gradient Ti6Al4V alloy mimicking the properties of human cortical bones: The design of TPMS structures by selective laser melting. *Mater Sci Eng A*. 2024;915:147220.

doi: 10.1016/j.msea.2024.147220

49. Barui S, Chatterjee S, Mandal S, Kumar A, Basu B. Microstructure and compression properties of 3D powder printed Ti-6Al-4V scaffolds with designed porosity: Experimental and computational analysis. *Mater Sci Eng C Mater Biol Appl*. 2017;70:812-823.

doi: 10.1016/j.msec.2016.09.040

50. Li X, Wang CT, Zhang WG, Li YC. Properties of a porous Ti-6Al-4V implant with a low stiffness for biomedical application. *Proc Inst Mech Eng H*. 2009;223(2):173-178.

doi: 10.1243/09544119JEIM466

51. Suresh S, Sun CN, Tekumalla S, Rosa V, Ling Nai SM, Wong RC. Mechanical properties and *in vitro* cytocompatibility of dense and porous Ti-6Al-4V ELI manufactured by selective laser melting technology for biomedical applications. *J Mech Behav Biomed Mater*. 2021;123:104712.

doi: 10.1016/j.jmbbm.2021.104712

52. Timercan A, Sheremetyev V, Brailovski V. Mechanical properties and fluid permeability of gyroid and diamond lattice structures for intervertebral devices: Functional requirements and comparative analysis. *Sci Technol Adv Mater*. 2021;22:285-300.

doi: 10.1080/14686996.2021.1907222

53. Anatolie, T.; Sheremetyev, V.; Brailovski, V., Mechanical properties and fluid permeability of gyroid and diamond lattice structures for intervertebral devices: Functional requirements and comparative analysis. Science and Technology of Advanced Materials 2021, 22.

54. Naghavi, S. A.; Tamaddon, M.; Garcia-Souto, P.; Moazen, M.; Taylor, S.; Hua, J.; Liu, C., A novel hybrid design and modelling of a customised graded Ti-6Al-4V porous hip implant to reduce stress-shielding: An experimental and numerical analysis. Front Bioeng Biotechnol 2023, 11, 1092361.

ACCSCIENCE PUBLISHING

Materials Science in Additive Manufacturing

ORIGINAL RESEARCH ARTICLE

On the surface integrity resulting from laser powder bed fusion of Ti6Al4V: Improvements by cavitation abrasive surface finishing

Rohin Petram[1†], Conall Wisdom[1†], Alex Montelione[1†], Cole Nouwens[2], Angelina Martinez[1], Marquiz Silvestre[1], Dan Sanders[2,3*], Mamidala Ramulu[2], and Dwayne Arola[1,2*]

[1]Department of Materials Science and Engineering, University of Washington, Seattle, Washington, United States of America

[2]Department of Mechanical Engineering, University of Washington, Seattle, Washington, United States of America

[3]Sugino Machine Ltd., Toyama, Japan

Abstract

As the manufacturing readiness level of laser powder bed fusion (L-PBF) advances, post-processing has become increasingly important for achieving net-shape components and to enhance surface texture and integrity. Apart from surface roughness, one concern is the unique morphology of printed surfaces with vertical, upskin, and downskin inclinations. In this study, we characterized the surface texture and integrity of L-PBF Ti6Al4V with respect to build orientation. In the as-built condition, the downskin surfaces possessed the highest roughness, the largest effective surface stress concentration ($\overline{K_t}$), and the greatest presence of partially melted powder particles fused to the surface. Cavitation abrasive surface finishing (CASF) was adopted to improve surface quality, with consideration of the build orientation. The results indicated that CASF reduced roughness, lowered K_t posed by the surface texture, and introduced compressive residual stress regardless of the build orientation. Downskin surfaces were the most challenging to treat; they exhibited substantially greater $\overline{K_t}$ than the other orientations after treatment (>2×) and lower compressive residual stress (50%). More extensive powder coverage of the downskin surfaces appears to shield the underlying substrate from abrasive attack and direct implosion of cavitation bubbles, which are central to the CASF treatment mechanism. The importance of orientation to the effectiveness of CASF treatment is discussed, as well as strategies to overcome this challenge. Overall, downskin surfaces require greater surface treatment intensity or duration to obtain the same degree of improvement.

Keywords: Additive manufacturing; Laser powder bed fusion; Post-processing; Residual stress; Roughness; Stress concentration; Surface treatment; Titanium

†These authors contributed equally to this work

***Corresponding authors:**
Dwayne Arola
(darola@uw.edu)
Dan Sanders
(dsanders@suginocorp.com)

Citation: Petram R, Wisdom C, Montelione A, *et al*. On the surface integrity resulting from laser powder bed fusion of Ti6Al4V: Improvements by cavitation abrasive surface finishing. *Mater Sci Add Manuf*. 2026;5(1):025280062. doi: 10.36922/MSAM025280062

Received: July 12, 2025

Revised: August 15, 2025

Accepted: August 15, 2025

Published online: October 14, 2025

1. Introduction

Laser powder bed fusion (L-PBF) is a method of additive manufacturing (AM) that involves sequential deposition and melting of metal powder in a layer-by-layer process

to produce components of desired geometry. Notably, there are several advantages of L-PBF over traditional manufacturing techniques (*e.g.*, forging and machining), including comparatively low material waste, nearly unlimited geometric complexity, and the capability for producing customized components simultaneously in a single build.[1-4] While the geometric complexity achievable with L-PBF enables the manufacture of components unattainable by traditional methods,[5] it also introduces challenges. Specifically, increasing geometric complexity limits the available methods for post-processing of L-PBF components and their effectiveness.[6]

Fatigue is an important design consideration for many components produced by L-PBF, especially for those of titanium alloys.[7-12] It is widely recognized that the fatigue life of metal components is highly dependent on the surface texture and integrity resulting from the methods of processing.[13,14] Rough surfaces create stress concentrations that can reduce strength, depending on the level of ductility, as well as accelerate fatigue crack initiation and fatigue failure.[15-17] As such, surface quality and the corresponding surface topography, associated with the lay and profile valley distribution, are important to the overall fatigue performance of engineering components.[18-21] Components that are produced by powder bed fusion (PBF), including electron beam and laser, are recognized for their high surface roughness in the as-built condition, making surface integrity a major concern.[22-24] To reduce the detrimental effects of these surface qualities, L-PBF parts often require post-processing to improve their surface integrity.[25-27]

A unique aspect of metal components produced by PBF is that the surface texture is dependent on the geometric complexity and orientation of the part surface relative to the build plane.[5,6,28-31] To address metrology challenges, Cabanettes *et al.*[5] performed a detailed analysis of surfaces developed by L-PBF. They evaluated the utility of various methods for characterizing surface texture and roughness parameters for describing the quality and discriminating the effects of build/surface orientation. Equally relevant, the wide range of surface orientations in the build and their corresponding characteristics can affect the effectiveness of post-processing techniques employed to improve surface quality.[6] There are three primary surface orientations to consider. Component surfaces that are orthogonal to the build plane are regarded as vertical surfaces and do not incline relative to the incident laser. In contrast, when the exposed surface has an inclination and is facing upward toward the incident laser, it is referred to as an upskin surface. Upskin surfaces are supported by previously solidified metal layers underneath, and they typically exhibit less partially melted powder adhered to the surface.[22,32] In contrast, downskin surfaces face toward the build plate and are oriented toward unmelted powder without a previously solidified metal layer. This surface inclination typically results in higher levels of powder melted or sintered to the exterior surface.[22,32,33] Relevant to this specific surface topography is the "staircase" or stair-stepping effect.[34,35] However, partially melted powder accumulated on the surface can mask the staircase quality. Surfaces that are printed vertically do not exhibit the same staircase geometry and typically display intermediate powder concentrations. Therefore, components that are manufactured by L-PBF can have substantially different surface morphology in different areas, and assessments of new post-processing treatments should consider this variation in surface characteristics.

At present, chemical milling serves as the industry standard for reducing the roughness of L-PBF parts and is widely regarded as an effective method for improving surface finish.[36-38] However, due to the hazardous and toxic chemicals involved, there are workforce and environmental concerns with chemical milling.[39] In addition, if improving fatigue resistance is the objective of surface treatment, there are three aspects of consideration: surface roughness, effective stress concentration, and the residual stress.[40] While chemical milling is effective at removing material, it is not capable of introducing compressive residual stresses, a key component to improving the fatigue resistance of metallic parts. Shot peening can introduce residual stress, but requires line of sight, which is less compatible with complex AM parts that are designed with passages or internal cavities.[41,42] Several other peening techniques do not use solid shot particles. Waterjet peening (WJP)[43] and abrasive WJP,[44-46] a derivative of WJP, are potential surface treatment processes. Alternatively, cavitation peening uses a cavitating waterjet to peen the surface through the implosion of vapor bubbles.[47] While cavitation bubbles are often introduced by waterjet processes, they can also be induced using laser pulses and ultrasonic waves. However, limited information is available concerning the degree of smoothing and resulting residual stress applied to metal additive components using these methods.[47,48]

Cavitation abrasive surface finishing (CASF) is a variant of cavitation peening, whereby a cavitating waterjet is used to peen the surface of the targeted component that is submerged within an abrasive slurry tank. The implosion of the cavitation bubbles energizes the abrasive particles in the slurry, facilitating material removal and reducing surface roughness. Simultaneously, when cavitation bubbles implode upon contacting the part surface, they generate shock waves that induce localized plastic deformation and introduce compressive residual

stresses in the near-surface layers.[49-51] The nature of the CASF method of impingement has several advantages over its more well-known contemporaries. First, the slurry of water and abrasives is environmentally inert and does not pose the same risk as the acids used in chemical milling. In addition, compared to other treatments that are capable of reducing surface roughness or introducing compressive residual stress, CASF is capable of improving both of these qualities simultaneously.[36,37,52] However, it is unclear how the process varies when applied to surfaces with different textures arising from unique build orientations, and this aspect of treatment effectiveness has received limited attention.[52]

In this investigation, Ti6Al4V samples were printed by L-PBF with either vertical, upskin, or downskin orientations. The objective of this study was to evaluate the effectiveness of CASF surface treatment in improving the surface integrity of L-PBF Ti6Al4V parts with respect to the as-built condition. The improvements were characterized by changes in residual stress, surface texture, and surface stress concentration over several different printing orientations. The printed surfaces were characterized in terms of the surface roughness, effective stress concentration posed by the dominant valleys, and both the surface and subsurface residual stress. In addition, selected samples underwent CASF treatment at oblique angles of impingement to evaluate the effectiveness of non-orthogonal treatment. The unique capabilities of the CASF process and limitations are highlighted with respect to other post-processing methods.

2. Methods

2.1. Sample preparation

In this study, samples were prepared using Ti6Al4V powder via L-PBF with an EOS M290 printer (Electro Optical Systems, Germany). The Ti6Al4V powder was used in prior production builds and thus was in the "reused" condition without provenance. Additional details regarding the vendor, number of prior builds, or hours of exposure were not available. Nevertheless, the powder conformed to the requirements outlined in ASTM F2924,[53] which establishes the composition limits of potential contaminants. These details are not highly relevant to assessing the effects of the CASF process on surface texture and integrity.

The printed samples consisted of rectangular plates with a width and length of 25 and 50 mm, respectively, and with thicknesses of 2, 4, and 6 mm. Half of the plates were printed with vertical orientation, aligned parallel with the XZ-plane (as defined by ASTM 52921).[54] The other half was printed with the same orientation but with an offset angle of 45° with respect to the XZ plane (Figure 1A). Plates printed with 45° offset provided an upskin and downskin surface with identical orientation as the vertical surfaces. Printing was conducted in accordance with manufacturer-recommended settings, which were the default settings for Ti6Al4V.

2.2. Post-processing

After printing, the builds were heat-treated in an argon environment at 745°C for 2 h. The plates were then removed from the build plate using a band saw, and the stabilizing brackets and other unnecessary support structures were removed. The plates were then subjected to CASF treatment at Sugino Machine Ltd. (Toyama, Japan), using a newly developed automated system with computer numerical control. The plates were clamped along the edges, and a CASF jet was passed over the samples with a standoff distance from nozzle to plate surface of 50 mm. The CASF jet traversed along the major axis of the plate, which was perpendicular to the lay of the surface introduced by the layerwise progression of the build. Each pass was 4 mm apart, and the initial and final passes were outside the bounds of the plate to ensure complete treatment (Figure 1B). The slurry tank consisted of alumina abrasives with #200 mesh and approximately 30% abrasive concentration by weight. Several treatments were conducted, which spanned a jet traverse rate of 60–120 mm/min. These parameters were selected in partnership with Sugino Machine Ltd., based on an internal preliminary investigation that distinguished the most appropriate range of treatment conditions for this scoping study.

2.3. Surface texture

After the CASF treatments were conducted, the surfaces were evaluated using a commercial contact profilometer (Mahr MarSurf GD 25, Mahr, United States of America [USA]) with an MFW II Tip attachment having a 90° angle and 2 µm radius of curvature. Three-line scans were conducted for each specimen; all scans were performed along the major axis of the plate in the build direction, which is perpendicular to the principal lay to capture the surface height variation of the additive layers. For each profile, the average roughness (R_a), 10-point roughness (R_z), and peak to valley height (R_y) were calculated according to the ISO 4288 standard.[55] As defined by this standard, for a measured R_a of ≤10 µm, a cutoff length of 2.5 mm and traverse length of 15 mm were used. Some of the roughness scans produced an R_a above 10 µm. According to the ISO 4288 standard, a larger cutoff length and traverse length should be used to calculate roughness for these samples. However, the measurement stroke of the profilometer was only 25 mm long, negating the potential for the 8 and 48 mm cutoff and traverse lengths. As such, the longer scan

was not possible, and all roughness measurements used the 2.5 mm cutoff length.

2.4. Stress concentration factor

The profile data exported from the profilometer was used to select the most prominent valleys of each surface. Then, a graphical radius gauge was used to estimate the radius of curvature according to previously reported methods.[15,16] The six deepest valleys of each roughness scan were selected to estimate the degree of stress concentration. The root radius (ρ) of each valley was estimated graphically (Figure 2). The effective stress concentration factor ($\overline{K_t}$) was then calculated using the following equation:

$$\overline{K_t} = 1 + n\left(\frac{R_a}{\overline{\rho}}\right)\left(\frac{R_y}{R_z}\right) \quad \text{(I}$$

where the R_a, R_z, and R_y values refer to the arithmetic average roughness, 10-point roughness, and peak-to-valley roughness measurements, respectively. The value ($\overline{\rho}$) refers to the average profile valley radius estimated from the six dominant valleys assessed over the profile traverse length. According to this approach, the estimated ($\overline{K_t}$) for each surface represents the upper bound of stress concentration, which is represented by the family of notches present in the topography. Analysis of variance (ANOVA) was conducted to evaluate differences in the measured $\overline{K_t}$ values, with significance defined by a $p<0.05$.

2.5. Residual stress measurements

Residual stress in the Ti6Al4V samples was measured using the $\sin^2(\psi)$ measurement method.[56] X-ray diffraction was performed using a Bruker D8 Discover diffractometer

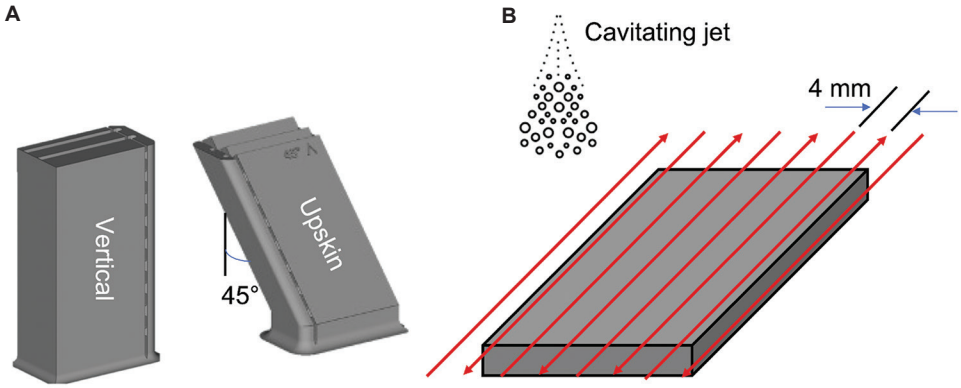

Figure 1. Samples and treatment. (A) The samples were built in clusters of rectangular plates with 2, 4, and 6 mm thickness and with either a vertical or 45° orientation. The 45° orientation provided surfaces with an upskin or downskin inclination. (B) The plate surfaces were treated by cavitation abrasive surface finishing with a raster pattern consisting of a 4 mm path center offset

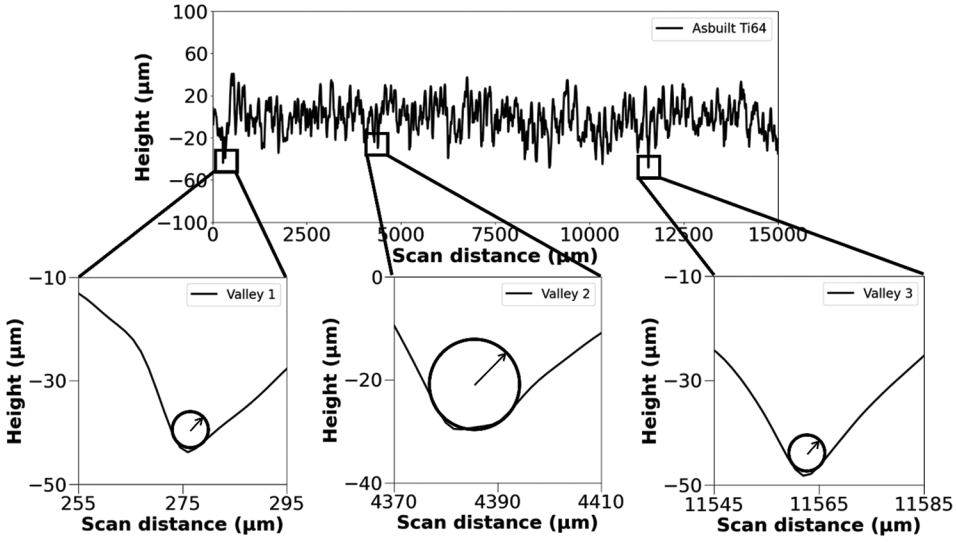

Figure 2. Representative surface profile from an as-built surface with vertical build orientation and measurement of selected profile valley root radii (ρ)

(Bruker, USA) equipped with a copper target (Cu Kα) operating at 50 kV and 1000 μA. A 0.5 mm collimator was used to focus the beam, and measurements from the diffracted [312] plane at 2θ = 110° were recorded using a Pilatus 100K large-area 2D detector. Each sample was analyzed at nine distinct orientations, combining Φ angles of 0°, 45°, and 90° with ψ angles of 0°, 22.5°, and 45°. The detector captured a 2θ range of 107°–113° over a 4-min scan for each orientation.[57] Residual stress values were determined from the diffraction peak positions using Bruker's Diffrac.Leptos7 software (Bruker, USA).

To measure residual stress as a function of depth beneath the treated surface, a sequential etching technique was used to remove material from the surface a few microns at a time without changing the underlying residual stress profile. Specifically, Kroll's reagent (etchant #192 of ASTM E407-7)[58] was applied for 3 min and then rinsed off with DI water. After each etching session, a micrometer was used to measure the remaining sample thickness, which was then used to calculate the thickness of material removed by etching. This process was repeated multiple times to achieve measurements as a function of depth, continuing until the depth at which no residual stress was detectable. To enhance the statistical power of the measurements, the treated surface was divided into four quadrants, and the residual stress was measured in each. These quadrants were then outlined with a thin layer of nail polish. The nail polish acted as a masking agent to protect the metal that it covered.

2.6. Microscopy

Scanning electron microscopy (SEM) was performed to observe the detailed surface morphology and validate the roughness measurements. The SEM analysis was performed using an Apreo-S SEM (ThermoFisher Scientific, USA) at voltage and current values of 25 kV and 3.2 nA, respectively.

To characterize changes in the surface texture resulting from CASF, the treated specimens were sectioned to expose the layered structure of the AM material for optical imaging. The specimens were mounted in black glass-filled epoxy (Allied 150-10105, Allied High Tech Products, Inc., USA) in cylindrical molds. The exposed surfaces were then polished using silicon carbide abrasive mesh pads from #240 to #800 mesh to level the surface (Allied 50 series, Allied High Tech Products, Inc., USA). Subsequently, abrasive polishing was performed using a 9 μm DiaLube diamond suspension on a Struers MD-Dac pad (Struers, USA), followed by a chemical polishing on a Struers MD-Chem pad with a solution of 10 mL 0.05 μm colloidal silica, 0.5 mL 5% ammonium hydroxide, and a few drops of 40% hydrogen peroxide. Micrographs were taken from the polished cross-section using an Olympus BX51M optical microscope (Olympus, USA) at between 5× and 50× magnifications.

3. Results

3.1. Surface morphology and texture

Representative SEM images of the sample surfaces in the as-built condition are displayed in Figure 3A-C for the vertical, upskin, and downskin inclinations, respectively. As evident from these images, numerous partially melted particles adhered to the substrate, and the density of coverage depends on the build orientation. The layer orientation is visible in the horizontal plane for both the vertical and upskin surfaces, whereas it is obscured on the downskin surface due to the higher density of adhered particles. Based on image analysis, estimates for the particle count were roughly 250, 40, and 540 particles/mm^2, respectively; these differences are statistically significant ($p \leq 0.05$).

The average surface roughness for the surfaces with vertical, upskin, and downskin inclinations is presented in Figure 4 as a function of treatment feed rate. The shaded background represents the range of roughness in the as-built condition, whereas the R_a values after CASF treatment are presented for each surface orientation as the mean ± standard deviation from three profiles. The direction of measurement is parallel to the build direction (z-axis), which is perpendicular to the layer orientation noted in Figure 2. As evident from Figure 4, CASF treatment reduced roughness for all three printing orientations across all feed rates. The largest reduction in R_a occurred on surfaces with a vertical orientation. Although the vertical and downskin surfaces displayed similar maximum reduction in roughness (approximately 50%), the downskin orientation had the highest roughness after CASF treatment. In addition, the downskin surfaces exhibited the highest sensitivity to the treatment feed rate, with a decrease of approximately 10 μm at the lowest feed rate. In contrast, the upskin surfaces exhibited a reduction in Ra of approximately 30% following CASF treatment, but the feed rate had no significant influence on the outcome.

3.2. Stress concentration

In addition to evaluating surface roughness, the radius of curvature (ρ) of the prominent valleys was measured for the three surface orientations in the as-built condition and after CASF. The effective valley root radii ($\bar{\rho}$) representing the average values are shown in Figure 5A as a function of the treatment feed rate. In the as-built condition, the valley radii ranged from 3 to 15 μm, independent of the

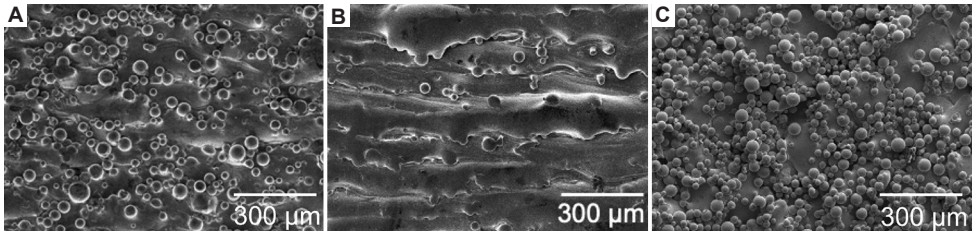

Figure 3. Scanning electron microscope images of the (A) vertical, (B) upskin, and (C) downskin surfaces in the as-built condition. The build direction is from bottom to top. The upskin and downskin surfaces resulted from printing a plate with a 45° inclination. Scale bars: 300 µm

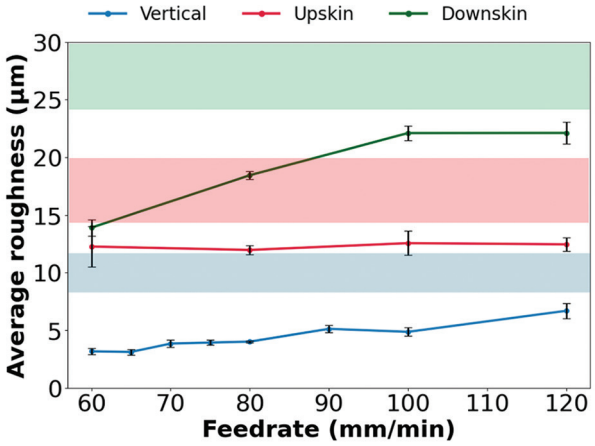

Figure 4. Comparison of the average surface roughness for the three surface orientations (vertical, upskin, and downskin) as a function of feed rate. The colored lines indicate the average roughness for each printing orientation (n = 5), and the lighter colored bars in the background represent the range of roughness in the as-built condition for the three surface orientations

orientation. Surprisingly, CASF treatment increased the $\overline{\rho}$, but only for the vertical orientation and at the lowest feed rate. In comparison, there are essentially negligible increases in the profile valley radii of the upskin and downskin surfaces after CASF treatment.

The effective stress concentration factor ($\overline{K_t}$) of the surfaces for the as-built condition and after CASF treatment is presented in Figure 5B. The importance of surface orientation is further apparent in the changes in $\overline{K_t}$ before and after treatment. Most notable is the reduction in stress concentration for the vertical orientation, approaching a stress concentration of 1 at the lowest feed rate. The reduction in $\overline{K_t}$ for the downskin surfaces is significant, ranging between 50% and 75% reduction over the feed rate range. The upskin surfaces exhibited the smallest reduction in $\overline{K_t}$ overall, with only a slight reduction at higher feed rates. Due to the absence of changes in $\overline{\rho}$ for the upskin and downskin conditions (Figure 5A), the reduction in $\overline{K_t}$ for these surfaces appears to be limited to the reduction in surface roughness. ANOVA results indicated that changes in $\overline{K_t}$ values with feed rate were significant ($p \leq 0.05$) for all orientations, except for the upskin orientation.

3.3. CASF treatment orientation

Several complementary CASF treatments were conducted to assess the influence of jet incident angle on the improvement of the surface quality. Performed as a preliminary effort, these experiments were conducted using the vertically printed samples, which were fixtured at a 45° angle with respect to the incident jet. These treatments were compared with the results of those conducted with a normal impingement angle (90°). Results for the R_a and $\overline{K_t}$ responses are displayed in Figures 6 and 7, respectively. As evident in Figure 6, treatment with non-orthogonal orientation resulted in lower reduction in roughness and higher post-treated roughness than the 90° orientation. Although the differences between the R_a for the 90° and 45° treatment orientations were significant over the majority of feed rates ($p \leq 0.05$), the difference was limited to approximately only 1 µm for all feed rates. The influence of treatment orientation on $\overline{\rho}$ and $\overline{K_t}$, as featured in Figure 7A and B, follows similar trends to the surface roughness. Although a reduction in treatment angle slightly diminished effectiveness—particularly at lower feed rates—the angled treatments still produced a substantial decrease in $\overline{K_t}$. As evident from Figure 6, this reduction in $\overline{K_t}$ is primarily attributed to the decrease in surface roughness rather than changes in $\overline{\rho}$.

3.4. Residual stress

Figure 8 features the surface residual stress distribution in samples printed with the vertical, upskin, and downskin orientations at different feed rates. All conditions resulted in compressive residual stress. While no clear dependence on feed rate was observed, a significant difference ($p \leq 0.05$) was found between the build orientations. Specifically, the upskin orientation had the highest residual stress, followed

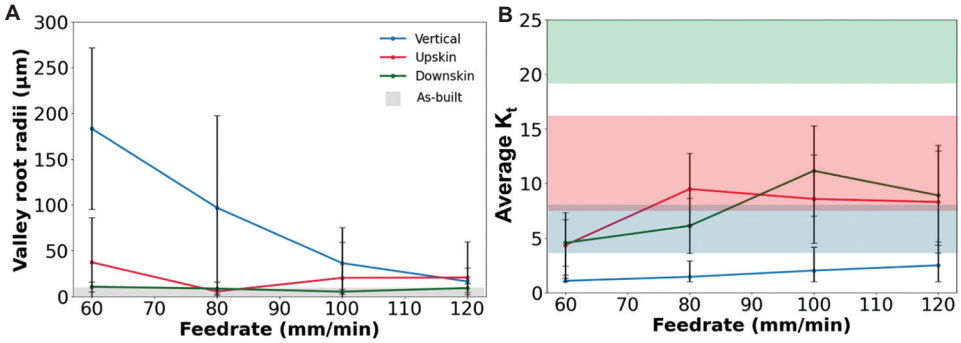

Figure 5. Comparison of surface characteristics of the three orientations (vertical, upskin, and downskin) after treatment and across different feed rates. (A) Effective valley root radii ($\bar{\rho}$) (n = 5). The gray bar represents the range in valley radii in the as-built condition for all three surface orientations. (B) Effective stress concentration factor ($\overline{K_t}$) (n = 5). The colored bars represent the $\overline{K_t}$ range for the as-built condition

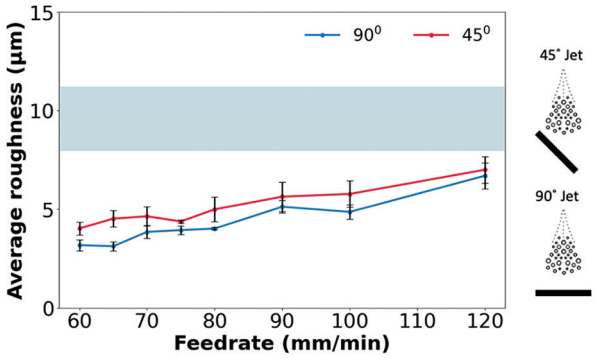

Figure 6. Comparison of average roughness for the vertically printed plates as a function of feed rate and the CASF treatment angle (n = 5). The light blue bar represents the range of as-built roughness before treatment
Abbreviation: CASF: Cavitation abrasive surface finishing

by the vertical and downskin orientations. This trend appears to correlate with the extent of powder coverage on the surface (Figure 3), suggesting that the residual stress introduced by CASF depends on the degree of powder coverage, which may inhibit deformation of the underlying substrate.

Figure 9 displays the influence of treatment orientation (45° vs. 90°) on the residual stress for samples printed with a vertical orientation. Akin to the trends in roughness (Figure 6), there was no significant difference in residual stress over the tested feed rates. However, the differences associated with the impingement angle were significant. Independent of feed rate, treated samples with a 45° impingement angle exhibited approximately 50% lower residual stress than treated surfaces with an orthogonal jet arrangement ($p \leq 0.05$).

Figure 10 presents the residual stress distribution within a single vertical orientation sample as a function of depth beneath the surface. The sample was treated with the jet oriented orthogonal to the surface and at a feed rate of 80 mm/min. The subsurface stress was measured at four different positions on the samples. The residual stress was highly consistent across all sites, with surface stress of approximately 400 MPa, in agreement with the distribution displayed in Figure 8. The stress decreased to 80 MPa within 30 µm from the treated surface, and measurements beyond this depth featured no further reduction in residual stress.

4. Discussion

The results revealed that CASF has the potential for improving the overall surface quality of Ti6Al4V components produced by L-PBF, as observed by the reduced surface roughness, a decrease in $\overline{K_t}$, and the introduction of compressive residual stress. However, the effectiveness of the process is influenced by both the printed surface orientation and the jet impingement angle, which warrants further discussion.

For all printing orientations and feed rates, the CASF process resulted in a reduction in R_a (Figure 4). Considering all three build orientations, the highest reduction occurred at the lowest feed rate. Notably, the treatment intensity increases with decreasing feed rate, which reflects the treatment duration per unit area. Moreover, the degree of improvement over the range of feed rate was not consistent among the three orientations. The upskin surfaces exhibited negligible changes at lower feed rates, whereas the downskin surfaces underwent significant improvement when the feed rate was reduced from 120 to 60 mm/min; the vertically printed metal exhibited a trend between these two extremes.

The orientation dependence in roughness improvements can be attributed to the particle coverage evident in Figure 3, which affects two components of smoothing: (i) the removal of partially melted particles through erosion, and (ii) the abrasive wear of the substrate peaks beneath

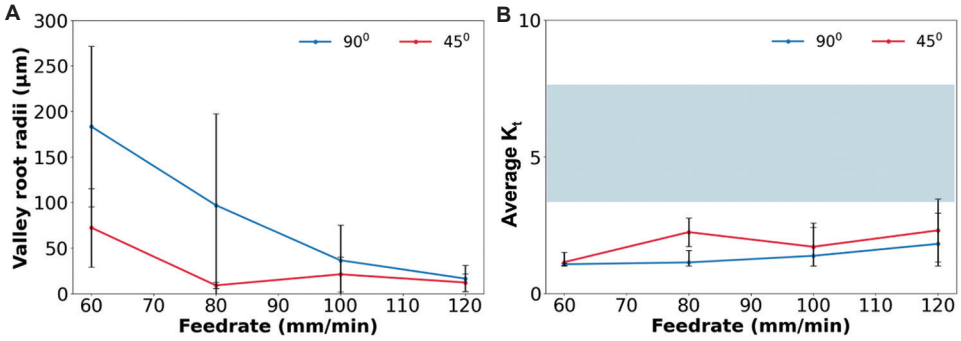

Figure 7. Comparison of surface characteristics of the two treatment orientations at different feed rates: (A) valley root radii and (B) effective stress concentration factor (K_t) ($n = 5$). The light blue shaded area indicates the range of K_t before CASF treatment
Abbreviation: CASF: Cavitation abrasive surface finishing

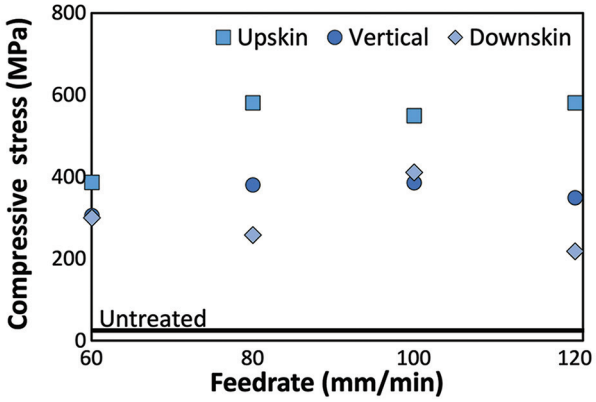

Figure 8. Comparison of compressive residual stress induced by CASF across the range of feed rates for samples with three build orientations: Vertical, upskin, and downskin surfaces
Abbreviation: CASF: Cavitation abrasive surface finishing

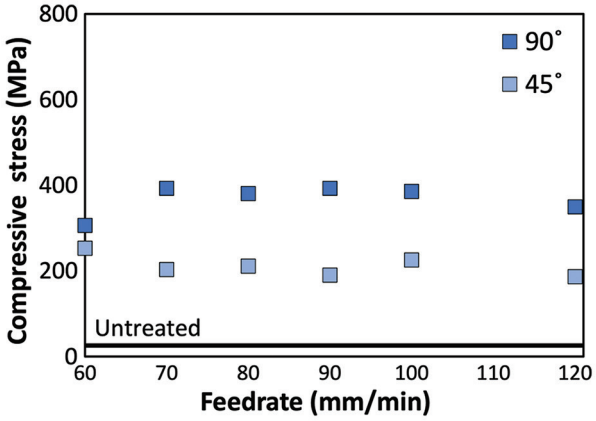

Figure 9. Comparison of residual stress from CASF treatment with jet impingement angles of 45° and 90°
Abbreviation: CASF: Cavitation abrasive surface finishing

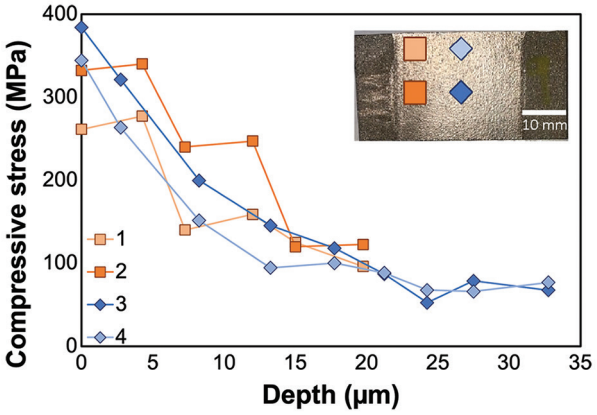

Figure 10. Subsurface residual stress gradient at four different locations. CASF treatment was conducted at a feed rate of 80 mm/min on a 6 mm thick vertically oriented L-PBF sample. Scale bar: 10 mm (inset)
Abbreviations: CASF: Cavitation abrasive surface finishing; LPBF: Laser powder bed fusion

the particle coverage. The more extensive changes in the downskin surface appear to result from the removal of the powder layer, which is most effective at low feed rates. In the case of the upskin surface, nearly all changes are related to the second component, i.e., abrasive wear, whereas the increase in treatment intensity coupled with a reduction in feed rate had a limited effect. Therefore, optimizing the effectiveness of CASF will require special consideration of feed rate as it relates to the metal target properties and build orientation. A slower feed rate should be applied to the downskin regions, whereas a higher speed could be used during the treatment of vertical and upskin surfaces. A full parametric study is warranted to further improve the effects of CASF treatment. Abrasive size, standoff distance, slurry concentration, and raster spacing are all parameters that could be explored and considered in the treatment of primary material candidates.

Although measurable, the difference in roughness reduction of the vertically printed surfaces treated by CASF at 90° and 45° was limited. This indicates that

CASF can significantly improve L-PBF surface quality even when the jet is not directly perpendicular to the surface. Such flexibility is advantageous for treating metal AM components with complex geometries, as well as the commercial viability of CASF as a practical finishing method. Both surface texture and integrity can be enhanced even under oblique treatment angles.

The reduction in R_a of L-PBF components using CASF depends on the as-built condition of the surface metal and the extent of powder coverage. For vertically printed samples, R_a decreased from approximately 10 μm to as low as 4 μm, which is comparable to shot peening (≈ 4 μm)[40,41] and appears superior to laser shock peening (≈ 15 μm).[40,59] It is important to highlight that comparing surface roughness results from different treatments is limited by the variability of AM parts, including the treatment parameters, the starting surface texture, and powder coverage. Figures 4 and 5 suggest that CASF is more effective at lower feed rates, though this may reduce productivity unless other parameters are adjusted. Further development efforts could potentially achieve surface quality comparable to leading industry treatments, including laser polishing and centrifugal finishing.[40]

The primary objective of applying CASF is arguably to improve the fatigue life of L-PBF components. An important aspect of the surface structure that contributes to fatigue crack initiation is the root valley radii (ρ).[60-63] Interestingly, while there was a reduction in $\overline{K_t}$ for all surfaces evaluated, the increase in $\overline{\rho}$ was most substantial for the vertical surfaces and at the lowest feed rates. Meanwhile, the upskin and downskin surfaces exhibited less improvement across the full feed rate range. For downskin surfaces, this is partly due to powder coverage, but it also relates to valley geometry—profile valleys between layers are too deep for the abrasives to fully smooth. In addition, the orientation of layer boundaries on upskin and downskin surfaces makes them more pronounced, providing shielding that limits CASF effectiveness.

The difference in surface structures is important to understanding their treatability. Cross-sectional views of the treated surfaces for the three build orientations are displayed in Figure 11. While most of the surface has undergone smoothing and reduction in surface height variation, some regions have notch-like residual features. These are apparent in the cross-sections of the upskin and downskin surfaces (Figures 11 and 12). The angular offset of the layers, combined with gravity, produced narrow valley openings, much smaller than the abrasive diameter, shielding them from CASF treatment while remaining potential sites for fatigue crack initiation. Although cross-sections are commonly used to study particle attachment, there is limited focus on valley geometry, orientation-related differences, and residual features that threaten durability.[5,34,64] The higher initial roughness of the upskin and downskin surfaces, combined with the aforementioned aspects of valley orientation, hampers the effectiveness of CASF. Residual valleys that are not fully treated remain a concern for these orientations. Designing L-PBF components for effective post-processing could minimize fatigue-critical regions in upskin and downskin areas, but the most impactful approach would be to enhance CASF effectiveness for these more challenging orientations.

Residual stress analysis revealed that CASF feed rate had little effect on surface stress, whereas printed build orientation played a significant role. Specifically, the highest surface residual stress reached up to 600 MPa and was observed in the upskin surfaces. The vertical and downskin surfaces reported surface stresses of 350 and 250 MPa, respectively. Comparison with the as-built surface morphology (Figure 3) indicates an inverse correlation between residual stress and the density of surface powder particles. The interaction of the CASF jet with these powder particles does not generate residual stress. Mechanistically, the cavitation bubbles are shielded from implosion on the underlying substrate until the partially melted particles are removed by erosion. Consequently, surfaces with lower particle density, such as upskin and vertical orientations, experience greater substrate deformation during treatment, resulting in higher residual stress. Optimizing CASF parameters to first remove particle coverage and then maximize residual stress, or combining CASF with complementary surface treatments, could further enhance this effect.

In addition to surface morphology, the impingement angle was identified as a key factor contributing to residual stress (Figure 9). Compressive residual stresses induced by CASF are greatest when the treatment is orthogonal to the surface. While smoothing during CASF is not largely dependent on the impingement angle (Figures 6 and 7), treating at an oblique angle can reduce surface residual stress by nearly 50% compared to a 90° angle. These results suggest that to maximize residual stress, the surfaces should be oriented orthogonal to the incident jet, which also results in the maximum degree of smoothing and reduction of the $\overline{K_t}$. However, if surface texture is the primary concern and residual stress is less critical, oblique treatment is acceptable.

In addition to the magnitude of surface stress, the depth of compressive stress is an equally important metric for fatigue resistance, as deeper stresses help reduce the effective stress around potential anomalies or near-surface stress

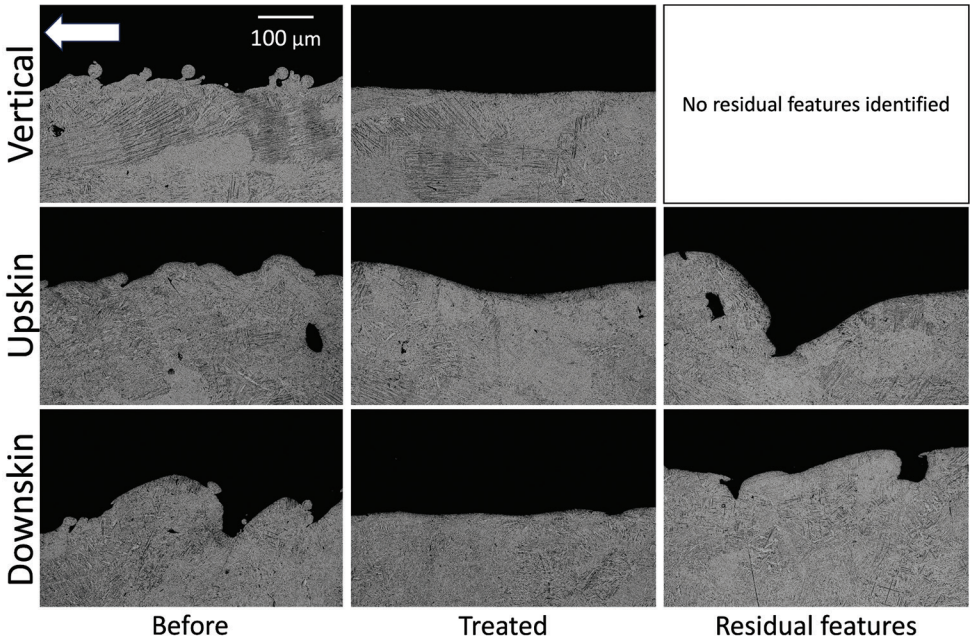

Figure 11. Cross-sectional images of printed samples with vertical, upskin, and downskin surfaces. The build direction is indicated by the arrow. Scale bar: 100 µm

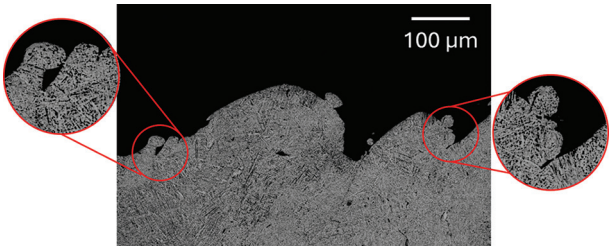

Figure 12. Cross-sectional view of a representative area of a downskin surface in the as-built condition, highlighting potential hidden valleys that are shielded from treatment

concentrations. Subsurface mapping (Figure 10) indicated a plateau in residual stress at a depth of approximately 30 µm. Shot peening, the mainstream surface treatment, can introduce residual stress up to depths of 150 µm or more below the surface.[65,66] Thus, when compared to shot peening, CASF has a lower depth of residual stress penetration within the range of treatment conditions used. However, the depth is compatible with other treatments. Water jet peening has been reported to induce residual stress up to 40 µm below the surface in similar titanium alloys.[43] It is plausible that increasing treatment pressure or intensity could enhance the depth of CASF-induced residual stress, warranting further investigation.

The compressive residual stress resulting from CASF of the upskin surface reached 600 MPa. Assuming that the lower stresses observed on vertical and downskin surfaces result from shielding by partially melted powder particles, it should be feasible to achieve comparable stress levels across all orientations by removing the particles and applying sufficient treatment intensity. Nevertheless, the surface residual stress achieved by CASF exceeds that of tribofinishing (500 MPa) and is similar to shot peening (350–650 MPa),[48,67] while also matching or surpassing recent results for laser cavitation peening (400–450 MPa).[48,49] These findings highlight the considerable potential of CASF as a post-processing technique for L-PBF titanium components, both for enhancing surface quality and introducing compressive residual stresses.[41,48-49,67] While the exact outcomes depend on material properties, similar benefits are anticipated for other metals processed via L-PBF.

Despite the novelty of the findings and new evidence supporting the use of CASF for post-processing L-PBF components, several limitations should be noted. First, the study was limited to Ti6Al4V. While similar results are expected for other sufficiently ductile metals, experimental validation is required to confirm this assumption. Second, the study relied on the use of $\overline{K_t}$ to describe surface stress concentration and quantify the influence of CASF on surface structures relevant to fatigue behavior. The $\overline{K_t}$ approach is considered appropriate for industrial applications due to its simplicity and use of conventional roughness parameters. However, a fracture mechanics approach[68,69] has been proposed to account for the influence of surface notches indicative of L-PBF builds on fatigue, as

well as other treatments based on stress concentration.[70] These alternative approaches were not considered in this study, as they are beyond the scope of the primary objective. Finally, while a major motivation for imposing compressive residual stress is to improve the fatigue life, fatigue testing was not included in this study. As a scoping study, the primary objective was to evaluate the overall potential for CASF to improve the surface integrity of L-PBF components. Future investigations should include fatigue testing post-CASF treatment to validate the anticipated improvements in component performance.

The combined effects of reduced surface roughness, lowered effective stress concentrations, and the introduction of compressive residual stress suggest that CASF could improve the fatigue resistance of metal components regardless of the AM method used. A notable advantage of CASF is its reliance solely on water and abrasives, avoiding the chemical hazards associated with many conventional treatments for Ti6Al4V, which pose risks to both operators and the environment. Nevertheless, the treatment conditions used in this investigation were based on a developing understanding of the process and have not yet been fully optimized. To enable widespread adoption, further work is required to refine CASF parameters for different materials and manufacturing conditions, ensuring consistent and maximized performance.

5. Conclusion

In this study, we evaluated the effect of CASF treatment on the surface texture, stress concentration, and residual stress of Ti6Al4V samples manufactured by L-PBF. In summary, the results showed that:

(i) The CASF process significantly improved surface smoothness for all build orientations, achieving an overall reduction in R_a of up to 50%. The upskin and downskin surfaces exhibited higher initial roughness in the as-built condition, and CASF produced a smaller overall reduction in roughness compared to the vertical orientation. For all surfaces except the upskin, the reduction in surface roughness increased as the treatment feed rate decreased.

(ii) The residual stresses introduced by CASF treatment were compressive for all treatment conditions and were generally independent of feed rate. However, residual stress was highly dependent on the build orientation and the treatment orientation. Although the residual stress reached up to 600 MPa at the surface for the upskin orientation, it decreased with depth to a nearly stress-free state within 30 μm of the treated surface.

(iii) Jet impingement orientation had little effect on the surface roughness achieved by the CASF treatment. However, it significantly affected the residual stress, where oblique impingement angles (<90°) resulted in significantly lower residual stress compared to orthogonal treatment.

(iv) The CASF process reduced the effective surface stress concentration ($\overline{K_t}$) for all treatment conditions and surface orientations, with values in the as-built condition (up to $\overline{K_t} \approx 30$) reduced by as much as a factor of 5. However, the reduction in $\overline{K_t}$ was lowest for the upskin and downskin surfaces, likely due to the limited changes in the profile valley radii.

(v) The effectiveness of CASF treatment—in reducing roughness and introducing residual stress—appeared to depend on the build surface orientation, which is correlated with the presence of unmelted particles. The particles shielded the abrasives and cavitating bubbles, limiting material removal and near-surface deformation.

Acknowledgments

The authors are grateful to Cory Cunningham, Patrick Buffington, and Dr. Reid Schur of the Boeing Company for their encouragement, guidance, and technical discussions.

Funding

The authors gratefully acknowledge that support for this work was provided by the Joint Center for Aerospace Technology Innovation (JCATI) in Washington State. The authors also gratefully acknowledge support for this investigation from The Boeing Company through the Boeing Advanced Research Collaboration and from the Sugino Corporation, Ltd. Part of this work was supported by the Washington Nanofabrication Facility/Molecular Analysis Facility, a National Nanotechnology Coordinated Infrastructure (NNCI) site at the University of Washington with partial support from the National Science Foundation (NNCI-1542101 and NNCI-2025489).

Conflict of interest

Dr. Dan Sanders declares that he is an employee of Sugino Corporation as a chief technical officer, which may be perceived as a conflict.

Author contributions

Conceptualization: Dan Sanders, Mamidala Ramulu, Dwayne Arola

Formal analysis: Rohin Petram, Conall Wisdom, Alex Montelione, Cole Nouwens, Angelina Martinez, Marquiz Silvestre

Investigation: Rohin Petram, Conall Wisdom, Alex Montelione, Cole Nouwens, Angelina Martinez, Marquiz Silvestre

Methodology: Dan Sanders, Mamidala Ramulu, Dwayne Arola
Writing—original draft: Rohin Petram, Conall Wisdom
Writing—review & editing: Alex Montelione, Dan Sanders, Mamidala Ramulu, Dwayne Arola

Ethics approval and consent to participate

Not applicable.

Consent for publication

Not applicable.

Availability of data

Data are available from the corresponding authors upon reasonable request.

References

1. Diegel O, Nordin A, Motte D. A practical guide to design for additive manufacturing. *Springer Series in Advanced Manufacturing*. Berlin: Springer; 2019.

   doi: 10.1007/978-981-13-8281-9_2

2. Galati M, Calignano F, Viccica M, Iuliano L. Additive manufacturing redesigning of metallic parts for high precision machines. *Crystals (Basel)*. 2020;10(3):161.

   doi: 10.3390/cryst10030161

3. Zegard T, Paulino GH. Bridging topology optimization and additive manufacturing. *Struct Multidiscipl Optim*. 2016;53(1):175-192.

   doi: 10.1007/s00158-015-1274-4

4. Allen J. An Investigation into the Comparative Costs of Additive Manufacture vs. Machine from Solid for Aero Engine Parts. In: *Cost Effective Manufacture via Net-Shape Processing*. France: Neuilly-sur-Seine; 2006.

5. Cabanettes F, Joubert A, Chardon G, *et al*. Topography of as built surfaces generated in metal additive manufacturing: A multi scale analysis from form to roughness. *Precis Eng*. 2018;52:249-265.

   doi: 10.1016/j.precisioneng.2018.01.002

6. Elambasseril J, Rogers J, Wallbrink C, Munk D, Leary M, Qian M. Laser powder bed fusion additive manufacturing (LPBF-AM): The influence of design features and LPBF variables on surface topography and effect on fatigue properties. *Crit Rev Solid State Mater Sci*. 2023;48(1):132-168.

   doi: 10.1080/10408436.2022.2041396

7. Gomez-Gallegos A, Mandal P, Gonzalez D, Zuelli N, Blackwell P. Studies on titanium alloys for aerospace application. *Defect Diffus Forum*. 2018;385:419-423.

   doi: 10.4028/www.scientific.net/DDF.385.419

8. Williams JC, Boyer RR. Opportunities and issues in the application of titanium alloys for aerospace components. *Metals (Basel)*. 2020;10(6):705.

   doi: 10.3390/met10060705

9. Boyer RR. An overview on the use of titanium in the aerospace industry. *Mater Sci Eng A*. 1996;213(1):103-114.

   doi: 10.1016/0921-5093(96)10233-1

10. Singh P, Pungotra H, Kalsi NS. On the characteristics of titanium alloys for the aircraft applications. In: *Mater Today: Proceedings*. Vol. 4. Netherlands: Elsevier Ltd.; 2017. p. 8971-8982.

    doi: 10.1016/j.matpr.2017.07.249

11. Bache MR. Processing titanium alloys for optimum fatigue performance. *Int J Fatigue*. 1999;21:S105-S111.

    doi: 10.1016/S0142-1123(99)00061-4

12. Hosseini S. *Fatigue of Ti-6Al-4V*. London: IntechOpen; 2012.

    doi: 10.5772/45753

13. Novovic D, Dewes RC, Aspinwall DK, Voice W, Bowen P. The effect of machined topography and integrity on fatigue life. *Int J Machine Tools Manuf*. 2004;44(2):125-134.

    doi: 10.1016/j.ijmachtools.2003.10.018

14. Javidi A, Rieger U, Eichlseder W. The effect of machining on the surface integrity and fatigue life. *Int J Fatigue*. 2008;30(10):2050-2055.

    doi: 10.1016/j.ijfatigue.2008.01.005

15. Arola D, Williams CL. Estimating the fatigue stress concentration factor of machined surfaces. *Int J Fatigue*. 2002;24(9):923-930.

    doi: 10.1016/S0142-1123(02)00012-9

16. Arola D, Ramulu M. An Examination of the effects from surface texture on the strength of fiber reinforced plastics. *J Compos Mater*. 1999;33(2):102-123.

    doi: 10.1177/002199839903300201

17. Persson BNJ. Surface roughness-induced stress concentration. *Tribol Lett*. 2023;71(2):66.

    doi: 10.1007/s11249-023-01741-4

18. Ye C, Zhang C, Zhao J, Dong Y. Effects of post-processing on the surface finish, porosity, residual stresses, and fatigue performance of additive manufactured metals: A review. *J Mater Eng Perform*. 2021;30(9):6407-6425.

    doi: 10.1007/s11665-021-06021-7

19. Pegues J, Roach M, Scott Williamson R, Shamsaei N. Surface roughness effects on the fatigue strength of additively manufactured Ti-6Al-4V. *Int J Fatigue*. 2018;116:543-552.

    doi: 10.1016/j.ijfatigue.2018.07.013

20. Vayssette B, Saintier N, Brugger C, Elmay M, Pessard E.

Surface roughness of Ti-6Al-4V parts obtained by SLM and EBM: Effect on the high cycle fatigue life. *Procedia Eng*. 2018;213:89-97.

doi: 10.1016/j.proeng.2018.02.010

21. Singh K, Sadeghi F, Correns M, Blass T. A microstructure based approach to model effects of surface roughness on tensile fatigue. *Int J Fatigue*. 2019;129:105229.

doi: 10.1016/j.ijfatigue.2019.105229

22. Snyder JC, Thole KA. Understanding laser powder bed fusion surface roughness. *J Manuf Sci Eng*. 2020;142(7):1-37.

doi: 10.1115/1.4046504

23. Whip B, Sheridan L, Gockel J. The effect of primary processing parameters on surface roughness in laser powder bed additive manufacturing. *Int J Adv Manuf Technol*. 2019;103(9-12):4411-4422.

doi: 10.1007/s00170-019-03716-z

24. Obilanade D, Dordlofva C, Törlind P. Surface roughness considerations in design for additive manufacturing - a literature review. In: *Proceedings of the Design Society*. Vol. 1. Cambridge University Press; 2021. p. 2841-2850.

doi: 10.1017/pds.2021.545

25. Khan HM, Karabulut Y, Kitay O, Kaynak Y, Jawahir IS. Influence of the post-processing operations on surface integrity of metal components produced by laser powder bed fusion additive manufacturing: A review. *Mach Sci Technol*. 2020;25(1):118-176.

doi: 10.1080/10910344.2020.1855649

26. Lu D, Liu Z, Wei X, Chen C, Wang D. Effect of post-processing methods on the surface quality of Ti6Al4V fabricated by laser powder bed fusion. *Front Mater*. 2023;10:1126749.

doi: 10.3389/fmats.2023.1126749

27. Makhetha WMI, Becker TH, Sacks N. Post-processing framework for as-built LPBF Ti-6Al-4V parts towards meeting industry functional requirements. *JOM (1989)*. 2022;74(3):764-776.

doi: 10.1007/s11837-021-05078-y

28. Triantaphyllou A, Giusca CL, Macaulay GD, *et al*. Surface texture measurement for additive manufacturing. *Surf Topogr Metrol Prop*. 2015;3(2):24002.

doi: 10.1088/2051-672X/3/2/024002

29. Covarrubias EE, Eshraghi M. Effect of build angle on surface properties of nickel superalloys processed by selective laser melting. *JOM (1989)*. 2018;70(3):336-342.

doi: 10.1007/s11837-017-2706-y

30. Leach RK, Bourell D, Carmignato S, Donmez A, Senin N, Dewulf W. Geometrical metrology for metal additive manufacturing. *CIRP Ann*. 2019;68(2):677-700.

doi: 10.1016/j.cirp.2019.05.004

31. Rott S, Ladewig A, Friedberger K, Casper J, Full M, Schleifenbaum JH. Surface roughness in laser powder bed fusion - Interdependency of surface orientation and laser incidence. *Add Manuf*. 2020;36:101437.

doi: 10.1016/j.addma.2020.101437

32. Shange M, Yadroitsava I, Pityana S, Yadroitsev I, Bester D. Surface morphology characterisation for parts produced by the high speed selective laser melting. *IOP Conf Ser Mater Sci Eng*. 2019;655(1):12045.

doi: 10.1088/1757-899X/655/1/012045

33. Lizzul L, Bertolini R, Ghiotti A, Bruschi S. Effect of AM-induced anisotropy on the surface integrity of laser powder bed fused Ti6Al4V machined parts. *Proc Manuf*. 2020;47:505-510.

doi: 10.1016/j.promfg.2020.04.149

34. Metelkova J, Vanmunster L, Haitjema H, Van Hooreweder B. Texture of inclined up-facing surfaces in laser powder bed fusion of metals. *Add Manuf*. 2021;42:101970.

doi: 10.1016/j.addma.2021.101970

35. Calignano F. Investigation of the accuracy and roughness in the laser powder bed fusion process. *Virtual Phys Prototyp*. 2018;13(2):97-104.

doi: 10.1080/17452759.2018.1426368

36. Jurg M, Medvedev AE, Yan W, Molotnikov A. Surface improvement of laser powder bed fusion processed Ti6Al4V for fatigue applications. *Add Manuf Lett*. 2022;3:100070.

doi: 10.1016/j.addlet.2022.100070

37. Soe AN, Sombatmai A, Promoppatum P, Srimaneepong V, Trachoo V, Pandee P. Effect of post-processing treatments on surface roughness and mechanical properties of laser powder bed fusion of Ti-6Al-4V Effect of post-processing treatments on surface roughness and mechanical properties of laser powder bed fusion of Ti-6Al-4V. *J Mater Res Technol*. 2024;32:3788-3803.

38. Risposi T, Rusnati L, Patriarca L, Hardaker A, Luczyniec D, Beretta S. Fatigue of Ti6Al4V manufactured by PBF-LB: A comparison of failure mechanisms between net-shape and electro-chemically milled surface conditions. *Eng Failure Anal*. 2025;172:109403.

doi: 10.1016/j.engfailanal.2025.109403

39. Bertolini JC. Hydrofluoric acid: A review of toxicity. *J Emerg Med*. 1992;10(2):163-168.

doi: 10.1016/0736-4679(92)90211-B

40. Kahlin M, Ansell H, Basu D, *et al*. Improved fatigue strength of additively manufactured Ti6Al4V by surface post processing. *Int J Fatigue*. 2020;134:105497.

doi: 10.1016/j.ijfatigue.2020.105497

41. Maleki E, Bagherifard S, Bandini M, Guagliano M. Surface

post-treatments for metal additive manufacturing: Progress, challenges, and opportunities. *Add Manuf* 2021;37:101619.

doi: 10.1016/j.addma.2020.101619

42. Grover HJ. *Factors by Which Shot Peening Influences the Fatigue Strength of Parts. SAE Technical Paper 540138*; 1954.

doi: 10.4271/540138

43. Huang L, Kinnell P, Shipway PH. Removal of heat-formed coating from a titanium alloy using high pressure waterjet: Influence of machining parameters on surface texture and residual stress. *J Mater Process Technol*. 2015;223:129-138.

doi: 10.1016/j.jmatprotec.2015.03.053

44. Arola DD, McCain ML. Abrasive waterjet peening: A new method of surface preparation for metal orthopedic implants. *J Biomed Mater Res*. 2000;53(5):536-546.

doi: 10.1002/1097-4636(200009)53:5<536:AID-JBM13>3.0.CO;2-V

45. Arola D, Alade AE, Weber W. Improving fatigue strength of metals using abrasive waterjet peening. *Mach Sci Technol*. 2006;10(2):197-218.

doi: 10.1080/10910340600710105

46. Yao SL, Wang GY, Yu H, *et al*. Influence of submerged micro-abrasive waterjet peening on surface integrity and fatigue performance of TA19 titanium alloy. *Int J Fatigue*. 2022;164:107076.

doi: 10.1016/j.ijfatigue.2022.107076

47. Soyama H. Cavitation peening: A review. *Metals (Basel)*. 2020;10(2):270.

doi: 10.3390/met10020270

48. Soyama H, Korsunsky AM. A critical comparative review of cavitation peening and other surface peening methods. *J Mater Process Technol*. 2022;305:117586.

doi: 10.1016/j.jmatprotec.2022.117586

49. Soyama H, Kuji C. Improving effects of cavitation peening, using a pulsed laser or a cavitating jet, and shot peening on the fatigue properties of additively manufactured titanium alloy Ti6Al4V. *Surf Coat Technol*. 2022;451:129047.

doi: 10.1016/j.surfcoat.2022.129047

50. Soyama H, Iga Y. Laser cavitation peening: A review. *Appl Sci*. 2023;13(11):6702.

doi: 10.3390/app13116702

51. Sato M, Takakuwa O, Nakai M, Niinomi M, Takeo F, Soyama H. Using cavitation peening to improve the fatigue life of titanium alloy Ti-6Al-4V manufactured by electron beam melting. *Mater Sci Appl*. 2016;7(4):181-191.

doi: 10.4236/msa.2016.74018

52. Petram R, Wisdom C, Montelione A, *et al*. Removing alpha case from laser powder bed fusion components by cavitation abrasive surface finishing. *Materials*. 2025;18(9):1977.

doi: 10.3390/ma18091977

53. ASTM International. *F2924-14: Standard Specification for Additive Manufacturing Titanium-6 Aluminum-4 Vanadium with Powder Bed Fusion*. Vol. 1. United States: ASTM International; 2021.

54. Standard Terminology for Additive Manufacturing Coordinate Systems and Test Methodologies ASTM Standard: ISO/ASTM 52921-13 (Reapproved 2019), ASTM International, United States.

55. International Organization for Standardization, ISO 4288:1998. *Geometrical Product Specifications (GPS) - Surface Texture: Profile Method - Rules and Procedures for the Assessment of Surface Texture, Geometrical Product Specifications (GPS)*. Vol. 1998. United Kingdom: International Organization for Standardization; 1998.

56. Noyan IC, Cohen JB. *Residual Stress: Measurement by Diffraction and Interpretation*. Berlin: Springer-Verlag; 1987.

57. He BB. *Two-Dimensional x-Ray Diffraction*. 2nd ed. United States: John Wiley & Sons, Inc.; 2018. p. 249-325.

58. ASTM E407-07. *Designation: E407- 07 (Reapproved 2015) Standard Practice for Microetching Metals and Alloys*. United States: ASTM International; 2015.

59. Soyama H, Okura Y. The use of various peening methods to improve the fatigue strength of titanium alloy Ti6Al4V manufactured by electron beam melting. *AIMS Mater Sci*. 2018;5(5):1000-1015.

doi: 10.3934/matersci.2018.5.1000

60. Du Plessis A, Beretta S. Killer notches: The effect of as-built surface roughness on fatigue failure in AlSi10Mg produced by laser powder bed fusion. *Add Manuf*. 2020;35:101424.

doi: 10.1016/j.addma.2020.101424

61. Vilardell AM, Krakhmalev P, Fredriksson G, *et al*. Influence of surface topography on fatigue behavior of Ti6Al4V alloy by laser powder bed fusion. In: *Procedia CIRP*. Vol. 74. Elsevier B.V; 2018. p. 49-52.

doi: 10.1016/j.procir.2018.08.028

62. Barricelli L, Patriarca L, du Plessis A, Beretta S. A comparison of fatigue analysis methods for L-PBF net-shape surfaces in Ti6Al4V parts. *Theor Appl Fracture Mech*. 2023;128:104143.

doi: 10.1016/j.tafmec.2023.104143

63. Nicoletto G. Influence of rough as-built surfaces on smooth and notched fatigue behavior of L-PBF AlSi10Mg. *Add Manuf*. 2020;34:101251.

doi: 10.1016/j.addma.2020.101251

64. Simson D, Subbu SK. Effect of process parameters on surface integrity of LPBF Ti6Al4V. *Proceedia CIRP*. 2022;108: 716-721.

doi: 10.1016/j.procir.2022.03.111

65. Wang N, Zhu J, Liu B, Zhang X, Zhang J, Tu S. Influence of ultrasonic surface rolling process and shot peening on fretting fatigue performance of Ti-6Al-4V. *Chin J Mech Eng*. 2021;34(1):1-13.

doi: 10.1186/s10033-021-00611-1

66. Li K, Fu XS, Li RD, *et al*. Fretting fatigue characteristic of Ti–6Al–4V strengthened by wet peening. *Int J Fatigue*. 2016;85:65-69.

doi: 10.1016/j.ijfatigue.2015.12.013

67. Mancisidor AM, García-Blanco MB, Quintana I, *et al*. Effect of post-processing treatment on fatigue performance of Ti6Al4V alloy manufactured by laser powder bed fusion. *J Manuf Mater Process*. 2023;7(4):119.

doi: 10.3390/jmmp7040119

68. Rigon D, Coppola F, Meneghetti G. Fracture mechanics-based analysis of the fatigue limit of Ti6Al4V alloy specimens manufactured by SLM in as-built surface conditions by means of areal measurements. *Eng Fracture Mech*. 2024;295:109720.

doi: 10.1016/j.engfracmech.2023.109720

69. Meneghetti G, Rigon D, Gennari C. An analysis of defects influence on axial fatigue strength of maraging steel specimens produced by additive manufacturing. *Int J Fatigue*. 2019;118:54-64.

doi: 10.1016/j.ijfatigue.2018.08.034

70. Lee S, Rasoolian B, Silva DF, Pegues JW, Shamsaei N. Surface roughness parameter and modeling for fatigue behavior of additive manufactured parts: A non-destructive data-driven approach. *Addit Manuf*. 2021;46:102094.

doi: 10.1016/j.addma.2021.102094

ACCSCIENCE PUBLISHING

Materials Science in Additive Manufacturing

ORIGINAL RESEARCH ARTICLE

Unlocking the sustainable potential of 3D concrete printing with large aggregates and steam–CO_2 curing

Suvash Chandra Paul[1]*, Junghyun Lee[1], Yi Wei Daniel Tay[1], Sean Gip Lim[1], Jihye Jhun[1], Bandar A. Fadhel[2], Issam T. Amr[2], and Ming Jen Tan[1]*

[1]Singapore Centre for 3D Printing, School of Mechanical and Aerospace Engineering, College of Engineering, Nanyang Technological University, Singapore

[2]Saudi Aramco Research & Development Center, Dhahran, Eastern Province, Saudi Arabia

Abstract

Three-dimensional concrete printing (3DCP) has emerged as a promising innovation in the construction industry, significantly reducing its reliance on intensive labor while minimizing material waste. Despite its benefits, a major limitation of current 3DCP practices is the high reliance on cement as the primary binder, which often exceeds 60% of the total solid content. This high cement usage contributes significantly to CO_2 emissions, raising sustainability concerns. In this study, a 3D-printable concrete mix incorporating large aggregates (up to 10 mm) was developed, replacing over 7% of fine aggregate and reducing cement content to approximately 29% by weight. The effects of CO_2 gas and a steam–CO_2 mixture on the mechanical performance and CO_2 uptake of the printed concrete were assessed. Thermogravimetric analysis was used to quantify CO_2 sequestration over time. Compared to control samples without gas treatment, those exposed to the steam–CO_2 mixture showed enhanced buildability, improved compressive and flexural strength, and greater CO_2 uptake. The results suggest that surface spraying of the steam–CO_2 mixture during the 3D printing process offers a viable and scalable approach to improving both the structural performance and environmental footprint of printed concrete elements.

Keywords: 3D concrete printing; Carbon dioxide uptake; Large-aggregate printing; Steam–CO_2 injection; 3DCP buildability; CO_2 emission cost; Mechanical strength

***Corresponding authors:**
Suvash Chandra Paul
(suvash.cp@ntu.edu.sg)
Ming Jen Tan
(mmjtan@ntu.edu.sg)

Citation: Paul SC, Lee J, Daniel Tay YW, *et al.* Unlocking the sustainable potential of 3D concrete printing with large aggregates and steam–CO_2 curing. *Mater Sci Add Manuf.* 2026;5(1):025330076. doi: 10.36922/MSAM025330076

Received: August 15, 2025

Revised: September 8, 2025

Accepted: September 12, 2025

Published Online: October 29, 2025

1. Introduction

Additive manufacturing, commonly known as three-dimensional concrete printing (3DCP) in the construction sector, offers numerous advantages,[1] including design freedom, reduced material waste, lowered labor requirements, and formwork elimination, ultimately leading to a significant reduction in costs. Once the printer is configured and the appropriate material is selected, it can print continuously without intensive human intervention until the desired structural shape is complete. Many countries have already successfully constructed functional concrete structures[2] and restored naturally formed structures[3] using three-dimensional (3D) printing technology, demonstrating its practical capabilities.

In recent years, researchers from both academia and industry have conducted extensive studies on the application of 3DCP. These efforts have primarily focused on evaluating a wide range of materials and their properties to determine their suitability for 3DCP technology.[4-6] However, unlike conventional concrete casting, 3DCP builds structures layer by layer, which can introduce anisotropic behavior and weak interlayer bonding due to pore formation.[7] The absence of compaction or vibration during printing further increases porosity, potentially reducing mechanical strength and durability.[8] These structural challenges highlight the need for enhanced material formulations and curing methods, such as the steam–CO_2 integration proposed in this study.

One major drawback of the 3DCP technology is its high binder demand. For example, the use of fine aggregate particles, typically less than 4 mm in size, requires a substantial amount of binder or cement to produce printable materials. This is because the materials need to be mixed and transported through pumps and hose pipes to the printing head or nozzle before being deposited in layers. Cement is the most used binder in both conventional and 3DCP construction processes. However, the production of cement is known to be one of the major contributors to CO_2 emissions, which contribute to atmospheric greenhouse gases. A large amount of CO_2 is released during cement manufacturing, both due to energy use and the calcination chemical process.[9] To mitigate this issue, one potential strategy is to substitute fine particles with larger aggregates in the printable materials, which would significantly decrease the amount of cement used and associated carbon emissions. From a sustainability perspective, alternative binder materials, such as slag, silica fume, and fly ash, can be used to replace cement. Another challenge with 3DCP is the absence of formwork, leaving most printed surfaces directly exposed to the environment. This exposure may impact the curing process and, subsequently, the mechanical and durability properties of 3DCP structures.[10,11]

Carbonation technology offers several benefits for concrete. It not only improves the properties of concrete but also permanently sequesters CO_2 in it.[12] One commonly used method of carbonation technology is curing concrete samples in a CO_2 chamber. This allows CO_2 to react with different hydration products of cement at different stages, resulting in the formation of minerals for carbon sequestration. The key reactions that take place between CO_2 and the cement matrix are illustrated in Equations I–IV.[13-15]

$$3CaO.SiO_2 + 3CO_2 + xH_2O \rightarrow SiO_2.xH_2O + 3CaCO_3 \quad (I)$$

$$2CaO.SiO_2 + 2CO_2 + xH_2O \rightarrow SiO_2.xH_2O + 2CaCO_3 \quad (II)$$

$$Ca(OH)_2 + CO_2 \rightarrow CaCO_3 + H_2O \quad (III)$$

$$C-S-H + 2CO_2 \rightarrow SiO_2 + 2CaCO_3 + H_2O \quad (IV)$$

During the carbonation reaction in cement, the primary products are calcium carbonate ($CaCO_3$) and silica (SiO_2). These products are primarily formed through the decalcification of silicate phases or dehydrated cement particles, as well as through the formation of calcium–silicate–hydrate (C–S–H) gel. In the curing process, the carbonation of tricalcium silicate ($3CaO.SiO_2$ or C_3S) and dicalcium silicate ($2CaO.SiO_2$ or C_2S) phases governs the process, resulting in the production of silica gel and calcite, as shown in Equations I and II.[13] In the weathering carbonation process, calcium hydroxide ($Ca(OH)_2$) is consumed, and $CaCO_3$ is produced, as shown in Equation III.[14] However, with excessive exposure to CO_2, the C–S–H gel decomposes, as shown in Equation IV.[15]

The presence of CO_2 in concrete lowers the pH value in the pore solution of the carbonated area. In general, natural carbonation is considered a long-term process and can result in depassivation and corrosion of the reinforcement. In addition, the rate of CO_2-related reaction in concrete depends on various factors, such as the water–cement ratio (w/c) of the concrete, the composition of materials, the type of curing, the quantity of pores, temperature, and internal humidity.[14]

In numerous studies, scientists have attempted to utilize CO_2 to directly or indirectly modify the properties of materials, both in their fresh and hardened states. The X-ray diffraction test reveals that as the concentration of CO_2 increases, the amount of calcite also increases. Conversely, in the case of portlandite, the amount decreases as CO_2 levels rise.[14] It is reported that the prolonged mixing of CO_2 can significantly impact the workability of materials. According to a report, as the duration of CO_2 exposure increases, the workability of the materials decreases.[12] This is due to the rapid hydration of C_3S and C_3A, forming $CaCO_3$ through the reaction of CO_2 with $Ca(OH)_2$. Similarly, Monkman *et al.*[16] confirmed this decreased workability behavior of materials exposed to CO_2. The initial slump value was reduced by 25–33% compared to the reference materials. Rapid hydration is also a contributing factor to the lower setting time of the materials.[12]

Researchers have investigated the effects of large aggregates on various properties of 3DCP.[17-19] The inclusion of large aggregates increases the paste volume and the thickness of the water film in mixers, reducing the yield stress and viscosity of fresh materials, ultimately

affecting printability.[17] Similar findings of decreased yield stress and viscosity have been reported by Wang *et al.*[19] Moreover, the researcher has investigated various chemical admixtures to optimize the rheological properties, such as yield stress and viscosity, of 3D-printable cementitious materials.[20]

The buildability of 3D-printable materials is reported to improve with the inclusion of large aggregates.[17] Furthermore, large aggregates can diminish the anisotropic behavior of 3D-printed samples and enhance mechanical properties, including compressive strength, flexural strength, bond strength, and elastic modulus. The redistribution of aggregates during the printing process and their penetration through the interlayer have been shown to increase bond strength and other mechanical properties in samples containing large aggregates. This redistribution positively affects the anisotropic behavior of 3D-printed samples.[18]

However, if materials are not properly selected, specifically regarding the types and content of aggregates, the inclusion of large aggregates may negatively affect the properties of 3D-printed samples.[19] Overall, positive outcomes have been reported for the use of large aggregates in 3DCP.[21,22] In addition, incorporating large aggregates can reduce the need for an excessive amount of cement and natural sand compared to conventional 3D-printed mortar mixes, potentially offering a beneficial environmental impact.[21] The use of large aggregates in printing can decrease cement volume fraction by approximately 50% compared to 3D-printed mortar mixes.[23]

This study analyzed the effects of directly injecting CO_2 and a steam–CO_2 mixture into fresh 3D-printed concrete samples incorporating large aggregates on their mechanical properties and printability. The printability of the 3D-printed materials was evaluated by assessing the maximum buildable layers of the fresh material under varying CO_2 and steam–CO_2 pressures. In addition, the hardened 3D-printed samples underwent compression and flexural testing to determine the influences of CO_2 and steam–CO_2 integration. To quantify the amount of CO_2 sequestered by the materials, a thermogravimetric analysis (TGA) test was performed. The results demonstrated that the injection of CO_2 and steam–CO_2 enhanced both the printability and mechanical strength of the large-aggregate-based 3D–printed materials compared to the control mix. To the best of the authors' knowledge, the research methodology employed in this study, involving CO_2 and steam–CO_2 injection into the large aggregates of 3D-printed concrete samples, is unique and has not been extensively documented in the scientific literature.

2. Materials and methods

2.1. Materials

Material composition is a crucial part of 3D printing technology. As a 3D-printed material undergoes mixing, pumping, and extrusion through a designated nozzle orifice, each component of the material plays a significant role in the printing process. In this study, a 3D-printable material was developed, consisting of large aggregates with a maximum size of 10 mm. These aggregates were used to replace a portion of the sand, which typically provides volumetric stability in 3DCP structures. The main materials used in this research work included ordinary Portland cement (CEM-I), undensified silica fume, a polycarboxylate superplasticizer, potable water, natural river sand (maximum size 2.3 mm), and gravel as large aggregates (maximum size of 10 mm), as presented in Table 1. The chemical compositions of the cement and silica fume utilized in this study are detailed in Table 2.

2.2. Printer and material delivery system

A six-axis robotic arm (KR 120 R3900 ultra K, KUKA, Germany) mounted with a customized nozzle (Figure 1A) was used to control the movement of the print head. Slicer software (Mastercam 2017, United States [US]) was used to create the 3D design in an XYZ coordinate system. A progressive cavity feed pump (Taurus pump, MAI

Table 1. Material compositions by weight (%) for 3D concrete printing

Materials	Weight (%)
Cement	29.3
Silica fume	2.89
Sand	48.21
Large aggregate	7.28
Water	12.02
Superplasticizer	0.29

Table 2. Chemical compositions (% w/w) of cement and silica fume used in the research

Compositions	Cement (%)	Silica fume (%)
CaO	61.09	0.68
SiO_2	18.69	95.78
Al_2O_3	6	0.12
Fe_2O_3	2.86	0.03
SO_3	2.75	-
MgO	2.55	0.42
K_2O	0.51	1.44
$Na_2O_{eq.}$	0.38	0.43

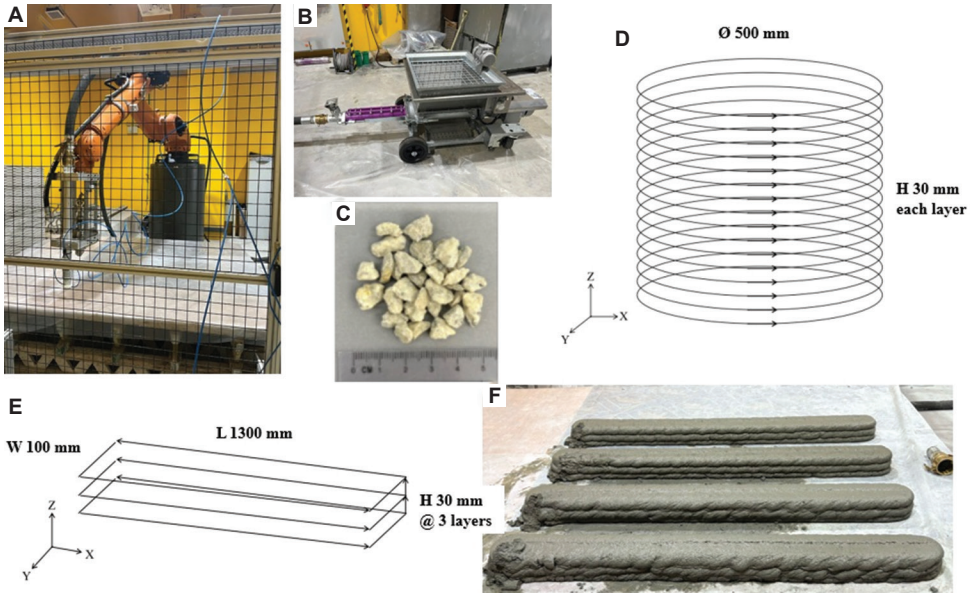

Figure 1. Set up of the 3D-printed large-aggregate concrete. (A) Six-axis robotic arm printer. (B) Pump for material delivery. (C) Large aggregates. (D) Tool path for buildability. (E) Tool path for mechanical testing samples. (F) Printed samples for mechanical properties testing

International GmbH, Austria) with a material extrusion rate of approximately 30 L/min was used as the printer's pumping system. The printer is capable of producing objects with a diameter of up to 2.5 m. It was equipped with a circular nozzle measuring 45 mm in diameter and a 50 mm-diameter hose for transporting materials to the nozzle head. The nozzle head operated at a print speed of 150 mm/s to ensure smooth printing of 3D samples for buildability and mechanical testing. Figure 1A-F illustrates the printer, pump, large aggregates, toolpaths for buildability tests, toolpaths for mechanical testing samples, and printed samples used for mechanical strength evaluation.

2.3. Steam and CO_2 injection in 3D-concrete-printing structures

Current carbon capture and sequestration methods often face challenges, including slow kinetics, limited CO_2 uptake, high costs, and lengthy processing times. In general, natural carbonation requires long-term treatment due to its slow reaction rate, which significantly increases production costs.[24] To address these issues, researchers have developed a straightforward technique that utilizes porous structures for rapid CO_2 capture.[25] However, this approach compromises the strength of concrete, as increased porosity reduces its structural integrity. Therefore, to evaluate the CO_2 sequestration efficiency, this study employed a method[26] in which pure CO_2 (99% purity) was sprayed onto the surface of the printing layer during the 3D printing of structures. CO_2 was applied at pressures of 2 bar, 4 bar, or 6 bar. In addition, to further enhance CO_2 capturing, the study also conducted experiments that involved injecting steam alongside CO_2. The effects of CO_2 spraying and steam–CO_2 spraying on the properties of 3D-printed concrete materials were compared with a control mix that did not involve CO_2 or steam injection.[24,25]

2.4. Buildability test of 3D-printed concrete

The maximum height achievable with 3DCP was determined through the material's strength, which must withstand the increasing compressive stresses from its own weight during printing. If these stresses exceed the yield strength, structural failure occurs. To assess buildability, a circular object with a 500-mm diameter was printed layer by layer vertically until it collapsed. The nozzle size and printing speed, as mentioned earlier, remained consistent throughout the experiments. The buildability of the materials was evaluated under different CO_2 pressures, both with and without steam, and their performance was compared to the control mix.

2.5. Mechanical properties and microstructure test

The samples for the compressive and flexural strength tests were obtained from the printed specimens, as shown in Figure 1F. For each testing batch conducted on different days, a minimum of four samples were collected: cubes measuring approximately 90 mm × 90 mm × 90 mm for the compression test, and prisms measuring 90 mm × 90 mm × 300 mm for the flexural test. The printing took place in a laboratory environment with an average temperature of 22 ± 2°C and relative humidity of 60 ± 5%. All samples were stored in the laboratory until

testing, and no additional curing methods were employed. It is important to note that only a CO_2 pressure of 2 bar was used for mechanical testing and CO_2 uptake calculations. Higher CO_2 pressures result in rough surfaces on the 3D-printed structures, potentially leading to uneven load distribution during mechanical testing.[27]

For the compressive strength test, a universal compression testing machine (B-001, ALFA Testing Equipment, Turkey) with a capacity of 2,000 kN was used to apply load gradually and uniformly to the samples. The loading rate was maintained at 900 N/s, in accordance with the ASTM C109/C109M standard[28] for measuring the compressive strength of hydraulic cement mortar samples. The flexural strength was determined using an Instron machine (5969, US), following the ASTM C293 standard,[29] which outlines the standard test method for flexural strength of concrete. In this test, a three-point bending load was applied to the samples, centered between two lower supports, with the distance between the supports set to three times the sample depth (i.e., 270 mm).

For microstructural analysis, images were obtained from hardened samples using a JSM 5600 LV scanning electron microscope (SEM; JEOL, Japan) with a magnification of ×100 and a scale bar of 100 μm. Small samples, measuring 2–3 mm in thickness and approximately 20 mm × 20 mm in area, were cut from the hardened concrete at 28 days of age and immersed in ethanol for an additional 7 days to halt the hydration process. Subsequently, the samples were placed in an oven at 60°C for 24 h before the SEM test. In addition, a metal coating was applied to the samples to ensure a smooth surface for testing.

2.6. Thermogravimetric analysis for the CO_2 uptake test

Thermogravimetric analysis was employed to measure mass loss resulting from the decomposition of hydration products, including ettringite, calcium silicate hydrate, calcium hydroxide, and carbonated calcium hydroxide, under different printing conditions. This mass loss reflects the decomposition of chemically bound water in the hydration products, providing an estimate of the degree of cement hydration as well as the decomposition of $CaCO_3$ corresponding to the release of CO_2 that was taken up during carbonation. For the TGA test, the peripheral region of samples from the compressive strength tests was collected after 7 and 28 days of testing. These samples were immersed in an ethanol solution for 7 days to halt the hydration process of the binders. After immersion, the samples were removed from the ethanol and placed in an oven at 60°C for 24 h. They were then ground into powder samples using a mortar and pestle and sieved through a 250-μm sieve. The prepared samples were analyzed at a ramping rate of 20°C/min over a temperature range of 25°C to 1,000°C to measure and monitor the mass loss of the concrete samples. The extent of hydration reactions and the amount of CO_2 uptake by the materials were determined using Equations V–XIII:[30]

$$Dehydration\ (Ldh) = m_{105^oC} - m_{400^oC} \quad \text{(V)}$$

$$Dehydroxylation\ (Ldx) = m_{400^oC} - m_{500^oC} \quad \text{(VI)}$$

$$Decarbonation\ (Ldc) = m_{500^oC} - m_{950^oC} \quad \text{(VII)}$$

$$Bound\ water\ (W_c) = \left(Ldh + Ldx\right) + 0.41\left(Ldc\right) \quad \text{(VIII)}$$

$$Free\ Ca\left(OH\right)_2\ (CH_f) = 4.11\left(Ldx\right) + 1.68\left(Ldc\right) \quad \text{(IX)}$$

$$Poorly\ crystalline\ CaCO_3\ (DC) = m_{500^oC} - m_{700^oC} \quad \text{(X)}$$

$$Well\ crystalline\ CaCO_3\ (HC) = m_{700^oC} - m_{950^oC} \quad \text{(XI)}$$

$$Degree\ of\ hydration\ (DOH) = 100 \times \frac{W_c}{0.24} \quad \text{(XII)}$$

$$\text{Carbon uptake}\left(\text{wt \% binder}; \xi\right) = \frac{m_{500^oC} - m_{950^oC}}{n \times (m_{105^oC} - W_c - CH_f)} \quad \text{(XIII)}$$

where n is the solid binder constitutions (wt.% dry mix), W_c is the chemically bound water (wt.% sample), and CH_f is the free calcium hydroxide (wt.% sample).

Note that the carbonation of metal oxides was not included due to its low concentration and hence was considered negligible. In addition, various methods are available for quantifying CO_2 in cement-based materials, depending on the specific materials and their decomposition processes. These methods include back-titration, Fourier-transform infrared spectroscopy, and Raman spectroscopy.[31] However, this study was limited to TGA analysis only.

3. Results and discussion

Most studies on carbonation have primarily concentrated on the carbonation curing of concrete samples or the mixing of CO_2 with aggregates or binders before combining them with other concrete constituents.[32,33] This study employed spraying techniques to apply CO_2 and steam onto the surface of freshly printed layers.

3.1. Number of buildable layers of 3D-concrete-printing structures

The number of buildable layers of the 3DCP structures under various conditions, including the presence and

absence of CO_2 and steam, is illustrated in Figures 2 and 3. It is evident that the buildability of the materials improved with increasing CO_2 pressure during printing, compared to the control mix. The maximum buildability was observed at a CO_2 spraying pressure of 6 bar. In addition, the application of steam combined with a CO_2 spraying pressure of 4 bar also showed a positive effect. Thus, it can be concluded that spraying CO_2 and steam onto the surface of the printed layers enhanced the buildability of concrete. This effect is attributed to CO_2 spraying, which aids in drying the layer's surface and reduces setting time by altering the kinetics of cement hydration. The reaction between CO_2 and CaO or $Ca(OH)_2$, after mixing with water, will produce $CaCO_3$, contributing to an increased buildable height of the 3D-printed structure. When steam is introduced alongside CO_2, the printed layer's surface becomes wet, enhancing the formation of C–S–H and $CaCO_3$ and forming a strong bond with subsequent layers, thereby enhancing the buildable layers (Figure 3A).

The material developed in this research was also used to print 1.5 m-tall walls (roughly 50 layers), as displayed in Figure 3. Figure 3B illustrates the toolpath used for wall printing, while Figure 3C displays the printed wall.

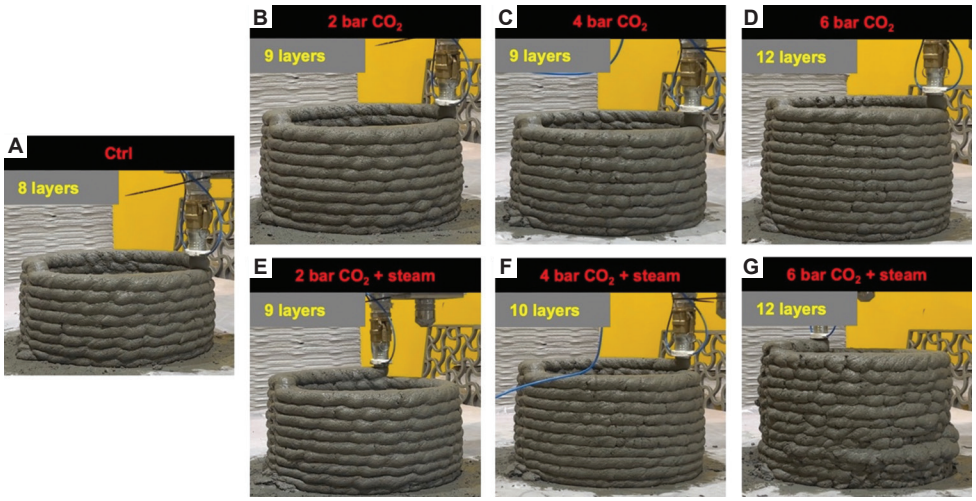

Figure 2. Buildable layers of the 3D-printed large-aggregate concrete. (A) Control mix (Ctrl). (B) CO_2 pressure of 2 bar. (C) CO_2 pressure of 2 bar with steam. (D) CO_2 pressure of 4 bar. (E) CO_2 pressure of 4 bar with steam. (F) CO_2 pressure of 6 bar. (G) CO_2 pressure of 6 bar with steam.

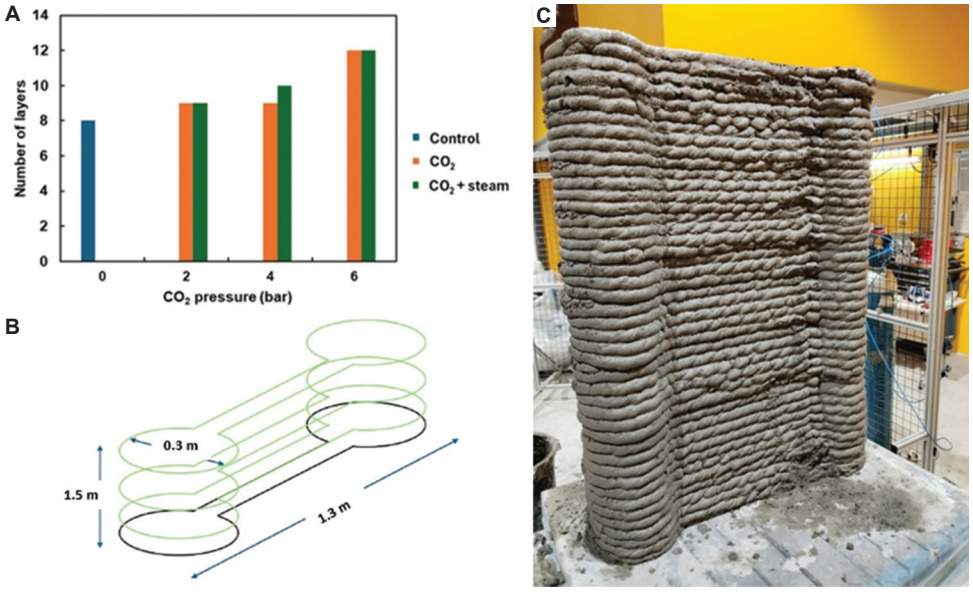

Figure 3. Buildability of large aggregate 3D printing materials. (A) Number of buildable layers across varying CO_2 pressures. (B) Toolpath and dimension for wall printing. (C) 1.5 m-high wall printed with large-aggregate concrete at a CO_2 pressure of 2 bar with steam.

During wall printing, the process was paused every 5–6 layers for 7–10 min to mix a new batch of materials. As a result, the total time to complete the wall was 90–100 min. This experiment aimed to print a scalable structure using the large-aggregate 3D-printable material, combined with a steam–CO_2 mixture as a potential alternative to traditional accelerating agents in concrete construction. This method could also serve as a means for permanent CO_2 sequestration in fresh concrete. In a previous study, Li *et al.*[12] examined the effects of directly incorporating CO_2 into materials during mixing. The study found that this approach resulted in lower workability and reduced setting time. Their SEM images further indicated that the formation of reaction products on the surface of cement grains due to CO_2 mixing accelerated the hydration of both tri-calcium aluminate (C_3A) and tricalcium sulfate (C_3S).

3.2. Compressive and flexural strength of the 3D-concrete-printing structure

The development of compressive strength and the failure patterns of 3D-printed large-aggregate samples at 7 and 28 days are illustrated in Figure 4A and B. On both days, samples treated with a steam–CO_2 mixture exhibited enhanced strength. By 28 days, the strength of the CO_2-treated and steam–CO_2-treated samples was approximately 25% and 28% higher, respectively, compared to the control sample. This improvement aligns with the buildability results. The enhanced strength can be attributed to the formation of nanoscale calcite ($CaCO_3$) particles, which refined the pore structures in the hardened concrete due to the reaction between sprayed CO_2 and the CaO in the cement.[34]

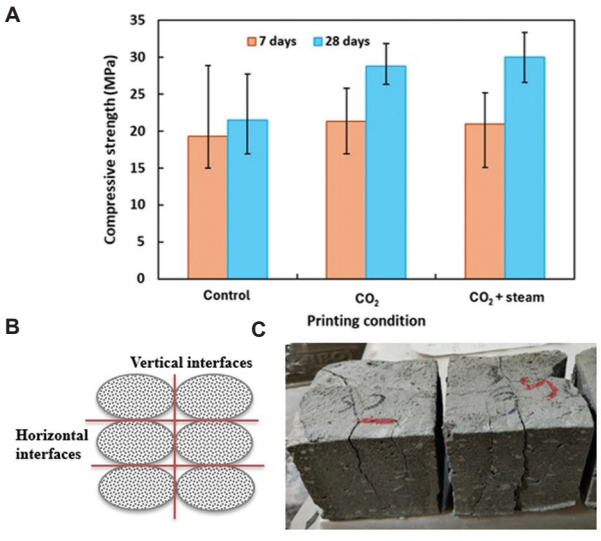

Figure 4. Strength and cracking patterns in the 3D-printed samples. (A) Compressive strength development in large-aggregate 3D-concrete-printing samples under varying conditions. (B) Illustration of a 3D-printed cube sample with a dimension of 90 mm × 90 mm. (C) Failure patterns of tested cube samples.

In 3D-printed samples, the interfaces between layers contribute to anisotropic mechanical behavior, in contrast to cast samples.[35,36] These interfaces often serve as weak points that affect the stress–strain response, energy dissipation, and crack formation.[35] Cracks can develop on both vertical and horizontal interfaces (refer to the red lines in Figure 4B), influenced by factors such as the loading orientation relative to the printed sample, the type of loading (bending or compression), and the dimensions of the samples. Figure 4C clearly shows that a crack occurred on the vertical interface of the cube samples before failure during the compression test. Although not depicted here, horizontal cracks were also observed in some samples. Detailed discussions on crack propagation in 3D-printed concrete samples, both with and without fibers, can be found in.[35,37]

The flexural strength of the 3D-printed samples was also enhanced with the incorporation of a steam–CO_2 mixture during printing, as shown in Figure 5. Compared to the control mix, the concrete samples sprayed with CO_2 or a steam–CO_2 mixture exhibited approximately 2% and 4% higher strength, respectively, at the 28-day mark. The strength development of flexural samples from 7 days to 28 days was not as significant as that observed in compressive strength samples. Previous research has shown that CO_2-cured concrete exhibited higher strength development at an early age of 3 days compared to water-cured conventional concrete.[38] However, this difference became negligible at later ages of 28 and 90 days for both CO_2-cured and conventional concrete samples. The size of the samples also affects the strength of CO_2-cured samples. Specifically, smaller 5 cm × 10 cm cylinder samples demonstrated greater strength development than larger sizes, such as 10 cm × 20 cm and 15 cm × 30 cm cylinders.

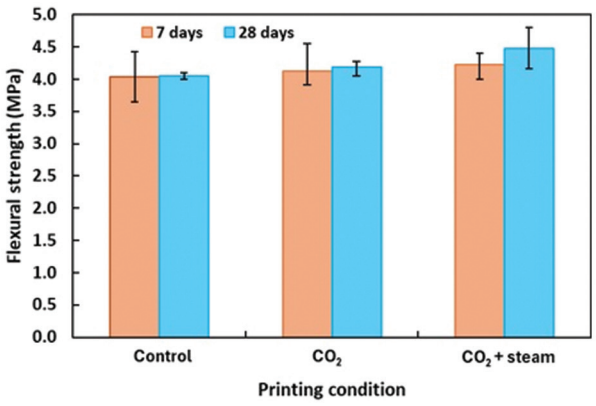

Figure 5. Flexural strength development in large-aggregate 3D-concrete-printing samples

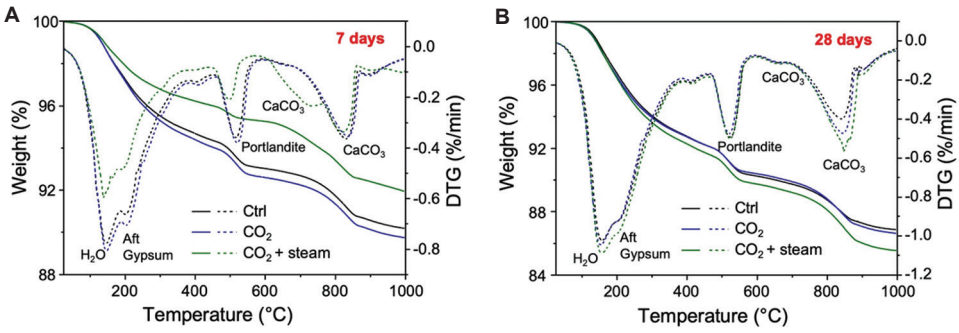

Figure 6. Thermogravimetric (TGA) and derivative thermogravimetric (DTG) curves of the 3D-printed concrete with large aggregate at (A) 7 days and (B) 28 days

In addition to sample size, curing conditions, including CO_2 pressure, concentration, and curing time, are also crucial for strength development.

Both concrete strength and the degree of CO_2 curing increase with longer curing times and higher CO_2 pressures.[39] Notably, the reaction between CO_2 and cement within the concrete occurs rapidly, within 15 min, regardless of CO_2 pressure and pre-conditioning environment. CO_2 spraying on wet concrete initiates a carbonation reaction alongside cement hydration, leading to early-age carbonation.[40] Importantly, no adverse effects on the long-term development of concrete properties have been observed due to early-age carbonation. The interaction between CO_2 and cement contributes to the formation of nanosized $CaCO_3$, which helps fill voids and improve strength. However, some researchers have reported negative effects on cement hydration caused by CO_2, attributed mainly to variations in material compositions and carbonation conditions.[41-43] Therefore, further research is needed to understand the carbon dynamics in these factors and confirm their effects on carbonated concrete.

3.3. CO_2 uptake in 3D-concrete-printing samples

As shown in Figure 6, the TGA curve and derivative thermogravimetric (DTG) curve for 3D-printed concrete samples provide invaluable information about their hydration and carbonation state. The TGA and DTG curves typically show several distinct mass loss steps, each corresponding to the thermal decomposition of different compounds present in the concrete.[25,27,44] Among them, for CO_2 sequestration of 3D-printed concrete samples, it is necessary to examine in detail the decomposition range of $CaCO_3$ located within the temperature range of 600–950°C.

At the early stage of curing (7 days), the integration of CO_2 with steam enhanced the carbonation process in the 3D-printed concrete sample, as illustrated in Figure 6A. However, the amount of CO_2 sequestration calculated using Equation XIII did not show a significant difference across

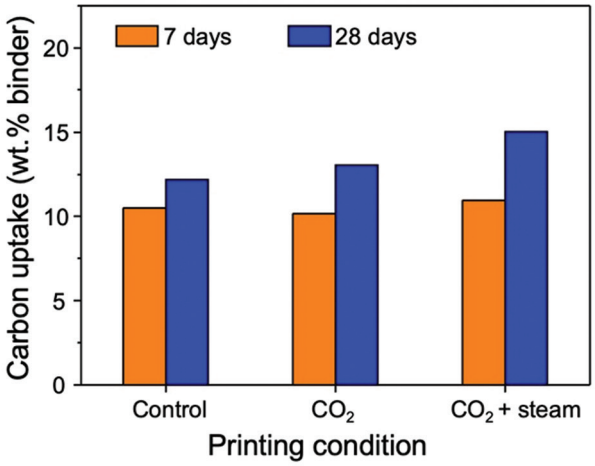

Figure 7. Comparison of CO_2 uptake under three different printing conditions at 7 and 28 days

printing conditions. At longer curing times (28 days), changes depending on printing conditions became more evident. Compared to the 7th day's TGA and DTG curves, more hydrated and carbonated products were formed. In the carbonation process, well-crystallized $CaCO_3$ can be more dominant, and the integration of CO_2 or a steam–CO_2 mixture increased the amount of well-crystallized $CaCO_3$, as shown in Figures 6B and 7. Compared to the control samples at 28 days, the CO_2 uptake of the CO_2-sprayed 3DCP samples increased by 7%, while that of the steam–CO_2-treated samples increased by 23%. The results indicate that spraying CO_2 or a steam–CO_2 mixture not only accelerates carbonation during 3D printing, thereby improving buildability but also enhances CO_2 sequestration during the curing process. These findings open new avenues for future research on varying CO_2 concentrations, pressures, and their effects on different concrete compositions for the permanent sequestration of CO_2 from the atmosphere. Moreover, CO_2 uptake in concrete depends on several factors, including the water-to-solid ratio and reaction time. Studies have shown that

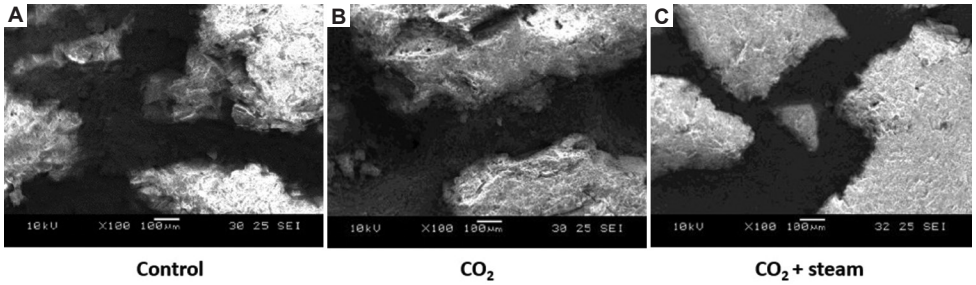

Figure 8. Scanning electron microscopy images of the microstructures of the 3D-printed large-aggregate concrete. (A) Control. (B) CO_2-treated sample. (C) Steam–CO_2-treated sample. Scale bar: 100 μm; magnification: ×100.

when the water-to-solid ratio exceeds 0.40, CO_2 uptake decreases significantly. In addition, the capability for CO_2 uptake increases with reaction time, reaching a peak between 1 and 72 h before saturation, as demonstrated in experiments with concrete slurry waste,[32] which is beyond the scope of this research.

3.4. Scanning electron microscopy of 3D-concrete-printing samples

Figure 8 displays the microstructure images of hardened concrete samples. Notably, the CO_2-treated and steam–CO_2-treated samples showed a denser and less porous region surrounding the aggregates and cement paste compared to the control sample. This indicates strong bonding between the cement paste and aggregates, contributing to the formation of a robust interfacial transition zone and enhancing the mechanical strength of the concrete samples.

3.5. CO_2 emission and cost analysis

This study conducted a computational analysis of the potential environmental impacts of 3D-printed large-aggregate concretes. The CO_2 emissions and costs associated with concrete are directly related to the quantity of materials used, particularly the cement in the mixture. The CO_2 emissions and costs associated with the strength of concrete samples were calculated under three conditions: control, CO_2, and steam–CO_2, using Equations XIV–XVII, recommended by Meng *et al.*[45]:

(i) Material cost per unit volume (USD/m^3):

$$C_M = \sum_i^i \left(m_i \times P_i\right) \quad \text{(XIV)}$$

(ii) Material cost per 1 MPa of strength (USD/MPa):

$$U_M = \frac{C_M}{f_{c(t)}} \quad \text{(XV)}$$

(iii) Carbon emission per 1 MPa of strength (kg/MPa):

$$C_{CO2} = \frac{\sum_i^i \left(m_i \times C_{CO2i}\right)}{f_{c(t)}} \quad \text{(XVI)}$$

Table 3. Materials, emission factors, and the approximate price of materials used in the study

Materials	Emission factors (kg CO_2 e/kg)	Price (USD/kg)
Cement	0.900	0.230
Stone chips	0.005	0.045
Sand	0.005	0.050
Silica fume	0.020	2.000
Superplasticizer	0.010	4.000
Water	0.0003	0.004
2 Bar CO_2	1.000	0.766
Steam	0.010	0.250
Carbon price, P_{CO2}	-	0.032

(iv) Carbon emission cost per 1 MPa of strength (USD/MPa):

$$U_{CO2} = P_{CO2} \times C_{CO2} \quad \text{(XVII)}$$

where m_i and P_i are the mass and price of each component, respectively, $f_{c(t)}$ represents the concrete strength, C_{CO2i} represents the carbon emissions from each component, and P_{CO2} represents the current average carbon price per kg of CO_2, which is USD 0.032.[46]

Table 3 presents the materials, their corresponding emission factors, and the approximate prices in the local market of Singapore. Using these equations, the approximate cost of materials, including carbon costs per 1 MPa of strength, is calculated and shown in Table 4. The results indicate that incorporating CO_2 and steam into 3D-printed concrete structures can reduce costs compared to control. Specifically, the use of a steam–CO_2 mixture resulted in a maximum cost reduction of 28% compared to control, while the use of CO_2 alone resulted in a reduction of approximately 25%. These findings suggest that combining steam with CO_2 offers greater potential than using CO_2 alone. It is important to note that other costs associated with printing, such as workforce, equipment, and transportation, were not included in this analysis, as

Table 4. Materials and carbon emissions cost per unit strength

Mix	Compressive strength (MPa)	C_M (USD/m^3)	U_M (USD/MPa)	C_{CO2} (kg/MPa)	U_{CO2} (USD/MPa)	U_M+U_{CO2} (USD/MPa)	Difference (%)
Control	21.52	390.19	18.13	29.38	0.94	19.07	0
CO_2	28.78	390.42	13.56	21.98	0.70	14.27	25.19
CO_2 + steam	29.98	390.67	13.03	21.11	0.68	13.71	28.13

Notes: C_{CO2} is the carbon emission per 1 MPa of strength; C_M is the material cost per unit volume; U_{CO2} is the carbon emission cost per 1 MPa of strength; U_M is the material cost per 1 MPa of strength.

their actual values depend on various factors that were not considered in the current calculations.

In sustainable construction, decisions should be made based on specific optimization objectives.[43] The model results presented in this research can serve as a valuable guide for these decisions. This research focused solely on the environmental impacts of the raw materials. As a result, other costs mentioned above are considered negligible. Nonetheless, the cost comparisons provided can provide readers a relative understanding of the costs of materials with or without CO_2 or a steam–CO_2 mixture during the 3D printing of structures. For a more comprehensive comparison, additional factors must be included in future calculations to develop a solid solution.

4. Conclusion

This study investigated the dual effects of CO_2 and a steam–CO_2 mixture on 3D-printed large-aggregate concrete samples. The following conclusions can be drawn from the research findings:

- The study demonstrates that employing CO_2 or steam–CO_2 in large-aggregate 3DCP has significant potential, as they can enhance both the buildability and mechanical properties of the structures.
- The buildability of 3D-printed samples is closely linked to CO_2 pressure. When CO_2 pressure increased from 2 bar to 6 bar, there was a 33% improvement in buildability for the steam–CO_2 mix compared to the control mix. However, there was no significant difference in buildability between concrete samples using CO_2 alone and those using the steam–CO_2 mixture. Notably, elevated CO_2 levels can lead to rough surface formation, detracting from achieving a smooth finish in 3D-printed structures.
- At 28 days of testing, the compressive strength of the 3D-printed samples treated with CO_2 or steam–CO2 was found to be 24% and 28% higher than that of the control samples, respectively. For flexural strength, the improvements were approximately 2% and 4%, respectively.
- The concrete samples treated with steam–CO_2 demonstrated a significant increase in CO_2 uptake compared to samples treated with only CO_2 or control. Specifically, the samples sprayed with steam–CO_2 showed 23% higher CO_2 uptake compared to the control samples.
- Regarding material and carbon costs, the integrated use of steam–CO_2 resulted in a maximum cost reduction of 28% compared to the control. For samples using CO_2 alone, the cost reduction was approximately 25%.

The primary challenge in 3D printing with large aggregates is the slump of fresh concrete. It is well established that concrete or mortar with low to zero slump is preferable for successful printing, as it prevents layer deformation. However, achieving such low-slump concrete is difficult and necessitates careful selection of material compositions and delivery systems. In addition, the lack of standardized sample sizes for various tests is concerning, as sample size can significantly affect results even when identical material compositions are used. To fully harness the benefits of this technology, these issues must be addressed through prompt collaboration between academia and industry.

Acknowledgments

None.

Funding

This research was supported by Saudi Aramco Technologies Company (SATC) and the National Research Foundation, Prime Minister's Office, Singapore, under its Medium-Sized Centre funding scheme for the Singapore Centre for 3D Printing.

Conflict of interest

The authors declare that they have no competing interests.

Author contributions

Conceptualization: Suvash Chandra Paul
Data curation: Suvash Chandra Paul
Formal analysis: Suvash Chandra Paul, Junghyun Lee, and Yi Wei Daniel Tay
Funding acquisition: Ming Jen Tan
Investigation: Suvash Chandra Paul, Junghyun Lee, Yi Wei Daniel Tay, Sean Gip Lim, Jihye Jhun, and Issam T. Amr

Methodology: Suvash Chandra Paul, Junghyun Lee, and Yi Wei Daniel Tay
Supervision: Bandar A. Fadhel, and Ming Jen Tan
Writing–original draft: Suvash Chandra Paul
Writing–review & editing: All authors

Ethics approval and consent to participate

Not applicable.

Consent for publication

Not applicable.

Availability of data

The datasets generated during and/or analyzed during the present study are available from the corresponding author on reasonable request.

Further disclosure

Parts of the findings have been presented at the Future AM 2025 conference in Singapore (August 5–7, 2025). The paper has never been uploaded to or deposited in a preprint server.

References

1. Pongwisuthiruchte A, Potiyaraj P. Challenges and innovations in sustainable 3D printing. *Mater Today Sustain*. 2025;31:101134.

   doi: 10.1016/j.mtsust.2025.101134

2. Available from: https://builtin.com/articles/3d-printed-house [Last accessed on 2025 Jun 04].

3. Jia Y, Abdelrahman S, Hauser CA. Developing a sustainable resin for 3D printing in coral restoration. *MSAM*. 2024;3(2):3125.

   doi: 10.36922/msam.3125

4. Rahul AV, Santhanam M, Meena H, Ghani Z. Mechanical characterization of 3D printable concrete. *Constr Build Mater.* 2019;227:116710.

   doi: 10.1016/j.conbuildmat.2019.116710

5. Bhattacherjee S, Basavaraj AS, Rahul AV, *et al*. Sustainable materials for 3D concrete printing. *Cem Concr Compos.* 2021;122:104156.

   doi: 10.1016/j.cemconcomp.2021.104156

6. Wolfs RJM, Bos FP, Salet TAM. Hardened properties of 3D printed concrete: The influence of process parameters on interlayer adhesion. *Cem Concr Res.* 2019;119:132-140.

   doi: 10.1016/j.cemconres.2019.02.017

7. Ding T, Xiao J, Zou S, Zhou X. Anisotropic behavior in bending of 3D printed concrete reinforced with fibers. *Compos Struct.* 2020;254:112808.

   doi: 10.1016/j.compstruct.2020.112808

8. Wang D, Xiao J, Sun B, Zhang S, Poon CS. Mechanical properties of 3D printed mortar cured by CO_2. *Cem Concr Compos.* 2023;139:105009.

   doi: 10.1016/j.cemconcomp.2023.105009

9. Haselbach L. Potential for carbon dioxide absorption in concrete. *J Environ Eng.* 2009;135(6):465-472.

   doi: 10.1061/(asce)ee.1943-7870.0000004

10. Sikora P, Techman M, Federowicz K, *et al*. Insight into the microstructural and durability characteristics of 3D printed concrete: Cast versus printed specimens. *Case Stud Constr Mat.* 2022;17:e01320.

    doi: 10.1016/j.cscm.2022.e01320

11. Sun B, Dominicus R, Dong E, Li P, Ye Z, Wang W. Predicting the strength development of 3D printed concrete considering the synergistic effect of curing temperature and humidity: From perspective of modified maturity model. *Constr Build Mater.* 2024;427:136291.

    doi: 10.1016/j.conbuildmat.2024.136291

12. Li L, Hao L, Li X, Xiao J, Zhang S, Poon CS. Development of CO_2-integrated 3D printing concrete. *Constr Build Mater.* 2023;409:134233.

    doi: 10.1016/j.conbuildmat.2023.134233

13. Kazemian M, Shafei B. Carbon sequestration and storage in concrete: A state-of-the-art review of compositions, methods, and developments. *J CO_2 Util.* 2023;70:102443.

    doi: 10.1016/j.jcou.2023.102443

14. Castellote M, Fernandez L, Andrade C, Alonso C. Chemical changes and phase analysis of OPC pastes carbonated at different CO_2 concentrations. *Mater Struct.* 2009;42:515-525.

    doi: 10.1617/s11527-008-9399-1

15. Kashef-Haghighi S, Ghoshal S. CO_2 sequestration in concrete through accelerated carbonation curing in a flow-through reactor. *Ind Eng Chem Res.* 2010;49(3):1143-1149.

    doi: 10.1021/ie900703d

16. Monkman S, Hwang SD, Khayat, K. Rheology modification of flowable mortar with CO_2. *Cem Concr Compos.* 2024;151:105584.

    doi: 10.1016/j.cemconcomp.2024.105584

17. Rahul AV, Mohan MK, De Schutter G, Van Tittelboom K. 3D printable concrete with natural and recycled coarse aggregates: Rheological, mechanical and shrinkage behaviour. *Cem Concr Compos.* 2022;125:104311.

    doi: 10.1016/j.cemconcomp.2021.104311

18. An D, Zhang YX, Yang R. Incorporating coarse aggregates into 3D concrete printing from mixture design and process control to structural behaviours and practical applications: A review. *Virtual Phys Prototyp.* 2024;19(1):e2351154.

doi: 10.1080/17452759.2024.2351154

19. Wang X, Jia L, Jia Z, *et al*. Optimization of 3D printing concrete with coarse aggregate via proper mix design and printing process. *J Build Eng.* 2022;56:104745.

doi: 10.1016/j.jobe.2022.104745

20. Li M, Weng Y, Liu Z, Zhang D, Wong TN. Optimizing of chemical admixtures for 3D printable cementitious materials by central composite design. *MSAM.* 2022;1(3):16.

doi: 10.18063/msam.v1i3.16

21. Liu H, Liu C, Wu Y, *et al*. 3D printing concrete with recycled coarse aggregates: The influence of pore structure on interlayer adhesion. *Cem Concr Compos.* 2022;134:104742.

doi: 10.1016/j.cemconcomp.2022.104742

22. Liu H, Liu C, Wu Y, *et al*. Hardened properties of 3D printed concrete with recycled coarse aggregate. *Cem Concr Res.* 2022;159:106868.

doi: 10.1016/j.cemconres.2022.106868

23. Mai I, Brohmann L, Freund N, *et al*. Large particle 3D concrete printing-a green and viable solution. *Materials (Basel).* 2021;14(20):6125.

doi: 10.3390/ma14206125

24. Wang D, Xiao J, Duan Z. Strategies to accelerate CO_2 sequestration of cement-based materials and their application prospects. *Constr Build Mater.* 2022;314:125646.

doi: 10.1016/j.conbuildmat.2021.125646

25. Singh R, Wang L, Ostrikov K, Huang J. Designing carbon-based porous materials for carbon dioxide capture. *Adv Mater Interf.* 2024;11(4):2202290.

doi: 10.1002/admi.202202290

26. Al-Khowaiter AO, Jamal A, Amr IT, Bamagain R, Al-Hunaidy AS, Fadhel BA. *Cementitious Print Head, 3D Printing Architecture, and Cementitious Printing Methodology*. Patent No. US011236517B2; 2022.

27. Lim SG, Tay YWD, Paul SC, *et al*. Carbon capture and sequestration with *in-situ* CO_2 and steam integrated 3D concrete printing. *Carbon Capture Sci Technol.* 2024;13:100306.

doi: 10.1016/j.ccst.2024.100306

28. ASTM. *C109/C109M-20: Standard Test Method for Compressive Strength of Hydraulic Cement Mortars (Using 2-in. or [50-mm] Cube Specimens)*. West Conshohocken, PA, United States: ASTM.

29. ASTM. *C293/C293M-16. Standard Test Method for Flexural Strength of Concrete (Using Simple Beam With Center-Point Loading)*. West Conshohocken, PA, United States: ASTM.

30. Bhatty JI. Hydration versus strength in a portland cement developed from domestic mineral wastes-A comparative study. *Thermochim Acta.* 1986;106:93-103.

doi: 10.1016/0040-6031(86)85120-6

31. Takahashi H, Maruyama I. Quantification of CO_2 in cement pastes with different degrees of carbonation. *J Adv Concr Technol.* 2024;22(11):706-715.

doi: 10.3151/jact.22.706

32. Fang X, Xuan D, Poon CS. Empirical modelling of CO_2 uptake by recycled concrete aggregates under accelerated carbonation conditions. *Mater Struct.* 2017;50:1-13.

doi: 10.1617/s11527-017-1066-y

33. Bernal SA, Provis JL, Mejía de Gutiérrez R, Van Deventer JS. Accelerated carbonation testing of alkali-activated slag/metakaolin blended concretes: Effect of exposure conditions. *Mater Struct.* 2015;48:653-669.

doi: 10.1617/s11527-014-0289-4

34. Kaliyavaradhan SK, Ling TC, Mo KH. CO_2 sequestration of fresh concrete slurry waste: Optimization of CO_2 uptake and feasible use as a potential cement binder. *J CO2 Util.* 2020;42:101330.

doi: 10.1016/j.jcou.2020.101330

35. Moini R, Rodriguez F, Olek J, Youngblood JP, Zavattieri PD. Mechanical properties and fracture phenomena in 3D-printed helical cementitious architected materials under compression. *Mater Struct.* 2024;57(7):170.

doi: 10.1617/s11527-024-02437-4

36. Panda B, Paul SC, Tan MJ. Anisotropic mechanical performance of 3D printed fiber reinforced sustainable construction material. *Mater Lett.* 2017;209:146-149.

doi: 10.1016/j.matlet.2017.07.123

37. Pi Y, Lu C, Li B, Zhou J. Crack propagation and failure mechanism of 3D printing engineered cementitious composites (3DP-ECC) under bending loads. *Constr Build Mater.* 2023;408:133809.

doi: 10.1016/j.conbuildmat.2023.133809

38. Wang YC, Lee MG, Wang WC, Kan YC, Kao SH, Chang HW. CO_2 curing on the mechanical properties of Portland cement concrete. *Buildings.* 2022;12(6):817.

doi: 10.3390/buildings12060817

39. Shi C, Wu Y. Studies on some factors affecting CO_2 curing of lightweight concrete products. *Resour Conserv Recycle.* 2008;52(8-9):1087-1092.

doi: 10.1016/j.resconrec.2008.05.002

40. Kamal NLM, Itam Z, Sivaganese Y, Beddu S. Carbon dioxide sequestration in concrete and its effects on concrete compressive strength. *Mater Today Proc.* 2020;31:A18-A21.

doi: 10.1016/j.matpr.2020.11.185

41. Lippiatt N, Ling TC. Rapid hydration mechanism of carbonic acid and cement. *J Build Eng.* 2020;31:101357.

doi: 10.1016/j.jobe.2020.101357

42. Han Y, Meng LY, Lin R, Kim S, Kim T, Wang XY. Evaluating the sustainability of microwave pre-cured high-volume slag concrete: Mechanical properties, environmental impact and cost-benefit analysis. *J Build Eng.* 2024;96:110663.

doi: 10.1016/j.jobe.2024.110663

43. Gao Y, Jiang Y, Tao Y, Shen P, Poon CS. Accelerated carbonation of recycled concrete aggregate in semi-wet environments: A promising technique for CO_2 utilization. *Cem Concr Res.* 2024;180:107486.

doi: 10.1016/j.cemconres.2024.107486

44. Dixit A, Du H, Dai Pang S. Carbon capture in ultra-high performance concrete using pressurized CO_2 curing. *Constr Build Mater.* 2021;288:123076.

doi: 10.1016/j.conbuildmat.2021.123076

45. Meng LY, Wang YS, Sun F, Lin R, Wang XY. An integrated strength-carbon emissions-total cost model for silica fume concrete. *Case Stud Constr Mat.* 2025;22:e04327.

doi: 10.1016/j.cscm.2025.e04327

46. O˘Guz S, Bellefontaine R, West J. Visualized: The Price of Carbon around the World in 2024. Available from: https://www.visualcapitalist.com/sp/visualized-the-price- of-carbon-around-the-world-in-2024 [Last accessed on 2025 Jul 24].

ACCSCIENCE PUBLISHING

Materials Science in Additive Manufacturing

ORIGINAL RESEARCH ARTICLE

Preparation of porous magnesium alloy scaffolds with high formation quality and dimensional accuracy through contour scan optimization in laser powder bed fusion

Zeyu Feng[1], Hao Zheng[1], Baoxue Zhou[1], Bozun Miao[1], Penghuai Fu[1], Deli Wang[2], Hua Huang[1]*, and Guangyin Yuan[1,2]*

[1]National Engineering Research Center of Light Alloy Net Forming and Key State Laboratory of Metal Matrix Composites, School of Materials Science and Engineering, Shanghai Jiao Tong University, Shanghai 200240, China

[2]National and Local Joint Engineering Research Center of Orthopaedic Biomaterials, Peking University Shenzhen Hospital, Shenzhen, Guangdong 518036, China

Abstract

Biodegradable magnesium-based scaffolds for bone tissue engineering are considered a promising treatment approach for repairing large bone defects. In this study, porous magnesium-neodymium-zinc-zirconium alloy (JDBM) scaffolds were fabricated using laser powder bed fusion (L-PBF) followed by dynamic electrochemical polishing. The effects of laser energy input and contour scan strategy on the formation quality of L-PBF scaffolds were systematically investigated. A novel scanning strategy, C64F84, combining low laser power for contour scans with high laser power for filling scans, was developed to achieve good fusion quality while controlling surface powder adhesion and dross defects. The printed specimens achieved a maximum relative density of 99.54%. The effects of electrochemical polishing on L-PBF scaffolds with different contour scan strategies were further evaluated. Electrochemical polishing effectively removed excess adhered powder and brought the scaffold porosity in line with the intended design value. The polished C64F84 scaffold exhibited higher dimensional accuracy, with smaller mean deviations, due to improved geometric consistency in the L-PBF process. Finite element analysis results were consistent with compression test data, confirming the high quality of the prepared C64F84 scaffolds. The yield strength (23.88 MPa) and elastic modulus (0.855 GPa) were comparable to those of cancellous bone, highlighting the medical potential of L-PBF-fabricated JDBM scaffolds.

Keywords: Magnesium alloy scaffolds; Laser powder bed fusion; Formation quality; Dimensional accuracy; Finite element analysis

***Corresponding authors:**
Hua Huang
(huangh@sjtu.edu.cn)
Guangyin Yuan
(gyyuan@sjtu.edu.cn)

Citation: Feng Z, Zheng H, Zhou B, *et al*. Preparation of porous magnesium alloy scaffolds with high formation quality and dimensional accuracy through contour scan optimization in laser powder bed fusion. *Mater Sci Add Manuf.* 2026;5(1):025350080. doi: 10.36922/MSAM025350080

Received: August 26, 2025

Revised: September 17, 2025

Accepted: September 26, 2025

Published online: October 30, 2025

1. Introduction

Bone tissue possesses the ability to self-repair and regenerate; however, bone defects exceeding the critical size (typically defined as a defect length >1.5 times the diameter of the long bone) cannot recover unaided.[1] Bone tissue engineering scaffolds, designed

to temporarily fulfill the role of the extracellular matrix during new tissue regeneration, have attracted extensive attention for their potential in treating large bone defects.[2] Magnesium (Mg) and its alloys possess suitable mechanical properties, excellent biocompatibility, and ideal biodegradation.[3,4] Moreover, Mg^{2+} has been shown to promote osteogenesis and angiogenesis during bone regeneration.[5] Consequently, Mg alloys have been recognized as highly promising biomaterials for bone tissue engineering scaffolds.[6]

An ideal bone scaffold should feature an interconnected porous structure to support cell migration and nutrient transport.[7] Furthermore, high porosity and an appropriate pore size range (400–800 μm) can facilitate cell attachment and bone growth.[8] Traditional fabrication methods for Mg scaffolds, such as powder metallurgy, negative salt-pattern molding, and laser perforation, cannot reliably control pore morphology and distribution.[9] By contrast, laser powder bed fusion (L-PBF) offers clear advantages in fabricating porous scaffolds with complex internal structures and customized geometries at high precision, making L-PBF the preferred method for manufacturing porous Mg scaffolds.[10] However, L-PBF specimens cannot typically be used in the as-built state due to their high surface roughness. Surface treatment, therefore, is required to smooth scaffold surfaces, which is critical to enhance corrosion resistance and prevent fatigue failure.[11] For Mg scaffolds with intricate structures, L-PBF followed by electrochemical polishing has proven to be the most effective preparation route.[12]

The performance of porous Mg scaffolds is highly sensitive to formation defects and geometric deviations. Formation defects reduce scaffold mechanical properties and accelerate pitting corrosion during degradation.[13] Geometric deviations, in turn, compromise accurate performance evaluation by altering structural characteristics. With increasing porosity, the mechanical properties of porous scaffolds decrease exponentially, satisfying the Gibson-Ashby model.[11] Factors such as pore size, specific surface area, permeability, and gradient design also strongly influence the corrosion behavior and biological performance of porous scaffolds.[14,15] Across careful parameter optimization of L-PBF conditions, numerous studies have reported the successful fabrication of Mg scaffolds with high relative density.[16,17] However, geometric deviation has often been overlooked in prior research.

In L-PBF Mg scaffolds, substantial powder adhesion frequently occurs on down-facing surfaces, sometimes forming dross defects that decrease porosity and obstruct pores.[18] These deviations can be alleviated by polishing; however, if the deviations are too severe, polishing alone may not yield satisfactory results. For example, Xie *et al.*[19] fabricated Mg-neodymium (Nd)–zinc (Zn)–zirconium (Zr) scaffolds for antibacterial evaluation with a porosity of 32.1%. After polishing, porosity increased to 52.1%, which remained far below the designed value of 80%. Wang *et al.*[20] applied dynamic electropolishing to three types of L-PBF scaffolds. Although the resulting porosity values were only 1% lower than the design, radially graded pores emerged due to prolonged asymmetric polishing, and irregular protrusions caused by dross persisted. Therefore, reducing geometric deviations during the L-PBF process is critical to ensuring the dimensional accuracy of as-polished scaffolds.

Due to the high reactivity and low boiling point of Mg, the L-PBF process of Mg alloys often results in various microscale imperfections.[21] Compared to bulk samples, the processing window for achieving dense porous structures is narrower.[22] Liu *et al.*[23] fabricated WE43 scaffolds and found that relatively high energy input improved fusion quality but also caused increased powder adhesion and dimensional errors. Using a single L-PBF parameter thus presents a dilemma between achieving high fusion quality and maintaining high dimensional accuracy. In the contour area, the laser acts directly on the unconsolidated powder bed, where severe heat accumulation occurs, resulting in greater powder adhesion and dross defects.[24] Across multi-physics simulations, Wang *et al.*[22] discovered that a deeper molten pool formed during contour scanning and proposed that lower energy density should be applied at the edges. Similarly, Charles *et al.*[25] reported that reducing linear energy density near contour regions could suppress dross formation and dimensional deviations in inclined struts. For porous scaffolds with high specific surface area, contour formation accounts for a large proportion of the structure. Although these findings indicate that using low laser energy in contour scans can improve printing accuracy, research focusing specifically on this strategy remains inadequate, especially for high-precision porous Mg scaffolds.

In this study, we employed the novel biodegradable Mg-Nd-Zn-Zr alloy (JDBM) developed by our group, which has demonstrated excellent biocompatibility and corrosion resistance in both *in vitro* and *in vivo* investigations.[26,27] The aim was to prepare JDBM scaffolds with high formation quality and dimensional accuracy. An optimized L-PBF process was developed to reduce formation defects and geometric deviations by customizing energy input during contour scanning. The effectiveness of dynamic electrochemical polishing under different contour processes was compared, and the dimensional accuracy of the polished scaffolds was evaluated. Furthermore, the mechanical properties of the scaffolds were tested, and the experimental compressive strength was compared with finite element analysis (FEA) results.

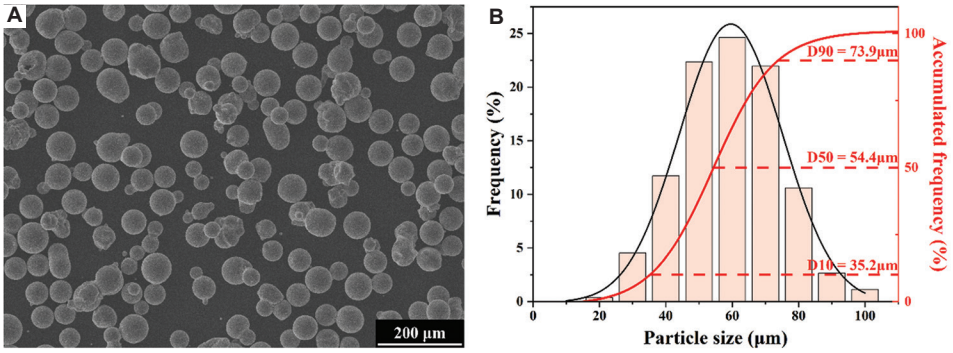

Figure 1. Characteristics of JDBM powders for laser powder bed fusion. (A) Scanning electron microscopy image of powder morphology. Scale bars: 200 μm; magnification: ×200. (B) Powder size distribution

2. Materials and methods

2.1. Materials

The JDBM alloy powder was prepared by centrifugal atomization (WHCA-40, Tangshan Weihao, China). As shown in Figure 1A, the particles were spherical and dense, with few satellite granules, indicating good powder quality. The particle size distribution, shown in Figure 1B, approximately followed a normal distribution. The statistical values for D10, D50, and D90 were 35.2 μm, 54.4 μm, and 73.9 μm, respectively. Table 1 presents the chemical composition of the powder and the L-PBF scaffolds, measured by inductively coupled plasma atomic emission spectroscopy (iCAP7600, Thermo, USA). The alloying element contents in the L-PBF scaffolds increased slightly, which may be attributed to the higher vaporization tendency of Mg during laser melting.

Table 1. Chemical composition of JDBM powder and laser powder bed fusion (L-PBF) scaffolds (wt.%)

Elements	Neodymium	Zinc	Zirconium	Magnesium
Powder	2.35	0.19	0.37	Balance
L-PBF scaffolds	2.74	0.19	0.39	Balance

2.2. Scaffold preparation

The pore topology of the scaffolds was defined using sheet gyroid units with a unit size of 2 mm, as shown in Figure 2A. Typically, a porosity of >70% is required for bone scaffolds.[28] Therefore, the target porosity was designed as 70%. The designed strut thickness and pore diameter were 210 μm and 800 μm, respectively. The porous scaffolds were fabricated using an L-PBF machine (iSLM160, ZRapid Tech, China) equipped with a laser spot diameter of 50 μm. The powder bed and Mg baseplate were pre-heated at 100°C for 1 h before printing. During printing, an inert atmosphere was maintained in the chamber with oxygen content below 200 ppm. Hatch spacing and layer thickness were set to 50 μm and 20 μm, respectively. Laser power (P) and scanning speed (V) were set in the ranges of 50–90 W and 200–600 mm/s, based on our previous work on JDBM cubes.[22] Figure 2B illustrates the scanning strategy, which involved contour scanning followed by filling for each layer. The offset distance (δ_C) between the contour line and filling line was set to 20 μm to ensure the effectiveness of contour scanning.[29] The scanning direction was rotated by 67° between adjacent layers.

After printing, the samples were removed from the baseplate and ultrasonically cleaned in 99 vol.% ethanol for 5 min. All samples were then subjected to dynamic electrochemical polishing until the porosity approached the designed value, using the apparatus shown in Figure 3A. The electrolyte consisted of 30 vol.% phosphoric acid and 70 vol.% C_2H_5OH. During polishing, the electrolyte temperature was maintained at 40°C, the voltage was set to 20 V, and the magnetic stirrer speed was 400 rpm. After polishing, the samples were cleaned in ethanol for 5 min to remove residual electrolytes.

2.3. Scaffold characterization

The formation quality of the L-PBF sample cross-sections was examined using optical microscopy (OM; Axio Observer A1, Zeiss, Germany). Relative density was calculated using ImageJ software (version 1.51; https://imagej.net/ij/). In ImageJ, OM images were converted to grayscale, and the thresholding tool was employed to determine the pore area fraction. Relative density was reported as the average of three different measurement regions. Surface morphology of the scaffolds was observed using scanning electron microscopy (SEM; VEGA 3 (LaB6); (TESCAN, Czech). Porosity was measured using the Archimedean method. Surface roughness was determined using a laser scanning confocal microscope (VK-X3000, KEYENCE, China). The internal structure was analyzed using an X-ray micro-computed tomography (micro-CT; Xradia 520 Versa,

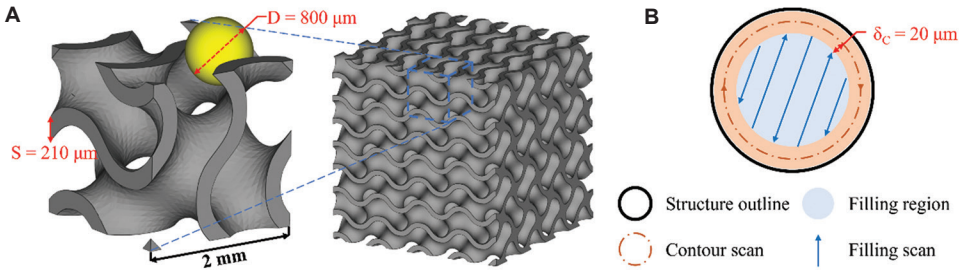

Figure 2. Design of the laser powder bed fusion process. (A) Gyroid unit cell and scaffold models. (B) Schematic of the scanning strategy

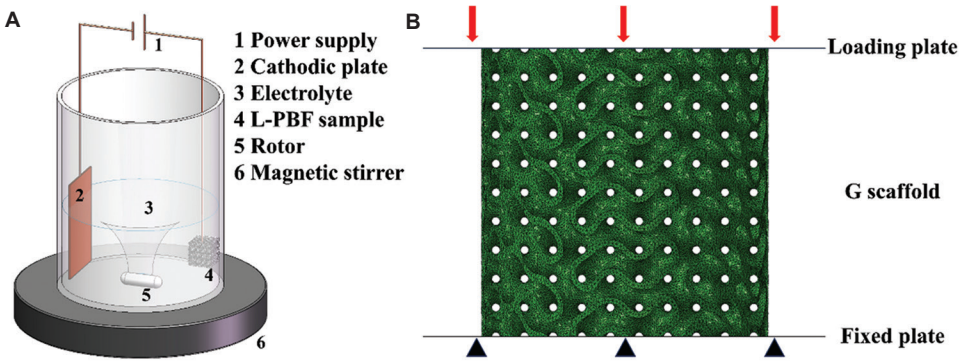

Figure 3. Experimental methods. (A) Schematic of the electrochemical polishing device. (B) Model setup for finite element analysis
Abbreviations: AM: Additively manufacture; G: Gyroid

Zeiss, Germany) at a resolution of 10 μm. The scanned data were imported into AvizoFire software (version 2019.1), Thermo Fisher Scientific, USA) for reconstruction. Geometric deviations of the reconstructed scaffold models were quantified based on the statistical distributions of the nearest neighbor distance between CT-derived point data and the design model surfaces, calculated using Materialise 3-matic software (version 11.0, Materialise, Belgium).

2.4. Mechanical testing

Compression tests were performed on cylindrical scaffolds (Ø10 × 10 mm) using a Zwick AG-100KN testing machine (ZwickRoell, Germany) at room temperature, at a crosshead speed of 1 mm/min, with three specimens tested for each condition.

FEA was conducted using Abaqus/Explicit (version 2022, Dassault Systèmes Simulia Corp., France) to investigate stress distribution. Scaffold models were meshed with C3D10M tetrahedral elements, with a grid size of 0.1 mm. Material properties were obtained from tensile tests on specimens fabricated under optimized parameters. The material was assumed to be homogeneous and isotropic, with an elastic modulus of 30.8 GPa and a Poisson's ratio of 0.35. The yield strength and ultimate tensile strength were 185 MPa and 252 MPa, respectively. Analysis steps were dynamic and explicit. Boundary conditions are shown in Figure 3B: The top plate was subjected to a displacement of 5 mm along the Z-axis, while the bottom plate was fixed.

3. Results and discussion

3.1. Formation quality

Figure 4A displays representative OM images of the cross-sections of porous scaffolds fabricated under different combinations of P and V. The linear energy density, P/V (J/mm), reflects the laser energy input. At high energy input, numerous large circular keyholes were observed (Figure 4A1). At low energy input, irregularly shaped lack-of-fusion defects appeared in two distribution patterns: (i) Uniformly distributed unfused cracks (Figure 4A4); and (ii) defects localized mainly at the central junction region, with fewer defects in the wall regions (Figure 4A3). At moderate energy input, relatively dense cross-sections with only a few small circular gas pores were observed (Figure 4A2). The relative density of these samples is presented in Figure 4C. The highest relative density of 99.44% was achieved at P = 80 W and V = 400 mm/s.

In L-PBF of Mg alloys, the primary defect types are lack-of-fusion defects and keyhole defects, both of which are closely linked to laser parameters.[28] Insufficient heat input leads to incomplete melting of the powder and

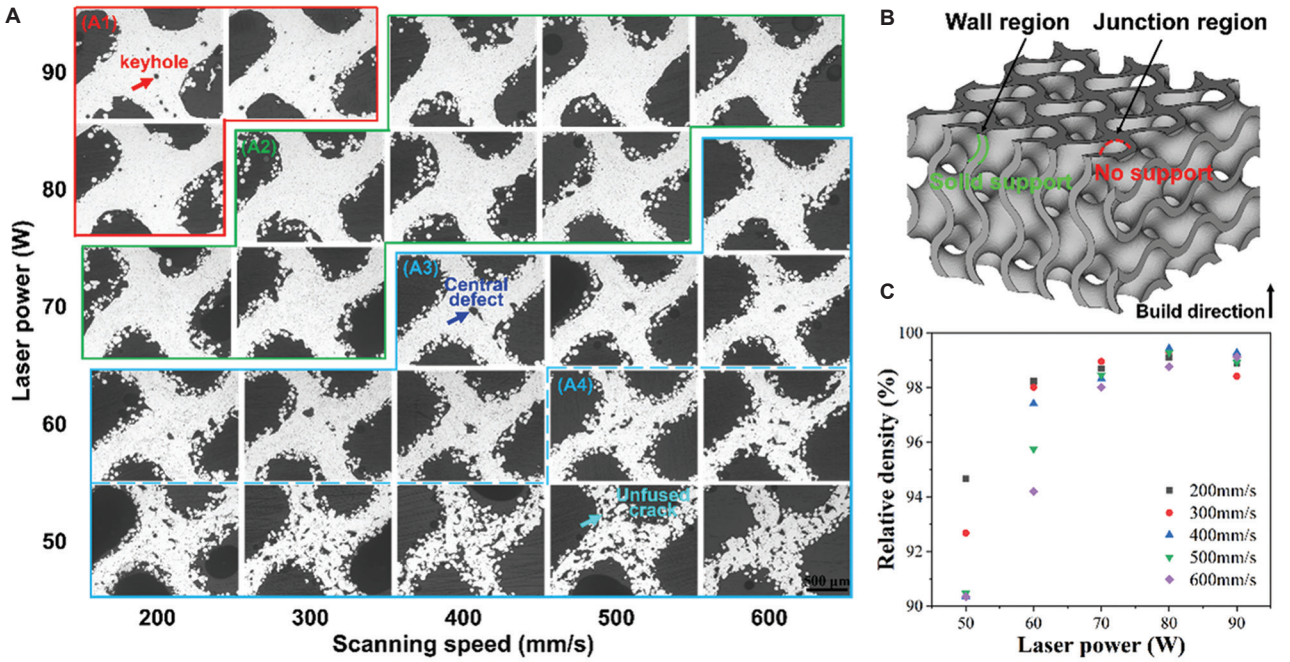

Figure 4. Fusion quality of porous scaffolds under various laser power and scanning speed. (A) Optical microscopy images of cross-sections at the junction region. Scale bars: 500 μm; magnification: ×50. (B) Typical regions of the porous structure. (C) Relative density

an unstable molten pool, ultimately causing elongated and sharp unfused cracks.[30] Increasing the energy input promotes complete melting and reduces crack defects, but central lack-of-fusion defects may persist. Considering the porous structure shown in Figure 4B, the junction region is located above the interconnected pores without effective support. During laser melting, the molten pool rests on loose powder, and under gravity, the bottom of the molten pool can deform or collapse, resulting in poor metallurgical bonding with adjacent tracks and the formation of central defects.[24] In addition, the thin junction regions consist of only a few slices in the design and lack sufficient interlayer remelting to eliminate central defects.[31] Therefore, for L-PBF porous scaffolds, structural factors also affect the manufacturability of specific regions and contribute to defect formation. At higher energy input, the remelting overlap between adjacent tracks expands, improving density in the junction regions. However, excessive heat input changes the molten pool from conduction mode to unstable keyhole mode.[32] A deep vapor cavity then forms, trapping gases within the solidified material and resulting in keyhole defects. Unlike lack-of-fusion or keyhole defects, the small gas pores observed in otherwise dense samples originate from gases dissolved in the melt or entrapped metal vapor, which are difficult to eliminate.[33] The high vaporization tendency of Mg exacerbates the formation of such pores.

Based on these results, P = 80 W and V = 400 mm/s were identified as optimal parameters for the filling scan. Unlike the filling region, the contour region tolerated a wider parameter range, as central defects were absent. Considering heat accumulation, lower laser power should be applied during contour scanning to reduce heat input. At P = 60 W, the laser energy was sufficient to form well-defined contours, whereas lower powers produced unfused cracks. Accordingly, four scanning strategies were designed to investigate the effects of contour scanning on formation quality: NCF84 (no contour scan, filling scan: 80 W/400 mm/s), C84F84 (both contour and filling scan: 80 W/400 mm/s), C64F64 (both contour and filling scan: 60 W/400 mm/s), and C64F84 (contour scan: 60 W/400 mm/s, filling scan: 80 W/400 mm/s).

As shown in Figure 5A, the top surfaces of all four scaffolds exhibited similar quality and structural accuracy, with only a few powder particles observed along the edges. In contrast, the side surfaces exhibited poorer quality due to extensive adhesion of unmelted powder (Figure 5B). Contour processing had a more significant influence on side surface morphology. In the NCF84 and C84F84 scaffolds, large powder agglomerates accumulated on the lower surfaces of the porous structures, forming dross that nearly blocked the pores. Powder adhesion and dross defects also increased sidewall thickness, resulting in significant structural deviations. By comparison, the C64F64 and C64F84 scaffolds exhibited more distinct pore structures, with fewer adhered particles and more consistent surface morphology. These results indicate that

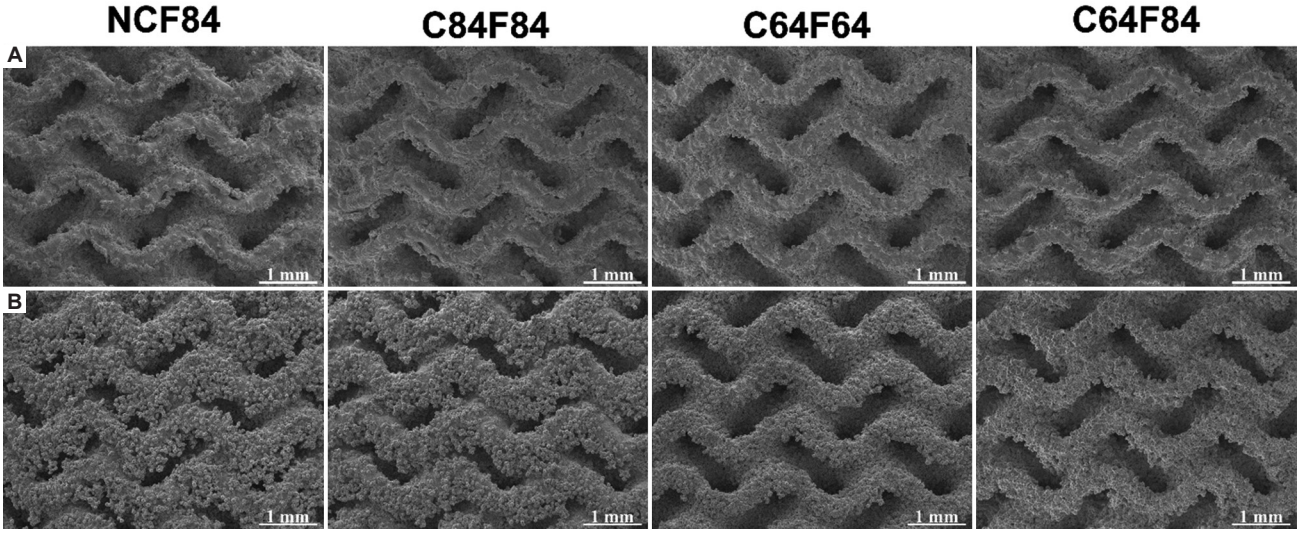

Figure 5. Scanning electron microscopy of the surface morphologies of scaffolds fabricated under four scanning strategies. (A)Top surfaces. (B) Side surfaces. Scale bars: 1 mm; magnification: ×50

powder adhesion and dross defects are strongly influenced by contour scan parameters.

The mechanism of dross formation is as follows: When the laser scan enters the powder region near an inclined solid edge, the low thermal conductivity of the loose powder causes the molten pool to overheat and transition to a keyhole-like mode. This produces a deeper depression in the powder bed and subsequent dross formation, referred to as the drilling effect.[34] Higher molten pool temperatures and slower cooling rates further promote partial melting and wetting of surrounding powder particles, increasing powder adhesion.[35] Reducing laser power during contour scanning is therefore an effective strategy to control powder adhesion and dross defects in porous scaffolds.

Figure 6A displays the CT-reconstructed models of the four scaffolds. The C64F84 and C64F64 scaffolds exhibited better geometric consistency with the design model at the macroscale. According to the CT cross-sectional images (Figure 6B), more residual powder particles were observed inside the cavities of the C84F84 and NCF84 scaffolds. For the C64F64 scaffold, contour scanning did not eliminate unfused defects in the junction regions. Analysis of the CT-reconstructed models revealed 9580, 7818, and 5043 gas pore defects in the NCF84, C84F84, and C64F84 scaffolds, respectively. The C64F84 scaffold contained fewer gas pores than the C84F84 and NCF84 scaffolds, likely because the lower-energy contour scan reduced the severe evaporation that occurs when the laser irradiates the powder bed. As shown in Figure 6C, in the longitudinal CT sections parallel to the printing direction, the NCF84 scaffold exhibited many protrusions and notches that compromised structural integrity. These side-surface defects were caused by the staircase effect resulting from distinct boundaries between adjacent layers.[36] Border melting introduced by contour scanning smoothed the surfaces and improved structural uniformity. For the C84F84 scaffolds, in addition to small powder particles, powder agglomerates were observed on the lower surfaces. In the C64F64 scaffold, unfused defects occurred at inclined struts instead of at the junction regions, confirming that defect location was related to porous structure geometry. Overall, the C64F84 scaffold exhibited the best formation quality and the least powder adhesion inside the structure.

Because the resolution of CT images was limited, Figure 7A presented OM cross-sectional images of the C64F84 scaffold, which showed a relative density of 99.54%. The circular gas pores had an average size of 5 μm. The porosities of the four scaffolds are shown in Figure 7B. Contour scanning with low laser power increased the porosity of the scaffolds. The average wall thickness, measured from the CT models, is shown in Figure 7C. With higher energy input, a larger contour region formed, which also led to greater dimensional deviations. Compared to the NCF84 scaffold, the wall thickness of the C64F84 scaffold decreased after applying a low-power contour scan. This was due to the single-digit percentage of laser absorptivity in solid bulk metals, which is much lower than that of the powder bed.[37] In the C64F84 scaffold, powder in the contour region melted into solid metal during the contour scan. In the subsequent filling scan, when the laser re-irradiated the contour region at the track endpoint, a smaller melt zone formed because of the reduced absorptivity of the solid.[38] Overall, high laser energy input increased molten pool size and improved fusion quality, while low laser

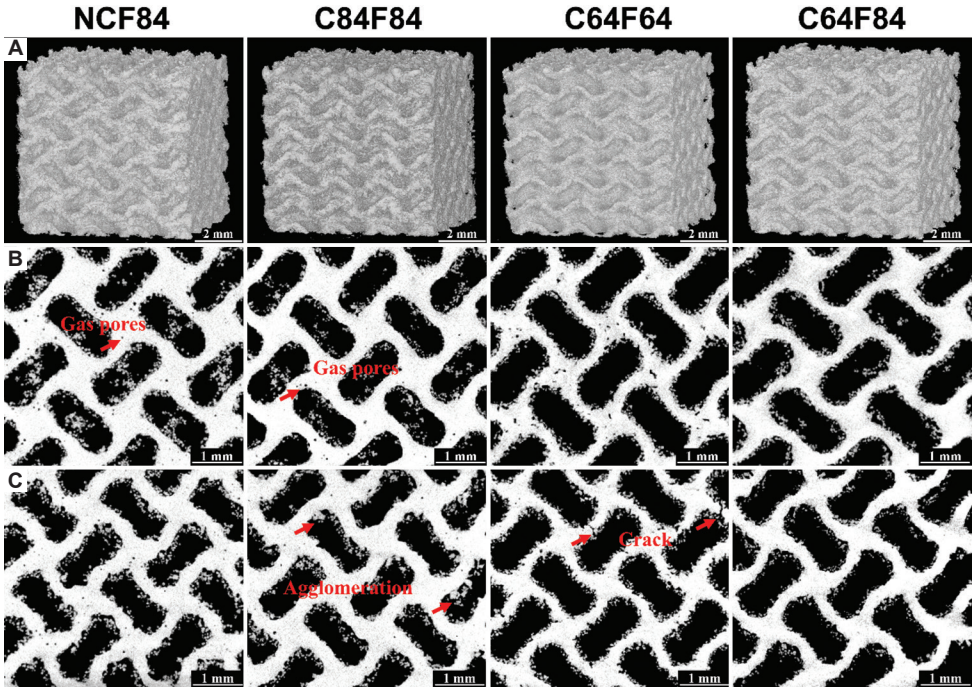

Figure 6. Formation quality of porous scaffolds under four scanning strategies. (A) Macroscopic computed tomography (CT)-reconstructed models. (B) Cross-sectional CT images. (C) Longitudinal CT images. Scale bars: (A) 2 mm, (B and C) 1 mm; magnification: A, B, and C 10 μm

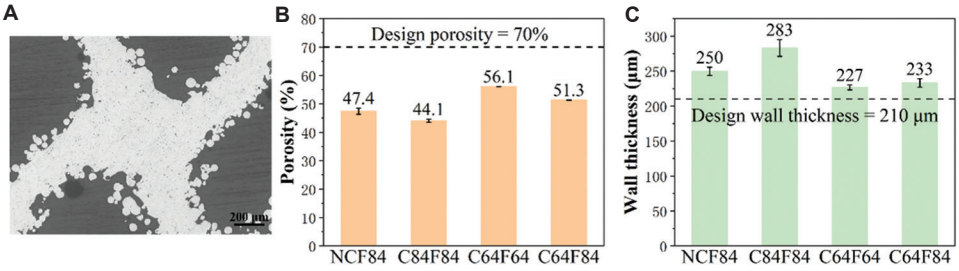

Figure 7. Characteristics of scaffolds. (A) Optical microscopy images of the C64F84 scaffold cross-section. Scale bars: 200 μm; magnification: ×50. (B) Porosity of porous scaffolds fabricated under four scanning strategies. (C) Wall thickness of porous scaffolds under four scanning strategies

energy input reduced powder adhesion and dross defects, thereby decreasing geometric deviation. Compared to the single-parameter strategies, the C64F84 strategy effectively combined the advantages of both processes.

3.2. Electrochemical polishing quality

To achieve smooth surfaces, the L-PBF scaffolds required electrochemical polishing. Based on fusion quality, the NCF84, C84F84, and C64F84 scaffolds were selected to compare polishing quality under different contour processes. Due to differences in porosity among the scaffolds, unequal polishing times were required. By monitoring porosity variation during polishing, the polishing times for the NCF84, C84F84, and C64F84 scaffolds were determined as 14, 20, and 10 min, respectively. After polishing, the porosity of all three scaffolds closely matched the design value of 70%, with a deviation of <0.5%.

As shown in Figure 8A, SEM images of the polished scaffolds revealed that most unmelted powder was removed, and the porous structures were clearly visible. For the NCF84 and C84F84 scaffolds, residual dross in solid form remained due to the lack of local targeting during polishing (Figure 8B). This finding underscores the need to minimize dross formation during the L-PBF process. The surface roughness (Sa) of the polished NCF84, C84F84, and C64F84 scaffolds was 22.8 μm, 11.4 μm, and 9.9 μm, respectively (Figure 8C). Electropolishing had a limited ability to improve surface roughness, and the initial surface roughness strongly influenced the final polished surface quality.[39] Incorporating contour scanning can reduce the surface roughness of L-PBF parts.[40]; accordingly, the C84F84 and C64F84

scaffolds exhibited lower surface roughness than the NCF84 scaffold after polishing. During polishing, surface roughness typically decreases rapidly at the beginning, following an exponential decay pattern similar to that of the material removal rate.[39] Larger geometric deviations significantly increased polishing inefficiency. Although the C84F84 scaffold required longer polishing than the C64F84 scaffold, both ultimately exhibited similar surface roughness.

To assess internal polishing quality, longitudinal CT images of the C84F84 and C64F84 scaffolds are shown in Figure 9A. The polishing process effectively removed residual powder within the scaffolds while also reducing wall thickness to a certain extent. The C84F84 scaffold retained some residual powder particles at its center and exhibited gradient structures. The wall thickness of the outer region was approximately 180 μm, whereas that of the inner region was approximately 260 μm, indicating uneven polishing. In comparison, the polished C64F84 scaffold displayed interconnected pores and relatively uniform wall thickness, with a measured pore size of 794.37 μm. CT-reconstructed models of the polished

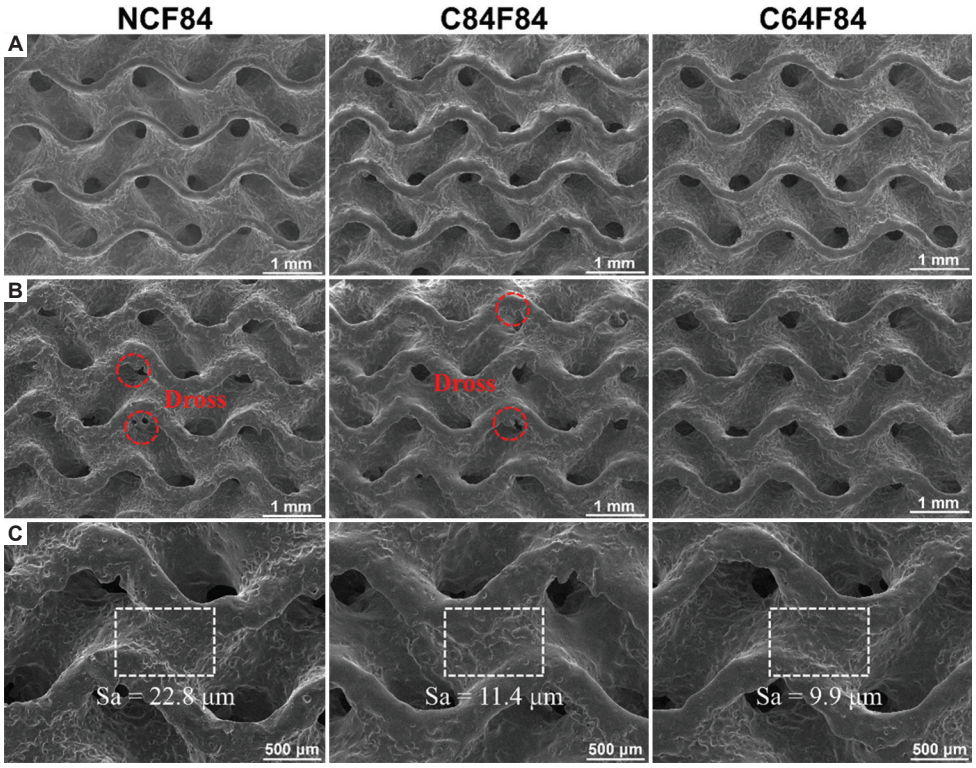

Figure 8. Scanning electron microscopy of the surface morphologies of the polished scaffolds under different contour processes. (A) Top surfaces. (B, C) Side surfaces. Scale bars: (A and B) 1 mm, (C) 500 μm; magnification: (A and B) ×50, (C) ×100

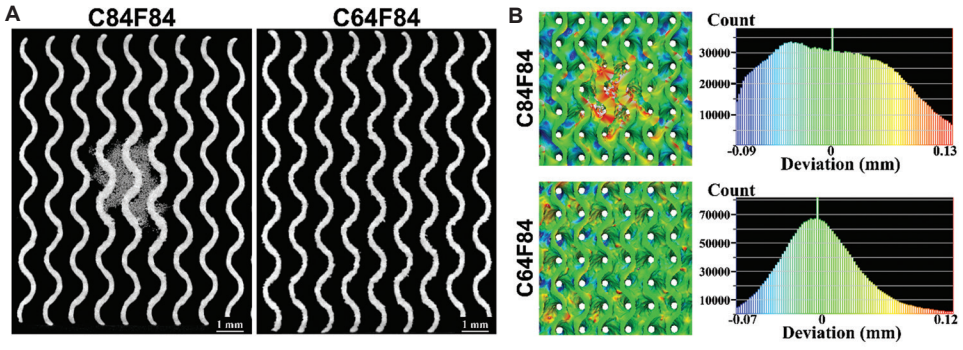

Figure 9. Polishing quality of the C84F84 and C64F84 scaffolds. Scale bars: 1 mm; magnification: 10 μm. (A) Longitudinal computed tomography images. (B) Three-dimensional deviation maps and corresponding histograms

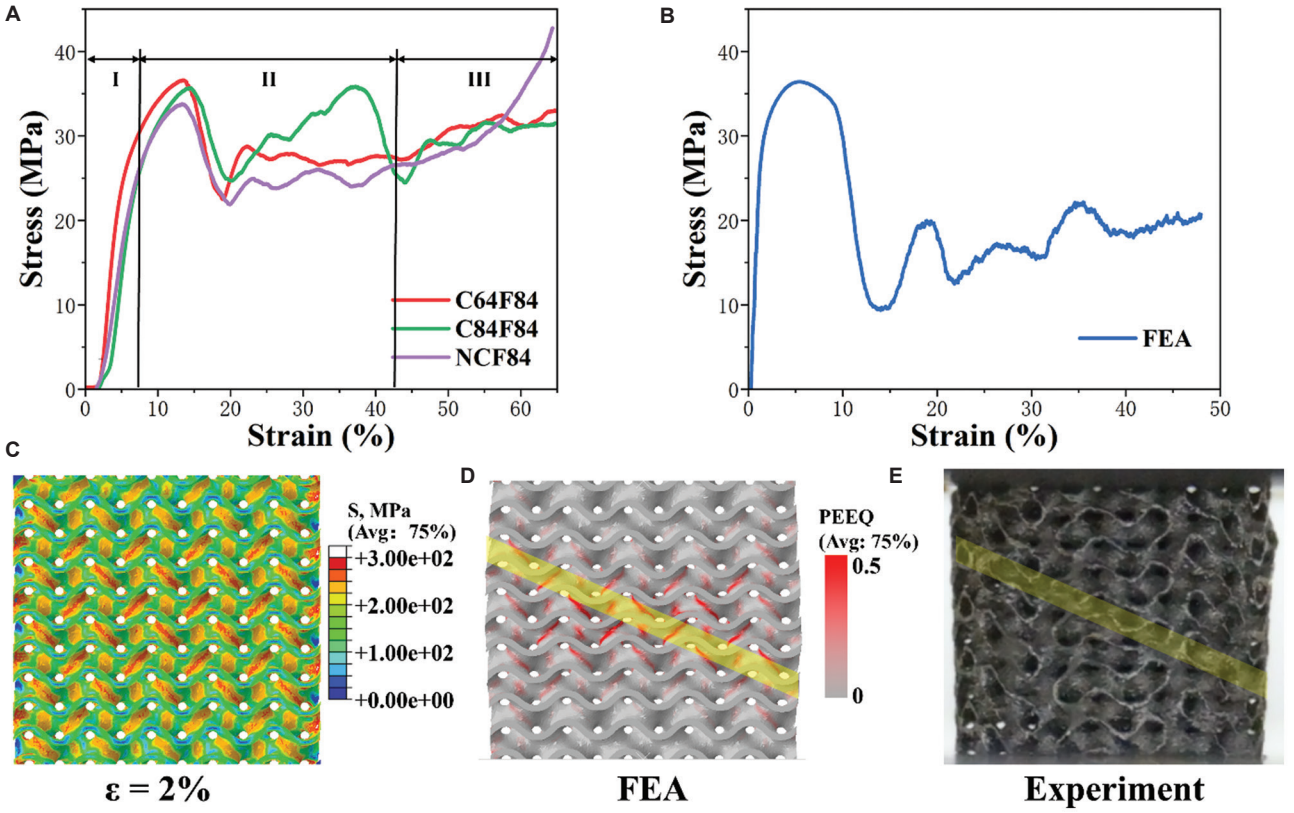

Figure 10. Mechanical properties of scaffolds. (A) Compression stress-strain curves. (B) Stress-strain curves predicted by finite element analysis (FEA). (C) Cross-sectional stress distribution predicted by FEA. (D) Cross-sectional plastic equivalent strain (PEEQ) nephogram predicted by FEA. (E) Compression deformation at the first stress peak

scaffolds were compared with the design model, and three-dimensional deviation maps were generated (Figure 9B). Red and blue regions indicate structural increasement and structural reduction, respectively. For the C84F84 scaffold, the internal structures showed more positive deviations, whereas the external structures showed negative deviations, confirming that polishing preferentially removed external material. For the C64F84 scaffold, the distribution of geometric deviations followed a Gaussian profile centered near zero. In contrast, the C84F84 scaffold displayed a higher proportion of large deviations, confirming the superior dimensional accuracy of the C64F84 scaffold. The mean deviation values for the C84F84 and C64F84 scaffolds were 0.008 mm and 0.003 mm, respectively, compared to 0.032 mm reported in previous studies.[20] These minor deviations aligned well with the measured porosity of 70%.

Electrochemical polishing is explained by the "viscous film theory": On rough surfaces, viscous films of different thickness and high electrical resistance form at protruding and recessed regions, resulting in higher dissolution rates at protrusions and eventual surface smoothing.[39] Because the electrolyte is fluid and flows into inner regions with stirring, electropolishing can treat both internal and external surfaces of porous scaffolds.[21] However, during the electropolishing of Mg, the electrolyte is consumed by reactions, and significant hydrogen gas evolves on the surface. For external regions, hydrogen gas readily dissipates into the solution, promoting electrolyte replenishment. For internal regions, however, hydrogen must diffuse through long pore channels, often coalescing into larger bubbles. These bubbles can block pores and hinder electrolyte flow, leading to insufficient replenishment and low local electrolyte density in inner regions.[20] Consequently, the dissolution rate inside the scaffold is slower than outside, generating uneven polishing. Prolonged polishing further aggravates this unevenness. In the C84F84 scaffolds, dross-blocked pores and narrower channels further inhibited dynamic electrolyte penetration, resulting in pronounced gradient structures. In contrast, the C64F84 scaffold exhibited better geometric consistency and required shorter polishing time, reducing asymmetry. Considering that polishing inevitably reduces wall thickness, a small positive geometric deviation is desirable in L-PBF scaffolds. Therefore, the C64F84 strategy proved to be the most suitable for preparing Mg scaffolds by L-PBF.

3.3. Mechanical properties

Cylindrical NCF84, C84F84, and C64F84 scaffolds were prepared for compression testing. Figure 10A displays the compressive stress–strain curves, which exhibited the three typical stages of porous structures: The elastic stage (I), the long plateau stage (II), and the densification stage (III). Compared to the NCF84 scaffold, the addition of contour scanning improved the compressive strength. Considering the small total volume of gas pores, formation defects were not the dominant factor accounting for strength differences among the scaffolds. With similar porosity, the enhanced strength can be attributed to higher damage tolerance resulting from improved surface quality and geometrical uniformity.[36] Due to strength variation across layers in the gradient structure, the C84F84 scaffold exhibited greater stress fluctuations. The C64F84 scaffold demonstrated the best mechanical performance, with an elastic modulus of 0.855 ± 0.017 GPa, a yield strength of 23.88 ± 0.72 MPa, and a compressive strength of 36.61 ± 0.19 MPa. These values match the mechanical properties of human cancellous bone, which has a compressive strength of 0.2–80.0 MPa and an elastic modulus of 0.01–2.00 GPa.[41] Thus, JDBM scaffolds could mitigate the stress shielding effect and support bone growth. The compressive strength calculated using FEA was 36.43 MPa (Figure 10B). The close agreement between the experimental and simulated results confirmed the high quality of the C64F84 scaffold. The cross-sectional von Mises stress distribution within the FEA models (Figure 10C) revealed that stress concentrations were primarily located in the junction regions and distributed diagonally, with more severe concentrations toward the center. Corresponding to this stress distribution, scaffolds failed by shear damage at the first stress peak. As shown in Figure 10D, shear bands were distinguishable in the cross-sectional plastic equivalent strain nephogram from FEA results. Similar shear bands were observed in the experimental results (Figure 10E).

4. Conclusion

This study investigated the fabrication of JDBM porous scaffolds with high formation quality and dimensional accuracy using the L-PBF process combined with electrochemical polishing. The main findings are summarized as follows:

(i) The optimal L-PBF parameters for the filling scan were P = 80 W and V = 400 mm/s. Contour scanning significantly influenced surface quality. Using low laser power for the contour scan reduced powder adhesion and dross defects on side surfaces, improving geometric consistency. With the optimal C64F84 scanning strategies, the relative density of L-PBF scaffolds reached 99.54%.

(ii) Electrochemical polishing effectively removed adhered powder particles from L-PBF scaffolds. However, different contour processes produced different polishing outcomes. Excessive polishing time and pore blockage caused uneven polishing between internal and external structures. Benefitting from the small positive geometric deviation of the L-PBF process, the polished C64F84 scaffolds exhibited higher dimensional accuracy and porosity consistent with the design value.

(iii) The C64F84 scaffold exhibited superior mechanical performance, with an elastic modulus of 0.855 GPa, a yield strength of 23.88 MPa, and a compressive strength of 36.61 MPa. Experimental compression results closely matched FEA predictions, confirming the high quality of the prepared JDBM scaffolds.

Acknowledgments

None.

Funding

This work was supported by the National Key Research and Development Program of China (No.2024YFB4610100, No.2024YFC2418602), the National Natural Science Foundation of China (No.52130104), Shanghai Jiao Tong University Medial-Engineering Cross Fund (YG2024LC05), the Scientific Research Foundation for Shenzhen high-level talents (No.RC2022-003), Guangdong Basic and Applied Basic Research Foundation (No.2022B1515120046), Sanming Project of Medicine in Shenzhen (No.SZSM202211038) and Shanghai Science and Technology Committee(23JC1402400).

Conflict of interest

The authors declare that they have no known competing financial interests or personal relationships that could have appeared to influence the work reported in this paper.

Author contributions

Conceptualization: Guangyin Yuan
Funding acquisition: Guangyin Yuan, Penghuai Fu, and Deli Wang
Investigation: Zeyu Feng, Hao Zheng, and Bozun Miao
Methodology: Zeyu Feng and Baoxue Zhou
Writing – original draft: Zeyu Feng
Writing – review and editing: Zeyu Feng, Guangyin Yuan, and Hua Huang

Ethics approval and consent to participate

Not applicable.

Consent for publication

Not applicable.

Availability of data

Data are available from the corresponding author on reasonable request.

References

1. Turnbull G, Clarke J, Picard F, *et al.* 3D bioactive composite scaffolds for bone tissue engineering. *Bioact Mater.* 2018;3(3):278-314.

   doi: 10.1016/j.bioactmat.2017.10.001

2. Koons GL, Diba ML, Mikos AG. Materials design for bone-tissue engineering. *Nat Rev Mater.* 2020;5(8):584-603.

   doi: 10.1038/s41578-020-0204-2

3. Chen Y, Xu Z, Smith C, Sankar J. Recent advances on the development of magnesium alloys for biodegradable implants. *Acta Biomater.* 2014;10(11):4561-4573.

   doi: 10.1016/j.actbio.2014.07.005

4. Shanmugavadivu A, Lekhavadhani S, Babu S, Suresh N, Selvamurugan N. Magnesium-incorporated biocomposite scaffolds: A novel frontier in bone tissue engineering. *J Magnesium Alloys*. 2024;12(6):2231-2248.

   doi: 10.1016/j.jma.2024.06.001

5. Xing F, Li S, Yin D, *et al.* Recent progress in Mg-based alloys as a novel bioabsorbable biomaterials for orthopedic applications. *J. Magnesium Alloys*. 2022;10(6):1428-1456.

   doi: 10.1016/j.jma.2022.02.013

6. Wang W, Jia G, Wang Q, *et al.* The *in vitro* and *in vivo* biological effects and osteogenic activity of novel biodegradable porous Mg alloy scaffolds. *Mater Des.* 2020;189:108514.

   doi: 10.1016/j.matdes.2020.108514

7. Alex Y, Vincent S, Divakaran N, *et al.* Pioneering bone regeneration: A review of cutting-edge scaffolds in tissue engineering. *Bioprinting*. 2024;43:e00364.

   doi: 10.1016/j.bprint.2024.e00364

8. Jia G, Huang H, Niu J, *et al.* Exploring the interconnectivity of biomimetic hierarchical porous Mg scaffolds for bone tissue engineering: Effects of pore size distribution on mechanical properties, degradation behavior and cell migration ability. *J Magnesium Alloys*. 2021;9(6):1954-1966.

   doi: 10.1016/j.jma.2021.02.001

9. Zheng YF, Gu XN, Witte F. Biodegradable metals. *Mater Sci Eng R Rep.* 2024;77:1-34.

   doi: 10.1016/j.mser.2014.01.001

10. Li Y, Jahr H, Zhou J, Zadpoor AA. Additively manufactured biodegradable porous metals. *Acta Biomater.* 2020;115:29-50.

    doi: 10.1016/j.actbio.2020.08.018

11. Sezer N, Evis Z, Koç M. Additive manufacturing of biodegradable magnesium implants and scaffolds: Review of the recent advances and research trends. *J Magnesium Alloys*. 2021;9(2):392-415.

    doi: 10.1016/j.jma.2020.09.014

12. Pourrahimi S, Hof LA. On the post-processing of complex additive manufactured metallic parts: A review. *Adv Eng Mater.* 2024;26(10):2301511.

    doi: 10.1002/adem.202301511

13. Niu X, Shen H, Fu J, *et al.* Corrosion behaviour of laser powder bed fused bulk pure magnesium in hank's solution. *Corros Sci.* 2019;157:284-294.

    doi: 10.1016/j.corsci.2019.05.026

14. Peng B, Xu H, Song F, *et al.* Additive manufacturing of porous magnesium alloys for biodegradable orthopedic implants: Process, design, and modification. *J Mater Sci Technol.* 2024;182:79-110.

    doi: 10.1016/j.jmst.2023.08.072

15. Qin Y, Wen P, Guo H, *et al.* Additive manufacturing of biodegradable metals: Current research status and future perspectives. *Acta Biomater.* 2019;98:3-22.

    doi: 10.1016/j.actbio.2019.04.046

16. Yin B, Liu J, Peng B, *et al.* Influence of layer thickness on formation quality, microstructure, mechanical properties, and corrosion resistance of WE43 magnesium alloy fabricated by laser powder bed fusion. *J Magnesium Alloys*. 2024;12(4):1367-1385.

    doi: 10.1016/j.jma.2022.09.016

17. Li K, Ji C, Bai S, *et al.* Selective laser melting of magnesium alloys: Necessity, formability, performance, optimization and applications. *J Mater Sci Technol.* 2023;154:65-93.

    doi: 10.1016/j.jmst.2022.12.053

18. Sadat Hashemi T, Jaiswal S, McCarthy HO, Levingstone TJ, Dunne NJ. Biofunctionalisation of porous additively manufactured magnesium-based alloys for Orthopaedic applications: A review. *Biomater Adv.* 2025;169:214170.

    doi: 10.1016/j.bioadv.2024.214170

19. Xie K, Wang N, Guo Y, *et al.* Additively manufactured biodegradable porous magnesium implants for elimination of implant-related infections: An *in vitro* and *in vivo* study. *Bioact Mater.* 2021;8:140-152.

    doi: 10.1016/j.bioactmat.2021.06.032

20. Wang Y, Huang H, Jia G, Zeng H, Yuan G. Fatigue and dynamic biodegradation behavior of additively manufactured Mg scaffolds. *Acta Biomater.* 2021;135:705-722.

    doi: 10.sci1016/j.actbio.2021.08.040

21. Ansari N, Alabtah FG, Albakri MI, Khraisheh M. Post

processing of additive manufactured Mg alloys: Current status, challenges, and opportunities. *J Magnesium Alloys*. 2024;12(4):1283-1310.

doi: 10.1016/j.jma.2024.04.017

22. Wang Y, Wang L, Liu D, *et al.* Mechanisms of processing map difference between laser powder bed fusion of Mg solid cubes and lattice structures. *Addit Manuf.* 2023;76:103773.

doi: 10.1016/j.addma.2023.103773

23. Liu J, Liu B, Min S, *et al.* Biodegradable magnesium alloy WE43 porous scaffolds fabricated by laser powder bed fusion for orthopedic applications: Process optimization, *in vitro* and *in vivo* investigation. *Bioact Mater.* 2022;16:301-319.

doi: 10.1016/j.bioactmat.2022.02.020

24. Chen H, Gu D, Xiong J, *et al.* Improving additive manufacturing processability of hard-to-process overhanging structure by selective laser melting. *J Mater Process Technol.* 2017;250:99-108.

doi: 10.1016/j.jmatprotec.2017.06.044

25. Charles A, Bayat M, Elkaseer A, *et al.* Elucidation of dross formation in laser powder bed fusion at down-facing surfaces: Phenomenon-oriented multiphysics simulation and experimental validation. *Addit Manuf.* 2022;50:102551.

doi: 10.1016/j.addma.2021.102551

26. Qin H, Zhao Y, An Z, *et al.* Enhanced antibacterial properties, biocompatibility, and corrosion resistance of degradable Mg-Nd-Zn-Zr alloy. *Biomaterials*. 2015;53:211-220.

doi: 10.1016/j.biomaterials.2015.02.096

27. Xie K, Wang L, Guo Y, *et al.* Effectiveness and safety of biodegradable Mg-Nd-Zn-Zr alloy screws for the treatment of medial malleolar fractures. *J Orthop Transl.* 2021;27:96-100.

doi: 10.1016/j.jot.2020.11.007

28. Xuehua W, Junying L, Youwen Y, *et al.* Laser powder bed fusion of biodegradable magnesium alloys: Process, microstructure and properties. *Int J Extreme Manuf.* 2025;7(2):022007.

doi: 10.1088/2631-7990/ad967e

29. Tan C, Li S, Essa K, *et al.* Laser Powder Bed Fusion of Ti-rich TiNi lattice structures: Process optimisation, geometrical integrity, and phase transformations. *Int J Mach Tools Manuf.* 2019;141:19-29.

doi: 10.1016/j.ijmachtools.2019.04.002

30. Kasperovich G, Haubrich J, Gussone J, *et al.* Correlation between porosity and processing parameters in TiAl6V4 produced by selective laser melting. *Mater Des.* 2016;105:160-170.

doi: 10.1016/j.matdes.2016.05.070

31. Zhang C, Zheng H, Yang L, *et al.* Mechanical responses of sheet-based gyroid-type triply periodic minimal surface lattice structures fabricated using selective laser melting. *Mater Des.* 2022;214:110407.

doi: 10.1016/j.matdes.2022.110407

32. Snow Z, Nassar AR, Reutzel EW. Invited Review Article: Review of the formation and impact of flaws in powder bed fusion additive manufacturing. *Addit Manuf.* 2020;36:101457.

doi: 10.1016/j.addma.2020.101457

33. Wei HL, Mukherjee T, Zhang W, *et al.* Mechanistic models for additive manufacturing of metallic components. *Prog Mater Sci.* 2021;116:100703.

doi: 10.1016/j.pmatsci.2020.100703

34. Hussain A, Kim D. Fabrication of metal alloy structures with overhang features in laser-based powder bed fusion: A critical review of challenges and latest developments. *J Manuf Processes*. 2025;135:112-130.

doi: 10.1016/j.jmapro.2025.01.031

35. Carter LN, Villapún VM, Grover L, *et al.* Exploring the duality of powder adhesion and underlying surface roughness in laser powder bed fusion processed Ti-6Al-4V. *J Manuf Processes*. 2022;81:14-26.

doi: 10.1016/j.jmapro.2022.06.057

36. Huang L, Wan H, Han Q, *et al.* Mitigating surface notches for enhanced fatigue performance of metallic gyroid structures via contour scanning. *Int J Mech Sci.* 2025;286:109913.

doi: 10.1016/j.ijmecsci.2024.109913

37. Liu J, Wen P. Metal vaporization and its influence during laser powder bed fusion process. *Mater Des.* 2022;215:110505.

doi: 10.1016/j.matdes.2022.110505

38. Ren Z, Wei D, Wang S, Zhang DZ, Mao S. On the role of pre- and post-contour scanning in laser powder bed fusion: Thermal-fluid dynamics and laser reflections. *Int J Mech Sci.* 2022;226:107389.

doi: 10.1016/j.ijmecsci.2022.107389

39. Han W, Fang F. Fundamental aspects and recent developments in electropolishing. *Int J Mach Tools Manuf.* 2019;139:1-23.

doi: 10.1016/j.ijmachtools.2019.01.001

40. Maleki E, Salehnasab B, Paul M, Shao S, Shamsaei N. Dimensional accuracy of fabricated geometries through powder bed fusion: An overview and a new benchmark artifact proposal. *Mater Des.* 2025;114361.

doi: 10.1016/j.matdes.2025.114361

41. Wang Y, Fu P, Wang N, *et al.* Challenges and solutions for the additive manufacturing of biodegradable magnesium implants. *Engineering*. 2020;6(11):1267-1275.

doi: 10.1016/j.eng.2020.02.015

ACCSCIENCE PUBLISHING

Materials Science in Additive Manufacturing

ORIGINAL RESEARCH ARTICLE

Reactive selective laser melting of silicon carbide

Tsovinar Ghaltaghchyan[1]*, Khachik Nazaretyan[2], Ani Khachikyan[1], and Marina Aghayan[1]

[1]3D printing Research Laboratory, A.B. Nalbandyan Institute of Chemical Physics NAS RA, Yerevan, Armenia

[2]Laboratory of Macrokinetics of Solid-State Reactions, A.B. Nalbandyan Institute of Chemical Physics NAS RA, Yerevan, Armenia

Abstract

Additive manufacturing of silicon carbide (SiC) is challenging due to uncontrollable quality, surface roughness of fabricated parts, expensive post-processing, and long production times for customized components. Developing cost-effective, rapid manufacturing techniques that maintain high quality and design freedom is therefore highly desirable. In this study, laser powder bed fusion (LPBF) followed by ultra-fast post heat treatment was applied to produce SiC-based composites using silicon and carbon powders as raw materials. The influence of processing parameters on silicon-carbon reaction and sintering was investigated. Boron carbide was used as an additive to enhance sintering. Substantial SiC formation occurred despite the limited heating time. Boron carbide influenced both SiC formation and grain growth. The maximum Vickers hardness (1218 $HV_{0.2}$) was achieved in boron carbide-containing heat-treated samples printed at a laser power of 48 W. This novel approach enables the efficient fabrication of SiC-based composites with enhanced hardness, underscoring the potential of LPBF for cost-effective and customizable ceramic component manufacturing.

Keywords: Laser powder bed fusion; Selective laser melting; Silicon carbide; Ultra-fast heating; High-speed temperature scanner; Reactive sintering

***Corresponding author:** Tsovinar Ghaltaghchyan (tsovinar.ghaltaghchyan@ichph.sci.am)

Citation: Ghaltaghchyan T, Nazaretyan K, Khachikyan A, Aghayan M. Reactive selective laser melting of silicon carbide. *Mater Sci Add Manuf*. 2026;5(1):025340079. doi: 10.36922/MSAM025340079

Received: August 22, 2025

Revised: September 18, 2025

Accepted: September 24, 2025

Published online: October 31, 2025

1. Introduction

Silicon carbide (SiC) is an advanced ceramic with high hardness, strength, thermal conductivity, and chemical stability, making it suitable for cutting tools, armor, aerospace components, and electronics.[1] Conventional manufacturing methods, such as dry pressing,[2] slip casting,[3] tape casting,[4] and injection molding,[5] enable achieving high performance of ceramic; however, machining to obtain more complex geometries is challenging. Ceramics have poor machining performance because of their brittleness, low shear strength, and excessive tool wear.[6,7] Therefore, the production of components with near-net-shape designs is crucial.

Recent advances in laser powder bed fusion (LPBF) technologies have enabled the successful fabrication of high-performance metallic materials with tailored microstructures and mechanical properties.[8-10] These techniques have demonstrated notable achievements in producing dense, defect-minimized components with superior strength and hardness. However, despite such successes in metals, the application of

these AM methods of SiC remains highly challenging due to its high melting point,[11] intrinsic brittleness, and low fracture toughness.[12] Most reported SiC-based materials rely on complex, high-temperature sintering, which limits scalability and compatibility with AM.

Recently, AM of SiC has garnered the attention of industrial leaders and researchers. Considering that the mechanical properties of the ceramic are a sign of its defects, many researchers focused on improving the strength of SiC. Table 1 summarizes different AM and traditional techniques to manufacture SiC.

Although the post-processing of additive-manufactured samples plays a crucial role in the density and mechanical properties thereof,[17] this technology has not yet achieved the production of fully defect-free components. Overall, traditional manufacturing technologies result in higher density and sometimes significantly higher mechanical properties than AM. Consequently, there is a clear research gap in developing processing routes for SiC-based systems that can deliver competitive mechanical performance while being more time-efficient, cost-effective, and environmentally friendly.

The present work responds to this challenge by exploiting the advantages provided by LPBF, in addition to its high geometric flexibility and the ability to fabricate complex near-net-shape components directly from digital models.[26,27] This design freedom is particularly significant for ceramics and composites, where conventional shaping methods are constrained by brittleness and strict processing requirements.[28,29]

However, ceramics are generally challenging to process via laser-based AM.[30] Several studies have reported varying outcomes depending on the feedstock and process parameters. Meyers[31] produced SiC parts with ~95% relative density by LPBF using a mixture of 67 wt% SiC and 33 wt% Si, followed by carbon impregnation and molten silicon infiltration.[31] Zou *et al.*[32] used SiC with short carbon fibers, followed by two-stage carbonization and silicon infiltration.

Ghaltaghchyan *et al.*[33] fabricated SiC preforms via direct LPBF using a bimodal mixture of SiC, Si, and hexagonal boron nitride, which reached up to 87% relative density and a Young's modulus of 59.8 ± 0.3 GPa without post-processing.[33] These studies highlight the importance of feedstock selection, process parameters, and heating rates in achieving high-density, mechanically robust SiC parts.

This article aims to present a novel approach for manufacturing SiC using selective laser melting within LPBF technologies. In this method, the feedstock containing silicon and activated carbon is rapidly heated by the laser beam, promoting the *in situ* formation of SiC within the printer's chamber. The process consolidates material layer by layer while simultaneously enabling chemical reactions between the constituent powders, effectively combining AM with *in situ* reactive phase formation.

The influence of LPBF process parameters on SiC formation was investigated. The effect of boron carbide (B_4C) on reactions and subsequent post-processing was studied. This is the first study to apply an ultra-high heating rate of 3400°C/min during post-processing of the LPBF-printed samples for the purposes of enhancing Si–C reaction and densification.

2. Materials and methods

2.1. Powder feedstock preparation

The first powder feedstock (Feed 1) was prepared using silicon powder (microcut <20 µm; SILGRAIN, Elkem ASA, Norway) mixed with activated carbon (Lach: ner, Czech Republic). The second feedstock (Feed 2) was obtained by adding 5 wt.% B_4C (particle size 1–7 µm, purity >98%; Sigma Aldrich, Germany) powder into the Feed 1 as a sintering additive. The composition of both feedstocks is presented in Table 2.

In Feed 1, a slightly higher fraction of silicon was used, compared to stoichiometric calculations, to ensure complete reaction with carbon and to compensate for potential losses or incomplete conversion during the rapid laser heating process. This excess of silicon facilitates the formation of dense SiC while minimizing residual unreacted carbon.

Initial powders were mixed in acetone using a magnetic stirrer for 30 min inside a closed jar. The lid of the jar was then removed, and the stirrer was heated while stirring continued to facilitate the drying of the feedstock. The final drying of powder was performed in the forced air-drying oven WGLL-65BE series (FAITHFUL, China) at 80°C for 3 h.

2.2. LPBF

The solid samples were built with dimensions of 10 × 10 × 5 mm. The LPBF process was carried out in a pure argon environment with an oxygen level kept below 0.1%. The printing parameters were systematically varied to identify the optimal process window. Parameter optimization was based on multiple output responses, including visual inspection for macroscopic defects, X-ray diffraction (XRD) analysis to assess phase composition (SiC-to-Si ratio), and practical considerations such as energy efficiency and processing stability.

Macroscopic quality was first assessed through visual inspection, focusing on surface integrity, the presence

Table 1. Various techniques for SiC processing

Composition	Method of sintering and conditions	Density and porosity	Mechanical properties	References
Si+α-SiC	Direct laser sintering+phenolic resin infiltration with liquid silicon infiltration	Up to 84% SiC content	Young's modulus: 285±5 GPa Flexural strength: 162±7 MPa Hardness: 2045±252 HV	13
SiC+Si	Direct laser powder bed fusion with chemical vapor infiltration	78.3%	Compressive strength: 90±8 MPa	14
Whisker-reinforced SiC	Binder jetting and chemical vapor infiltration	2.77 g/cm^3	Flexural strength: 200 MPa Fracture toughness: 3.4 MPa m$^{1/2}$ Elastic modulus (with nanoindentation): 458 GPa	15
SiC	Selective laser sintering+precursor infiltration and pyrolysis	2.59 g/cm^3	Flexural strength: 220 MPa	16
SiC+10 wt.% Al_2O_3–Y_2O_3	Stereolithography+liquid phase sintering	78.2±1.36%	Flexural strength: 77±5.2 MPa	17
SiC	Stereolithography+precursor infiltration and pyrolysis	82.6±0.48%	Flexural strength: 184.2±8.5 MPa	17
SiC+Si powder	Stereolithography+liquid silicon infiltration	96.2±0.32%	Flexural strength: 210.4±10.3 MPa	17
SiC+Si (5.2 vol.%)	Binder jetting	2.89 g/cm^3	Flexural strength: 385±25 MPa Fracture toughness: 5.93±0.32 MPa m$^{1/2}$	18
SiC	Spark plasma sintering, 2050°C	3.187 g/cm^3	Young's modulus: 440±20 GPa Flexural strength: 490±70 MPa Hardness: 20±2 GPa to 32±0.7 GPa	19
SiC+1.65 wt% Al	Hot pressing, 28 MPa, 2100°C	3.20–3.21 g/cm^3	Hardness: 24.6±0.5 HV1 (GPa) Strength: 705±63 MPa	20
SiC+2.52 wt.% AlN			Hardness: 23.3±0.3 HV1 (GPa) Strength: 640±100 MPa	
SiC+1 wt.% C+0.25 wt.% B_4C			Hardness: 26.9±1.0 HV1 (GPa) Strength: 447±113 MPa	
SiC+α-Al_2O_3+graphite	Bidirectionally pressing, sintering in air, 1400–1550°C	Open porosity of 43.4%	Flexural strength: 24.0 MPa	21
SiC+carbon black	Reaction bonding with molten silicon at 1600°C, 20 min under vacuum	<50%, 2.85 g/cm^3	Flexure strength: 260±50 MPa to 310±40 MPa	22
SiC+B_4C	Uniaxially compacting under 180 MPa, infiltrated with liquid silicon at 1480°C	2.79–2.92 g/cm^3	Young's modulus: 343–353 GPa Flexural strength: 171–270 MPa Hardness: 1534±202 to 1963±331 HV	23
Amorphous carbon black+micro-spherical carbon+molten Si	Uniaxial die-pressing at 80 MPa for 60 s, thermal treatment at 1550–1850°C	3.14 g/cm^3	Young's modulus: 443 GPa Hardness: 25.3 GPa	24
SiC+paraffin-based binder	Injection to a mold, thermal debinding, four times impregnation with phenolic resin and pyrolysis, and infiltration with silicon	3.14±0.02 g/cm^3	Flexural strength: 225±52 MPa	25

of cracks, and signs of warping. Phase composition was evaluated using XRD analysis to determine the SiC-to-Si ratio and to identify any potential decomposition or formation of secondary phases. Processing stability includes build repeatability and powder recoating behavior during fabrication. Finally, energy input was optimized to avoid excessive overheating or material degradation while still achieving adequate densification. These combined

factors were used to identify the most effective and reliable set of processing parameters. Table 3 summarizes the main printing parameters applied for the consolidation of powders.

2.3. Heat treatment

The high-speed temperature scanner (HSTS) technique was used to heat the printed samples.[34] Each sample was enclosed in a carbon envelope, which was heated directly by an electrical current, following a programmed temperature schedule managed by a PC-assisted controller. The heating process occurred in an argon-protective atmosphere at a controlled heating rate. The samples were heated at a rate of 3400°C/min up to 1730°C and cooled down at 100°C/min. The dwell time was 3 min.

The selected sintering temperature of 1730°C was chosen considering the melting point of silicon (~1410°C),[35] to ensure the formation of liquid silicon and thereby promote its reaction with carbon to form SiC. The sintering temperature was kept below the decomposition temperature of SiC.

The chosen maximum heating rate of 3400°C/min for the HSTS setup was based on our earlier research, which showed that elevated heating rates enhance SiC formation.[36] Under slow heating conditions, the initially formed SiC layer acts as a diffusion barrier between silicon and carbon powders, hindering further reaction. Rapid heating reduces this effect by promoting more uniform reaction throughout the entire material.

These parameters were selected to promote rapid Si–C reaction and densification while reducing excessive grain growth, secondary phase formation, or thermal damage to the preforms.

The temperature of the samples was monitored using tungsten-rhenium thermocouples positioned at the center of each sample. The thermocouples' output signals were processed through a multichannel acquisition system and logged by a computer. Throughout the process, both the temperature profile and the applied current were continuously documented.

Table 2. Composition of raw powders for LPBF printing

Feedstock number	Composition
Feed 1	Si (72 wt.%)+C (28 wt.%)
Feed 2	Si (68.4 wt.%)+C (26.6 wt.%)+B_4C (5 wt.%)

Abbreviation: LPBF: Laser powder bed fusion.

Table 3. The main printing parameters for the LPBF process

Printing parameters	Values tested in experiments	Optimized values
Laser power (W)	30–50	48
Powder layer thickness (μm)	25–35	35
Hatch distance (μm)	60–80	60
Focal length of the focusing lens (mm)	4; 9.8; 14	4
Rotation between layers (°)	60; 90	60
Exposure time (μs)	40; 80; 120; 160	40
Point distance (μm)	5–15	5
Baseplate material	Ti, SiC	SiC
Heating of baseplate (°C)	RT; 100; 150	100

Abbreviations: LPBF: Laser powder bed fusion; RT: Room temperature.

2.4. Characterization

To examine the porosity and microstructural characteristics, the produced rectangular samples were put in epoxy resin, cross-sectioned, and polished in the direction perpendicular to the printing plane. The universal grinding and polishing device was applied (Qpol GO model, Mammelzen, Germany).

A scanning electron microscope (SEM; Prisma E, Thermo Fisher Scientific, Hillsboro, OR, USA), equipped with an energy dispersive spectroscopy detector, was employed. Samples were subjected to coating with a thin layer of gold to provide sufficient conductivity.

The composition of the samples after the printing and heat treatment was determined by means of XRD using a Mini Flex 600 X-ray Diffractometer (Rigaku, Japan) with these settings: 40 mA, 40 kV, Cu Kα radiation, $\lambda = 0.1542$ nm, and a step size of 0.02°. The samples were broken and ground for analysis.

The Vickers hardness of the heat-treated samples was measured using FALCON 600G2FA Automated Hardness Testing System (INNOVATEST Europe BV, Maastricht, Netherlands). The indenter has a square base with a 136° angle between opposite faces. The load applied to the indenter was 0.2 kgf.

The carbon concentration in feedstock and samples was measured through combustion in an induction furnace above 2000°C in the presence of oxygen and a catalyst. This converts the element into gaseous CO_2, which was then separated and measured sequentially by infrared absorption. The elemental analyzer ELEMENTRAC CS (ELTRA Elemental Analyzers, Germany) was used in this regard.

3. Results and discussion

3.1. Feedstock characterization

The flowability of the feedstock powders has a significant impact on their distribution on the LPBF printing platform.

The flowability is influenced by the size and form of the particles. Microstructural analysis indicates that both final powder mixture particles contained angular structures and did not exhibit aggregation (Figure 1).

The powders were not as spherical as preferred for ideal flowability; however, mixing within the acetone environment positively influenced the powder distribution in a 2D layer. It is assumed that acetone acts as a dispersing agent, reducing interparticle forces and preventing agglomeration of fine particles during mixing. This results in a more uniform microscale distribution of silicon and carbon powders, improving feedstock homogeneity. Moreover, wet mixing also breaks down soft agglomerates that persist in dry mixing, and after solvent evaporation, a finely dispersed powder with reduced clustering is obtained, enhancing powder flow and layer uniformity.

Although spherical powders are generally preferred in LPBF due to superior flowability and packing density, angular powders can provide unique benefits for processing ceramics. The irregular geometry of angular particles promotes multiple internal reflections of the incident laser beam on the particle surfaces. This effect enhances light absorption compared to smooth, spherical powders, which is particularly advantageous for highly reflective ceramic systems such as silicon and SiC.[37] Ultimately, a balanced feedstock structure was obtained, where the non-spherical particles enabled uniform spreading on the baseplate and provided adequate absorptivity and sinterability for efficient LPBF processing.

The powder mixtures were processed using selective laser melting, a unique technique under the umbrella of LPBF. Powder distribution on the building platform was assessed visually. In case of local accumulation of powder, the platform height and the tension of the leveling rubbers on the wiper were adjusted. After the adjustments, printing was conducted in a pure argon atmosphere to prevent oxidation.

The elemental analysis indicates that the carbon content in Feeds 1 and 2 is 21% and 20%, respectively. These are slightly lower than the carbon content in a raw material (Table 2).

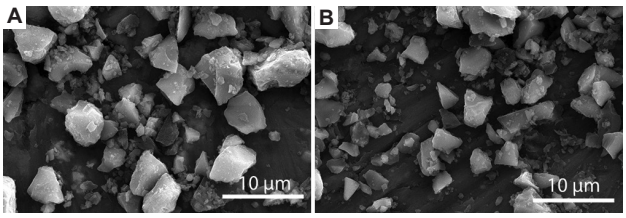

Figure 1. SEM images of final raw powders—Feed 1 (A) and Feed 2 (B)—at high magnification (10 000×)
Abbreviation: SEM: Scanning electron microscopy

3.2. LPBF

Laser power was identified as a critical parameter governing the printing process. At powers below 31 W, only partial sintering occurred, yielding highly brittle samples that disintegrated upon removal from the platform. Conversely, powers above 48 W led to excessive energy input, causing sparking, smoke generation, and the formation of brittle parts. Hence, the range of 31–48 W was established as optimal for stable fabrication. The influence of sintering agents, particularly B_4C, on the sinterability and silicon-carbon reaction was investigated, too. The complete set of samples fabricated by LPBF is summarized in Table 4.

3.3. Effect of laser focus and exposure time

Exposure time was varied between 40 and 160 µs to optimize energy input. Although XRD showed a modest increase in the SiC/Si ratio with higher exposure times (Figure 2B), the improvement was limited, and 40 µs was therefore considered sufficient to balance productivity and SiC formation.

Compared to exposure time, focal length had a stronger influence. According to Equation I, increasing the focal length enlarges the spot size, thereby reducing energy density.

$$d_s = 4\lambda f/\pi D \quad (I)$$

where d_s represents spot size (diameter of the laser beam at the focal point); λ represents laser wavelength; f represents focal length of the focusing lens; and D represents

Table 4. List of LPBF-printed samples

Sample ID	Composition	Laser power (W)	Focal length (mm)	Exposure time (µs)	Post-processing
S1	Feed 1	31	4	40	No
S2	Feed 1	36	4	40	No
S3	Feed 1	48	4	40	No
S2H	Feed 1	36	4	40	Yes
S3H	Feed 1	48	4	40	Yes
S4	Feed 1	48	9.8	40	No
S5	Feed 1	48	9.8	80	No
S6	Feed 1	48	9.8	160	No
S7	Feed 1	48	14	40	No
S8	Feed 2	31	4	40	No
S9	Feed 2	36	4	40	No
S10	Feed 2	48	4	40	No
S9H	Feed 2	36	4	40	Yes
S10H	Feed 2	48	4	40	Yes

Abbreviation: LPBF: Laser powder bed fusion.

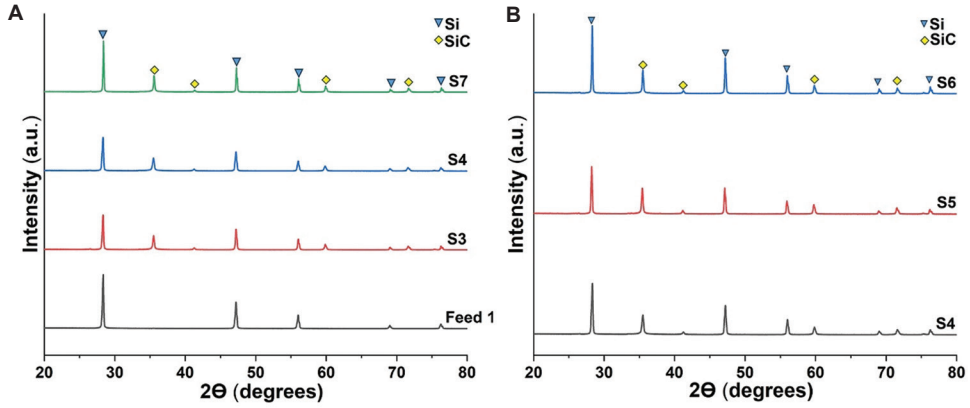

Figure 2. XRD analysis of LPBF-printed samples at different focal length (A) and exposure time (B)
Abbreviations: LPBF: Laser powder bed fusion; XRD: X-ray diffraction

input beam diameter before focusing. Therefore, a longer focal length results in a larger spot size. Reducing the focal length from 14 mm to 4 mm increased local energy input, which enhanced the SiC-to-Si ratio (Figure 2A).

3.4. Effect of B_4C as a sintering agent

The influence of B_4C on the microstructure of LPBF-printed samples was studied. The cross-sections of the samples S3 and S10 are illustrated in Figure 3.

SiC-based ceramic was chosen as the substrate of all the samples, due to its ability to enhance adhesion of the feedstock. Figure 3A illustrates the microstructure of the LPBF-printed sample S3 using Feed 1. The as-obtained SiC–Si grains had elongated structures with different sizes. However, the sintering process left enormous pores in the samples. Adding 5 wt.% B_4C led to reduced porosity (Figure 3B). Overall, the samples (S8, S9, S10) containing B_4C in the feedstock (Feed 2) exhibited a more uniform structure with fewer pores compared to the feedstock without an additive. Moreover, B_4C enhanced carbidization of silicon. XRD analysis showed that the Si-to-SiC ratio decreases when using B_4C in the feedstock (S9 and S10) compared with the B_4C-free samples (S2, S3) (Figure 3C). As it has been mentioned in the literature, the incorporation of B_4C changes the microstructure and reaction kinetics of SiC.[38] During the reactive sintering process, boron–silicon–carbon liquid phase forms, which enhances both the sintering of SiC and its formation.[39,40]

The Redfield analysis showed that the obtained SiC content in the printed samples (S1, S2, S3) was ~45 %. Thus, this indicates that raising laser power from 31 W to 48 W does not influence the rate of interaction between Si and C when Feed 1 is utilized. However, samples containing B_4C (S8, S9, and S10) show another behavior. The increased amount of SiC from 50% to 55% necessitated

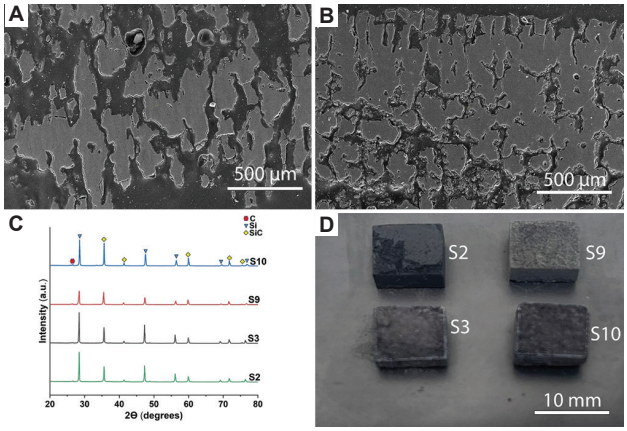

Figure 3. The samples after LPBF printing using Feed 1 and Feed 2. (A) Microstructure of S3; (B) Microstructure of S10; (C) XRD analysis of S2, S3, S9, and S10; (D) LPBF-printed samples. Magnification: 200× (A–B)
Abbreviations: LPBF: Laser powder bed fusion; XRD: X-ray diffraction

a laser power increase from 31 W to 36 W (in S8 and S9, respectively). The further increase of laser power to 48 W does not influence the SiC content (in S10). In all of these cases, it was possible to obtain samples with clearly defined contours (Figure 3D).

Although the SiC fraction achieved in this study reached ~55%, with residual silicon remaining after post-printing heat treatment. Residual silicon can compromise high-temperature performance, including thermal stability and oxidation resistance, significantly limiting the material's maximum service temperature and restricting its use in harsh environments.[38] However, it can also enhance machinability in certain applications. For applications requiring high thermal or chemical stability, strategies to further increase SiC formation are necessary.

Future experiments will focus on maximizing SiC formation by combining extended dwell times, multi-step

heating protocols (controlled pre-heating stages and ramp rates), and optimized feedstock composition with potential sintering aids. These strategies are expected to enhance Si–C reaction kinetics, promote uniform SiC growth, and achieve higher carbidization levels in the printed samples.

Another limitation is the discrepancy between the intended and actual carbon content in the feedstock. This reduction likely arises from the partial loss of fine carbon particles during wet mixing, drying, and handling, which prevented the full incorporation of the initially added carbon into the final powder mixture. The lower carbon content may have limited the Si–C reaction, reducing the final SiC fraction and influencing the microstructure and hardness of the printed samples. Consequently, the presented results may underestimate the maximum achievable SiC formation under the selected processing conditions.

Compared to the literature reported in Table 1, where SiC densification typically requires multi-step infiltration or hot pressing, our results highlight that direct LPBF with B_4C achieves comparable SiC formation in a single step, albeit with some residual porosity.

3.5. Heat treatment of LPBF-printed samples

Our previous research demonstrated that the heating rate strongly influences the Si–C reaction mechanism and yield.[36] At high heating rates, silicon melts and wets the carbon surface before a continuous SiC layer can form, thereby accelerating Si–C interaction. Figure 4 presents the microstructure and XRD patterns of heat-treated samples (S2H, S3H, S9H, and S10H).

Microstructural analysis revealed that the samples consisted of silicon, SiC, and pores. Samples without B_4C exhibited a heterogeneous microstructure, characterized by unevenly distributed fine SiC grains within the silicon matrix (Figure 4A and B). Samples produced at higher laser power (S3H and S10H, at 48 W) were less homogeneous compared to those fabricated at lower power (S2H and S9H). XRD and SEM analyses confirmed that the highest SiC content was obtained in sample S9H, which contained B_4C and was processed at 36 W (Figure 4C and E). At higher power (for S10H), coarser SiC grains were observed (Figure 4D), although the overall SiC content was lower than in sample S9H.

During the LPBF process, silicon reacts with carbon to form SiC. However, the initially formed SiC may act as a diffusion barrier, limiting further carbidization during subsequent heat treatment. At higher laser powers, larger amounts of SiC were generated, and post-treatment primarily promoted the growth and coarsening of existing SiC grains (Figure 4D). In contrast, post-heat treatment of sample S9 facilitated additional Si–C interaction, leading to the nucleation of new SiC grains and the enlargement of pre-existing ones.

These results indicated that B_4C not only facilitates the Si–C reaction but also improves microstructural uniformity. This observation is consistent with earlier reports that B_4C promotes transient B–Si–C liquid phase formation, enhancing diffusion and carbidization efficiency.[40,41] Furthermore, our results demonstrate that excessive laser energy input can promote grain coarsening and reduce effective SiC yield, in line with literature on laser processing, where localized overheating is known to limit densification by promoting exaggerated grain growth.[42]

Compared to conventional sintering or infiltration-based approaches, where SiC densification often requires prolonged thermal treatments at >2000°C,[43,44] the combined effect of B_4C addition and optimized laser power in our study enabled significant SiC formation and improved microstructural

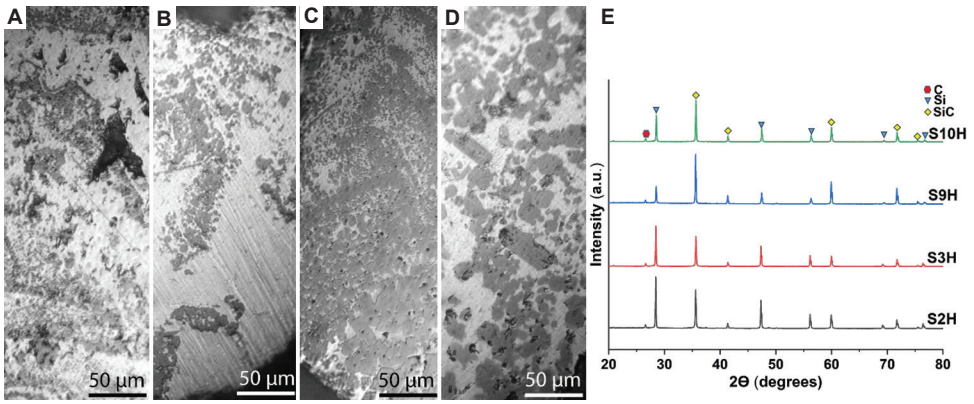

Figure 4. The LPBF-printed samples following heat treatment at a rate of 3400°C/min up to 1730°C (A–D) and XRD analysis of these samples (E). (A) Microstructure of S2H; (B) Microstructure of S3H; (C) Microstructure of S9H; (D) Microstructure of S10H; (E) XRD analysis of S2H, S3H, S9H, and S10H. Magnification: 50× (A–D)
Abbreviations: LPBF: Laser powder bed fusion; XRD: X-ray diffraction

quality at relatively lower processing temperatures. This highlights the potential of direct LPBF combined with reactive agents for producing SiC-based materials with tailored microstructures in a single-step process.

The Vickers hardness values of samples S2H, S3H, S9H, and S10H, measured with a 0.2 kgf load, were 1168, 933, 1091, and 1218, respectively. Indentations were performed on SiC grains. Among them, sample S10H exhibited the highest hardness, which can be attributed to the coarse SiC grain size. Since the SiC grains are embedded in a silicon matrix, the measured hardness values may be lower than those of pure SiC. A similar observation was reported by Chaugule *et al.*,[45] who showed that in 3D-printed Si–SiC composites, the hardness of the silicon regions was nearly half that of the SiC regions.[45] In our case, the smaller SiC grain size and the surrounding silicon phase likely contributed to the measured hardness values.

For comparison, the hardness of dense monolithic SiC typically exceeds 2000 HV, depending on grain size and processing route.[46,47] The lower values obtained in this work can be explained by the presence of residual silicon and porosity, which reduce the effective hardness of the composite microstructure. Nevertheless, the achieved hardness values fall within the range reported for reaction-bonded Si–SiC systems, highlighting the potential of LPBF combined with post-treatment for fabricating mechanically robust SiC-based parts.

4. Conclusion

LPBF of SiC from silicon and carbon powders was successfully performed. The effects of printing parameters and the addition of B_4C on the process yield were systematically investigated. As-fabricated samples contained up to 55 % SiC, with B_4C promoting the carbidization of silicon during the LPBF process.

The printed samples were subjected to fast heat treatment, with a heating rate of 3400°C/min up to 1730°C and a dwell time of 3 min. Enhanced carbidization was observed in B_4C-containing samples produced at lower laser power. After heat treatment, samples containing B_4C printed at higher laser power exhibited larger SiC grains and achieved the highest Vickers hardness of 1218 $HV_{0.2}$.

Acknowledgments

None.

Funding

This work was supported by the Higher Education and Science Committee of MESCS RA under grant numbers 22AA-2F022 and 22IRF-05.

Conflict of interest

The authors declare they have no competing interests.

Author contributions

Conceptualization: Marina Aghayan
Formal analysis: Ani Khachikyan
Investigation: Tsovinar Ghaltaghchyan, Khachik Nazaretyan
Methodology: Marina Aghayan, Tsovinar Ghaltaghchyan
Writing–original draft: Tsovinar Ghaltaghchyan
Writing–review & editing: Marina Aghayan

Ethics approval and consent to participate

Not applicable.

Consent for publication

Not applicable.

Availability of data

All raw data generated and analyzed during this study are stored in the personal research storage of the corresponding author. These data are not publicly available due to internal storage policy but can be provided by the author upon reasonable request for further verification or processing related to the article.

Further disclosure

Findings included in this article were previously presented as a poster at the "*Materials Today 2025*" conference, held on June 23–26, 2025 at Sitges, Spain.

References

1. Izhevskyi VA, Genova LA, Bressiani JC, Bressiani AHA. Review article: Silicon carbide. Structure, properties and processing. *Cerâmica*. 2000;46(297):4-13.

   doi: 10.1590/S0366-69132000000100002

2. Freedman MR, Millard ML. Improved consolidation of silicon carbide. In: *10th Annual Conference on Composites and Advanced Ceramic Materials: Ceramic Engineering and Science Proceedings*. Vol. 7. United States: John Wiley & Sons, Inc.; 1986. p. 884-892.

   doi: 10.1002/9780470320341.ch15

3. Frolova MG, Leonov AV, Kargin Yu F, *et al.* Molding features of silicon carbide products by the method of hot slip casting. *Inorgan Mater Appl Res*. 2018;9(4):675-678.

   doi: 10.1134/S2075113318040123

4. Luo ZH, Jiang DL, Zhang JX, Lin QL, Chen ZM, Huang ZR. Preparation of reaction-bonded silicon carbide with well controlled structure by tape casting method. *Ceram Int*.

2012;38(3):2125-2128.

doi: 10.1016/j.ceramint.2011.10.053

5. Zhang Z, Zhang Y, Gong H, *et al*. Influence of carbon content on ceramic injection molding of reaction-bonded silicon carbide. *Int J Appl Ceram Technol*. 2016;13(5):838-843.

doi: 10.1111/ijac.12570

6. Bharathi V, Anilchandra AR, Sangam SS, Shreyas S, Shankar SB. A review on the challenges in machining of ceramics. *Mater Today Proc*. 2021;46:1451-1458.

doi: 10.1016/j.matpr.2021.03.019

7. Sharma D, Khurana M, Manghnani S, Chhatrawat RS, Goswami C, Yadav AK. The Challenges in Machining of Ceramics- A Short Review. In: *Proceedings of the Advancement in Electronics and Communication Engineering*; 2022. Available from: https://ssrn.com/abstract=4186512 [Last accessed on 2025 Oct 15].

8. Niu Z, Zhang J, Liu F, *et al*. Forming quality control of laser powder bed fusion GH3536 alloy: Surface quality, defects, and microstructure. *Mater Sci Addit Manuf*. 2025;4(4):025220042.

doi: 10.36922/MSAM025220042

9. Lu Z, San SLL, Tan MJ, An J, Zhang Y, Chua CK. Preliminary investigation on tensile and fatigue properties of Ti6Al4V manufactured by selected laser melting. *Mater Sci Addit Manuf*. 2023;2(2):0912.

doi: 10.36922/msam.0912

10. Gunasekaran J, Sevvel P, John Solomon I. Metallic materials fabrication by selective laser melting: A review. *Mater Today Proc*. 2021;37:252-256.

doi: 10.1016/j.matpr.2020.05.162

11. Langpoklakpam C, Liu AC, Chu KH, *et al*. Review of silicon carbide processing for power MOSFET. *Crystals (Basel)*. 2022;12(2):245.

doi: 10.3390/cryst12020245

12. Fan Z, Zhang J, Wang Z, Shan C, Huang C, Wang F. A state-of-the-art review of fracture toughness of silicon carbide: Implications for high-precision laser dicing techniques. *Processes*. 2024;12(12):2696.

doi: 10.3390/pr12122696

13. Meyers S, De Leersnijder L, Vleugels J, Kruth JP. Direct laser sintering of reaction bonded silicon carbide with low residual silicon content. *J Eur Ceram Soc*. 2018;38(11):3709-3717.

doi: 10.1016/j.jeurceramsoc.2018.04.055

14. Wang Y, Wang P, Li L, *et al*. Effect of Si addition on microstructure and mechanical properties of SiC ceramic fabricated by direct LPBF with CVI technology. *Applied Sciences*. 2025;15(15):8585.

doi: 10.3390/app15158585

15. Lv X, Ye F, Cheng L, Fan S, Liu Y. Fabrication of SiC whisker-reinforced SiC ceramic matrix composites based on 3D printing and chemical vapor infiltration technology. *J Eur Ceram Soc*. 2019;39(11):3380-3386.

doi: 10.1016/j.jeurceramsoc.2019.04.043

16. Xu T, Cheng S, Jin L, Zhang K, Zeng T. High-temperature flexural strength of SiC ceramics prepared by additive manufacturing. *Int J Appl Ceram Technol*. 2020;17(2):438-448.

doi: 10.1111/ijac.13454

17. Bai X, Ding G, Zhang K, *et al*. Stereolithography additive manufacturing and sintering approaches of SiC ceramics. *Open Ceramics*. 2021;5:100046.

doi: 10.1016/j.oceram.2020.100046

18. Lv X, Gao L, Cui X, *et al*. Binder jetting additive manufacturing of hierarchical structural SiCw/SiC composites. *Addit Manuf*. 2024;93:104434.

doi: 10.1016/j.addma.2024.104434

19. Hayun S, Paris V, Mitrani R, *et al*. Microstructure and mechanical properties of silicon carbide processed by Spark Plasma Sintering (SPS). *Ceram Int*. 2012;38(8):6335-6340.

doi: 10.1016/j.ceramint.2012.05.003

20. Ray DA, Kaur S, Cutler RA, Shetty DK. Effect of additives on the activation energy for sintering of silicon carbide. *J Am Ceramic Soc*. 2008;91(4):1135-1140.

doi: 10.1111/j.1551-2916.2008.02271.x

21. Ding S, Zhu S, Zeng YP, Jiang D. Fabrication of mullite-bonded porous silicon carbide ceramics by *in situ* reaction bonding. *J Eur Ceram Soc*. 2007;27(4):2095-2102.

doi: 10.1016/j.jeurceramsoc.2006.06.003

22. Paik U, Park HC, Choi SC, Ha CG, Kim JW, Jung YG. Effect of particle dispersion on microstructure and strength of reaction-bonded silicon carbide. *Mater Sci Eng A*. 2002;334(1-2):267-274.

doi: 10.1016/S0921-5093(01)01897-4

23. Aroati S, Cafri M, Dilman H, Dariel MP, Frage N. Preparation of reaction bonded silicon carbide (RBSC) using boron carbide as an alternative source of carbon. *J Eur Ceram Soc*. 2011;31(5):841-845.

doi: 10.1016/j.jeurceramsoc.2010.11.032

24. Zhang NL, Yang JF, Deng YC, Wang B, Yin P. Preparation and properties of reaction bonded silicon carbide (RB-SiC) ceramics with high SiC percentage by two-step sintering using compound carbon sources. *Ceram Int*. 2019;45(12):15715-15719.

doi: 10.1016/j.ceramint.2019.04.224

25. Grinchuk PS, Kiyashko MV, Abuhimd HM, *et al*. Advanced technology for fabrication of reaction-bonded SiC with controlled composition and properties. *J Eur Ceram Soc*.

2021;41(12):5813-5824.

doi: 10.1016/j.jeurceramsoc.2021.05.017

26. Grant GT. Direct digital manufacturing. In: *Clinical Applications of Digital Dental Technology*. United States: Wiley; 2023. p. 46-59.

doi: 10.1002/9781119800613.ch3

27. Hopkinson N, Hague RJM, Dickens PM, editors. *Rapid Manufacturing*. United States: Wiley; 2005.

doi: 10.1002/0470033991

28. Gavalda-Diaz O, Saiz E, Chevalier J, Bouville F. Toughening of ceramics and ceramic composites through microstructure engineering: A review. *Int Mater Rev*. 2025;70(1):3-30.

doi: 10.1177/09506608241308337

29. Karadimas G, Salonitis K. Ceramic matrix composites for aero engine applications-a review. *Appl Sci*. 2023;13(5):3017.

doi: 10.3390/app13053017

30. Ur Rehman A, Saleem MA, Liu T, Zhang K, Pitir F, Salamci MU. Influence of silicon carbide on direct powder bed selective laser process (sintering/melting) of alumina. *Materials*. 2022;15(2):637.

doi: 10.3390/ma15020637

31. Meyers S. *Direct Selective Laser Sintering of Reaction Bonded Silicon Carbide*. Available from: https://hdl.handle.net/2152/89454 [Last accessed on 2025 Oct 10].

32. Zou Y, Li CH, Tang Y, *et al*. Preform impregnation to optimize the properties and microstructure of RB-SiC prepared with laser sintering and reactive melt infiltration. *J Eur Ceram Soc*. 2020;40(15):5186-5195.

doi: 10.1016/j.jeurceramsoc.2020.07.023

33. Ghaltaghchyan T, Khachatryan H, Asatryan K, Rstakyan V, Aghayan M. Effect of additives on selective laser sintering of silicon carbide. *Bol Soc Esp Cerám Vidrio*. 2023;62(6):504-514.

doi: 10.1016/j.bsecv.2023.01.001

34. Zakaryan M, Nazaretyan K, Aydinyan S, Kharatyan S. Joint reduction of NiO/WO3 pair and NiWO4 by Mg + C combined reducer at high heating rates. *Metals (Basel)*. 2021;11(9):1351.

doi: 10.3390/met11091351

35. Gayler ML. Melting point of high-purity silicon. *Nature*. 1938;142(3593):478-478.

doi: 10.1038/142478a0

36. Ghaltaghchyan T, Nazaretyan K, Rstakyan V, Aghayan M. Fast carbidization of silicon in additive manufactured Si-C-SiC composite. Results Mater. 2025;25:100653.

doi: 10.1016/j.rinma.2024.100653

37. Gu D, Yang Y, Xi L, Yang J, Xia M. Laser absorption behavior of randomly packed powder-bed during selective laser melting of SiC and TiB2 reinforced Al matrix composites. *Opt Laser Technol*. 2019;119:105600.

doi: 10.1016/j.optlastec.2019.105600

38. Liu R, Chen G, Qiu Y, *et al*. Fabrication of porous SiC by direct selective laser sintering effect of boron carbide. *Metals (Basel)*. 2021;11(5):737.

doi: 10.3390/met11050737

39. Stobierski L, Gubernat A. Sintering of silicon carbide II. Effect of boron. *Ceram Int*. 2003;29(4):355-361.

doi: 10.1016/S0272-8842(02)00144-X

40. Chen J, Chen P, Li X, Zhu Y, Wang F. Effect of B4C on the microstructure and mechanical properties of SiC refractory ceramics. 2022. Available from: https://www.researchgate.net/publication/363930570_Effect_of_B4C_on_the_Microstructure_and_Mechanical_Properties_of_SiC_Refractory_Ceramics [Last accessed on 2025 Oct 10].

41. Stobierski L, Gubernat A. Sintering of silicon carbide I. Effect of carbon. *Ceram Int*. 2003;29(3):287-292.

doi: 10.1016/S0272-8842(02)00117-7

42. Fang J, Tan YC, Yang Y, *et al*. Influence of laser power on microstructure and performance of SiC/Ti composite fabricated through selective laser melting. *J Mater Res Technol*. 2025;34:1130-1143.

doi: 10.1016/j.jmrt.2024.12.044

43. Lee EJ, Lee DH, Kim JC, Kim DJ. Densification behavior of high purity SiC by hot pressing. *Ceram Int*. 2014;40(10):16389-16392.

doi: 10.1016/j.ceramint.2014.07.143

44. Shin S, Kim M, Kim M, *et al*. Ultrafast high-temperature sintering of reaction-bonded SiC with Y2O3-Al2O3 sintering additives. *Mater Lett*. 2025;382:137956.

doi: 10.1016/j.matlet.2024.137956

45. Chaugule PS, Du W, Kamath RR, Barua B, Messner MC, Singh D. Reliability comparisons between additively manufactured and conventional SiC-Si ceramic composites. *J Am Ceramic Soc*. 2024;107(5):3117-3133.

doi: 10.1111/jace.19682

46. Yu YT, Naik GK, Lim YB, Yoon JM. Sintering behavior of spark plasma sintered SiC with Si-SiC composite nanoparticles prepared by thermal DC plasma process. *Nanoscale Res Lett*. 2017;12(1):606.

doi: 10.1186/s11671-017-2370-8

47. Zhang ZH, Wang FC, Luo J, Lee SK, Wang L. Processing and characterization of fine-grained monolithic SiC ceramic synthesized by spark plasma sintering. *Mater Sci Eng A*. 2010;527(7-8):2099-2103.

doi: 10.1016/j.msea.2009.12.027

ACCSCIENCE PUBLISHING

Materials Science in Additive Manufacturing

ORIGINAL RESEARCH ARTICLE

Laser powder bed fusion of atomized industrial waste-derived Inconel 725 alloy powders: A machine learning-assisted process optimization

Gabriele Locatelli*, Sara Bocchi, Mariangela Quarto, and Gianluca D'Urso

Department of Management, Information and Production Engineering, University of Bergamo, Bergamo, Lombardy, Italy

Abstract

Among nickel-based superalloys, Inconel® 725 (IN725) stands out for its excellent strength and corrosion resistance. Despite this, its application in additive manufacturing remains largely unexplored. This study investigates laser powder bed fusion of metals (PBF-LB/M) applied to IN725 powder derived from recycled industrial waste, addressing sustainability and process optimization goals. Using the design of experiments approach, the laser power–scan speed process parameter space was explored. Gaussian process regression models were developed to predict surface roughness, relative density, and microhardness. Both direct process parameters and volumetric energy density were evaluated as model inputs to assess predictive performance. The findings established a broad optimal process window for manufacturing high-quality IN725 parts using PBF-LB/M. Specifically, an optimal combination of 99.99% relative density, 7.3 μm roughness, and 311 HV microhardness was achieved by processing the powder at 250 W and 1,500 mm/s. By demonstrating the feasibility of using recycled IN725 powder, this study contributes to the development of sustainable manufacturing practices and supports wider adoption of PBF-LB/M in oil and gas, marine, and chemical processing industries, where IN725 is widely employed.

Keywords: Powder bed fusion; Inconel 725; Waste recycling; Process optimization; Machine learning

***Corresponding author:**
Gabriele Locatelli
(gabriele.locatelli@unibg.it)

Citation: Locatelli G, Bocchi S, Quarto M, D'Urso G. Laser powder bed fusion of atomized industrial waste-derived Inconel 725 alloy powders: A machine learning-assisted process optimization. *Mater Sci Add Manuf*. 2026;5(1):025320072. doi: 10.36922/MSAM025320072

Received: August 06, 2025

Revised: September 02, 2025

Accepted: September 10, 2025

Published online: November 5, 2025

1. Introduction

Nickel-based superalloys are high-performing materials renowned for combining exceptional mechanical strength and toughness with high resistance to corrosion and oxidation, properties that are maintained at temperatures up to 1,000°C.[1] Due to these properties, nickel-based superalloys have been extensively employed in the fabrication of components operating in safety-critical applications, including aerospace, power generation, and chemical processing industries.[2,3] Despite their outstanding performance in critical environments, nickel-based superalloys are also considered difficult-to-machine materials. Work hardening, high melting points, and low thermal

conductivity result in high cutting temperatures and a fast tool wear rate.[4,5]

In the last decade, laser powder bed fusion of metals (PBF-LB/M) has emerged as a valuable alternative for manufacturing nickel-based superalloy components, due to its potential in enhancing mechanical properties by optimizing microstructure formation.[6] Furthermore, PBF-LB/M offers the possibility to produce complex geometries and enable design flexibility that goes beyond conventional manufacturing constraints, as fine layers of metal powder are selectively melted by a laser beam, according to a three-dimensional model, until parts are completed.[7,8]

Since the laser–powder interaction in the PBF-LB/M process causes rapid localized melting and high thermal gradients, the metal weldability is regarded as a useful indicator in determining the challenge rate for manufacturing parts with acceptable integrity.[9] Among nickel-based superalloys, nickel-chromium Inconel® 625 (IN625) and 718 (IN718) alloys have garnered substantial attention in the context of PBF-LB/M, due to their excellent weldability and favorable response to this additive manufacturing technique.[10,11] IN625 is a solid-solution strengthened alloy that exhibits superior corrosion resistance and thermal fatigue performance, especially in marine and chemical environments, and is generally easier to process via PBF-LB/M due to its lower susceptibility to hot cracking and segregation phenomena during solidification.[12] IN718 is a precipitation-hardened alloy that excels in the fabrication of aerospace components and gas turbines, given that it can maintain excellent creep resistance and high strength at elevated temperatures, up to approximately 650°C.[13] Due to the possibility of achieving unprecedented property tuning through tailored microstructure adjustments and process parameter optimization,[6,14] PBF-LB/M processing holds potential for adapting several other commercial superalloys. In addition to the well-established IN718 and IN625, research has been increasingly focused on more complex alloys such as IN738 and IN939, which offer superior high-temperature performance but pose difficulties during processing due to their high gamma prime content and crack sensitivity.[15-17] To a minor extent, other high-performance superalloys are at the center of research efforts for PBF-LB/M production, including Hastelloy X, René 80, Haynes 230, and Nimonic 263.[18-21]

In the wake of the growing interest in extending PBF-LB/M processing to a wider portfolio of superalloys, the nickel-chromium-molybdenum-niobium alloy IN725 emerges as a suitable candidate, as it was developed to combine the high strength of IN718 with the excellent corrosion resistance of IN625.[22] In particular, the high molybdenum content contributes to superior corrosion resistance in sour brine and high-temperature environments, making IN725 particularly attractive for applications in the oil and gas, marine, and nuclear industries.[23] The ability of PBF-LB/M to produce complex geometries and reduce lead times could position IN725 as a strategic alloy for future additive manufacturing-driven innovation in these sectors. Despite the promising premises for IN725, only one study has investigated its feasibility for laser powder bed fusion manufacturing. Todaro *et al.*[24] demonstrated for the 1st time the printability of IN725 with PBF-LB/M using thermodynamic and metallurgical analyses, confirming the low susceptibility of IN725 to solidification and strain–age cracking, highlighting its excellent printability compared to other high-strength superalloys. Todaro *et al.*[24] also demonstrated that the alloy can be processed with a crack-free and near-pore-free microstructure across a wide process parameter window, achieving relative densities up to 99.6% through laser scan speed and hatch spacing optimization. The present study builds on the early work of Todaro. While that work represents a fundamental reference for the preliminary validation of the material, the approach adopted here focuses on systematically optimizing the printing process through predictive modeling based on machine learning (ML) techniques. This study extends the investigation of IN725 manufactured by PBF-LB/M to include powders recycled from industrial waste, thereby contributing to a sustainable approach.

Accurate and reliable models that relate the process parameters to their properties are required to perform an effective optimization. Numerical modeling efforts at multiple length scales in additive manufacturing can provide the input-output relation needed for process optimization with high accuracy. However, high computational times and costs make numerical models unsuitable for optimization studies.[25] Therefore, experimental optimization coupled with simplified statistical models is still commonly performed. Due to the complexity of additive manufacturing processes, ML has emerged as a valuable tool for identifying process–structure–property relations while providing sufficiently accurate predictions for optimization. Neural network methods are preferred for high-dimensional datasets, while data-driven methods typically perform better when less training data is available.[26]

The process optimization was conducted by combining a design of experiments (DoE) approach with Gaussian process regression (GPR) models to model the relationship between process parameters and product outputs (e.g., surface roughness, relative density, and microhardness).

The use of recycled powders promotes closed-loop material flows and reduces carbon dioxide emissions compared to the atomization of fresh powders,[27] promoting the adoption of sustainable manufacturing and industrial ecology practice.[28] A DoE was employed to explore and optimize the laser power–scan speed parameter space, as these input variables are the most critical in laser powder bed fusion. GPR modeling was selected among ML algorithms due to its suitability for small datasets and its ability to quantify predictive uncertainty,[29,30] which are essential features for guiding the selection of suitable models for PBF-LB/M.[31] GPR has emerged as a valuable tool for exploring and exploiting scenarios in metal additive manufacturing, as it allows the identification of optimal process windows and a deeper understanding of process–structure–property relations. Lee *et al.*[32] developed a GPR optimization model to enhance the productivity and quality metrics in wire-arc additive manufacturing.[32] Liu *et al.*[26] and Li *et al.*[33] were able to define optimized process windows for the PBF-LB/M processing of AlSi10Mg[26] and CoCrMo alloy,[33] respectively. Similarly, Maitra *et al.*[34] used GPR to predict the density of Ti6Al4V parts.

In this study, GPR models were trained using both direct process parameters (laser power and scan speed) and the volumetric energy density (VED) to draw a comparison based on predictive accuracy. The reliability of VED as a predictor for part quality is debated, as it fails to account for unequal contributions and interaction effects of individual parameters.[35] This study provides a solid foundation for the sustainable adoption of PBF-LB/M in industrial sectors that utilize IN725, while informing future efforts in model selection, parameter optimization, and the adaptation of high-performance superalloys for additive manufacturing. In summary, this work defines an optimal process window for producing dense, smooth, and hard parts, and further compares the effectiveness of direct parameters against those based on VED.

2. Materials and methods

2.1. Powder feedstock

The material used in this study is IN725 recycled powder, supplied by Politecnico di Torino (Italy) after the vacuum inert gas atomization of waste materials. Specifically, the waste materials consisted of UNS N07725 turbine blades, which had been discarded after reaching their end-of-life stage. Detailed information regarding the vacuum inert gas atomization setup used for waste material atomization can be found in the study of Gobber *et al.*[36] As shown in Table 1, the chemical composition of the recycled alloy complies with the American Society for Testing and Materials (ASTM) B805 standard for UNS N07725.[37] The measured oxygen content was 0.00824 ± 0.0016%, well below the 0.3% threshold set as an indicative maximum limit for PBF processing of IN718.[38] The powder exhibited excellent sphericity, as observed in the micrograph reported in Figure 1A, with smooth particle surfaces and small satellites surrounding the larger particles. The particle size distribution was characterized by D_{10} = 21.3 µm, D_{50} = 42.4 µm, and D_{90} = 68.0 µm (Figure 1B). The flowability and apparent density of the powder batch, measured using a Hall flowmeter funnel, according to ASTM B213 and B212 standards,[39,40] were 10.50 ± 0.20s and 4.69 ± 0.007 g/cm^3, respectively. The morphological and physical characteristics of the powder were compatible with PBF-LB/M processing, confirming the suitability of recycled material to be used in additive manufacturing, despite being derived from end-of-life components.

2.2. Sample fabrication

To optimize the PBF-LB/M process, a full factorial DoE was defined to vary laser power (P) and scan speed (v) within the ranges of 100–300 W and 500– 00 mm/s, respectively, as these parameters exert a dominant influence on melt pool behavior, defect formation, and microstructural evolution.[41,42] In contrast, hatch distance (h) and powder layer thickness (t) were held constant, as their effects can be considered secondary during initial process window development.[43] The powder layer thickness was kept constant at 30 µm. Due to the lack of knowledge on the PBF-LB/M-processed IN725, hatch distance was set to 50 µm, a value previously shown to enhance part densification while mitigating excessive surface roughness associated with particle adhesion in other alloys.[44,45] The 20 parameter combinations resulting from the DoE are summarized in Table 2, and the corresponding VEDs were calculated according to Equation I:

$$VED = \frac{P}{v.h.t} \quad (I)$$

Table 1. Chemical composition of the Inconel 725 recycled powder (wt%)

Element	Nickel	Chromium	Molybdenum	Niobium	Titanium	Aluminum	Carbon	Sulfur	Iron
This study	57.45	21.25	7.86	3.40	1.65	0.29	0.008	0.00042	7.95
ASTM B805[37]	55–59	19–22.5	7–9.5	2.75–4	1–1.7	≤0.35	<0.03	<0.015	Balance

Abbreviation: ASTM: American society for testing and materials.

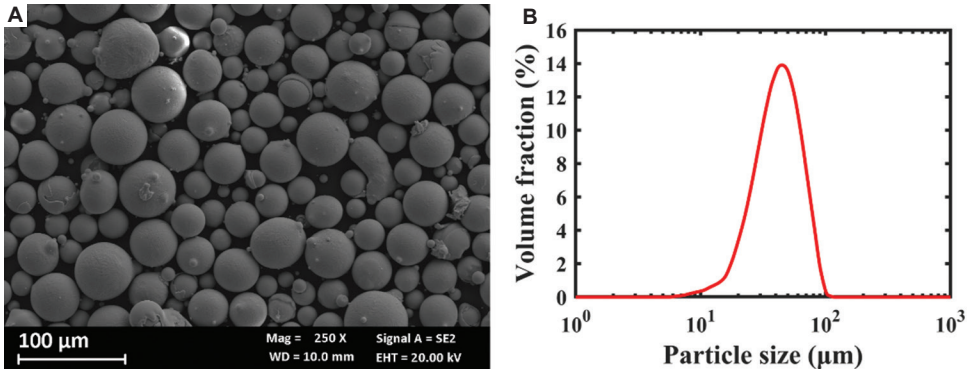

Figure 1. Inconel 725 recycled powder. (A) Scanning electron microscopy morphology. Scale bar: 100 µm; magnification: ×250. (B) Particle size distribution.

Table 2. Laser powder bed fusion process parameters used for the design of experiments

Sample	Laser power (W)	Scan speed (mm/s)	Volumetric energy density (Jmm^3)
1	100	500	133
2	100	1,000	66
3	100	1,500	44
4	100	2,000	33
5	150	500	200
6	150	1,000	100
7	150	1,500	67
8	150	2,000	50
9	200	500	267
10	200	1,000	133
11	200	1,500	89
12	200	2,000	667
13	250	500	333
14	250	1,000	167
15	250	1,500	111
16	250	2,000	83
17	300	500	400
18	300	1,000	200
19	300	1,500	133
20	300	2,000	100

A total of 20 cylindrical samples with 10 mm diameter and 6 mm height (Figure 2) were fabricated using a Print Genius 150 machine by Prima Additive S.r.l. (Italy). The machine has a 300 W ytterbium-fiber laser operating at a 1,070 nm continuous wavelength. All samples were fabricated using a 5 mm stripe pattern scanning strategy with a 67° counter-clockwise rotation between layers. The diameter of the laser spot was set to 100 µm. The build plate was preheated to 80°C to stabilize melt pools and ensure consistent melting and structural integrity of the initial layers, which are crucial for promoting successful adhesion between the substrate and the part.[46] High-purity argon was used as the shielding gas, keeping the oxygen level inside the build chamber below 0.1%, to avoid alloy oxidation during printing.

2.3. Characterization of surface roughness, relative density, and hardness

All the samples produced in this study were measured and tested in their as-built condition, without undergoing post-processing or post-heat treatment. After removing the build plate from the PBF-LB/M machine, the samples were cut using wire electrical discharge machining.

The surface roughness of all samples was measured using a Sensofar S-Neox optical profilometer (Sensofar metrology, Spain) utilizing the focus variation technique. All measurements were conducted with 10× magnification at the same region of interest locations over a 1,754.40 × 1,320.96 mm^2 area.

Microhardness was measured using a UHL VMH-001 Vickers hardness tester (Uhl technische Mikroskopie GmbH, Germany). Before testing, the top surface of all samples was polished up to a 1 µm surface finish. Four HV_{1000} indentations were performed on each sample under a 1,000 gf load applied for 15 s, according to the ASTM E384 standard,[47] and measured with a ×50 objective lens.

The specimens were then cut parallel to the build direction, mounted in phenolic resin, ground according to a sequence of 120, 180, 400, 1,200, 2,400, and 4,000 grit SiC emery paper, and polished using 3 µm diamond suspension. Micrographs of ×200 magnification were taken to cover the cross-section and stitched together using a Keyence VHX-7100 optical microscope (Keyence Corp., Japan). The ImageJ software ((version 1.54g); National Institutes of Health, United States)) was then used to measure porosity after binarization of the micrographs, following the pipeline detailed in a previous work.[48]

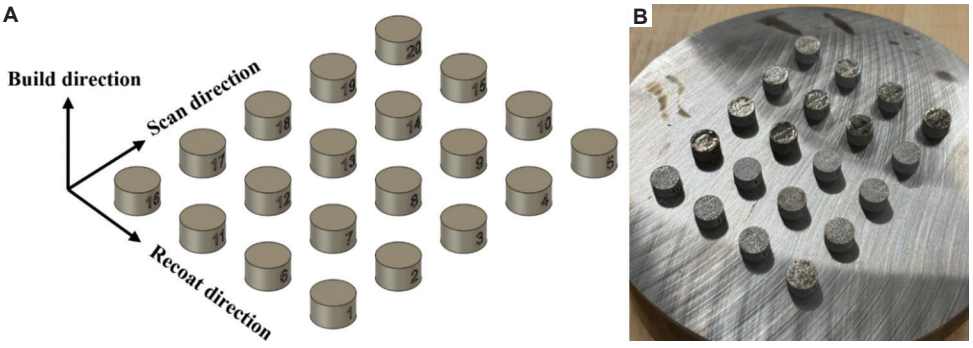

Figure 2. Sample layouts. Layout of the (A) as-designed and (B) as-printed cylindrical samples.

2.4. GPR

The GPR was used to model the relationship between the PBF-LB/M process parameters and the tested output properties of the IN725 alloy samples. The dataset comprised all data acquired during the experimental campaign based on the full factorial DoE. It represents the PBF-LB/M process, covering diverse processing conditions ranging from low to high energy density regimes.

GPR is a non-parametric, supervised ML algorithm that relies on Bayesian inference to learn the relationship between inputs and outputs that most likely generated a dataset, letting the data determine the level of complexity.[49] Since the Bayesian framework does not assume a fixed functional form, GPR yields robust predictions even with limited datasets.[50] Specifically, GPR draws the input-output relation from a Gaussian process with mean function μ and covariance function *k*, as per Equation II:

$$Y(x) = GP(\mu(x), k(x, x')) \quad \text{(II)}$$

Where *y* denotes the output variable, while x and x' represent the training and prediction input variables, respectively.

In this study, GPR was utilized to map the relationship between relative density (ρ), surface roughness (*Sa*), and microhardness (HV_{1000}) of IN725 alloy samples with two different sets of input variables. In the first case, laser power (*P*) and scan velocity (*v*) inputs were considered, while VED was used as the only input variable in the second case, as expressed in Equations III and IV:

$$\rho \mid Sa \mid HV_{1000}(P,v) = GP(\mu(P,v), k(P,v,P', v')) \quad \text{(III)}$$

$$(\rho \mid Sa \mid HV_{1000}(VED) = GP(\mu(VED), k(VED, VED')) \quad \text{(IV)}$$

Before training the models, min-max and z-score normalizations were applied to remove measurement scales from the input and output data. Regardless of the adopted ML approach, this preprocessing step facilitates model training and improves accuracy.[51] Since no strong prior trend is known, the models were trained assuming a zero-mean function (μ = 0). The covariance function was instead defined through a Matérn 5/2 kernel with automatic relevance determination (ARD-Matèrn 5/2). This kernel function was chosen because it is suited to model various spatial correlation structures while considering a separate length scale for each predictor.[52,53] Furthermore, the ARD-Matèrn 5/2 offers robust and accurate predictions of complex relationships.[54,55] The GPR models were trained in MATLAB (version R2024a) using the fitrgp function. Kernel hyperparameters (i.e., length scales, process variance, and noise variance) were tuned by maximizing the marginal log-likelihood using the built-in quasi-Newton solver, with default settings for convergence tolerances and maximum iterations.

No explicit resampling-based validation was performed, as the probabilistic nature of GPR intrinsically provides predictive variances alongside mean estimates. Hence, the full experimental dataset was used as the training dataset to generate input weights and facilitate the exploration of process–structure–property relationships. For each model, the predictive mean and standard deviation estimated by the GPR were used to plot the response surface and uncertainty map, after mapping results to physical units through inverse z-score transformation. Uncertainty maps served as internal validation to assess the reliability of the predicted response surfaces.

To quantitatively estimate the goodness-of-fit and absolute discrepancies in each model, the coefficient of determination (R^2) and the mean absolute error (MAE) were used as evaluation metrics. R^2 is well-established in regression analysis as it quantifies the proportion of variance in the output variable explained by the model, thus providing an intuitive measure of the overall goodness-of-fit.[56] Complementarily, MAE offers a scale-preserving indicator of average prediction error that is less sensitive to outliers than metrics such as root mean square error, making it particularly suitable for small experimental datasets.[57]

3. Results and discussion

3.1. Surface roughness determination

Figure 3A shows a general trend as surface roughness decreases when the power input increases. However, the magnitude and consistency of this trend varied depending on the specific scan speed value. Concurrently, surface roughness also appeared to generally coarsen when the scan speed used for processing was increased with equal laser power. Interestingly, samples fabricated with a scan speed equal to 1,500 mm/s showed a peculiar trend in which the surface finish strongly improved from 15.67 to 8.93 µm in the 150–250 W range and then stabilized when a 300 W power was used. Furthermore, the experimental data highlight that surface roughness values stabilize when 150 W power is exceeded. This plateau supports the hypothesis that while increasing power improves surface finish, the benefits diminish at high scan speeds.

Figure 3B shows the optical micrographs of characteristics of IN725 alloy surfaces, revealing the presence of spherical particles (indicated by white arrows) that adhered to track segments independently of the PBF-LB/M processing condition. This defect can be attributed to spheroidization, a phenomenon that occurs when molten metal is accelerated into the gas environment due to the Rayleigh–Taylor instability.[58] Under such conditions, surface tension leads to the fragmentation and rounding of elongated melt tracks into small spherical particles towards the edges of melt pools.[59] The consistent observation of such particles despite varying grades of surface roughness suggests that spheroidization is intrinsic to the dynamics of laser–powder interaction in the PBF-LB/M process.

3.2. Relative density analysis

Figure 4A shows that relative density was largely independent of scan speed in the 200–300 W laser power range, indicating that high power ensures complete melting and consolidation under higher scan speeds, as observed in Figure 4B. However, the trend slightly deteriorated under high power-low speed combinations due to excessive energy input, increasing the chance of keyhole formation, as observed in Figure 4C. A contrasting behavior was observed at lower laser powers (100–150 W), where increasing the scan speed generally led to a significant reduction in relative density. The underexposure of the powder bed at lower power inputs resulted in poor interlayer bonding and severe lack-of-fusion formation, as depicted in Figure 4D. Overall, 13 parameter combinations resulted in relative density values exceeding 99.5%, thus identifying a robust process window for near-pore-free fabrication of IN725 via PBF-LB/M. In particular, the highest density achieved in this study, 99.99%, was achieved at 250 W and 1,500 mm/s, corresponding to a VED of 167 J/mm^3.

3.3. Microhardness analysis

Figure 5 shows that microhardness stabilized when the laser power exceeded 200 W and the scan speed was higher than 1,000 mm/s. The relatively uniform values in this region suggest that a stable process regime was achieved, in which balanced energy input and rapid solidification rates promote consistent microstructural characteristics. In contrast, microhardness fluctuated noticeably across the entire power range at 500 mm/s, suggesting excessive energy inputs led to melt pool instabilities that unpredictably affected the final microstructure. The PBF-LB/M process achieved microhardness values that compare favorably with the 300 HV reported for annealed, heat-treated IN725 rods.[60]

3.4. Accuracy evaluation of GPR models

While VED provides a convenient scalar representation of the process energy input, the model evaluation metrics

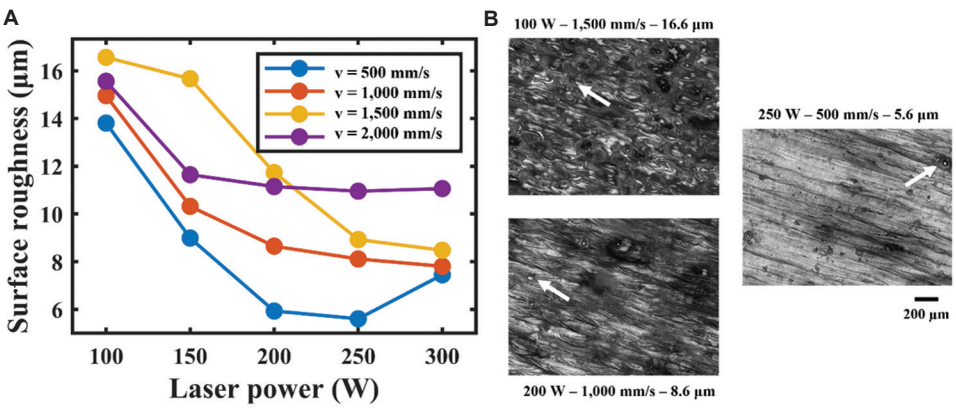

Figure 3. Surface roughness. (A) The relationships between surface roughness and laser power under different scan speed conditions, (B) Optical micrographs of characteristic samples showing surface morphology affected by spheroidization. Scale bar: 200 µm, magnification: ×10.

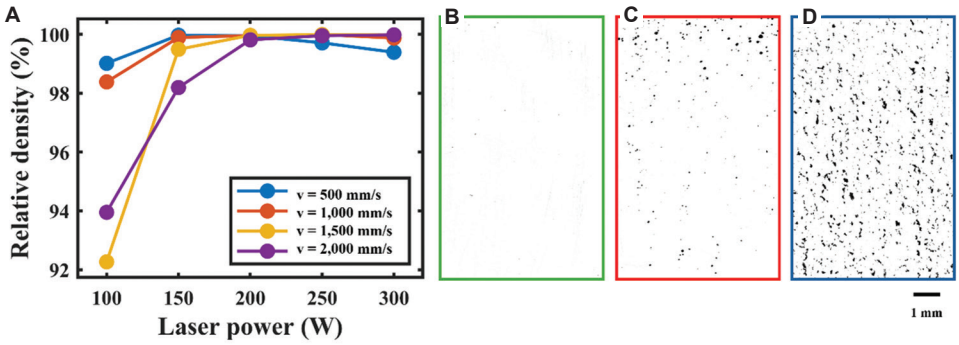

Figure 4. Relative density. (A) The relationships between relative density and laser power under different scan speed conditions. (B-D) Binarized optical images by ImageJ showing characteristic samples with (B) near-pore-free microstructure (p=250 W, *v* = 1,000 mm/s), (C) keyhole pores (p=300 W, *v* = 500 mm/s), and (D) lack-of-fusion pores (p=100 W, *v* = 1,500 mm/s). Scale bar: 1 mm; magnification: ×200.
Abbreviations: *P*: Laser power; *v*: Scan velocity.

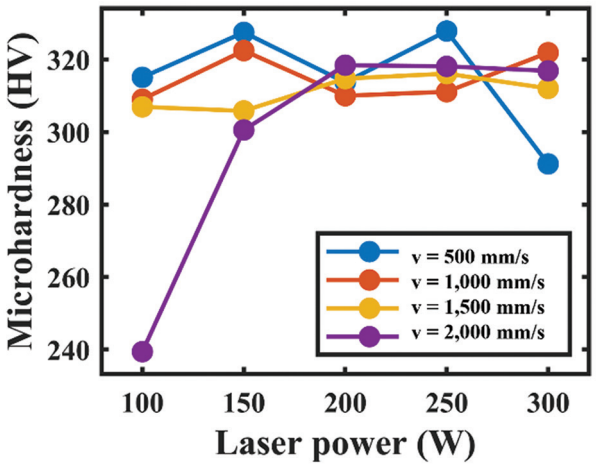

Figure 5. The relationship between microhardness and laser power under different scan speed conditions

Table 3. Evaluation metrics used to assess the accuracy of the Gaussian process regression models

Output variable	Input variable (s)	R^2	Mean absolute error
Relative density (ρ)	*P*, *v*	0.95	0.09%
	VED	0.82	0.24%
Surface roughness (*Sa*)	*P*, *v*	0.99	0.07 μm
	VED	0.73	0.42 μm
Microhardness ($HV_{1,000}$)	*P*, *v*	0.62	0.37 HV
	VED	0.98	0.10 HV

Abbreviations: *P*: Laser power; *v*: Scan velocity; VED: Volumetric energy density.

in Table 3 underline that its use in PBF-LB/M process modeling and optimization is significantly output-dependent. The relative density and surface roughness models trained using laser power and scan velocity as process inputs outperformed those based on VED, achieving higher goodness-of-fit and lower prediction errors. According to widely accepted guidelines,[56] R^2 values in the range of 0.7–0.9 are considered indicative of a good model fit. Hence, while the 0.82 and 0.73 R^2 values achieved in this study support the reliability of using VED as a predictor for process windows achieving high density and low surface roughness in PBF-LB/M, it is clear that these values are not capable of capturing the complexities of laser–powder interactions sensitive to the interplay between laser power and scan speed. Different parameter combinations may yield the same VED value but still result in different microstructures, porosity distributions, and thermal histories.[35] This outcome can be explained by VED condensing multiple parameters into a single scalar, thus neglecting the distinct influence of laser power and scan speed on melt pool dynamics. Different parameter combinations may yield identical VED. However, other dynamics and thermal histories may have characterized the resulting melt pools.

In contrast, microhardness appears to correlate more strongly with cumulative energy input. The VED-based model for microhardness achieved an excellent performance, with an R^2 of 0.98 and an MAE of just 0.10 HV, confirming that VED is a highly effective predictor for this specific output. However, the model trained on laser power and scan speed yielded a remarkably low MAE of 0.37 HV despite achieving a lower R^2 of 0.62. Therefore, the model can be considered highly reliable for practical applications, particularly in contexts where precise point-wise estimation is more critical than explaining the full variance of the data. Furthermore, this result supports the hypothesis that hardness is less sensitive to variations in specific parameter combinations, provided the overall energy density remains constant.[61,62]

Based on this comparative analysis, only GPR models using laser power and scan speed as inputs were considered for optimizing the PBF-LB/M processing of IN725.

3.5. GPR models with laser power and scan speed inputs

Figures 6-8 show the point-wise predictions made by the GPR models, along with corresponding prediction errors, for surface roughness, relative density, and microhardness, respectively. Distinct colors were used to address variations in the predicted outputs and standard deviations, while black dots mark the experimental data entries.

Figure 6A illustrates the response surface predicted by the GPR surface roughness model, indicating that surface finish progressively coarsens as the scanning speed increases and the laser power diminishes. However, laser power appears to substantially influence surface roughness more than scan speed. The model predicted that lower surface roughness is generally achieved at high laser power, regardless of the scan speed. Considering surface roughness ≤10 μm to be a suitable range for acceptable as-built surface roughness, the response surface suggests that optimal parameter combinations can be found at medium-to-high laser power (200–300 W) and low scan speed (500–1,000 mm/s). Figure 6B shows the standard deviations in the surface roughness predictions, identifying higher uncertainty where the model interpolates between sparse data points along the scan speed axis. This behavior indicates that the GPR model for surface roughness is more sensitive to scan speed. Notably, peaks are localized at the boundary of the dataset, thus indicating edge extrapolation errors.

In Figure 7A, the predicted relative density response surface identifies a wide and well-bounded process window for fabricating near-defect-free parts. In particular, parts with relative density ≥99.5% appeared to be preferentially achieved by combinations of medium-to-high laser power ($P \geq 150$) and medium-to-high scan speed ($v \geq 1000$). The plot suggests that the individual input parameters have limited influence on the density percentage of as-built parts, with the relative density predicted to decrease when increasing the scan speed and reducing the laser power concurrently. This behavior enabled the identification of the process window region, resulting in the formation of lack-of-fusion pores, as observed in Figure 4D, which

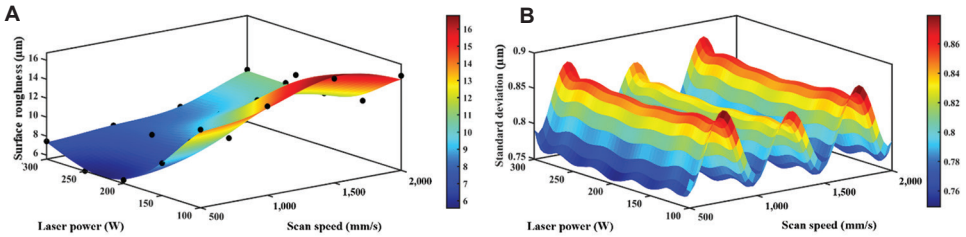

Figure 6. Surface roughness of Gaussian process regression models. (A) Predicted response surface and (B) predicted error surface.

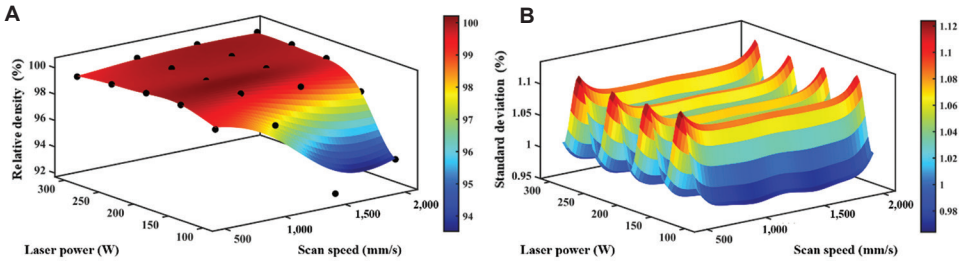

Figure 7. Relative density Gaussian process regression model results. (A) Predicted response surface and (B) predicted error surface.

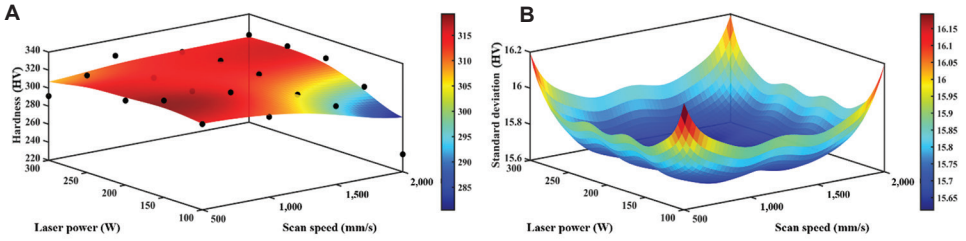

Figure 8. Microhardness of Gaussian process regression models. (A) Predicted response surface and (B) predicted error surface.

typically arise under insufficient melting due to higher scan speed and reduced power.[63] At a high power and low scan speed, the response surface identified a small region where the relative density decreased. Considering the sample printed under the corresponding input parameters (laser power = 300 W and scan speed = 500 mm/s) showed a sub-optimal microstructure characterized by keyhole porosities (Figure 4C), the response surface suggests that reducing the scan speed below 500 mm/s under medium-high laser power would exacerbate keyholing. High power-low velocity combinations result in excessive energy inputs, driving pore formation due to the periodic collapse of keyholes under intense recoil pressure.[63] The standard deviation surface in Figure 7B is consistent with the one presented in Figure 6A, albeit with the highest uncertainty identified along the laser power axis. This indicates that the relative density model is more sensitive to laser power. Again, peaks localized at the boundaries stem from edge extrapolation errors.

In Figure 8A, the predicted response surface clearly illustrates that microhardness tends to decrease as the scan speed increases and the laser power decreases. However, the GPR model predicts that the opposite processing condition also decreases Vickers microhardness progressively as the laser power exceeds 300 W and the scan speed is reduced below 500 mm/s. The observed behaviors are compatible with the trends predicted by the relative density response surface (Figure 7A), indicating that the achievable microhardness is strongly related to the extent of microstructural defect formation disrupting the densification of as-built IN725 parts. The standard deviation surface in Figure 8B shows localized peaks only at the four corners of the dataset, hinting at extrapolation errors. However, the flat surface at the center of the dataset space indicates that the microhardness GPR model is equally sensitive to both laser power and scan speed.

The GPR models are intended to describe parameter–process–property relationships within the investigated parameter space, where their predictions are most reliable. The increased predictive variance values at dataset boundaries highlight reduced confidence outside this range, confirming that the models should not be extrapolated but used primarily for mapping the explored process window.

3.6. Optimal process window

Figure 9 shows the laser power–scan speed process map for PBF-LB/M of the IN725 alloy, derived from the response surfaces of the GPR models in Figures 6A, 7A, and 8A. The predicted contour lines for surface roughness, relative density, and Vickers microhardness are plotted in red, blue, and green, respectively. Energy density contour lines are plotted in black. The light-yellow area in the plot identifies the optimal process window for fabricating IN725 parts with surface roughness ≤10 μm, relative density ≥99.5%, and microhardness ≥300 HV. Within the window, the red star marks the sample produced using 250 W laser power and 1,000 mm/s scan speed, which yielded the most optimal

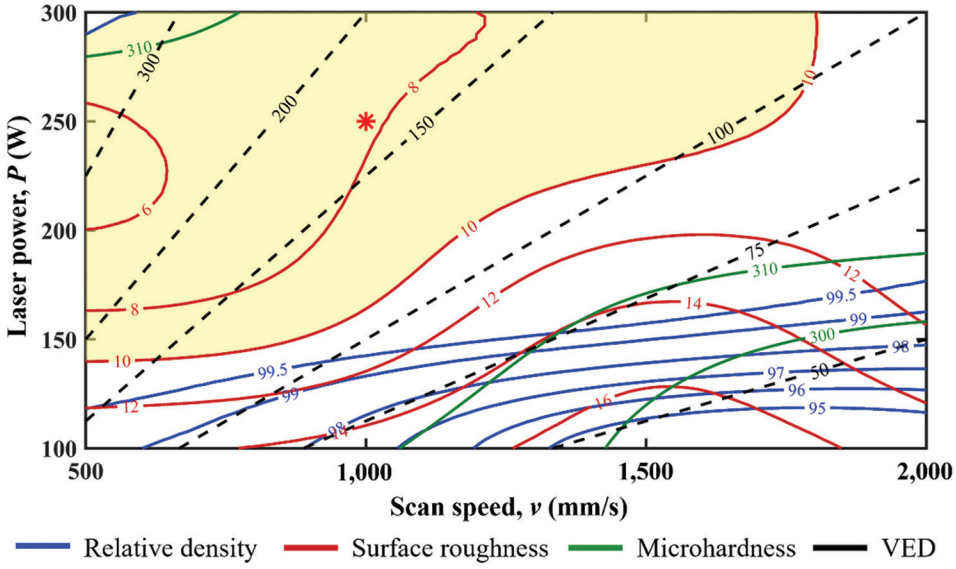

Figure 9. Laser power–scan speed process window based on Gaussian process regression models. The blue, red, and green lines represent relative density, surface roughness, and microhardness contours, respectively. The light yellow area highlights the predicted window to achieve near-pore-free parts with surface roughness ≤10 μm and microhardness ≥300 HV. The black dashed lines represent the VED contour lines. The red star indicates the optimal sample achieved in this study (relative density = 99.5%, surface roughness = 7.3 μm, and microhardness = 311 HV).

build with relative density = 99.5%, surface roughness = 7.3 μm, and microhardness = 311 HV. The process map in Figure 9 indicates that the optimal window offers a broader scan speed range to achieve the desired surface roughness, relative density, and microhardness values with a laser power of over 200 W. Specifically, concurrently optimizing all part properties within this laser power range appears unfeasible once the scan speed exceeds 1,750 mm/s. Furthermore, the tongue-shaped profile exhibited by the optimal window indicates a loss of optimization capability in the low-power region of the process map. The process was not able to meet all the target criteria below 150 W power, regardless of the scan speed. The shape of the optimal window also confirms that VED is a reliable predictor for surface roughness and relative density only in the high-power region. Despite the VED contour lines in Figure 9 bounding the optimal process window between 100 and 300 J/mm^3 in the first instance, this aggregate parameter cannot capture the complex interaction between laser power and scan speed. Under similar energy density conditions, specific power–speed combinations could not optimize IN725 parts manufactured by PBF-LB/M. In particular, in the low-power region of the process map, parts fabricated under optimal VED values may exhibit a coarse surface texture and microstructure characterized by lack-of-fusion pores. VED was confirmed to be a more precise indicator of microhardness.

Given that hatch spacing and layer thickness were not varied in this study, the process window in Figure 9 remains constrained to the specific combination of 30 μm layer thickness and 50 μm hatch distance. Its applicability to different parameter regimes should therefore be considered with caution.

4. Conclusion

This study optimized the process parameter combinations for PBF-LB/M to manufacture high-quality parts from waste material-derived IN725 alloy. Using recycled powder feedstock further demonstrated the feasibility of sustainable additive manufacturing for high-performance nickel-based superalloys. Experimental surface roughness, relative density, and microhardness measurements were used to train GPR models, considering either laser power and scan speed or VED as input variables. The high predictive accuracy of the models demonstrated the value of data-driven modeling in understanding and optimizing additive manufacturing processes. The promising results of the optimization mark a significant step toward establishing PBF-LB/M as a viable tool for establishing circular economy approaches within industrial practices and applying the process to different nickel-based superalloys. Compared to the prior work of Todaro *et al.*,[24] which was focused on the theoretical validation of IN725 printability, the present work provides a quantitative and application-oriented extension, offering a predictive framework for process control. Key findings include:

(i) The use of laser power and scan speed as separate inputs outperformed VED in predicting surface roughness and relative density. Even when fabricated under the same energy density, parts density and roughness can vary according to the specific combination of laser power and scan speed.

(ii) VED is a more accurate predictor of microhardness, reflecting a stronger correlation between energy input and mechanical properties. However, laser power and scan speed still offer precise point-wise predictions for microhardness when using a GPR model.

(iii) An optimal process window was identified in the laser power–scan speed space to achieve 99.5% relative density, 10 μm surface roughness, and 300 HV microhardness. The wide, tongue-shaped profile of the window underlined the higher sensitivity of the PBF-LB/M process to scan speed, as optimization loss was observed when reducing laser power.

While offering valuable insights and a robust foundation for PBF-LB/M process optimization using recycled IN725, the findings presented in this study represent a preliminary exploratory investigation. Future work should extend the present study by considering hatch distance and layer thickness, as process parameters are expected to influence defect formation and microstructural stability. Future studies could also investigate the effect of heat treatments on the mechanical properties of specimens manufactured with recycled IN725 powder. Furthermore, the modeling framework should be applied to a broader set of mechanical properties, including tensile, fatigue, and creep performance, to comprehensively evaluate recycled IN725 in demanding industrial environments. A comparative study with alternative approaches, including numerical models and other ML algorithms, could also be addressed. Such analyses would provide a clearer perspective on the relative merits and limitations of GPR. Due to its potential and accuracy, GPR offers a powerful tool for optimizing the production of this and other high-performance alloys across different metal additive manufacturing technologies. In this context, developing multi-output GPR models could favor a more holistic investigation of process–structure–property relationships, supporting more integrated optimization strategies.

Acknowledgments

The authors would like to thank Prof. Marco Actis of Politecnico di Torino for supplying the atomized powder used in this study.

Funding

This study was conducted within the MICS (Made in Italy-Circular and Sustainable) Extended Partnership and received funding from the European Union NextGenerationEU (PIANO NAZIONALE DI RIPRESA E RESILIENZA (PNRR)–MISSIONE 4 COMPONENTE 2, INVESTIMENTO 1.3–D.D. 1551.11-10-2022, PE00000004). This manuscript reflects only the authors' views and opinions; neither the European Union nor the European Commission can be considered responsible for them.

Conflict of interest

Mariangela Quarto and Gianluca D'Urso serve as the Editorial Board Members of the journal, but did not in any way involve in the editorial and peer-review process conducted for this paper, directly or indirectly. Other authors declare they have no competing interests.

Author contributions

Conceptualization: Gabriele Locatelli, Sara Bocchi
Data curation: Gabriele Locatelli, Sara Bocchi & Mariangela Quarto
Formal analysis: Gabriele Locatelli
Funding acquisition: Gianluca D'Urso
Investigation: Gabriele Locatelli
Methodology: Gabriele Locatelli, Sara Bocchi
Supervision: Mariangela Quarto Gianluca D'Urso
Writing–original draft: Gabriele Locatelli, Sara Bocchi
Writing–review & editing: Mariangela Quarto Gianluca D'Urso

Ethics approval and consent to participate

Not applicable.

Consent for publication

Not applicable.

Availability of data

Data are available from the corresponding author on reasonable request.

References

1. Reed RC. *The Superalloys*. Cambridge: Cambridge University Press; 2006.

   doi: 10.1017/CBO9780511541285

2. Smith RJ, Lewi GJ, Yates DH. Development and application of nickel alloys in aerospace engineering. *Aircr Eng Aerosp Tech.* 2001;73(2):138-147.

   doi: 10.1108/00022660110694995

3. Pollock TM, Tin S. Nickel-based superalloys for advanced turbine engines: Chemistry, microstructure and properties. *J Propuls Power.* 2006;22(2):361-374.

   doi: 10.2514/1.18239

4. Mali HS, Unune DR. Machinability of nickel-based superalloys: An overview. In: *Reference Module in Materials Science and Materials Engineering*. Netherlands: Elsevier; 2017.

   doi: 10.1016/B978-0-12-803581-8.09817-9

5. Tian Z, Zhang C, Wang D, *et al*. A review on laser powder bed fusion of inconel 625 nickel-based alloy. *Appl Sci.* 2020;10(1):81.

   doi: 10.3390/app10010081

6. Yu H, Zhao Q, Fu J, *et al*. The design of oxidation resistant Ni superalloys for additive manufacturing. *Addit Manuf.* 2025;97:104616.

   doi: 10.1016/j.addma.2024.104616

7. Chowdhury S, Yadaiah N, Prakash C, *et al*. Laser powder bed fusion: A state-of-the-art review of the technology, materials, properties & defects, and numerical modelling. *J Mater Res Technol.* 2022;20:2109-2172.

   doi: 10.1016/j.jmrt.2022.07.121

8. Zhao X, Wang T. Laser powder bed fusion of powder material: A review. *3D Print Addit Manuf.* 2023;10(6):1439-1454.

   doi: 10.1089/3dp.2021.0297

9. Sanchez S, Smith P, Xu Z, *et al*. Powder bed fusion of nickel-based superalloys: A review. *Int J Mach Tools Manuf.* 2021;165:103729.

   doi: 10.1016/j.ijmachtools.2021.103729

10. Kuntoğlu M, Salur E, Gupta MK, *et al*. A review on microstructure, mechanical behavior and post processing of additively manufactured Ni-based superalloys. *Rapid Prototyp J.* 2024;30(9):1890-1910.

    doi: 10.1108/RPJ-10-2023-0380

11. Volpato GM, Tetzlaff U, Fredel MC. A comprehensive literature review on laser powder bed fusion of Inconel superalloys. *Addit Manuf.* 2022;55:102871.

    doi: 10.1016/j.addma.2022.102871

12. Kim KS, Kang TH, Kassner ME, Son KT, Lee KA. High-temperature tensile and high cycle fatigue properties of inconel 625 alloy manufactured by laser powder bed fusion. *Addit Manuf.* 2020;35:101377.

    doi: 10.1016/j.addma.2020.101377

13. Serrano-Munoz I, Fritsch T, Mishurova T, *et al*. On the interplay of microstructure and residual stress in LPBF IN718. *J Mater Sci.* 2021;56(9):5845-5867.

    doi: 10.1007/s10853-020-05553-y

14. Song W, Yang J, Liang J, *et al*. A new approach to design

advanced superalloys for additive manufacturing. *Addit Manuf.* 2024;84:104098.

doi: 10.1016/j.addma.2024.104098

15. Enrique PD, Minasyan T, Toyserkani E. Laser powder bed fusion of difficult-to-print γ' Ni-based superalloys: A review of processing approaches, properties, and remaining challenges. *Addit Manuf.* 2025;106:104811.

doi: 10.1016/j.addma.2025.104811

16. Jena A, Atabay SE, Brochu M. Microstructure and mechanical properties of crack-free Inconel 738 fabricated by laser powder bed fusion. *Mater Sci Eng A.* 2022;850:143524.

doi: 10.1016/j.msea.2022.143524

17. Hu P, Liu Z, Zhang H, Li Y, Zhou Q, Xie J. Effect of remelting on cracking of Inconel 939 fabricated via laser powder bed fusion. *Mater Charact.* 2024;214:114087.

doi: 10.1016/J.MATCHAR.2024.114087

18. Wang Y, Li S, Ma R, *et al.* The effect of laser power on the microstructure and mechanical properties of LPBF Hastelloy X in as-built and heat-treated states. *Mater Charact.* 2025;227:115320.

doi: 10.1016/J.MATCHAR.2025.115320

19. Kenevisi MS, Martelli PA, Titonel I, Bassini E, Marchese G, Ugues D. The effect of solution annealing on additively manufactured and hot isostatically pressed René 80 Ni-based superalloy. *J Mater Res Technol.* 2024;33:6591-6600.

doi: 10.1016/j.jmrt.2024.11.003

20. Xi X, Lin D, Song X, *et al. In-situ* remelting induced healing of cracks and strength-ductility synergy in additively manufactured Haynes 230 alloy. *Addit Manuf.* 2025;98:104638.

doi: 10.1016/j.addma.2025.104638

21. Vilaro T, Colin C, Bartout JD, Nazé L, Sennour M. Microstructural and mechanical approaches of the selective laser melting process applied to a nickel-base superalloy. *Mater Sci Eng A.* 2012;534:446-451.

doi: 10.1016/j.msea.2011.11.092

22. Shoemaker LE. Alloys 625 and 725: Trends in properties and applications. In: *Conference. Superalloys 718, 625, 706 and Various Derivatives (2005).* TMS; 2005. p. 409-418.

doi: 10.7449/2005/Superalloys_2005_409_418

23. Sriwongsa K, Sirimongkolchaikul J, Sukrasorn C, *et al.* Radiation and fast neutron shielding properties of nickel-based superalloys: Inconel 600, 718 and 725 superalloys. *Integr Ferroelectr.* 2022;224(1):120-133.

doi: 10.1080/10584587.2022.2035602

24. Todaro CJ, Rashidi M, Liu RL, *et al.* Laser powder bed fusion of high-strength and corrosion-resistant Inconel alloy 725. *Mater Charact.* 2022;194:112454.

doi: 10.1016/j.matchar.2022.112454

25. Chia HY, Wu J, Wang X, Yan W. Process parameter optimization of metal additive manufacturing: A review and outlook. *J Mater Inform.* 2022;2(3):16.

doi: 10.20517/jmi.2022.18

26. Liu Q, Chen W, Yakubov V, Kruzic JJ, Wang CH, Li X. Interpretable machine learning approach for exploring process-structure-property relationships in metal additive manufacturing. *Addit Manuf.* 2024;85:104187.

doi: 10.1016/j.addma.2024.104187

27. Benedetti M, Perini M, Vanazzi M, Giorgini A, Macoretta G, Menapace C. Atomized scrap powder feedstock for sustainable Inconel 718 additive manufacturing via LPBF: A study of static and fatigue properties. *Prog Addit Manuf.* 2024;9(6):1843-1856.

doi: 10.1007/s40964-023-00547-z

28. Jelinski LW, Graedel TE, Laudise RA, McCall DW, Patel CK. Industrial ecology: Concepts and approaches. *Proc Natl Acad Sci USA.* 1992;89(3):793-797.

doi: 10.1073/pnas.89.3.793

29. Li J, Wang H. Gaussian processes regression for uncertainty quantification: An introductory tutorial. 2025.

doi: 10.48550/arXiv.2502.03090

30. Manfredi P, Trinchero R. A probabilistic machine learning approach for the uncertainty quantification of electronic circuits based on gaussian process regression. *IEEE Trans Comput Aided Des Integr Circ Syst.* 2022;41(8):2638-2651.

doi: 10.1109/TCAD.2021.3112138

31. Moges T, Ameta G, Witherell P. A review of model inaccuracy and parameter uncertainty in laser powder bed fusion models and simulations. *J Manuf Sci Eng.* 2019;141(4):040801.

doi: 10.1115/1.4042789

32. Lee SH. Optimization of cold metal transfer-based wire arc additive manufacturing processes using gaussian process regression. *Metals.* 2020;10(4):461.

doi: 10.3390/met10040461

33. Li H, Song B, Wang Y, Zhang J, Zhao W, Fang X. Laser powder bed fusion process optimization of CoCrMo alloy assisted by machine-learning. *J Mater Res Technol.* 2024;33:3901-3910.

doi: 10.1016/j.jmrt.2024.10.075

34. Maitra V, Shi J, Lu C. Robust prediction and validation of as-built density of Ti-6Al-4V parts manufactured via selective laser melting using a machine learning approach. *J Manuf Process.* 2022;78:183-201.

doi: 10.1016/j.jmapro.2022.04.020

35. El Hassanin A, Silvestri AT, Napolitano F, Borrelli D,

Caraviello A, Astarita A. Investigation of the laser-related parameters in laser-powder bed fusion of inconel 718-Cu blends at fixed volumetric energy density. *J Manuf Process.* 2023;99:456-468.

doi: 10.1016/j.jmapro.2023.05.068

36. Gobber FS, Priarone PC, Pennacchio A, Actis Grande M. Effect of inert gas pressure on the properties and carbon footprint of UNS S32760 powders made from waste materials by gas atomization. *J Mater Res Technol.* 2024;33:8814-8828.

doi: 10.1016/j.jmrt.2024.11.195

37. ASTM Standard B805-17 2017. *Specification for Precipitation Hardening Nickel Alloys Bar and Wire.* United States: ASTM International. Preprint posted online; 2017.

doi: 10.1520/B0805-06R17E01

38. ASTM Standard F3055-14a 2021. *Specification for Additive Manufacturing Nickel Alloy (UNS N07718) with Powder Bed Fusion*. United States: ASTM International. Preprint posted online; 2021.

doi: 10.1520/F3055-14AR21

39. ASTM Standard B212-25 2025. *Test Method for Apparent Density of Free-Flowing Metal Powders Using the Hall Flowmeter Funnel*. United States: ASTM International. Preprint posted online; 2025.

doi: 10.1520/B0212-25

40. ASTM Standard B213-25 2025. *Test Methods for Flow Rate of Metal Powders Using the Hall Flowmeter Funnel*. United States: ASTM International. Preprint posted online; 2025.

doi: 10.1520/B0213-25

41. King WE, Anderson AT, Ferencz RM, *et al*. Laser powder bed fusion additive manufacturing of metals; physics, computational, and materials challenges. *Appl Phys Rev.* 2015;2(4):041304.

doi: 10.1063/1.4937809

42. Yadroitsev I, Bertrand P, Smurov I. Parametric analysis of the selective laser melting process. *Appl Surf Sci.* 2007;253(19):8064-8069.

doi: 10.1016/J.APSUSC.2007.02.088

43. Kamath C, El-Dasher B, Gallegos GF, King WE, Sisto A. Density of additively-manufactured, 316L SS parts using laser powder-bed fusion at powers up to 400 W. *Int J Adv Manuf Technol.* 2014;74(1-4):65-78.

doi: 10.1007/S00170-014-5954-9/METRICS

44. Chen Z, Wie Z, Wie P, *et al*. Experimental research on selective laser melting AlSi10Mg alloys: Process, densification and performance. *J Mater Eng Perform*. 2017;26(12):5897-5905.

doi: 10.1007/s11665-017-3044-5

45. Tian Y, Tomus D, Rometsch P, Wu X. Influences of processing parameters on surface roughness of Hastelloy X produced by selective laser melting. *Addit Manuf.* 2017;13:103-112.

doi: 10.1016/j.addma.2016.10.010

46. Baldi N, Giorgetti A, Palladino M, Giovannetti I, Arcidiacono G, Citti P. Study on the effect of preheating temperatures on melt pool stability in inconel 718 components processed by laser powder bed fusion. *Metals*. 2023;13(10):1792.

doi: 10.3390/met13101792

47. ASTM Standard E384-22 2022. *Test Method for Microindentation Hardness of Materials.* United States: ASTM International. Preprint posted online; 2022.

doi: 10.1520/E0384-22

48. Locatelli G, Quarto M, D'Urso G, Giardini C. Addressing positional and laser source variability in laser powder bed fusion: A mapping method for quality optimization. *Int J Adv Manuf Technol*. 2025;139:4673-4686.

doi: 10.1007/s00170-025-16196-1

49. Williams CKI. Prediction with Gaussian processes: From linear regression to linear prediction and beyond. In: *Learning in Graphical Models*. Berlin: Springer Netherlands; 1998. p. 599-621.

doi: 10.1007/978-94-011-5014-9_23

50. Yang K, Lu J, Wan W, Zhang G, Hou L. Transfer learning based on sparse Gaussian process for regression. *Inform Sci.* 2022;605:286-300.

doi: 10.1016/j.ins.2022.05.028

51. Aggarwal CC. *Neural Networks and Deep Learning*. Berlin: Springer International Publishing; 2023.

doi: 10.1007/978-3-031-29642-0

52. De Oliveira V, Han Z. On information about covariance parameters in gaussian matérn random fields. *J Agric Biol Environ Stat*. 2022;27(4):690-712.

doi: 10.1007/s13253-022-00510-5

53. Neal RM. *Bayesian Learning for Neural Networks*. Vol. 118. Berlin: Springer New York; 1996.

doi: 10.1007/978-1-4612-0745-0

54. Pan R, Gu M, Wu J. Physics-informed Gaussian process regression of in operando capacitance for carbon supercapacitors. *Energy Adv.* 2023;2(6):843-853.

doi: 10.1039/D3YA00071K

55. Hashemi SH, Torabi F, Tontiwachwuthikul P. Machine learning-driven prediction of CO_2 solubility in brine: A hybrid grey wolf optimizer (GWO)-assisted gaussian process regression (GPR) *Approach Energies*. 2025;18(15):4205.

doi: 10.3390/en18154205

56. Hair JF, Black WC, Babin BJ, Anderson RE. *Multivariate Data Analysis.* London: Pearson Education Limited; 2014.

57. Willmott C, Matsuura K. Advantages of the mean absolute error (MAE) over the root mean square error (RMSE) in assessing average model performance. *Clim Res.* 2005;30:79-82.

doi: 10.3354/cr030079

58. Piriz AR, Cortázar OD, López Cela JJ, Tahir NA. The Rayleigh-Taylor instability. *Am J Phys.* 2006;74(12):1095-1098.

doi: 10.1119/1.2358158

59. Chivel Y. Optical in-process temperature monitoring of selective laser melting. *Phys Procedia.* 2013;41:904-910.

doi: 10.1016/j.phpro.2013.03.165

60. Mannan S, Veltry F. Time-temperature-transformation diagram of alloy 725. In: *Superalloys 718, 625, 706 and Various Derivatives (2001)*. Warrendale: TMS; 2001. p. 345-356.

61. Javidrad HR, Salemi S. Effect of the volume energy density and heat treatment on the defect, microstructure, and hardness of L-PBF inconel 625. *Metall Mater Trans A.* 2020;51(11):5880-5891.

doi: 10.1007/s11661-020-05992-x

62. Capelli A, Cacace S, Semeraro Q. XCT characterization and mechanical properties of Ti6Al4V produced by L-PBF using the same volumetric energy density. Progress in Additive Manufacturing. *Prog Addit Manuf.* 2025;10:4787-4802.

doi: 10.1007/s40964-024-00862-z

63. Wang S, Ning J, Zhu L, *et al.* Role of porosity defects in metal 3D printing: Formation mechanisms, impacts on properties and mitigation strategies. *Mater Today.* 2022;59:133-160.

doi: 10.1016/j.mattod.2022.08.014

Our Journals

International Journal of Bioprinting is an international journal covering the technology, science and clinical application of the broadly defined field of Bioprinting. Bioprinting is defined as the use of 3D printing technology with materials that incorporate viable living cells or biological elements to produce tissue or biotechnological products. We are interested in the scientific topics spanning all stages of bioprinting process from concept creation to fabrication and beyond. Knowledge generated in these researches must be related to bioprinting. *IJB* covers subject areas, including but not limited to the following:

- Information technologies and basic research
- Materials and formulation
- Cell source and biotechnology for additive manufacturing
- 3D Bioprinting technologies
- New design and fabrication paradigm
- Applied research purpose & evaluation of 3D printed products
- Associated social implications

International Journal of AI for Materials and Design is an international, peer-reviewed open-access journal that aims to bridge the cutting-edge research between AI and materials, AI and design. In recent years, the tremendous progress in AI is leading a radical shift of AI research from a mainly academic endeavor to a much broader field with increasing industrial and governmental investments. The maturation of AI technology brings about a step change in the scientific research of various domains, especially in the world of materials and design. Machine learning (ML) algorithms enable researchers to analyze extensive datasets on material properties and accurately predict their behavior in different conditions. This subsequently impact the industry to leverage on big data and advanced analytics to build scientific strategies, scale operational performance of processes and drive innovation. In addition, AI and ML are uniquely positioned to enable advanced manufacturing technologies across the value chain of different industries. Integration of multiple and complementary AI techniques, such as ML, search, reasoning, planning, and knowledge representation, will further accelerate advances in scientific discoveries, engineering excellence and the future of cyber-physical systems manufacturing.

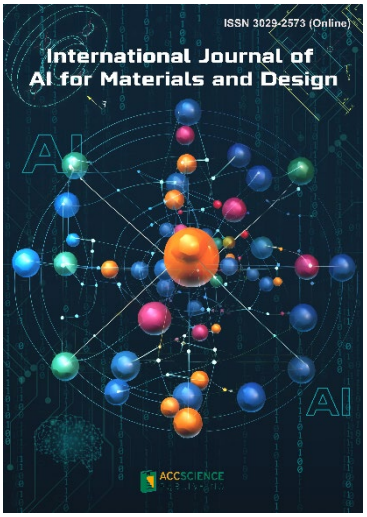

International Journal of AI for Materials and Design covers the following topics: AI or machine learning for material discovery, AI for process optimization, AI and data-driven approaches for product or systems design, application of AI in advanced manufacturing processes such as additive manufacturing, IoT, sensors, robotics, cloud-based manufacturing, intelligent manufacturing for various applications, autonomous experiments, material intelligence, energy intelligence, and AI-linked decarbonization technologies.

Start a new journal

Write to us via email if you are interested to start a new journal with AccScience Publishing. Please attach your CV, professional profile page and a brief pitch proposal in your email. We shall inform you of our decision whether we are interested to collaborate in starting a new journal.

Contact: info@accscience.com

https://accscience.com/journal/MSAM

Access Science Without Barriers

Contact

www.accscience.com
9 Raffles Place, Republic Plaza 1 #06-00 Singapore 048619
E-mail: editorial@accscience.com
Phone: +65 8182 1586